Development of Superconducting Thin Film Travelling Wave Parametric Amplifiers

Joseph Christopher Longden

Balliol College

University of Oxford

A thesis submitted for the degree of

Doctor of Philosophy

Michaelmas 2023

"Looking at these stars suddenly dwarfed my own troubles and all the gravities of terrestrial life."

- H.G. Wells,
The Time Machine

Abstract

Ultra low-noise amplification is crucial for various fundamental physics platforms, including microwave/mm/sub-mm astronomy, dark matter search experiments, neutrino mass experiments, and qubit readout. Superconducting kinetic inductance travelling-wave parametric amplifiers (KITWPAs) are a recent development in amplifier technology, which are able to achieve high gain over broad bandwidth by efficiently transferring power from a strong 'pump' wave to a detected weak 'signal' wave via the wave mixing mechanisms in a non-linear medium comprising a high kinetic inductance wire. They have been experimentally verified to achieve high gain over broad bandwidth and quantum-limited noise performance with negligible heat dissipation, making them a natural successor to the current generation of semiconductor-based high electron mobility transistor (HEMT) amplifiers, which are the current standard in low-noise amplification. The elimination of the resonant architecture associated with earlier parametric amplifiers removes the narrow-band restrictions on these KITWPAs, which combined with their low heat dissipation and power requirements makes them readily scalable to arrays for large pixel count applications, such as the readout of astronomical detector arrays or qubit arrays.

This thesis focuses on the development of microwave KITWPAs in the frequency range of 2-18 GHz, made from titanium nitride (TiN) superconducting transmission lines, a material chosen as it displays many of the desired characteristics for KITWPA operation, namely high resistivity, high kinetic inductance, and mechanical robustness, as well as being a commonly used material in the field of microwave kinetic inductance detectors (MKIDs). The choice in material and topology for a KITWPA device, however, is not typically discussed in the literature, hence to understand the design considerations for a KITWPA device, we commence an investigation into KITWPA material and topology choice. Based on this analysis, we present an optimised TiN KITWPA design, which was designed using a commercial 3-D electromagnetic simulator (HFSS) and a complementary python package (SuperTWPA).

Although measurements of our KITWPA devices revealed unexpected losses, we were able to achieve a peak averaged gain of 5 dB with a bandwidth of $\sim 3 - 13$ GHz when operating in a three-wave mixing (3WM) mode, making this, to the best of our knowledge, the first broadband gain measurement of a TiN KITWPA reported in the literature. The behaviour of the TiN film additionally points to physics beyond standard BCS theory, which could form the basis of future analysis of the

microphysics of the material. We conclude our experimental work with a number of design improvements, which we believe could ultimately lead to a high-gain TiN KITWPA device.

At time of writing this thesis, KITWPAs are yet to be widely used in large-scale experiments due to a number of operational obstacles. We, therefore, conclude this thesis with a number of design concepts that could provide solutions to these operational obstacles, beginning with a dual-pump KITWPA to provide wideband amplification at millimetre (mm) frequencies, before introducing a balanced KITWPA concept; a novel parallel TWPA architecture, which we demonstrate to be able solve the signal-idler contamination problem in KITWPAs and to simplify the pump injection and cancellation schemes, paving the way for the widespread operation of KITWPAs in ultra-sensitive experimental setups.

Statement of Originality

I carried out the work presented in thesis at the Department of Astrophysics, University of Oxford between October 2019 and October 2023, under the supervision of Dr Boon Kok Tan and Dr Peter Leek. My place was funded by a Science Technology Facilities Council (STFC) Studentship. I hereby declare that no part of this thesis has been submitted in support of another degree, diploma or other qualification at the University of Oxford or other higher learning institute. Except where otherwise stated or where reference is made to the work of others, the work in this thesis is entirely my own. The total length of this thesis does not exceed 250 pages.

The work in Chap. 3 was carried out in collaboration with Boon Kok Tan, Faouzi Boussaha, Christine Chaumont, and Javier Navarro Montilla and is published in [1]. The work carried out in § 2.7.3 was published in the Proceedings of SPIE 12190, Millimeter, Submillimeter, and Far-Infrared Detectors and Instrumentation for Astronomy XI, and I am the lead author [2]. The work in § 5.3 was published in the Proceedings of the International Symposium of Space Terahertz Technologies 2022 and I am the lead author [3]. The majority of the rest of Chap. 5 is presented in a manuscript where I am the first author, which is in preparation and will be submitted to Open Research Europe for peer review. The work in § 6.2 was carried out in collaboration with Boon Kok Tan, and has been summarised in a manuscript, which has been submitted to Engineering Research Express for peer review, for which I will be the lead author. The work in § 6.3 was carried out in collaboration with Boon Kok Tan and we have applied for IP protection via a patent with UK Patent Application No: 2311659.3. We have also submitted a manuscript of this work to Physica Scripta for peer review, for which I will be the lead author.

All devices in this thesis that were experimentally characterised in Oxford were fabricated at the Observatoire de Paris by our collaborators, Dr Faouzi Boussaha and Dr Christine Chaumont.

Joseph C. Longden
(*September 2023*)

COVID-19 Disclaimer

The majority of the work presented in this thesis was undertaken during the COVID-19 global pandemic. The onset of the pandemic and the Government-imposed lockdown in April 2020 came during the first year of my DPhil, which meant a prolonged period without lab access. Whilst this was mitigated somewhat by a shift in focus towards computational work, the lack of dedicated workspace and lack of social contact severely disrupted work. Even when I was permitted to return to the lab, progress was further hindered by a delay in getting the experimental cryostats online due to the inability of engineers to travel to Oxford from Finland, a lack of received KITWPA samples due to continued French lockdown rules imposed on our collaborators, and lasting disruption to global supply chains, meaning we could not order experimental components that we required. The result of this has meant that virtually all experimental data presented in this thesis was taken in the final nine months of my four-year DPhil programme.

I would further add to this that my DPhil project is the first project that my research group has undertaken on parametric amplifier research, hence there are many trivial techniques I had to learn that seem unimportant but are crucial to get right. Some of these tasks include, but are not limited to, cleaning the devices, mounting the devices, bonding the devices, etc. All of these minute details take years to sufficiently master, even though they seem unimportant and too trivial to be included in this thesis. With the COVID disruption, it was not just me but the whole group who were unable to access the lab and learn these subtle procedural details from the start of my DPhil programme, hence even in the final nine months, considerable time and effort was invested in getting these details correct.

List of Publications

- Joseph C. Longden, Faouzi M. Boussaha, Christine Chaumont, Kitti Ratter, and Boon-Kok Tan. "Preliminary characterisation of titanium nitride thin film at 300 mK for the development of kinetic inductance travelling wave parametric amplifiers." *Quantum Technology: Driving Commercialisation of an Enabling Science II*, 1188113(October 2021):38, 2021

- Joseph C. Longden, Christine Chaumont, Faouzi M. Boussaha, and Boon-Kok Tan. "A compact kinetic inductance travelling wave parametric amplifier with continuous periodic loading structure." *Proc. SPIE 12190, Millimeter, Submillimeter, and Far-Infrared Detectors and Instrumentation for Astronomy XI*, 12190(121902X):38, 2022

- Joseph C. Longden, Faouzi M. Boussaha, Christine Chaumont, Nikita Klimovich, and Boon-Kok Tan. "Measuring the nonlinearity of titanium nitride film for applications as kinetic inductance travelling wave parametric amplifiers." In *Proceedings of the 32nd International Symposium on Space Terahertz Technology*, 2022.

- Boon-Kok Tan, Faouzi M. Boussaha, Christine Chaumont, Joseph C. Longden, and Javier Navarro Montilla. "Engineering the thin film characteristics for optimal performance of superconducting kinetic inductance amplifiers using a rigorous modelling technique." *Open Research Europe*, 2:88, 2022

- Joseph C. Longden and Boon-Kok Tan. "Non-Degenerate Four-Wave Mixing Kinetic Inductance Travelling-Wave Parametric Amplifiers." Submitted to *Engineering Research Express*, 2023

- Joseph C. Longden, Javier Navarro Montilla, and Boon-Kok Tan. "Balanced Travelling-Wave Parametric Amplifiers for Practical Applications" Submitted to *Physica Scripta*, 2023

- Joseph C. Longden, Faouzi M. Boussaha, Christine Chaumont, Nikita Klimovich, Samuel Wood, and Boon-Kok Tan. "Preliminary Characterisation of Titanium Nitride Kinetic Inductance Travelling-Wave Parametric Amplifiers" In preparation, 2023.

Acknowledgements

A PhD is an enormous undertaking during the life of a researcher; however, it is not something that one undertakes alone, therefore, there are a number of people to whom I must express my deepest gratitude.

I would first like to thank my supervisor, Dr Boon Kok Tan, for his enormous support and guidance throughout my DPhil and for helping to shape me into an independent researcher, as well as for the copious number of pints bought for me over the years, I definitely owe you one! I would like to thank Prof Ghassan Yassin, for interesting discussions and insight related to both the theoretical and experimental aspects of my work, as well as for inviting me to lunch at Queen's College when I was applying for my DPhil at Oxford; it definitely sweetened the deal! I would like to say a huge thanks to our lab technician Rik Elliot for designing and building virtually every single electronics-related component in the lab; the lab wouldn't function without you! I would like to thank Dr Faouzi Boussaha and Dr Christine Chaumont at the Observatoire de Paris, for being completely dedicated to our group's KITWPA project and for always finding time to fabricate our devices. I'd like to say thanks to Paul Pattinson for training on the wire-bonder (not sure if that's a gift or a curse!) and for providing wisdom on anything and everything related to lab operations; except refilling the liquid nitrogen, of course! I'd like to thank Ashling Gordon and Leanne O'Donnell for being able to solve basically everything admin-related, or at least knowing the exact person who can solve it. I'd like to say thanks to group postdocs, Dr Kitti Ratter and Dr Nikita Klimovich, for providing support and guidance during the early and latter stages of my DPhil, respectively. I would like to say a special thanks to my master's supervisor from the University of Bristol, Prof Mark Birkinshaw, who died shortly before the completion of this thesis, for writing an academic reference for my DPhil application and for generally helping me along my way from my undergraduate to doctoral studies. I'd like to thank my fellow group DPhil students, Jakob Wenninger and Javier Navarro Montilla for our camaraderie through the good and the bad, as well as being a source of entertainment during those long (often fruitless) hours in the lab; I raise a *tinto de verano* to you both! I'd like to thank my friends and family, especially my parents, Su and Ju, and my sister, Liza, for their constant love and support throughout my DPhil and beyond. Last, but by no means least, I'd like to thank my dearest Vivian for her love, support, and for generally making life a brighter place. I love you xxx

Contents

List of Figures

List of Tables

Chapter 1

Introduction

1.1 Scientific Motivations

Amplifiers are crucial components in many scientific applications. They boost the power of an incoming signal, which reduces the degradation of the signal-to-noise ratio (SNR) of a receiver chain. Let us consider a chain of N cascaded components that each have a noise temperature of T_n and a gain of G_n. The total noise temperature of the system, T_{sys} is given by,

$$T_{\text{sys}} = T_1 + \frac{T_2}{G_1} + \frac{T_3}{G_1 G_2} + \cdots + \frac{T_N}{G_1 G_2 \ldots G_{N-1}}, \tag{1.1}$$

which is known as Friis' law [4]. If the gain of the first component, G_1, is sufficiently large, then T_{sys} is dominated by T_1, even when the noise temperatures of the proceeding components are reasonably large. It is clear, therefore, that to minimise T_{sys}, it is desired that the first component in the receiver chain is a low-noise amplifier.

1.1.1 Astrophysics

The 1 GHz - 1 THz range of the electromagnetic spectrum is rich in astronomical signals, the measurement of which will greatly improve our understanding of the Universe. Some recent examples of this are measurements of the CO $J = 3 \rightarrow 2$ emission line using the NOrthern Extended Millimeter Array (NOEMA) and the Atacama Large Millimeter/submillimeter Array (ALMA) to understand the star formation process in luminous galaxies [5], observations of the radio afterglow curves

from gamma-ray bursts (GRBs) using the enhanced Multi Element Remotely Linked Interferometer Network (eMERLIN) [6], measurements of interstellar dust emission using the Planck telescope [7], observations of the supermassive black hole at the centre of M87 using the Event Horizon Telescope [8], measurements of high-redshift quasars to understand early black hole formation [9], and studies of the cosmic microwave background (CMB) such as measurements of the Sunyaev-Zel'dovich effect [10].

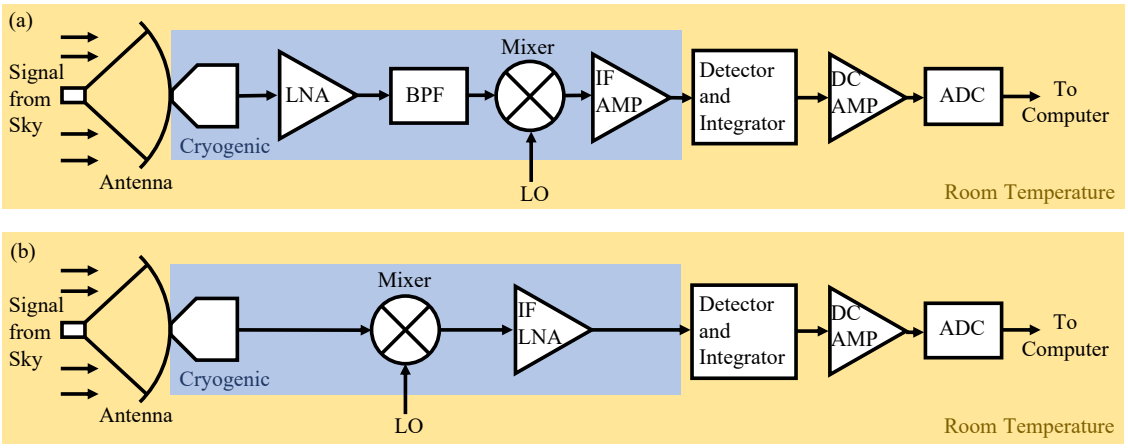

Figure 1.1: (a) Schematic of a typical radio telescope receiver [11]. From left to right: antenna comprising various warm and cold optics, low-noise amplifier (LNA), band-pass filter (BPF), mixer (which combines local oscillator (LO) with the signal from the sky), intermediate frequency (IF) amplifier, detector and integrator, DC amplifier, and analogue-to-digital converter (ADC). (b) Schematic of typical mm/sub-mm telescope receiver, which almost the same as (a), except the mixer is the first component after the antenna, which is followed by an IF LNA. Note that both configurations may contain other components, such as bias-tees and circulators, which are omitted here for clarity.

Measurements of these signals are carried out using radio/mm/sub-mm telescopes [12–16], which are carefully designed and optimised to measure and process signals over the 1 GHz - 1 THz frequency range. Fig. 1.1(a) shows the schematic of a typical radio/microwave telescope receiver, highlighting the key components required for the receiver to work. It naturally makes sense that the first component after the antenna is a high-gain, low-noise amplifier (LNA), as from (1.1), this means that the noise of the entire receiver chain is dominated mostly by the noise performance of the LNA. For mm/sub-mm receivers, as shown in Fig. 1.1(b), there currently exists no widely available amplifier technology that operates at these frequencies, hence the LNA is placed after the mixer where it amplifies the detected

signal after it has been down-converted to lower frequencies.

Quantum mechanics sets a fundamental limit on the minimum amount of noise that can be added to a received signal as half a photon of energy [17], hence it is desirable for the LNA to achieve as close to this performance as possible. The current state-of-the-art LNAs used in astronomical applications are mostly based on high electron mobility transistors (HEMTs), which typically operate at bath temperatures around 4 K [18–20]. Although these LNAs are able to achieve large gains over wide bandwidths, they have typical added noise values of 5 - 10 times the quantum limit [21]. In addition, these semiconductor-based devices dissipate a substantial amount of heat, which means scaling them for large pixel count applications in cryogenic environments becomes challenging due to the large cooling power requirements and large power consumption.

To understand the importance of quantum-noise-limited amplification, a recent study [22] analysed the additional scientific capabilities of an ALMA receiver if a sub-mm frequency quantum-limited amplifier was used prior to down-conversion. Using the Band 3 receivers as an example, which currently have noise temperatures of $\sim$38 K over their 84-116 GHz band [23], the authors demonstrated how the introduction of a quantum-limited front-end amplifier could lead to a factor of $\sim$5 improvement in the receiver noise temperature, which translates to a doubling of system sensitivity and a factor of four increase in observation efficiency/speed of the array. This is highly desirable for astronomers, who are keenly aware of the huge competition when applying for telescope time. This analysis highlights the importance in developing ultra-low-noise front-end amplifiers for radio/mm/sub-mm astronomy.

As an intermediate step, it would also be of merit to develop ultra-low-noise IF amplifiers for back-end sub-mm receivers, as this would still have an enormous impact on the noise performance of the receiver chain since the conversion gain of the mixers is often below 0 dB [24–26]. This is especially true for THz mixers [27,28] and HEB mixers [29,30], where the conversion gain is much worse, hence from (1.1), T_{sys} will be much higher. The use of quantum-limited amplifiers will, therefore, significantly improve T_{sys} of these receiver chains, even when they are used as IF amplifiers.

Quantum-limited amplifiers at these frequencies will also be of enormous importance for bolometric telescope receivers, such as those utilising microwave kinetic inductance detectors (MKIDs) [31], which are typically read out using the same

HEMT-based LNAs that are employed in the readout of heterodyne receivers. MKID detectors can be read out via frequency multiplexing, meaning that a single wide-band amplifier can read out many MKIDS simultaneously. The current and next generation of MKID array telescopes are demanding $10^5 - 10^7$ MKID pixels [32, 33], which means that even if a single LNA could read $\sim 10^3$ MKID detectors, then $10^2 - 10^4$ LNAs would be required to meet the array scaling demands. The substantial heat dissipation produced by the current generation of HEMT LNAs makes cryogenic MKID arrays of this size completely unfeasible without the development of new amplifier technology that deposits very little heat at the cryogenic stages of the receivers. This argument can also be extended to heterodyne SIS/HEB receiver arrays [34, 35], where, for example, a sideband-separated, dual-polarisation SIS mixer requires four LNAs per pixel [36], meaning large-scale pixel arrays quickly become impractical. This consideration is also crucial for space-based missions, where the cooling power provided by the on-board systems is typically much smaller than that provided by ground-based cryogenic systems, and is also finite. The lifetime space-based missions could, therefore, be greatly extended by the use of amplification with very low heat dissipation.

1.1.2 Quantum Computing

Quantum computing is an alternative paradigm of information processing that uses the principles of quantum mechanics to quickly perform extremely complex calculations that would take a classical computer an unfeasible amount of time to perform [37]. Whereas the building blocks of a classical computer, a bit, is assigned one of either two states, 0 or 1, the building block of a quantum computer, a quantum bit (qubit), can be in a linear superposition of both states, a property that is exploited by quantum algorithms to perform extremely fast calculations of certain problems.

The readout of superconducting [38] and semiconductor-based [39] qubits typically involves coupling the qubit to a readout resonator, the resonant frequency of which is dependent upon the state of the qubit. In order not to disturb the qubit state, the readout power must be extremely low, necessitating the use of cryogenic LNAs to achieve a high qubit readout fidelity. Since the readout frequencies are typically a few GHz, the amplification of the qubit readout was traditionally done with same type of HEMT-based LNAs as discussed in § 1.1.1, however, the relatively large noise performance and heat dissipation required relatively long readout times

for high-fidelity qubit measurements. A more recent development in qubit readout is the use of superconducting Josephson Parametric Amplifiers (JPAs), which will be discussed further in § 1.3.1. The use of JPAs has been demonstrated to improve the SNR of the qubit readout by a factor of 1000 due their superior noise performance [40], however, they are severely limited in their bandwidth, which means only a single qubit can be read out per amplifier, which presents a significant bottleneck in the scaling of quantum computers to thousands of qubits. Additionally, JPA operation requires the use of an additional circulator before the JPA, which degrades the signal and takes up valuable space in the cryogenic qubit environment.

1.1.3 Other Fundamental Physics Experiments

This section briefly describes a number of further fundamental physics experiments, which would greatly benefit from ultra-low-noise amplification at microwave frequencies.

It is postulated that dark matter could exist in the form of axions, which are hypothetical massive particles predicted by Peccei–Quinn theory [41] as a solution to the strong CP problem in particle physics. Axion dark matter search experiments [42–44] exploit a mixing term in the Lagrangian that, hypothetically, allows axion particles to couple to visible photons, allowing the presence of axions to be inferred from the detection of these photons. The radiation produced by this mechanism is very week, and since the mass of the axion particle is unknown, the frequency of the radiation is also unknown. Experiments searching for axion dark matter particles, therefore, require the use of quantum-limited, broadband amplifiers in order to efficiently search the huge parameter space with ultra-high sensitivity.

The mass of a neutrino was long held to be zero, however, measurements of oscillations between neutrino flavours revealed them to have a very small, non-zero mass [45]. Whilst neutrinos are now known to have a finite mass, measurements to date are only able to provide the difference in the mass squared between different mass eigenstaes, rather than their absolute mass. Despite this, experimental techniques have been identified, which could allow the absolute neutrino masses to be ascertained, such as the measurements of the cyclotron radiation emission spectrum from tritium decays [46]. The power of the cyclotron radiation from this process is expected to be extremely small, $\sim 1\,\mathrm{fW}$, and in the microwave frequency range [46], hence, quantum-noise limited amplifiers are crucial in making measurements of the

absolute neutrino mass, a property which could lead to a deeper understanding of the matter-antimatter asymmetry in the universe.

1.2 Amplifier Figures of Merit

This thesis concerns the design and characterisation of superconducting amplifier technology, hence it is useful to define some figures of merit for amplifier operation, which can be used to quantify the behaviour of an amplifier and compare it's performance to other amplifiers.

- **Gain** – A measure of the ability of a device to increase the power or amplitude of an incoming signal, typically expressed as the ratio of the output signal power to the input signal power.
- **Bandwidth** – For an amplifier, this is the difference between the highest and lowest frequencies in a continuous frequency band, and is a measure of the range of frequencies over which the amplifier operates. The endpoint frequencies are often defined as the frequencies at which the gain is 3 dB lower than the maximum gain.
- **Dynamic Range** – A measure of the range of signal powers over which the amplifier operates, and is typically defined as the ratio of the maximum power level that can be handled by the device to the minimum detectable power level.
- **Noise Figure** – A measure of the degradation of the signal-to-noise ratio (SNR) by an amplifier due to the introduction of additional noise by the device, typically defined as the ratio of the output SNR to the input SNR.
- **Gain Uniformity** – A measure of how the gain varies as a function of frequency, and can be interpreted as the flatness of the gain profile.
- **Stability** – A measure of how much the amplifier performance changes or oscillates when the input signal changes, and is often a chaotic response.

An ideal amplifier will produce a large gain over an infinite, continuous bandwidth and dynamic range whilst adding zero noise to the amplified signal. In reality, however, there are fundamental limits on the values of these figures of merit. Although Johnson-Nyquist noise [47–49] can be made vanishingly small by cooling the

amplifier to cryogenic temperatures, the total noise figure of an (phase-insensitive) amplifier will always be non-zero due to the existence of quantum noise, which arises due to the uncertainty principle. This added quantum noise is equal to half a photon of added energy [17], and is referred to as the standard quantum limit (SQL) of noise. This SQL can be expressed as a noise temperature using,

$$T_{\mathrm{SQL}} = \frac{hf}{2k_B}, \tag{1.2}$$

where T_{SQL} is the noise temperature at the SQL, h is Planck's constant, f is the frequency at which T_{SQL} is measured, and k_B is Boltzmann's constant. From (1.2), we clearly see that T_{SQL} is dependent on f, with T_{SQL} being approximately given as $\sim$24 mK GHz^{-1}, hence the lower limit of an amplifier's noise performance is also dependent on the operating frequency of the device.

The dynamic range is also in-part limited by the noise performance of the amplifier, as the minimum detectable signal power is given by the noise level at the input of the amplifier. The maximum power level of the amplifier is limited by the supply voltage in the case of transistor-based amplifiers, and by the critical current of the superconducting material in the case of superconducting amplifiers.

Whilst the gain and bandwidth are usually limited by amplifier design choices, another useful figure of merit to consider is the gain-bandwidth product. It is observed in operational amplifiers that the gain-bandwidth product is largely constant as the peak gain is varied [50], i.e., as the peak gain is increased, the bandwidth decreases, indicating constraints on this value, which have been explored theoretically [51–53]. Whilst the particular gain-bandwidth product value is dependent on the particular amplifier design, this example highlights additional limitations placed on the figures of merit listed above, as modifying one of them will have an effect on one or more of the other parameters, hence it is not possible to optimise all of the various figures of merit simultaneously.

Whilst the development of broadband superconducting parametric amplifiers promises to produce exceptionally good values for all the amplifier figures of merit listed above, this thesis focuses on the gain and bandwidth performances of the amplifier, as this is the natural first step in the development of a broadband amplifier. An investigation into the characterisation and optimisation of the noise performance and dynamic range of the amplifiers will form the basis of future work that is not discussed in this thesis.

1.3 Parametric Amplifiers

1.3.1 Operational Principles

Parametric amplifiers are a type of amplifier that transfer energy from a strong 'pump' tone to an incoming signal by modulating some non-linear parameter of the amplifier, a process known as 'pumping' [54]. Crucially, it should be stressed here that it is this non-linearity that allows power transfer to occur during any of the parametric processes discussed in this section. A classical example of parametric amplification, as shown in Fig. 1.2, is that of a child on a swing [55], whereby the motion of the child changes the moment of inertia of the swing. If the child 'pumps' on the swing by modulating the angle, θ, according to,

$$\theta = \theta_0 \cos \omega t, \tag{1.3}$$

where θ_0 is the amplitude of the angle modulation, ω is the angular frequency of the modulation, and t is time, a subsequent analysis of the equations of motion of the system reveals that the amplitude of ϕ, which is the angle between the swing and the vertical, increases, thus the motion of the swing is amplified.

Early RF parametric amplifiers operated by pumping the voltage-dependent capacitance of varactor diodes to achieve amplification of weak input signals [56]. These varactor-based amplifiers were demonstrated to have a much lower noise than their contemporary amplifier technologies based on transistors or vacuum tubes, since the pumping on the capacitance varied the reactive component of the amplifier impedance instead of resistive component, which is the component that induces extra noise.

The advancement of cryogenic technology over the last century has led to the development of superconducting parametric amplifiers. Early superconducting parametric amplifier designs utilised the non-linearity of Josephson Junctions (JJs) [57], to promote wave mixing between a strong pump tone and a weak signal tone. Since the amount of wave mixing, and hence gain, is dependent on the interaction time between the weak signal and the strong pump, the JJs were embedded within a multiple reflection resonant cavity [58] to increase the interaction time between the tones. These devices are known as Josephson parametric amplifiers (JPAs) and have found use in the readout of qubits [59–61] and dark matter search experiments [42, 62], where they have demonstrated quantum-limited noise and large

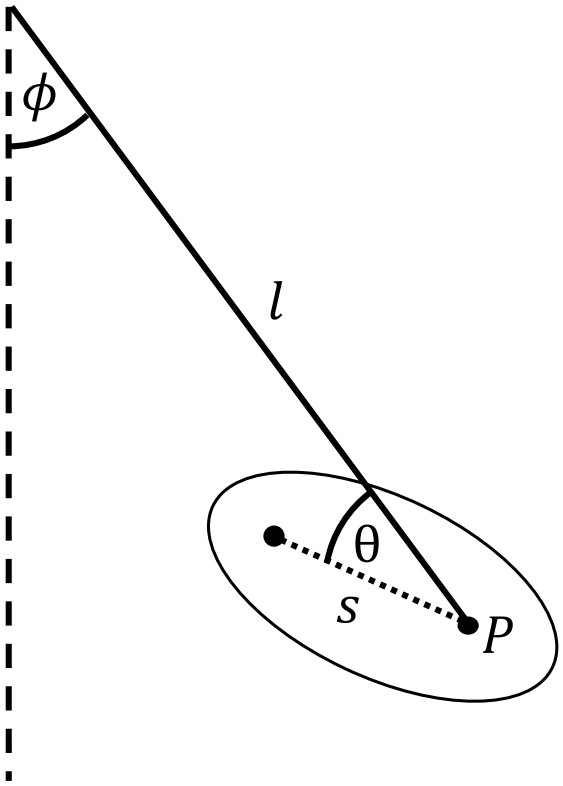

Figure 1.2: Schematic of child on swing, similar to that reported in [55]. Swing is modelled as a pendulum with a length, l, and an angle of ϕ to the vertical. The child is modelled as a rigid body with a centre of mass at a distance, s, that pivots about the end point, P, of the swing, with an angle of θ to the swing.

gains, however, the resonant cavity limits their operational bandwidth to only a few tens of MHz [58, 63, 64]. Whilst modern developments have widened the bandwidth of these devices up to 1 GHz [65] and some have in-situ frequency tunability, the instantaneous bandwidth of these devices remains inadequate for the readout of telescope receivers or multiplexed readout of qubit arrays, which require bandwidths of the order of a few GHz.

To circumvent this narrow-band restriction, the resonant cavity can be 'unfolded' into a long, non-linear transmission line, which produces a device known as a travelling-wave parametric amplifier (TWPA). TWPAs, as with JPAs, work by injecting a weak signal along with a strong local oscillator signal, called a pump, into a long non-linear propagation medium, where the waves interact. During this process, energy is transferred from the strong pump to the weak signal via wave mixing mechanisms, which amplifies the signal. As with JPAs, this process creates an additional tone called an idler, which is generated due to energy and momentum conservation [54], as shown in Fig. 1.3.

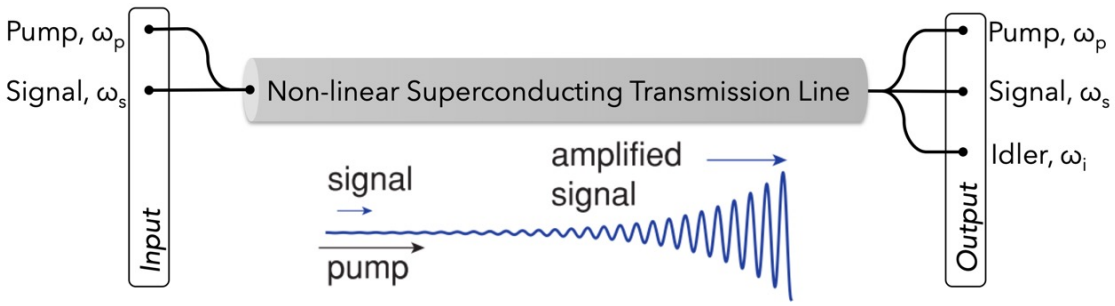

Figure 1.3: Schematic of TWPA, showing the propagating tones and highlighting the amplification.

The non-linearity of the transmission line can be achieved by embedding many JJs along the transmission line to create a Jospehson junction travelling-wave parametric amplifier (JTWPA) [66–69], or by exploiting the non-linear kinetic inductance (KI) of thin superconducting films to create a kinetic inductance travelling-wave parametric amplifier (KITWPA) [21,70–74]. KITWPAs typically have a larger dynamic range than JTWPAs [72] due to their higher current handling capability, since JTWPAs are limited by the critical current of JJs, $\sim 1\ \mu$A, whereas KITWPAs are limited by the critical current of the superconducting film, ~ 1 mA. Conversely, JTWPAs require smaller pump powers than KITWPAs to achieve the same gain and also require shorter transmission lines [67], since their lower critical current leads to a stronger non-linear inductance. An alternative configuration of JJs, known as superconducting quantum interference devices (SQUIDs) can also be used as the source of non-linearity. SQUIDs typically comprise a pair of JJs, or a JJ with an inductor, in a loop arrangement [75–77].

Being superconducting circuits, TWPAs, as with JPAs, dissipate only a minimal amount of heat, in contrast to HEMT-based amplifiers, meaning that they can be placed much closer to the signal source. This, as well as their quantum-limited noise performance and broad bandwidths, makes them ideal candidates as LNAs for ultra sensitive broad-band experiments. In fact, TWPAs are beginning to be used in such experiments to demonstrate the feasibility of their use; with examples of this including the readout of a microwave kinetic inductance detector (MKID) with a KITWPA [78] and the multiplexed readout of five superconducting qubits with a JTWPA [39].

Institution & Ref.	Year	Freq. [GHz]	Gain [dB]	Conductor Material	Bath Temp. [K]	Noise Temp. [K] (× SQL)
Caltech [21]	2012	9-14	10	NbTiN	0.08	1.54 (6.8)
NIST/ Stanford [70]	2014	4-11	10-15	NbTiN	0.03	N/A
NIST/ Stanford [72]	2016	4-8	15-25	NbTiN	0.03	0.48 (1.5)
Chalmers/ NPL [79]	2016	7-7.2	6	NbN-Al-Nb-NbN	1.8	N/A
Purple Mountain Obs./ Nat. Ast. Obs. Japan [71]	2016	5-7	4†	NbTiN	3.8	N/A
NIST/ Stanford [73]	2017	4-8	15††	NbTiN	0.1	N/A
Raytheon BBN Technologies/ NIST [80]	2018	4-12	12	NbTiN	0.01	0.67 (2.8)
NIST [74]	2020	3.5-5.5	17.6	NbTiN	0.03	0.2 (1.7)
Hebrew Uni. of Jerusalem [81]	2020	6-8	15	WSi	0.02	N/A
Caltech [82]	2021	3-34	10-18	NbTiN	1	N/A
NIST [83]	2021	3.3-5.5	18	NbTiN	4	1.9 (15.8)

† Parametric gain excluding transmission losses.
†† Gain of two cascaded devices.

Table 1.1: Summary of successful KITWPA devices reported in the literature. For the far-right column, the noise temperature is listed in Kelvin, with the number in the bracket showing the noise temperature relative to the standard quantum limit.

1.3.2 Current State of KITWPAs

This thesis focuses on the development of KITWPAs, with Tab. 1.1 summarising the successfully working KITWPAs that have been reported in the literature at time of

writing.

The first KITWPA device was reported by Eom, *et al.* in 2012 [21] and comprised a 0.8 m long co-planar waveguide (CPW) transmission line patterned into a niobium titanium nitride (NbTiN) film, which achieved a gain of 10 dB over a bandwidth of 9-14 GHz. Owing to the high inductance of the line, the transmission had a high characteristic impedance of 300 Ω, which necessitated long tapers in order to match to the 50 Ω external circuitry. Despite this, the result was groundbreaking in demonstrating that a KITWPA is in fact a viable concept.

To overcome the impedance mismatch caused by the high kinetic inductance, Chaudhuri, *et al.* in 2017 [73] presented an updated CPW-based NbTiN KITWPA, whereby the line was shunted with additional stubs, which had the effect of increasing the capacitance of the transmission line and allowing the characteristic impedance of the line to be tuned to 50 Ω to improve the impedance matching to the external circuitry. This increased capacitance additionally decreases the phase velocity, $v_{ph} = \frac{1}{\sqrt{LC}}$, of the transmission line, reducing the physical length of the KITWPA and leading to a more compact design. This stub-shunted style of transmission line has since become the standard transmission line style for CPW KITWPA devices.

More recent designs, such as those reported by Goldstein, *et al.* in 2020 and Shu, *et al.* in 2021 have abandoned CPW transmission lines in favour of inverted microstrip (IMS) lines, a design choice that has been facilitated by the development of ultra-low-loss dielectric materials such as hydrogenated amorphous silicon, a-Si:H, [84] and hydrogenated amorphous silicon carbide, a-SiC:H [85]. The advantages of these IMS devices is that their intrinsic high capacitance per unit length makes it easier to tune the characteristic impedance to 50 Ω by slightly adjusting the dielectric thickness or employing the same shunted stubs (albeit much shorter) as used in the CPW designs. The increased capacitance also allows for a lower v_{ph} and a more compact device. Additionally, in IMS transmission lines, the electromagnetic (EM) field lines are well confined, and they are easier to design than CPWs, which may have issues with cross-talk and radiation loss, although IMS lines are more prone to dielectric losses and TLS effects.

From Tab. 1.1, we see that most of the current generation of KITWPA designs operate around 4-12 GHz, corresponding to the C- and X-bands of the radio spectrum. At these frequencies, they are ideal candidates to replace HEMT-based amplifiers as first stage LNAs in radio/microwave telescope and qubit receivers and as IF LNAs in mm/sub-mm telescope receivers. We can see, however, that there is active work

in developing KITWPAs at higher frequencies, such as at the Ka-band [82] and even as high as the W-band [86], where the natural aim of this is to develop a front-end LNA for mm/sub-mm receivers. We also notice from Tab. 1.1 that the majority of the reported KITWPA devices are made from NbTiN films, which is a common material used in MKID detectors. Additionally, the operational temperature of most of the devices is of the order of 10 mK, however, some of the more recent devices have been tested at higher temperatures of up to 4 K, a clear indication of the direction of development for KITWPAs for astronomical purposes.

Crucially, as we see from the far-right column of Tab. 1.1, KITWPAs have been experimentally demonstrated to achieve noise performances very close to the SQL, with the two devices reported in Vissers, *et al*, 2016 and Malnou, *et al*, 2020, respectively, having noise performances less than one photon greater than the SQL. Comparing the noise performances reported in Malnou, *et al*, 2020 and Malnou, *et al*, 2021, however, we see that the noise temperature of a particular device dramatically increases when it is measured at a higher bath temperature, suggesting a KITWPA can only reach the SQL at ultra-low ($\sim$10 mK) temperatures. Recalling from (1.2), however, we see that the SQL is frequency-dependent, which suggests that a KITWPA may still be able to reach the SQL at higher temperatures, provided it is operating at a higher frequency. Nevertheless, the measurements of noise temperatures close to the SQL justify the potential of KITWPAs as the next standard in ultra-low-noise amplifier technology.

1.4 Thesis Outline

This thesis presents the development of TiN KITWPA devices, which is different to most NbTiN KITWPAs reported in the literature. The design and characterisation details of which are presented in the subsequent chapters.

Chapter 2 — Introduces the underlying theory of KITWPAs, including the physics of superconductivity, transmission line theory, wave mixing, and how these can be combined to model the behaviour of a KITWPA device.

Chapter 3 — Introduces the design methodology used to model a KITWPA, including electromagnetic (EM) simulation methods and important design considerations before proceeding to an analysis of different superconducting films to provide an insight into the film requirements for KITWPA operation.

Chapter 4 — Introduces the fabrication processes and experimental setups used to characterise the KITWPA devices.

Chapter 5 — Presents the experimental characterisation of the TiN KITWPA devices, including DC and RF characterisation, as well as a detailed analysis of the results and what we learnt about the devices.

Chapter 6 — Presents some additional design concepts, including a dual-pump KITWPA design and a balanced-TWPA configuration.

Chapter 2

Theory of Kinetic Inductance TWPAs

2.1 Introduction

A KITWPA is realised as a long superconducting transmission line (STL) made from a high kinetic inductance superconducting film, the non-linear properties of which promote wave mixing and allows the STL to function as a parametric amplifier. In order to design a successful KITWPA, the physics behind KITWPA operation, which is firmly rooted in the principles of superconductivity and transmission line theory, needs to be understood.

In this chapter, the theory that underpins KITWPA operation is introduced. I begin with an overview of superconductivity and wave mixing, introducing the different wave mixing regimes and their energy conservation relations. I will then progress to a derivation from first principles of a set of generalised coupled differential equations, which govern the behaviour of tones propagating in a KITWPA. Following this, I will provide further physical insight by analytically solving the differential equations to demonstrate how to optimise the gain performance of a KITWPA, before concluding the chapter with an introduction to dispersion engineering. The framework discussed in this chapter provides an insight into the physical mechanisms taking place in a KITWPA and how best to optimise their performance, allowing us to better design a KITWPA.

Whilst this thesis focuses on the development of wideband KITWPAs, consider-

able insight into their behaviour can be attained through the study of narrow-band superconducting resonators [87–90]. Not only do these resonators allow the microscopic physics of the superconducting material to be probed, such as the source of the non-linearity and losses, and the smearing of the superconducting gap [91], but these resonators made from superconducting thin films can also be used as parametric amplifiers, as discussed in [90]. One will notice from the gain curves in [90] that they are very clean, with an absence of the gain ripples that plague the gain curves of KITWPA devices reported to date. Understanding the physical reasons why these resonator-based parametric amplifiers produce gain curves without ripples, whilst KITWPAs do, is extremely important for understanding how to engineer a clean KITWPA gain profile. For the most part, however, the microscopic physical considerations of a KITWPA device are outside the scope of this thesis and are only discussed in a few places, where appropriate.

2.2 Superconductivity

2.2.1 Historical Background

Superconductivity is a property of certain materials, whereby below some critical temperature, T_c, their DC electrical resistance becomes zero and all magnetic fields are expelled from within the bulk of the material. It was first discovered in 1911 by Heike Kamerlingh Onnes, who shortly after first liquefying helium observed that the DC resistivity of mercury suddenly vanished when the temperature dropped below 4.2 K [92]. This phenomenon was subsequently observed in other materials, albeit with a different T_c each time, thus presenting the first key characteristic of superconductivity: perfect conductivity. The second key characteristic, perfect diamagnetism, was discovered by Walther Meissner and Robert Ochsenfeld in 1933, who observed that all magnetic fields are expelled from the bulk of a superconductor below T_c [93]. This discovery led to brothers Fritz and Heinz London to formulate the first phenomenological theory of superconductivity in 1935, namely the London Equations, which form the simplest meaningful description of superconducting phenomena [94]. In 1950, Vitaly Ginzburg and Lev Landau formulated an updated phenomenological theory of superconductivity based on Landau's previously established theory of second-order phase transitions [95, 96], and was later used by Alexei Abrikosov to classify Type I and Type II superconductors. It was not until 1957, however, that John Bardeen, Leon Cooper, and John Robert Schrieffer

developed the first microscopic theory of superconductivity, known as the Bardeen-Cooper-Schrieffer (BCS) theory [97, 98], where they described charge carriers in a superconductor as a Bose-Einstein condensate of Cooper pairs.

2.2.2 Conductivity in a Superconductor

The main charge carriers in a superconductor are Cooper pairs, which are pairs of quasi-electrons that condense into Bose-Einstein condensate below the T_c [99]. Whilst the binding of Cooper pairs is a quantum mechanical effect, a simplified explanation can be given in a classical sense, whereby a moving electron in an ionic lattice creates vibrations in the lattice, called phonons, which leads to areas of increased positive charge that attract further electrons. It is this electron-phonon interaction that mediates the Cooper pair binding. The binding of Cooper pairs also creates an energy gap in the density of states around the Fermi energy, with the size of the gap defined as Δ. Provided the total energy of a Cooper pair is less than 2Δ, they do not interact with the lattice or lose energy to it, giving superconductors the property of zero DC resistance. If an energy greater than 2Δ is applied, the Cooper pair is broken into separate (pseudo) electrons known as quasi-particles, which interact with the lattice, leading to a non-zero resistance, hence the superconducting state is destroyed. An AC resistance is still present in the superconducting state, however, due to the finite inertia of the charge carriers creating an electric field within the superconductor.

A superconducting material below T_c will remain in its superconducting state unless a current greater than the critical current, I_c, is applied, above which the superconductivity is broken and the material returns to it's normal state. From [91], the I_c of a superconducting wire with width, w, and thickness, t, can be calculated from,

$$I_c = \frac{3}{4} w t \Delta^{\frac{3}{2}} \sqrt{\frac{N_0 \sigma_N}{\hbar}}, \tag{2.1}$$

where N_0 is the number density of charge carriers in the wire, $\sigma_N = \frac{1}{\rho_N}$ is the normal state conductivity of the wire, which is the inverse of the normal-state resistivity of the wire, ρ_N, and $\hbar$ is the reduced Plank constant.

The conductivity of a superconductor is a complex value, which is dependent on the frequency of an oscillating electromagnetic field, and is typically represented by,

$$\sigma = \sigma_1 - i\sigma_2, \tag{2.2}$$

where the real component, σ_1 represents the resistive part of the conductivity, and the imaginary component, σ_2 represents the reactive component of the conductivity. The total conductivity can be calculated by solving the Mattis-Bardeen Equations [100], which are derived from BCS theory. Relative to the normal state conductivity, $\sigma_N = \frac{1}{\rho_N}$, the real component of the conductivity is given by,

$$\frac{\sigma_1(\omega)}{\sigma_n} = \frac{2}{\hbar\omega}\int_{\Delta}^{\infty} \frac{E^2+\Delta^2+\hbar\omega E}{\sqrt{E^2-\Delta^2}\sqrt{(E+\hbar\omega)^2-\Delta^2}}\left[f(E)-f(E+\hbar\omega)\right]dE, \quad (2.3a)$$

and the imaginary component is given by,

$$\frac{\sigma_2(\omega)}{\sigma_n} = \frac{1}{\hbar\omega}\int_{\Delta}^{\Delta+\hbar\omega} \frac{E^2+\Delta^2-\hbar\omega E}{\sqrt{E^2-\Delta^2}\sqrt{\Delta^2-(E-\hbar\omega)^2}}\left[1-2f(E)\right]dE, \quad (2.3b)$$

where,

$$f(E) = \frac{1}{e^{\frac{E}{kT}}+1}, \quad (2.4)$$

is the Fermi-Dirac distribution [101], E is energy, $\hbar$ is the reduced Planck constant, ω is the angular frequency, and k is the Boltzmann constant.

2.2.3 Kinetic Inductance

Kinetic inductance is a form of inductance that manifests from the inertia of moving charge carriers in a conductor [102]. This is in contrast to magnetic inductance, which arises due to energy being stored in the generated magnetic field. The current, I, passing through a material can be defined as,

$$I = nQAv_d, \quad (2.5)$$

where n is the charge carrier density, Q is the charge of each carrier, A is the cross-sectional area of the material, and v_d is the average drift velocity.

The charge carriers comprising the current have an associated mass and velocity, hence will have a kinetic energy. This kinetic energy can be equated with the expression for the energy stored in an inductor to define the kinetic inductance, L_k,

$$n\left(\frac{1}{2}mv_d^2\right)A = \frac{1}{2}L_kI^2. \quad (2.6)$$

In a normal resistive material, the scattering interactions between the charge carriers and the lattice mean that the drift velocity is relatively small. In superconductors, however, the lack of interactions means that the charge carriers can attain a very large drift velocity, hence a large kinetic inductance.

Substituting the Cooper pair mass, $2m_e$, charge, $-2e$, and density, n_s, into (2.6) gives an expression for the kinetic inductance per unit length in a superconductor,

$$L_k = \frac{m_e}{2n_s e^2 A}. \tag{2.7}$$

The Cooper pair density is not constant, however, and varies with both temperature and the superconducting coherence length. Full calculation of the kinetic inductance, therefore, requires the use of BCS theory.

In general, the kinetic inductance varies highly non-trivially to the applied current, however, the relationship can be sufficiently represented by a Taylor expansion,

$$L_k(I) = L_{k0}\left(1 + \frac{I^2}{I_*^2} + \dots\right), \tag{2.8}$$

where I_* is a term that sets the scale of the non-linearity. In the limit $I \ll I_*$, we can see from (2.8) that the kinetic inductance varies quadratically with I. It should be noted that the odd terms in the series expansion must be zero due to symmetry, i.e. $L_k(I) = L_k(-I)$ since the direction of the current should not effect the value of the kinetic inductance. From [82], I_* can be calculated from,

$$I_* = wt\kappa_* \sqrt{\frac{N_0\Delta^2}{\mu_0\lambda_L^2}}, \tag{2.9}$$

where,

$$\lambda_L = \sqrt{\frac{\hbar}{\mu_0\pi\sigma_N\Delta}}, \tag{2.10}$$

is the London penetration depth of the wire, κ_* is a constant of order unity, and μ_0 is the permeability of free space.

2.2.4 Concept of Surface Impedance

Calculating the full electromagnetic behaviour for an arbitrary superconductor can be a highly non-trivial task. To simplify this exercise somewhat, the concept of surface impedance is introduced, which allows the electromagnetic behaviour inside of a material to be neglected and can instead be represented by a surface impedance boundary condition.

The surface impedance of a material can be defined as,

$$Z_s = \frac{E_x}{H_y}, \tag{2.11}$$

where E_x and H_y are the electric and magnetic field components transverse to the surface of the material. From [103], the surface impedance for a material with a finite thickness, t, can be calculated from the complex conductivity introduced in § 2.2.2 using,

$$Z_s = \frac{k}{\sigma} \frac{e^{kt} + \frac{\sigma Z_\eta - k}{\sigma Z_\eta + k} e^{-kt}}{e^{kt} - \frac{\sigma Z_\eta - k}{\sigma Z_\eta + k} e^{-kt}}, \tag{2.12}$$

where $Z_\eta = \sqrt{\frac{\mu_0}{\epsilon_0}}$ is the characteristic impedance of free space, ϵ_0 is the permittivity of free space, and $k = (1+i)\sqrt{\frac{\omega\sigma\mu_0}{2}}$. In the limit where $Z_\eta \gg \frac{k}{\sigma}$, (2.12) reduces to,

$$Z_s = \frac{k}{\sigma} \tanh(kt). \tag{2.13}$$

From Z_s, the surface resistance can be defined as, $R_s = \Re[Z_s]$ and the surface inductance can be defined as $L_s = \frac{\Im[Z_s]}{\omega}$.

2.2.5 High ρ_N Superconductors

High ρ_N superconductors, such as titanium nitride (TiN) and niobium titanium nitride (NbTiN) have found uses in applications such as microwave kinetic inductance detectors (MKIDs), where their high normal-state resistivity produces a high surface impedance and hence small and sensitive detectors [104].

An MKID detector essentially comprises an LC resonator, where the inductance of the resonator is dominated by the kinetic inductance of the superconducting material [101, 104]. When an incident photon is absorbed by the resonator it breaks Cooper pairs, which from (2.7), will change the kinetic inductance and hence the resonant frequency of the resonator, $f_{\text{res}} = \frac{1}{2\pi\sqrt{LC}}$. In principle, the depth of the resonance will also change, as the breaking of Cooper pairs into quasiparticles leads to losses.

In 2012, Eom *et al.* observed that for their TiN and NbTiN resonators, an increase in the readout power through the resonator feedline shifted the position of the resonant frequency without changing the depth of the resonance, implying very little change to the dissipation of the resonator [105], which is in stark contrast to that of most superconducting materials. It was this observation of dissipationless non-linearity, however, that led the authors to deduce that a superconducting transmission line constructed from TiN or NbTiN could be used as a non-linear amplifier by utilising the high kinetic non-linearity in a similar manner to optical parametric amplifiers, hence the name KITWPA.

In another publication by Driessen *et al.* [106], an investigation into quarter-wavelength resonators patterned into high ρ_N TiN and NbTiN superconducting films found their behaviour deviated from that predicted by BCS theory as well. They observed that the resonant frequency of their resonators decayed more rapidly with increased temperature than expected for a complex conductivity calculated from the Mattis-Bardeen equations in (2.3a)-(2.3b), which they attribute to an intrinsic disorder-induced change in the superconducting state.

It is important to note for these superconducting films with high normal-state resistivity, that the density of states has been shown to be highly inhomogeneous [107]. Additionally, it has been shown that in some conditions, there is a strong decoupling of the Cooper pair and quasiparticle responses in simple resonators [108], as well as a non-linear inductance that does not induce extra losses [105]. Whilst this last phenomenon is essential for the proper operation of a KITWPA, it is currently not well understood, and goes beyond the framework of the Mattis-Bardeen equations in (2.3a)-(2.3b), which describe the response of a homogeneous superconductor.

2.3 Wave Mixing

Wave mixing is the principle physical phenomenon that underpins KITWPA operation, allowing photons of one frequency to interact with photons of other frequencies, hence, allowing energy exchange during this process. This section describes the wave mixing regimes that are used throughout this thesis.

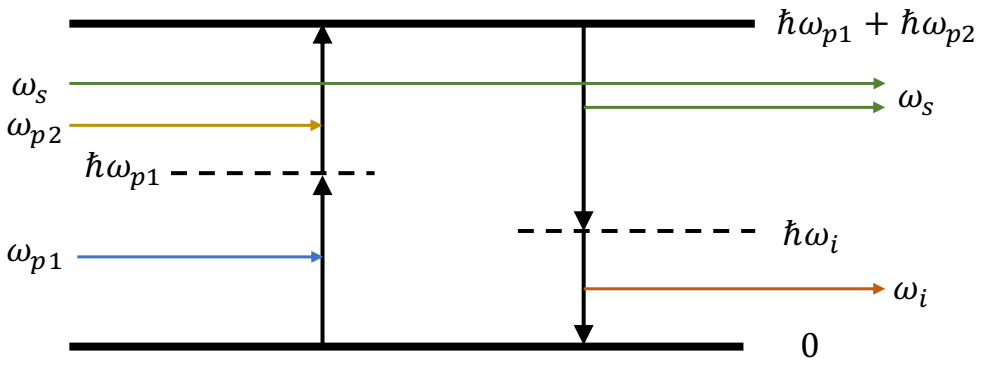

Figure 2.1: Energy diagram for ND-4WM.

Non-linear materials that mediate wave mixing can be assigned a Kerr non-linearity order, which specifies which type of wave mixing process is promoted.

Fig. 2.1 shows the energy diagram for the non-degenerate four-wave mixing (ND-4WM) process, during which two input photons with frequencies ω_{p1} and ω_{p2} are converted to two output photons with different frequencies to conserve the energy of the system. The presence of a weak signal with frequency ω_s at the input results in the output photon frequencies being ω_s and ω_i, where ω_i is known as the idler and has a frequency that satisfies the energy conservation relation given by,

$$\omega_{p1} + \omega_{p2} = \omega_s + \omega_i. \tag{2.14}$$

Four-wave mixing processes are mediated by Kerr-3 non-linear materials, which allow four photons or waves interact with each other. An example of a Kerr-3 material is a superconducting transmission line with a quadratic kinetic inductance described by (2.8).

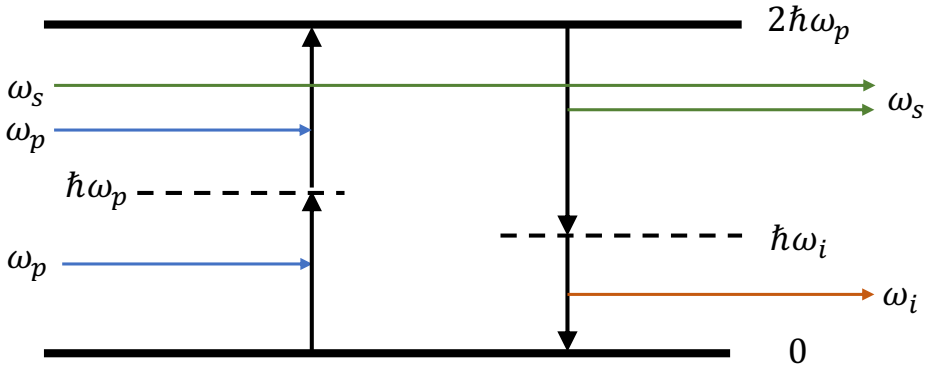

Figure 2.2: Energy diagram for D-4WM.

A special case of four-wave mixing is known as degenerate four-wave mixing (D-4WM), whereby the two incoming photons are at the same frequency, ω_p. This process is summarised in Fig. 2.2 and shows two pump photons being converted to a signal photon and idler photon, which satisfies,

$$2\omega_p = \omega_s + \omega_i. \tag{2.15}$$

Fig. 2.3 shows a three-wave mixing (3WM) process, whereby a single pump photon at frequency ω_p is converted to a signal photon with frequency, ω_s and an idler photon at frequency ω_i, such that the energy conservation relation,

$$\omega_p = \omega_s + \omega_i, \tag{2.16}$$

is satisfied. 3WM can occur in a Kerr-2 non-linear medium, such as some SQUID-based TWPA devices, which allow three photons or waves interact with each other.

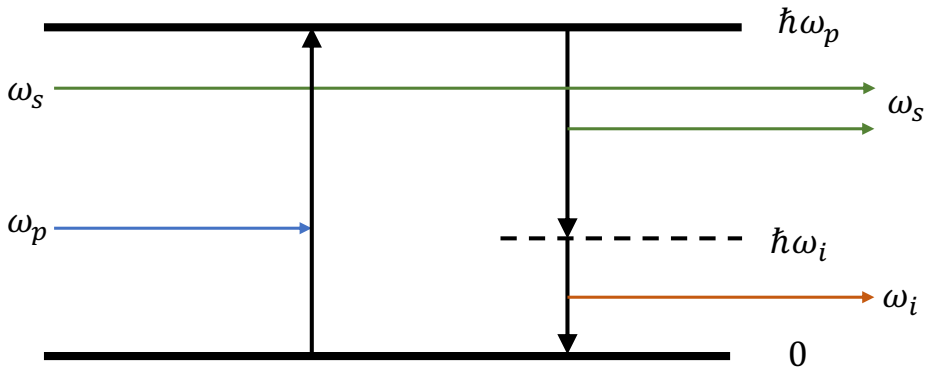

Figure 2.3: Energy diagram for 3WM.

3WM can also be promoted in a Kerr-3 medium if their symmetry is somehow broken; for example, taking a superconducting transmission line with a quadratic kinetic inductance and passing a DC signal along the line will break the symmetry of the line and adds a linear term in the current-dependence of the kinetic inductance. This linear term subsequently allows a DC-induced 3WM process (DC-3WM) to take place.

2.4 Telegrapher Equations

In transmission line theory, the size of components is typically a significant fraction of an electrical wavelength or even many wavelengths, hence are described as distributed elements. This is in contrast to circuit theory, which assumes that the components are significantly smaller than an electrical wavelength, hence a component is treated as a lumped element. Despite the fact that a KITWPA transmission line is typically several tens to hundreds of wavelengths long, it is still of academic merit to represent a transmission line using a lumped-element circuit model, as it readily allows the properties of superconductivity to be included, which can be justified by considering an infinitesimal length of transmission line that is much smaller than a wavelength. The following section derives a non-linear wave equation that describes a current propagating along the length of a STL with a current-dependent inductance.

Fig. 2.4 shows an $RLGC$ model for a transmission line with infinitesimal length, Δz, where R is the series resistance per unit length, L is the series inductance per unit length, G is the shunt conductance per unit length, and C is the shunt

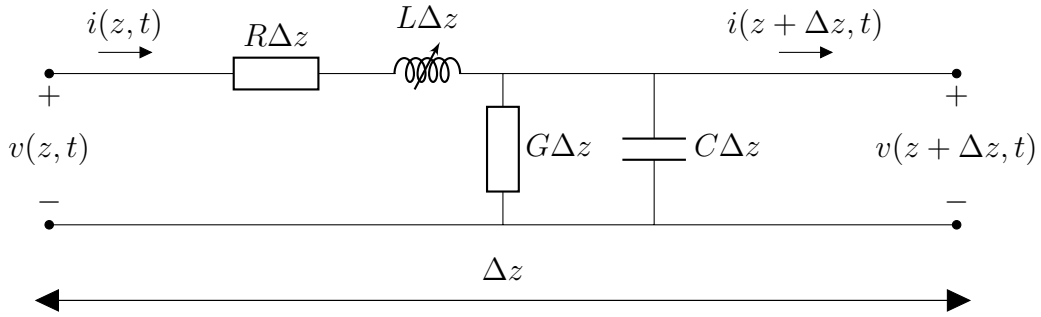

Figure 2.4: Lumped-element circuit model of transmission line with variable inductance.

capacitance per unit length. From [109], applying Kirchoff's voltage law to Fig. 2.4 gives,

$$v\left(z,t\right)-R\Delta z i\left(z,t\right)-L\Delta z\frac{\partial i\left(z,t\right)}{\partial t}-v\left(z+\Delta z,t\right)=0, \tag{2.17a}$$

and applying Kirchoff's current law gives,

$$i\left(z,t\right)-G\Delta z v\left(z+\Delta z,t\right)-C\Delta z\frac{\partial v\left(z+\Delta z,t\right)}{\partial t}-i\left(z+\Delta z,t\right)=0. \tag{2.17b}$$

Dividing (2.17a)-(2.17b) by Δz and taking the limit $\Delta z \to 0$ produces a pair of differential equations for the voltage and current in the transmission line,

$$-\frac{\partial V}{\partial z}=RI+L\frac{\partial I}{\partial t} \tag{2.18a}$$

$$-\frac{\partial I}{\partial z}=GV+C\frac{\partial V}{\partial t}, \tag{2.18b}$$

which are known as the telegrapher equations. Solving these equations simultaneously gives a wave equation for the voltage and current of the tones propagating along the transmission line.

The telegrapher equations in (2.18a)-(2.18b) represent a general transmission line, however, to model a STL, the effects of superconductivity need to be explicitly substituted in. Recall from (2.8) that the kinetic inductance, to a lowest order Taylor expansion, is quadratically dependent on I. The total inductance along a STL, therefore, contains contributions from the kinetic inductance and the geometry of the STL such that,

$$L(I)=L_{k0}\left(1+\frac{I^2}{I_*^2}\right)+L_g, \tag{2.19}$$

where L_g is the geometric inductance.

Substituting this current-dependent inductance into (2.18) produces a pair of telegrapher equations for a STL,

$$-\frac{\partial V}{\partial z} = RI + L_0\frac{\partial I}{\partial t} + \frac{L_{k0}}{I_*^2}I^2\frac{\partial I}{\partial t} \tag{2.20a}$$

$$-\frac{\partial I}{\partial z} = GV + C\frac{\partial V}{\partial t}, \tag{2.20b}$$

where $L_0 = (L_{k0} + L_g)$ is the total inductance when $I = 0$. To proceed further, we differentiate (2.20a) w.r.t. t and (2.20b) w.r.t. z to produce,

$$-\frac{\partial^2 V}{\partial t\,\partial z} = R\frac{\partial I}{\partial t} + L_0\frac{\partial^2 I}{\partial t^2} + \frac{L_{k0}}{I_*^2}\frac{\partial}{\partial t}\left[I^2\frac{\partial I}{\partial t}\right] \tag{2.21a}$$

$$-\frac{\partial^2 I}{\partial z^2} = G\frac{\partial V}{\partial z} + C\frac{\partial^2 V}{\partial z\,\partial t}. \tag{2.21b}$$

Eqs. (2.20a) and (2.21a) can then be substituted into (2.21b) to eliminate V and produce a non-linear wave equation in terms of I,

$$\frac{\partial^2 I}{\partial z^2} = RGI + (L_0G + RC)\frac{\partial I}{\partial t} + L_{k0}G\frac{I^2}{I_*^2}\frac{\partial I}{\partial t} + L_0C\frac{\partial^2 I}{\partial t^2} + L_{k0}C\frac{\partial}{\partial t}\left[\frac{I^2}{I_*^2}\frac{\partial I}{\partial t}\right], \tag{2.22}$$

which describes the current propagating along the STL.

The substitution of (2.19) into the telegrapher equations in (2.18a)-(2.18b), and the subsequent rearrangement into (2.22) assumes that the inductance is the only current-dependent parameter present in the STL, however, from previous discussions, one would also expect the film losses to vary as a function of current, hence we should also substitute $R(I)$ into (2.18a)-(2.18b). From the discussion of inhomogeneous superconductors in § 2.2.5, however, we see that certain materials induce very little to no losses in the presence of a supercurrent. Hence for this derivation, as well as for the remainder of this thesis, we make the assumption that R displays negligible current-dependence, provided that $I < I_c$ and $T < T_c$.

2.5 Coupled-Mode Equations

The non-linearity of the wave equation in (2.22) is the property that allows wave mixing to take place between the various tones propagating along the STL. To understand the behaviour of these tones, it is desirable to write down a set of equations that describe each of the tones as they propagate along the STL, namely the coupled-mode equations (CMEs). The majority of the CMEs reported in the

literature are either for D-4WM or DC-3WM, and typically assume the STL is completely lossless. In this section, I shall derive a set of generalised CMEs for the general case of ND-4WM and explicitly include losses and other effects of the STL such as L_g, which is frequently neglected. I will then demonstrate how the CMEs usually reported elsewhere are in fact special cases of the generalised CMEs presented here, demonstrating a unified mathematical framework for representing the different wave mixing modes in a KITWPA.

The derivation of the CMEs begins with an ansatz for the current components propagating along the STL, which is given by,

$$I = \frac{1}{2}\sum_j A_j(z)e^{i\omega_j t-\gamma_j z} + c.c., \tag{2.23}$$

where A_j is the slowly varying complex amplitude of the component, ω_j is the angular frequency of the component, $\gamma_j = \alpha_j + i\beta_j$ is the complex propagation constant of the component, j denotes the particular propagating component, and *c.c.* denotes the complex conjugate. The values of j signify the operational mode of the KITWPA, which is determined by the wave mixing regime of the KITWPA as introduced in § 2.3. In the following, we assume that only pump, signal, and idler terms are present, with any higher harmonics assumed to be very weak or suppressed. Recalling that for ND-4WM, two pump photons with angular frequency ω_{p1} and ω_{p2}, respectively, are converted to a signal photon with angular frequency ω_s and an idler photon with angular frequency ω_i, hence the values of j are given as: $j = p_1, p_2, s, i$.

Substituting (2.23) for the ND-4WM regime into the linear terms of (2.22) and simplifying using the slow-wave approximation, $\left|\frac{d^2A_j(z)}{dz^2}\right| \ll \left|k_j\frac{dA_j(z)}{dz}\right|$, and that $\gamma_j = \sqrt{(R+i\omega_j L_0)(G+i\omega_j C)}$ produces,

$$-\sum_{j=p_1,p_2,s,i}\gamma_j\frac{dA_j}{dz}e^{i\omega_j t-\gamma_j z} + \gamma_j^*\frac{dA_j^*}{dz}e^{-i\omega_j t-\gamma_j^* z} = L_{k0}G\frac{I^2}{I_*^2}\frac{\partial I}{\partial t} + L_{k0}C\frac{\partial}{\partial t}\left[\frac{I^2}{I_*^2}\frac{\partial I}{\partial t}\right]. \tag{2.24}$$

The terms on the right-hand side of (2.24) are the non-linear terms, which mediate the wave mixing along the transmission line. The substitution of (2.23) into these non-linear terms and subsequent expansion generates a large number of cross-terms, which require careful sorting, although this can be performed with a symbolic algebra manipulator such as Mathematica. The full expansion is lengthy and is presented in App. A.1.

Following the full substitution, expansion, and simplification, a set of coupled differential equations can be obtained by collecting terms with frequency components

$e^{i\omega_j t}$ for each $j = p_1, p_2, s, i$. This includes any frequency combination that satisfies the ND-4WM energy conservation equation presented in (2.14). These equations are given by,

$$\begin{aligned}\frac{dA_{p_1}}{dz} = \frac{\omega_{p_1}^2 L_{k0} C \eta_{p_1}}{8\gamma_{p_1} I_*^2}\Bigg[&\Big(\epsilon_{p_1,p_2} e^{-\left(\gamma_{p_1}+\gamma_{p_1}^*\right)z}|A_{p_1}|^2 + 2e^{-\left(\gamma_{p_2}+\gamma_{p_2}^*\right)z}|A_{p_2}|^2 \\ &+ 2e^{-(\gamma_s+\gamma_s^*)z}|A_s|^2 + 2e^{-\left(\gamma_i+\gamma_i^*\right)z}|A_i|^2\Big)A_{p_1} \\ &+ 2e^{\left(\gamma_{p_1}-\gamma_{p_2}^*-\gamma_s-\gamma_i\right)z} A_i A_s A_{p_2}^*\Bigg]\end{aligned} \tag{2.25a}$$

$$\begin{aligned}\frac{dA_{p_2}}{dz} = \frac{\omega_{p_2}^2 L_{k0} C \eta_{p_2}}{8\gamma_{p_2} I_*^2}\Bigg[&\Big(\epsilon_{p_1,p_2} e^{-\left(\gamma_{p_2}+\gamma_{p_2}^*\right)z}|A_{p_2}|^2 + 2e^{-(\gamma_s+\gamma_s^*)z}|A_s|^2 \\ &+ 2e^{-\left(\gamma_i+\gamma_i^*\right)z}|A_i|^2 + 2e^{-\left(\gamma_{p_1}+\gamma_{p_1}^*\right)z}|A_{p_1}|^2\Big)A_{p_2} \\ &+ 2e^{\left(\gamma_{p_2}-\gamma_{p_1}^*-\gamma_s-\gamma_i\right)z} A_i A_s A_{p_1}^*\Bigg]\end{aligned} \tag{2.25b}$$

$$\begin{aligned}\frac{dA_s}{dz} = \frac{\omega_s^2 L_{k0} C \eta_s}{8\gamma_s I_*^2}\Bigg[&\Big(e^{-(\gamma_s+\gamma_s^*)z}|A_s|^2 + 2\epsilon_{p_1,p_2} e^{-\left(\gamma_{p_2}+\gamma_{p_2}^*\right)z}|A_{p_2}|^2 \\ &+ 2e^{-\left(\gamma_i+\gamma_i^*\right)z}|A_i|^2 + 2\epsilon_{p_1,p_2} e^{-\left(\gamma_{p_1}+\gamma_{p_1}^*\right)z}|A_{p_1}|^2\Big)A_s \\ &+ 2\epsilon_{p_1,p_2} e^{\left(\gamma_s-\gamma_i^*-\gamma_{p_1}-\gamma_{p_2}\right)z} A_i^* A_{p_1} A_{p_2}\Bigg]\end{aligned} \tag{2.25c}$$

$$\begin{aligned}\frac{dA_i}{dz} = \frac{\omega_i^2 L_{k0} C \eta_i}{8\gamma_i I_*^2}\Bigg[&\Big(e^{-\left(\gamma_i+\gamma_i^*\right)z}|A_i|^2 + 2\epsilon_{p_1,p_2} e^{-\left(\gamma_{p_1}+\gamma_{p_1}^*\right)z}|A_{p_1}|^2 \\ &+ 2\epsilon_{p_1,p_2} e^{-\left(\gamma_{p_2}+\gamma_{p_2}^*\right)z}|A_{p_2}|^2 + 2e^{-(\gamma_s+\gamma_s^*)z}|A_s|^2\Big)A_i \\ &+ 2\epsilon_{p_1,p_2} e^{\left(\gamma_i-\gamma_s^*-\gamma_{p_1}-\gamma_{p_2}\right)z} A_s^* A_{p_1} A_{p_2}\Bigg],\end{aligned} \tag{2.25d}$$

where $\eta_j = \left(1 - i\frac{G}{\omega_j C}\right)$ and,

$$\epsilon_{p_1,p_2} = \begin{cases} 2 & \text{if } \omega_{p_1} = \omega_{p_2} \\ 1 & \text{otherwise.} \end{cases} \tag{2.26}$$

Eqs. (2.25a)-(2.25d) are the most generalised form of the CMEs, which unlike most CMEs reported in the literature, explicitly include the transmission line losses and the effects of geometric inductance. These equations, however, can easily be reduced to the form of equations typically reported by making some simple assumptions. First, a reasonable assumption for a STL is that it is operating in the 'low-loss'

limit since it is expected that $R \ll \omega_j L$ and $G \ll \omega_j C$ for all j propagating along the STL, implying $\eta_j \approx 1$ and that,

$$\gamma_j \simeq \frac{1}{2}\left(R\sqrt{\frac{C}{L_0}} + G\sqrt{\frac{L_0}{C}}\right) + i\omega_j\sqrt{L_0 C}. \tag{2.27}$$

Additionally, the high-KI STL used to construct a KITWPA implies that $L_{k0} \gg L_g$ and hence $L_0 = L_{k0} + L_g \approx L_{k0}$. Under these assumptions, the CMEs in (2.25a)-(2.25d) simplify to,

$$\begin{aligned}\frac{dA_{p_1}}{dz} = \frac{\beta_{p1}^2}{8\gamma_{p1}I_*^2}\Bigg[&\Big(\epsilon_{p_1,p_2}e^{-\left(\gamma_{p_1}+\gamma_{p_1}^*\right)z}\left|A_{p_1}\right|^2 + 2e^{-\left(\gamma_{p_2}+\gamma_{p_2}^*\right)z}\left|A_{p_2}\right|^2 \\ &+ 2e^{-(\gamma_s+\gamma_s^*)z}\left|A_s\right|^2 + 2e^{-\left(\gamma_i+\gamma_i^*\right)z}\left|A_i\right|^2\Big)A_{p_1} \\ &+ 2e^{\left(\gamma_{p_1}-\gamma_{p_2}^*-\gamma_s-\gamma_i\right)z}A_iA_sA_{p_2}^*\Bigg]\end{aligned} \tag{2.28a}$$

$$\begin{aligned}\frac{dA_{p_2}}{dz} = \frac{\beta_{p2}^2}{8\gamma_{p2}I_*^2}\Bigg[&\Big(\epsilon_{p_1,p_2}e^{-\left(\gamma_{p_2}+\gamma_{p_2}^*\right)z}\left|A_{p_2}\right|^2 + 2e^{-(\gamma_s+\gamma_s^*)z}\left|A_s\right|^2 \\ &+ 2e^{-\left(\gamma_i+\gamma_i^*\right)z}\left|A_i\right|^2 + 2e^{-\left(\gamma_{p_1}+\gamma_{p_1}^*\right)z}\left|A_{p_1}\right|^2\Big)A_{p_2} \\ &+ 2e^{\left(\gamma_{p_2}-\gamma_{p_1}^*-\gamma_s-\gamma_i\right)z}A_iA_sA_{p_1}^*\Bigg]\end{aligned} \tag{2.28b}$$

$$\begin{aligned}\frac{dA_s}{dz} = \frac{\beta_s^2}{8\gamma_sI_*^2}\Bigg[&\Big(e^{-(\gamma_s+\gamma_s^*)z}\left|A_s\right|^2 + 2\epsilon_{p_1,p_2}e^{-\left(\gamma_{p_2}+\gamma_{p_2}^*\right)z}\left|A_{p_2}\right|^2 \\ &+ 2e^{-\left(\gamma_i+\gamma_i^*\right)z}\left|A_i\right|^2 + 2\epsilon_{p_1,p_2}e^{-\left(\gamma_{p_1}+\gamma_{p_1}^*\right)z}\left|A_{p_1}\right|^2\Big)A_s \\ &+ 2\epsilon_{p_1,p_2}e^{\left(\gamma_s-\gamma_i^*-\gamma_{p_1}-\gamma_{p_2}\right)z}A_i^*A_{p_1}A_{p_2}\Bigg]\end{aligned} \tag{2.28c}$$

$$\begin{aligned}\frac{dA_i}{dz} = \frac{\beta_i^2}{8\gamma_iI_*^2}\Bigg[&\Big(e^{-\left(\gamma_i+\gamma_i^*\right)z}\left|A_i\right|^2 + 2\epsilon_{p_1,p_2}e^{-\left(\gamma_{p_1}+\gamma_{p_1}^*\right)z}\left|A_{p_1}\right|^2 \\ &+ 2\epsilon_{p_1,p_2}e^{-\left(\gamma_{p_2}+\gamma_{p_2}^*\right)z}\left|A_{p_2}\right|^2 + 2e^{-(\gamma_s+\gamma_s^*)z}\left|A_s\right|^2\Big)A_i \\ &+ 2\epsilon_{p_1,p_2}e^{\left(\gamma_i-\gamma_s^*-\gamma_{p_1}-\gamma_{p_2}\right)z}A_s^*A_{p_1}A_{p_2}\Bigg],\end{aligned} \tag{2.28d}$$

where $\beta_j \equiv \Im[\gamma_j]$.

As stated, the KITWPA devices reported in the literature operate either in the D-4WM regime or in the DC-3WM regime, with each regime having their own CMEs. I will now demonstrate how each of these sets of CMEs are in fact special cases of the generalised CMEs I have just derived.

2.5.1 Degenerate Four-Wave Mixing

As stated, D-4WM is a particular case of ND-4WM where the two pump tones are equal in frequency and magnitude, and is arguably the most straightforward wave mixing example for a KITWPA. Recall from § 2.3 that the energy conservation relation for D-4WM is $2\omega_p = \omega_s + \omega_i$, hence the values of j used for the substituted ansatz are $j = p, s, i$. The CMEs for D-4WM can be obtained simply by substituting the D-4WM specialisation, i.e. $\omega_{p1} = \omega_{p2} = \omega_p$ and $A_{p1} = A_{p2} = A_p$ into the ND-4WM CMEs. The CMEs in (2.28a)-(2.28d), therefore, reduce to the lossy CMEs for D-4WM,

$$\begin{aligned}\frac{dA_p}{dz} = \frac{\beta_p^2}{8\gamma_p I_*^2}\Bigg[\Big(&e^{-\left(\gamma_p+\gamma_p^*\right)z}\left|A_p\right|^2 + 2e^{-(\gamma_s+\gamma_s^*)z}\left|A_s\right|^2 \\ &+ 2e^{-\left(\gamma_i+\gamma_i^*\right)z}\left|A_i\right|^2\Big)A_p + 2e^{\left(\gamma_p-\gamma_p^*-\gamma_s-\gamma_i\right)z}A_iA_sA_p^*\Bigg]\end{aligned} \tag{2.29a}$$

$$\begin{aligned}\frac{dA_s}{dz} = \frac{\beta_s^2}{8\gamma_s I_*^2}\Bigg[\Big(&e^{-(\gamma_s+\gamma_s^*)z}|A_s|^2 + 2e^{-\left(\gamma_i+\gamma_i^*\right)z}|A_i|^2 \\ &+ 2e^{-\left(\gamma_p+\gamma_p^*\right)z}|A_p|^2\Big)A_s + e^{(\gamma_s-{\gamma_i}^*-2\gamma_p)z}A_i^*A_p^2\Bigg]\end{aligned} \tag{2.29b}$$

$$\begin{aligned}\frac{dA_i}{dz} = \frac{\beta_i^2}{8\gamma_i I_*^2}\Bigg[\Big(&e^{-\left(\gamma_i+\gamma_i^*\right)z}|A_i|^2 + 2e^{-\left(\gamma_p+\gamma_p^*\right)z}|A_p|^2 \\ &+ 2e^{-(\gamma_s+\gamma_s^*)z}|A_s|^2\Big)A_i + e^{(\gamma_i-{\gamma_s}^*-2\gamma_p)z}A_s^*A_p^2\Bigg],\end{aligned} \tag{2.29c}$$

which are equivalent to the CMEs reported in [110].

Taking the fully lossless limit where $\gamma = \alpha + i\beta \to i\beta$ recovers the lossless CMEs for D-4WM,

$$\frac{dA_p}{dz} = -\frac{i\beta_p}{8I_*^2}\left(\left(\left|A_p\right|^2 + 2\left|A_s\right|^2 + 2\left|A_i\right|^2\right)A_p + 2A_iA_sA_p^*e^{-i\Delta_\beta^{(D4)}z}\right) \tag{2.30a}$$

$$\frac{dA_s}{dz} = -\frac{i\beta_s}{8I_*^2}\left(\left(|A_s|^2 + 2|A_i|^2 + 2|A_p|^2\right)A_s + A_i^*A_p^2e^{i\Delta_\beta^{(D4)}z}\right) \tag{2.30b}$$

$$\frac{dA_i}{dz} = -\frac{i\beta_i}{8I_*^2}\left(\left(|A_i|^2 + 2|A_p|^2 + 2|A_s|^2\right)A_i + A_s^*A_p^2e^{i\Delta_\beta^{(D4)}z}\right), \tag{2.30c}$$

where $\Delta_\beta^{(D4)} = \beta_s + \beta_i - 2\beta_p$, which are identical to the CMEs reported in [105].

2.5.2 DC Three-Wave Mixing

If a DC current is passed along the STL, the symmetry of the line is broken and 3WM can take place. This regime is known as DC-3WM. Recall from § 2.3 that the energy conservation relation for DC-3WM is $\omega_p = \omega_s + \omega_i$, hence the values of j used for the substituted ansatz are $j = p, s, i$. DC-3WM can be considered as a specialisation of ND-4WM, where the DC tone is represented by one of the pump tones having a frequency of 0 and can be achieved by making the transformations: $\omega_{p2} \to 0$, $\gamma_{p2} \to 0$, $\omega_{p1} \to \omega_p$, $\gamma_{p1} \to \gamma_p$, $A_{p1} \to A_p$, and $A_{p2} = A_{p2}^* \to I_{\mathrm{DC}}$. Under this transformation, it can be shown that CMEs in (2.28a)-(2.28d) reduce to,

$$\begin{aligned}\frac{dA_p}{dz} = \frac{\beta_p^2}{8\gamma_p I_*^2}\Bigg[\Big(&e^{-\left(\gamma_p+\gamma_p^*\right)z}\left|A_p\right|^2 + 2I_{\mathrm{DC}}^2 + 2e^{-(\gamma_s+\gamma_s^*)z}\left|A_s\right|^2 \\ &+ 2e^{-\left(\gamma_i+\gamma_i^*\right)z}\left|A_i\right|^2\Big)A_p + 2e^{(\gamma_p-\gamma_s-\gamma_i)z}A_iA_sI_{\mathrm{DC}}\Bigg]\end{aligned} \tag{2.31a}$$

$$\begin{aligned}\frac{dA_s}{dz} = \frac{\beta_s^2}{8\gamma_s I_*^2}\Bigg[\Big(&e^{-(\gamma_s+\gamma_s^*)z}\left|A_s\right|^2 + 2I_{\mathrm{DC}}^2 + 2e^{-\left(\gamma_i+\gamma_i^*\right)z}\left|A_i\right|^2 \\ &+ 2e^{-\left(\gamma_p+\gamma_p^*\right)z}\left|A_p\right|^2\Big)A_s + 2e^{\left(\gamma_s-\gamma_i^*-\gamma_p\right)z}A_i^*A_pI_{\mathrm{DC}}\Bigg]\end{aligned} \tag{2.31b}$$

$$\begin{aligned}\frac{dA_i}{dz} = \frac{\beta_i^2}{8\gamma_i I_*^2}\Bigg[\Big(&e^{-\left(\gamma_i+\gamma_i^*\right)z}\left|A_i\right|^2 + 2e^{-\left(\gamma_p+\gamma_p^*\right)z}\left|A_p\right|^2 + 2I_{\mathrm{DC}}^2 \\ &+ 2e^{-(\gamma_s+\gamma_s^*)z}\left|A_s\right|^2\Big)A_i + 2e^{(\gamma_i-\gamma_s^*-\gamma_p)z}A_s^*A_pI_{\mathrm{DC}}\Bigg],\end{aligned} \tag{2.31c}$$

with (2.28b) reducing to the trivial $\frac{dI_{\mathrm{DC}}}{dz} = 0$. These are the lossy CMEs for DC-3WM. For completeness, the CMEs for the lossless DC-3WM regime are given by,

$$\frac{dA_p}{dz} = -\frac{i\beta_p}{8I_*^2}\left[\Big(\left|A_p\right|^2 + 2\left|A_s\right|^2 + 2\left|A_i\right|^2 + 2I_{\mathrm{DC}}^2\Big)A_p + 2A_iA_sI_{\mathrm{DC}}e^{-i\Delta_\beta^{(3)}z}\right] \tag{2.32a}$$

$$\frac{dA_s}{dz} = -\frac{i\beta_s}{8I_*^2}\left[\Big(\left|A_s\right|^2 + 2\left|A_i\right|^2 + 2\left|A_p\right|^2 + 2I_{\mathrm{DC}}^2\Big)A_s + 2A_i^*A_pI_{\mathrm{DC}}e^{i\Delta_\beta^{(3)}z}\right] \tag{2.32b}$$

$$\frac{dA_i}{dz} = -\frac{i\beta_i}{8I_*^2}\left[\Big(\left|A_i\right|^2 + 2\left|A_p\right|^2 + 2\left|A_s\right|^2 + 2I_{\mathrm{DC}}^2\Big)A_i + 2A_s^*A_pI_{\mathrm{DC}}e^{i\Delta_\beta^{(3)}z}\right], \tag{2.32c}$$

where $\Delta_\beta^{(3)} = \beta_s + \beta_i - \beta_p$.

2.6 Analytical Solution to the Coupled-Mode Equations

In general, the CMEs presented above require solving numerically, however, considerable insight of the wave mixing process can be attained by solving them analytically under certain assumptions. This process will be presented for ND-4WM, although the same technique can be applied to other wave mixing regimes, since I have demonstrated above how these are special cases that can be derived from ND-4WM using the relevant transformations.

First, it can be assumed that the pump tones are much stronger than the signal and the idler i.e. $A_{p1}, A_{p2} \gg A_s, A_i$. This is known as the strong pump approximation, and under this assumption, all terms of order A_s^2, A_i^2, and $A_s A_i$ can be ignored. The second approximation is known as the undepleted pump approximation, and states that $\frac{d|A_{p1}|}{dz} = \frac{d|A_{p2}|}{dz} = 0$. This is justifiable because A_s and A_i are typically at least an order of magnitude weaker the pump tone(s), even after amplification.

Working in the fully lossless regime and invoking the strong pump approximation, (2.28a)-(2.28b) reduce to,

$$\frac{dA_{p1}}{dz} + \frac{i\beta_{\mathrm{p1}}}{8I_*^2}\left(|A_{\mathrm{p1}}|^2 + 2|A_{\mathrm{p2}}|^2\right)A_{\mathrm{p1}} = 0 \tag{2.33a}$$

$$\frac{dA_{p2}}{dz} + \frac{i\beta_{p2}}{8I_*^2}\left(|A_{\mathrm{p2}}|^2 + 2|A_{\mathrm{p1}}|^2\right)A_{\mathrm{p2}} = 0, \tag{2.33b}$$

which under the undepleted pump approximation can be solved straightforwardly to give,

$$A_{p1}(z) = A_{p1}(0)e^{i\alpha_{p1}z} \tag{2.34a}$$

$$A_{p2}(z) = A_{p2}(0)e^{i\alpha_{p2}z}, \tag{2.34b}$$

where $\alpha_{p1} \equiv -\frac{\beta_{\mathrm{p1}}}{8I_*^2}\left(|A_{\mathrm{p1}}|^2 + 2|A_{\mathrm{p2}}|^2\right)$ and $\alpha_{p2} \equiv -\frac{\beta_{\mathrm{p2}}}{8I_*^2}\left(|A_{\mathrm{p2}}|^2 + 2|A_{\mathrm{p1}}|^2\right)$ represent the self-phase modulation (SPM) and cross-phase modulation (XPM) that the two pumps tones apply to each other.

The solutions in (2.34a)-(2.34b) can then be inserted into the CMEs for the signal and idler. This results in just two coupled equations to be solved,

$$\frac{\partial A_s}{\partial z} - i\alpha_s A_s - i\kappa_s A_i^* e^{i\left(\Delta_\beta^{(N4)} z + \alpha_{p1} + \alpha_{p2}\right)} = 0 \tag{2.35a}$$

$$\frac{\partial A_i}{\partial z} - i\alpha_i A_i - i\kappa_i A_s^* e^{i\left(\Delta_\beta^{(N4)} z + \alpha_{p1} + \alpha_{p2}\right)} = 0, \tag{2.35b}$$

where $\alpha_j \equiv -\frac{\beta_j}{4I_*^2}\left(|A_{p_1}(0)|^2 + |A_{p_2}(0)|^2\right)$ represents the XPM that the two pumps tones apply to the signal and idler, $\kappa_j \equiv -\frac{\beta_j}{4I_*^2}A_{p_1}(0)A_{p_2}(0)$ for $j = s, i$, and $\Delta_\beta^{(N4)} = \beta_s + \beta_i - \beta_{p_1} - \beta_{p_2}$.

The full solution to (2.35a)-(2.35b) is a lengthy exercise presented in [111], so is omitted here for brevity, although it is presented in appendix A.2. Following the solution process and defining the signal gain as,

$$G_s(z) \equiv \left|\frac{A\left(z\right)}{A\left(0\right)}\right|^2, \tag{2.36}$$

the following solution for the signal gain can be written down as,

$$G_s(z) = \left|\cosh(gz) - \frac{i\Delta_k}{2g}\sinh(gz)\right|^2, \tag{2.37}$$

with a corresponding expression for the idler,

$$G_i(z) = G_s(z) - 1, \tag{2.38}$$

where,

$$g = \sqrt{\kappa_s\kappa_i - \frac{\Delta_k^2}{4}}, \tag{2.39}$$

is the gain coefficient and,

$$\Delta_k \equiv \Delta_\beta^{(N4)} + \Delta_\alpha^{(N4)}, \tag{2.40}$$

is the total non-linear phase mismatch and is comprised of the linear phase-mismatch, $\Delta_\beta^{(N4)}$, and $\Delta_\alpha^{(N4)} = \alpha_s + \alpha_i - \alpha_{p_1} - \alpha_{p_2}$, which includes the contributions from SPM and XPM.

It is clear from (2.37) that $G_s(z)$ is maximised when the gain coefficient, g, is maximised (and real), which occurs when $\Delta_k = 0$. The phase-mismatch along a transmission line is essentially a measure of the conservation of momentum along that transmission line, and the SPM and XPM effects can be considered as momentum being added to the transmission line. Naturally, momentum must be conserved, hence any parametric process that is poorly phase matched will not conserve momentum and hence be suppressed.

As stated, the preceding derivation has been for ND-4WM, however, the solution in (2.37) is identical for each of the wave mixing regimes, albeit with different constants, which are summarised in Tab. 2.1.

Term	ND-4WM (N4)	D-4WM (D4)	DC-3WM (3)
Δ_β	$\beta_s + \beta_i - \beta_{p_1} - \beta_{p_2}$	$\beta_s + \beta_i - 2\beta_p$	$\beta_s + \beta_i - \beta_p$
Δ_α	$\alpha_s + \alpha_i - \alpha_{p_1} - \alpha_{p_2}$	$\alpha_s + \alpha_i - 2\alpha_p$	$\alpha_s + \alpha_i - \alpha_p$
α_{p_1}	$-\frac{\beta_{p_1}}{8I_*^2}\left(\lvert A_{p_1}\rvert^2 + 2\lvert A_{p_2}\rvert^2\right)$	N/A	N/A
α_{p_2}	$-\frac{k_{p_1}}{8I_*^2}\left(\lvert A_{p_2}\rvert^2 + 2\lvert A_{p_1}\rvert^2\right)$	N/A	N/A
α_p	N/A	$\frac{-\beta_p}{8I_*^2}\lvert A_p\rvert^2$	$-\frac{i\beta_p}{8I_*^2}\left(\lvert A_p\rvert^2 + 2I_{\mathrm{DC}}^2\right)$
α_s	$-\frac{\beta_s}{4I_*^2}\left(\lvert A_{p_1}(0)\rvert^2 + \lvert A_{p_2}(0)\rvert^2\right)$	$\frac{-\beta_s}{4I_*^2}\lvert A_p(0)\rvert^2$	$-\frac{\beta_s}{4I_*^2}\left(\lvert A_p(0)\rvert^2 + I_{\mathrm{DC}}^2\right)$
α_i	$-\frac{\beta_i}{4I_*^2}\left(\lvert A_{p_1}(0)\rvert^2 + \lvert A_{p_2}(0)\rvert^2\right)$	$\frac{-\beta_i}{4I_*^2}\lvert A_p(0)\rvert^2$	$-\frac{\beta_i}{4I_*^2}\left(\lvert A_p(0)\rvert^2 + I_{\mathrm{DC}}^2\right)$
κ_s	$-\frac{\beta_s}{4I_*^2}A_{p_1}(0)A_{p_2}(0)$	$\frac{-\beta_s}{8I_*^2}A_p^2(0)$	$-\frac{\beta_s}{4I_*^2}A_p(0)I_{\mathrm{DC}}$
κ_i	$-\frac{\beta_i}{4I_*^2}A_{p_1}(0)A_{p_2}(0)$	$\frac{-\beta_i}{8I_*^2}A_p^2(0)$	$-\frac{\beta_i}{4I_*^2}A_p(0)I_{\mathrm{DC}}$

Table 2.1: Summary of the coefficients for (2.37) for the different wave mixing regimes.

2.7 Dispersion Engineering

2.7.1 Harmonic Generation

The non-linear kinetic inductance of the superconducting transmission line is the key property that allows a KITWPA to operate, mediating wave mixing and transferring energy from the pump to the signal. As shown by (2.40), however, the effects of SPM and XPM, which are a consequence of a strong pump (or pumps) in a non-linear medium, lead Δ_k to deviate from 0. This phase-mismatch results in g not being maximised, hence the gain performance of the KITWPA is not optimised.

In addition to the phase mismatch caused by SPM and XPM, the non-linearity of the transmission line allows for the generation of harmonic tones of the pump. Owing to the wave equation in (2.22) being cubic in order, a strong pump tone will generate odd harmonics of itself at $3f_p, 5f_p, 7f_p, \ldots$ [112]. In the case of ND-4WM, the presence of two pumps will additionally lead to the generation of cross harmonics of the pump tones of the form, $2f_{p1} - f_{p2}, 2f_{p2} + f_{p1}, \ldots$, as well as odd harmonics of each pump tone. For DC-3WM, the break of symmetry means that even harmonics of the pump tone are generated as well odd harmonics, i.e. $2f_p, 3f_p, 4f_p, \ldots$.

The generation of harmonics of the pump tone(s) steals energy away from the pump and prevents the maximum amount of energy from being transferred to the signal, therefore, limiting the gain. Additionally, this harmonic generation process

can eventually generate a shock wave in the transmission line [113], suppressing any amplification process taking place in the KITWPA. The generation of the pump harmonics, therefore, requires suppression to achieve efficient parametric amplification.

2.7.2 Periodic Loading

To recover the optimal performance of the KITWPA, the effects of these undesirable phenomena can be mitigated using a technique known as dispersion engineering, which modifies the dispersion relation of the KITWPA to provide the pump with an additional phase to cancel the effects of SPM and XPM, and to creates band gaps to suppress unwanted harmonic generation. A convenient way to achieve this is to periodically modify the characteristic impedance of the STL along it's length.

Consider a STL with a characteristic impedance, Z_0, propagation constant, β, and length, l. For now, we will consider the case where the line is completely lossless to simplify the analysis, however, it can be generalised to include losses. This STL can be mathematically represented using a 2-port circuit model, such as the $ABCD$ matrices,

$$\begin{aligned}\begin{bmatrix} V_{\text{out}} \\ I_{\text{out}} \end{bmatrix} &= \begin{bmatrix} A & B \\ C & D \end{bmatrix} \begin{bmatrix} V_{\text{in}} \\ I_{\text{in}} \end{bmatrix} \\ &= \begin{bmatrix} \cos\beta l & iZ\sin\beta l \\ \frac{i}{Z}\sin\beta l & \cos\beta l \end{bmatrix} \begin{bmatrix} V_{\text{in}} \\ I_{\text{in}} \end{bmatrix},\end{aligned} \tag{2.41}$$

which relate the input current, I_{in}, and input voltage, V_{in}, of the STL to the output current, I_{out}, and output voltage, V_{out}.

Section	Z_s	l_s
a	Z_0	$\frac{l_0}{2}$
b	Z_1	l_1
c	Z_0	l_0
d	Z_3	l_1
e	Z_0	$l_0 + \frac{l_1 - l_3}{2}$
f	Z_1	l_3
g	Z_0	$\frac{l_0 + l_1 - l_3}{2}$

Table 2.2: Characteristic impedance (Z) and length (l) values for the sections that comprise a unit cell with periodic loading, corresponding to the diagram in Fig. 2.5.

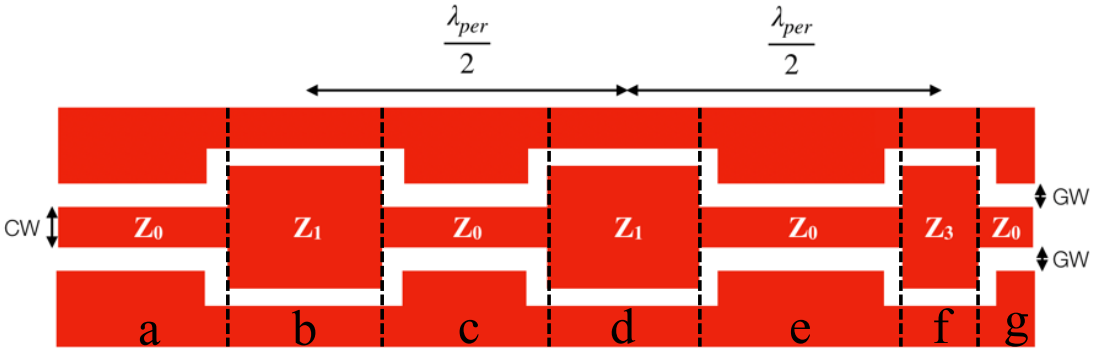

Figure 2.5: Schematic of a CPW that constitutes a unit cell with periodic loadings every $\frac{\lambda_{per}}{2}$ with every third loading being modulated. CW is the width of the CPW centre strip and GW is the width of the CPW gap.

Now consider a modification to the STL, where small, periodic perturbations are made to the characteristic impedance of the line after a certain length, $\frac{\lambda_{\text{per}}}{2}$, such as in the example shown in Fig. 2.5, which shows a transmission line with three impedance loadings made to the line. The characteristic impedance and length of each of these sections are summarised in Tab. 2.2, and using (2.41), it is a trivial task to write down an individual $ABCD$ matrix for each of the impedance sections. The $ABCD$ matrix for the STL in Fig. 2.5 can, therefore, be obtained by simply multiplying together the respective $ABCD$ matrices for each of the impedance sections, i.e.,

$$\begin{pmatrix} A & B \\ C & D \end{pmatrix}_{\text{unit cell}} = \prod_s \begin{pmatrix} \cos(\beta l_s) & iZ_s \sin(\beta l_s) \\ \frac{i}{Z_s} \sin(\beta l_s) & \cos(\beta l_s) \end{pmatrix}, \tag{2.42}$$

for $s = a, b, \ldots, g$. This length of STL is defined as a unit cell and a KITWPA can be formed by cascading many of these unit cells together using translational symmetry via Floquet Theorem,

$$\begin{pmatrix} A & B \\ C & D \end{pmatrix}_{\text{KITWPA}} = \begin{pmatrix} A & B \\ C & D \end{pmatrix}^m_{\text{unit cell}}, \tag{2.43}$$

where m is the number of cascaded unit cells that comprise a KITWPA.

Whilst the $ABCD$ matrices are mathematically convenient for STL modelling as they can be easily cascaded together, it is desirable to represent the STL using parameters that are more readily measurable in an experimental setup, such as the scattering parameters (or S-parameters),

$$\begin{bmatrix} b_1 \\ b_2 \end{bmatrix} = \begin{bmatrix} S_{11} & S_{12} \\ S_{21} & S_{22} \end{bmatrix} \begin{bmatrix} a_1 \\ a_2 \end{bmatrix}, \tag{2.44}$$

which are a set of complex parameters that relate the incident power waves, a_i, to the reflected power waves, b_i. In this representation, S_{ii} is interpreted as the reflection coefficient at port i and S_{ij} is interpreted as the transmission coefficient to port i from port j. Of principle interest to us in this analysis is the forward transmission, denoted by S_{21}, which can be calculated from the $ABCD$ coefficients using,

$$S_{21} = \frac{2}{A + \frac{B}{Z} + CZ + D}, \tag{2.45}$$

where Z is the characteristic impedance of that section. The dispersion relation for a KITWPA can then be calculated from the cumulative phase of the S_{21},

$$k = -\frac{\text{unwrap}[\arg(S_{21})]}{ml}, \tag{2.46}$$

where l is the unit cell length, and the transmission spectrum is simply given by the magnitude of the forward transmission, $|S_{21}|$.

The changes to the characteristic impedance along the length of a STL are known as periodic loadings (PLs) and have the effect of creating band gaps in the transmission spectrum and dispersion relation. For the particular example in Fig. 2.5, placing a loading every $\frac{\lambda_{\text{per}}}{2}$ will create a band-gap at a frequency of,

$$f_{\text{per}} = \frac{v_{\text{ph}}}{\lambda_{\text{per}}}, \tag{2.47}$$

and integer multiples thereof, where v_{ph} is the phase velocity in the STL. Additionally, the further modulation of, say, every third loading to an impedance different to the first two loadings creates smaller band gaps at integer multiples of $\frac{f_{\text{per}}}{3}$. Similarly, further modulating every forth loading would create smaller band gaps at integer multiples of $\frac{f_{\text{per}}}{4}$. Tones propagating along the STL that fall into these frequency band gaps will be heavily attenuated. These band gaps are shown graphically in Fig. 2.6(a), which highlights the position of the large third band gap at f_{per} and the smaller band gaps at integer multiples of $\frac{f_{\text{per}}}{3}$. Additionally, the dispersion relation near the edge of the band gaps varies exponentially, meaning that a tone propagating along the transmission line with a frequency at the edge of one of these band gaps will experience a substantial phase shift, as shown in Fig. 2.6(b), where the inset shows a clear deviation in the dispersion relation from an otherwise linear trend.

Consider this behaviour in the context of a KITWPA operating in the D-4WM regime for simplicity, although the same applies to other wave mixing regimes. If

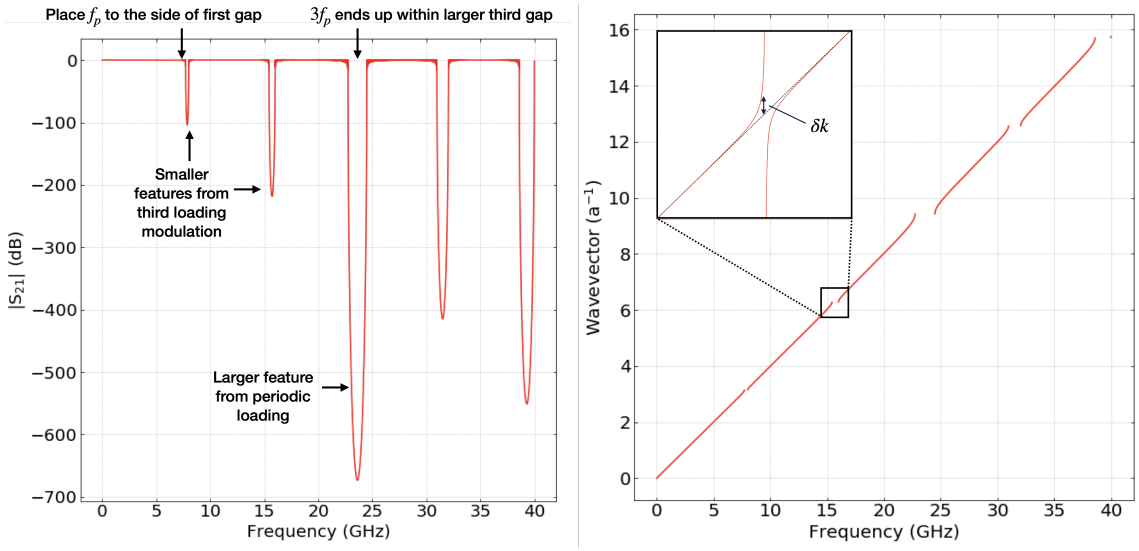

(a) Transmission, $|S_{21}|$. (b) Dispersion.

Figure 2.6: (a) Transmission spectrum and (b) dispersion relation for an ideal (lossless) KITWPA consisting of 100 unit cells with $Z_0 = 50\,\Omega$, $Z_1 = 80\,\Omega$, $Z_2 = 200\,\Omega$, $l_0 = 24l_1 = 24l_3$, and $f_{\text{per}} = 24\,\text{GHz}$. The dispersion feature in the inset of (b) has been extrapolated to highlight the the phase shift near the edge of the band-gap.

the pump tone is placed close to one of the band gaps, say the smaller one at $\frac{f_{\text{per}}}{3}$, it acquires an additional phase, $\delta\beta_p$, such that the total phase mismatch becomes,

$$\Delta_k = \Delta_\beta + \delta\beta_p - \Delta_\alpha. \tag{2.48}$$

If $\delta\beta_p$ is tuned appropriately such that $\delta\beta_p = -(\Delta_\beta - \Delta_\alpha)$, the non-linear phase mismatch along the STL can be corrected for, which maximises the amount of wave mixing and hence the gain. If the pump is placed close enough to the first band gap, the generation of a third harmonic of the pump tone is suppressed by the larger band gap at f_{per}, which prevents the generation of subsequent odd harmonics and, therefore, limits energy leakage from the pump and prevents shock wave formation [77].

2.7.3 Sinusoidal Transmission Line

The analysis in § 2.7.2 focused on achieving phase matching and harmonic suppression by implementing a discrete periodic loading structure. Dispersion engineering, however, need not be limited to discrete loading structures and can also be achieved using continuous impedance modulation, such as a sinusoidal variation [2, 76, 82].

Here, I derive a mathematical description for a transmission line with a sinusoidally varying impedance, before extending to a novel double sinusoidal loading technique, then further generalising to an arbitrary number of sinusoidal loadings.

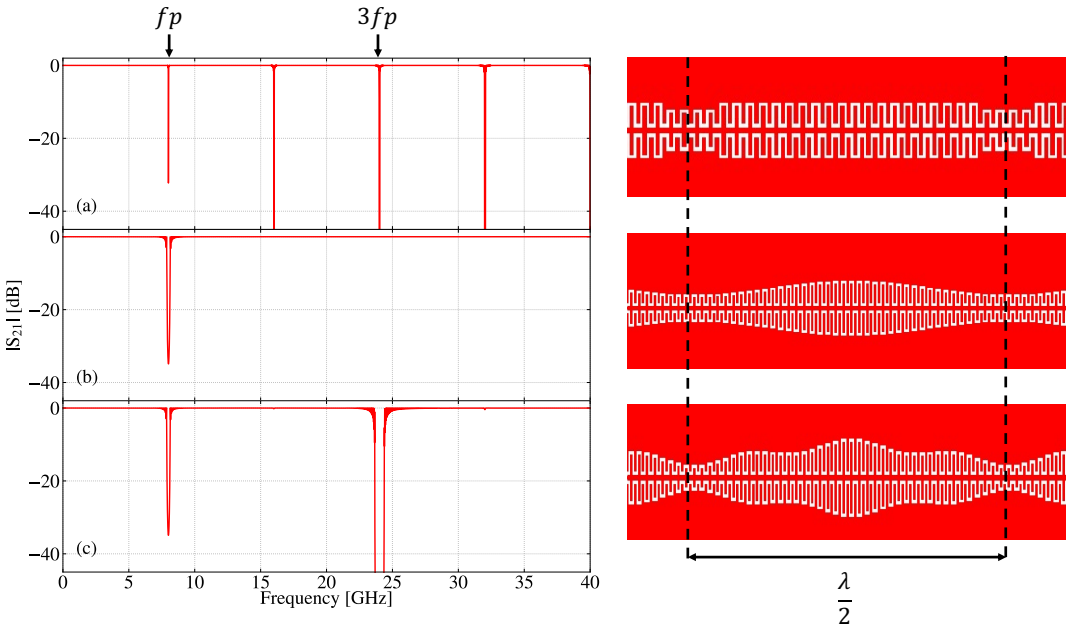

Figure 2.7: Transmission profile (left) and illustration of the loading scheme (right) for a standard discrete periodic loading structure (a), a single sinusoidal loading structure (b), and a double sinusoidal loading structure (c). Illustrations are not to scale for clarity.

Fig. 2.7(a)-(c) compares the transmission spectra for different periodic loading types, the structures of which are shown schematically on the right-hand side of the figure. The first periodic loading structure, as shown in Fig. 2.7(a), is a discrete periodic loading structure, which, as discussed previously, generates band gaps at integer multiples of f_{per} when a modulation to the impedance is made every $\frac{\lambda_{\text{per}}}{2}$. The second periodic loading structure is a single sinusoidal loading structure, which, as discussed in the following, creates a single band gap at f_{per} when a sinusoidal modulation to the impedance is made with a period of $\frac{\lambda_{\text{per}}}{2}$.

Consider a STL where the characteristic impedance is modulated sinusoidally along the length of the line according to,

$$Z(z) = Z_0 + Z_1 \cos\left(\frac{2\pi z}{l}\right), \tag{2.49}$$

where Z_0 is the nominal impedance, Z_1 is the loading impedance, z is the position along the length of the line, and $l = \frac{\lambda_{\text{per}}}{2}$ is the period of the section. The $ABCD$

parameters presented in (2.41) are valid only for a transmission line with a constant impedance, so to calculate the $ABCD$ parameters for a transmission line with a continuously modulating impedance, a unit cell, with length l can be further divided into N shorter transmission line segments, each with a length $\delta l = \frac{l}{N}$ and a constant characteristic impedance, Z_n, given by,

$$Z_n = Z_0 + Z_1 \cos\left(\frac{2\pi n}{N}\right), \tag{2.50}$$

The $ABCD$ matrix for a sinusoidal unit cell is calculated by cascading the $ABCD$ matrices of the N individual transmission line segments together via matrix multiplication. If the STL comprises m unit cells, the $ABCD$ matrix for the full line is given by,

$$\begin{pmatrix} A & B \\ C & D \end{pmatrix} = \prod_{n=0}^{mN} \begin{pmatrix} \cos(\beta\delta l) & iZ_n \sin(\beta\delta l) \\ \frac{i}{Z_n}\sin(\beta\delta l) & \cos(\beta\delta l) \end{pmatrix}. \tag{2.51}$$

In the limit that $N \to \infty$ and $\delta l \to 0$, (2.51) becomes the $ABCD$ matrix for a transmission line with a smoothly varying impedance, which can then be converted to the dispersion relation and transmission spectrum using (2.45).

Calculating the $ABCD$ parameters in (2.51) produces the transmission spectrum for a single sinusoidal loading structure as shown in Fig. 2.7(b). This analysis, however, is not restricted to a single sinusoidal impedance modulation as described by (2.50) and can be generalised to an arbitrary number of sinusoidal modulations as mathematically described by,

$$Z(z) = Z_0 + \sum_{j=1}^{J} Z_j \cos\left(c_j \frac{2\pi z}{l}\right), \tag{2.52}$$

where Z_0 is the nominal impedance, Z_j is the impedance amplitude of the j^{th} sinusoidal modulation, and c_j is a constant that sets the relative periodic length of the j^{th} sinusoidal modulation. Assuming $c_j \neq c_{j'}$ and that $c_1 = 1$, the impedance modulation described in (2.52) will create J band gaps at frequencies of $c_j f_{\text{per}}$. The power of this periodic loading scheme is that we are able to create an arbitrary number of band gaps at arbitrary frequencies, which can be tuned to suit the particular experimental needs. Furthermore, this formulation is not restricted to KITWPAs and could be applied to a range of other applications, for example a band-stop filter with an arbitrary number of band gaps at arbitrary frequencies could easily be constructed by including more sinusoidal modulations. Additionally, this formulation is not limited to sinusoidal periodic loading structures, and can be further generalised to describe a priodic loading structure made from any arbitrary waveform, depending on the Z_j and c_j values.

As an example, let us consider the case where we impose a double sinusoidal modulation to the impedance of the line, where one of the sinusoidal modulations has a period 3 times shorter than the other, as summarised by,

$$Z(z) = Z_0 + Z_1 \cos\left(\frac{2\pi z}{l}\right) + Z_2 \cos\left(3\frac{2\pi z}{l}\right). \tag{2.53}$$

This double sinusoidal periodic loading structure creates two distinct band gaps at f_{per} and $3f_{\text{per}}$, as shown in Fig. 2.7(c), which, as discussed in § 2.7.2, for a KITWPA can be used for phase matching of the pump tone and suppression of the third harmonic of the pump, respectively. This creates a neater transmission spectrum, which only contains the band gaps that are necessary.

2.8 Summary

In this chapter, I have discussed the core theoretical principles of KITWPA operation, providing an insight into the physical mechanisms taking place. I have derived the CMEs for a KITWPA from first principles and by making some simple transformations, I have demonstrated that the generalised CMEs that I derived in (2.25a)-(2.25d) can incorporate the behaviour of all wave mixing regimes. I then introduced the concepts of dispersion engineering and period loading, before developing a novel sinusoidal loading technique, which can create an arbitrary number of band gaps at arbitrary frequencies. The result of this discussion is that we are now able to to produce an electrical design of a KITWPA device. Subsequent chapters will extend upon the theoretical framework introduced in this chapter to develop a methodology for converted the electrical model into a physical model of a KITWPA device. For all the simulations presented in the next chapter, I use the CMEs presented in (2.29a)-(2.29c) for D-4WM, which include transmission line losses but ignore L_g, unless otherwise specified.

It should be noted here that we intended to develop a KITWPA using the double sinusoidal periodic loading scheme, and a design for this is presented in [2], although fabrication and experimental characterisation is left for future investigation. It should also be noted that there are other schemes that can be used for dispersion engineering and pump harmonic suppression, such as employing a coupled resonator or utilising the cut-off frequency of the STL, which achieve the same purpose but are not included here as I do not use these alternative schemes in my work.

Chapter 3

Electromagnetic Modelling Technique, Design Methodology and Considerations

3.1 Introduction

Chap. 2 introduced the fundamental theoretical concepts and frameworks to create a purely mathematical model of a KITWPA device. Whilst this gives considerable insight into the design motivations, we still need a technique that is able to produce a physical model of a KITWPA, which can translate the electrical parameters of a transmission line into physical dimensions. In this chapter, I will introduce a KITWPA design methodology using a rigorous, numerical EM-based approach, which uses the commercial EM solver package, ANSYS High Frequency Structure Simulator (HFSS) to model a superconducting transmission line.

The first part, which details the modelling technique and design methodology, begins with a discussion on transmission line types that can be used to construct a KITWPA, including their various advantages and drawbacks. We then proceed to demonstrate how HFSS can be used to simulate the transmission line properties of a KITWPA in order to extract the physical properties of the line, including the effects of the substrate losses, which are often neglected by other modelling techniques. I will then introduce SuperTWPA, a python-based software package written by me that allows the user to import a simulation model from HFSS and calculate the gain of the KITWPA by solving the CMEs, either numerically or analytically for

all wave mixing regimes. The second part then discusses some important design considerations when designing a KITWPA, including the choice of superconducting film, substrate, and topology. The chapter concludes with a final section on an optimised KITWPA design that can achieve the desired high-gain performance with the shortest possible length and lowest pump power.

3.2 Modelling Technique and Design Methodology

In this section, we discuss the techniques used to generate a physical model of a KITWPA comprising a superconducting transmission line.

3.2.1 Transmission Line Types

A transmission line is a structure that allows for the propagation of electromagnetic radiation in a contained manner and can be designed and optimised to suit a wide variety of applications. As discussed in Chap. 2, a KITWPA can be realised as a long, superconducting transmission line, the properties of which have a huge influence on the operational performance of the KITWPA.

Figs. 3.1(a)-(e) display some of the most commonly used planar transmission line topologies. The earliest KITWPA devices comprised a co-planar waveguide (CPW) transmission line with a length of order 1 m patterned into a NbTiN film [21, 70]. A CPW is a single current-conducting layer structure, comprising a central conducting strip with some finite width, surrounded by a pair of ground planes each separated from the central strip by some gap, as shown in Fig. 3.1(a). The fact that their characteristic impedance is determined only by the ratio between the strip width and gap width makes them a popular choice for on-chip integrated circuits. Additionally, their co-planar structure means only a single deposition layer is required during fabrication, which is naturally much simpler than multi-layer structures. In practice, the high kinetic inductance of the superconducting film used to construct a KITWPA means a superconducting CPW will typically have a high characteristic impedance, Z_0, since,

$$Z_0 = \sqrt{\frac{L}{C}}, \tag{3.1}$$

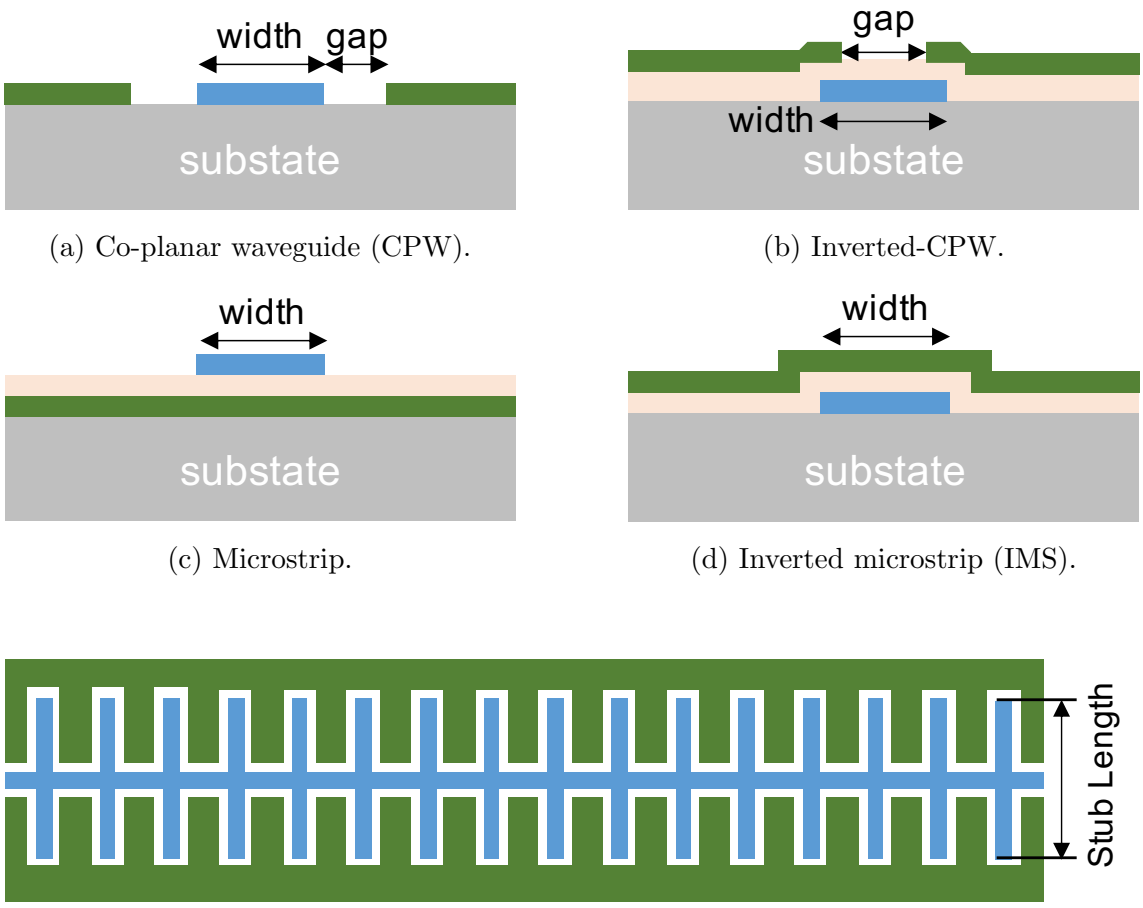

(a) Co-planar waveguide (CPW).

(b) Inverted-CPW.

(c) Microstrip.

(d) Inverted microstrip (IMS).

(e) Fishbone CPW.

Figure 3.1: Various types of transmission line topologies, where the ground layers are coloured green, the dielectric layers are light orange and the wiring layers are blue.

which is the expression for the characteristic impedance in the low-loss limit. We see that Z_0 is proportional $\sqrt{L}$, which makes it is difficult to match the impedance of the superconducting CPW line to $50\,\Omega$ without high capacitance. This can be overcome, however, by using a fishbone-style CPW, as shown in Fig. 3.1(e), where the superconducting CPW is shunted with additional stubs, which has the effect of increasing the capacitance, C, of the line [73]. From (3.1), this reduces Z and allows a $50\,\Omega$ to be achieved. Careful design consideration is needed, however, in order to avoid exciting parasitic propagation modes, such as the slotline mode, especially when the long STL is meandered into a compact structure, as CPW lines can interact easily with adjacent lines compared to other line topologies.

More recently reported KITWPA devices have been constructed from microstrip (MS) or, more specifically, inverted microstrip (IMS) transmission lines [81,82]. MS transmission lines, as shown in Fig. 3.1(c), have proved to be popular in the field of microwave engineering due to their ease of integration with other passive and active microwave devices [109]. They are also easier to design, as the majority of the field lines are contained within the dielectric material, which shields from the effects of the substrate. Additionally, there is no discontinuity in the ground plane, meaning no parasitic slotline mode. MS/IMS lines are typically trilayer devices, which require at least three fabrication steps to deposit the ground layer, dielectric layer and wiring layer. A variation of the MS line is the IMS line, as shown in Fig. 3.1(d), whereby the the fabrication layers are reversed, i.e., the wiring layer is closest to the substrate and is covered by the dielectric and the ground layers. The high capacitance of the MS and IMS line types, due to their resemblance of a parallel plate capacitor structure, has the effect of significantly reducing the physical length of a KITWPA. This, combined with the use of electron-beam (E-beam) lithography to pattern very fine features, allows MS/IMS-based KITWPAs, as well as those based on CPWs to be extremely compact.

The use of a dielectric layer in a MS/IMS line, however, means that they may be lossier than CPW lines due to dielectric losses and suffer more from two-level system (TLS) losses. The use of low-loss dielectric materials such as hydrogenated amorphous silicon (a-Si:H) [82, 114] and hydrogenated amorphous silicon carbide (a-SiC:H) [85], however, can potentially be used to mitigate these losses.

For completeness, Fig. 3.1(b) shows the inverted coplanar waveguide (ICPW) structure, which exhibits properties somewhere between that of a CPW and an IMS. Similar to an IMS, the wiring layer of an ICPW is protected by the dielectric layer, however, opening up a gap in the ground plane means that less of the electric field lines are going through the dielectric layer, hence reducing the effect of dielectric losses. One interesting advantage of this structure is that the ICPW gap can be made arbitrarily small, hence can provide another way to increase the capacitance of the transmission line.

A more detailed investigation into the optimum transmission line type for a KITWPA is described later in § 3.3.3. Note, however, that there are many other transmission line variants that, in principle, can be used to construct a KITWPA. These lines are not described here as MS/IMS and CPW lines are generally the most popular choice for KITWPAs as well as many other applications, and the use

of other transmission line types, e.g. striplines, parallel strip lines, etc, is generally reserved only for special cases.

3.2.2 Modelling a Superconducting Transmission Line

There are many ways of obtaining the physical properties of a transmission line from the electrical parameters. One method to achieve this is by using an analytical approach, such as conformal mapping, which calculates the transmission line parameters via transmission line theory [110]. Whilst this technique is frequently used, it has many limitations such as the many approximations involved as well as the fact that modifying these analytical models to simulate any generalised transmission line, including the simulation of arbitrary shapes such as the shunted capacitive stubs, is a highly non-trivial task. For instance, a completely separate mathematical model is required to describe each of the transmission lines in Fig. 3.1. Another approach reported in the literature is to use a finite-difference time-domain (FDTD) solver [115], although these approaches tend to be computationally intensive and are plagued with the same inflexibility as the analytical techniques.

To circumvent these problems, we employ a numerical-based approach [1] using HFSS, a finite-element solver that decomposes a 3D computer-aided design (CAD) model into a mesh grid and solves the differential form of Maxwell's equations on this mesh. The 3D CAD environment, as shown in Fig. 3.2, allows the user to draw arbitrary microwave structures and assign material properties to the different components of the structure, such as the transmission line's conducting material, dielectric, substrate, etc., without having to completely re-derive the line behaviour from transmission line theory. The main advantage of using such a numerical-based 3D modeller is the enormous flexibility that it offers in modelling arbitrary KITWPA designs. Additionally, HFSS has the capability to encompass all of the subtle EM properties of the structure, such as, but not limited to, subtle fringing effects of the field, radiative losses, discontinuities, geometric inductance and capacitance of the superconducting transmission line, etc.

The HFSS project libraries are equipped with a large range of materials to create an arbitrary structure from, however, superconductivity is a feature that is not explicitly built-in. To emulate the behaviour of a superconducting thin film in HFSS, therefore, we need to import the properties of the superconducting material,

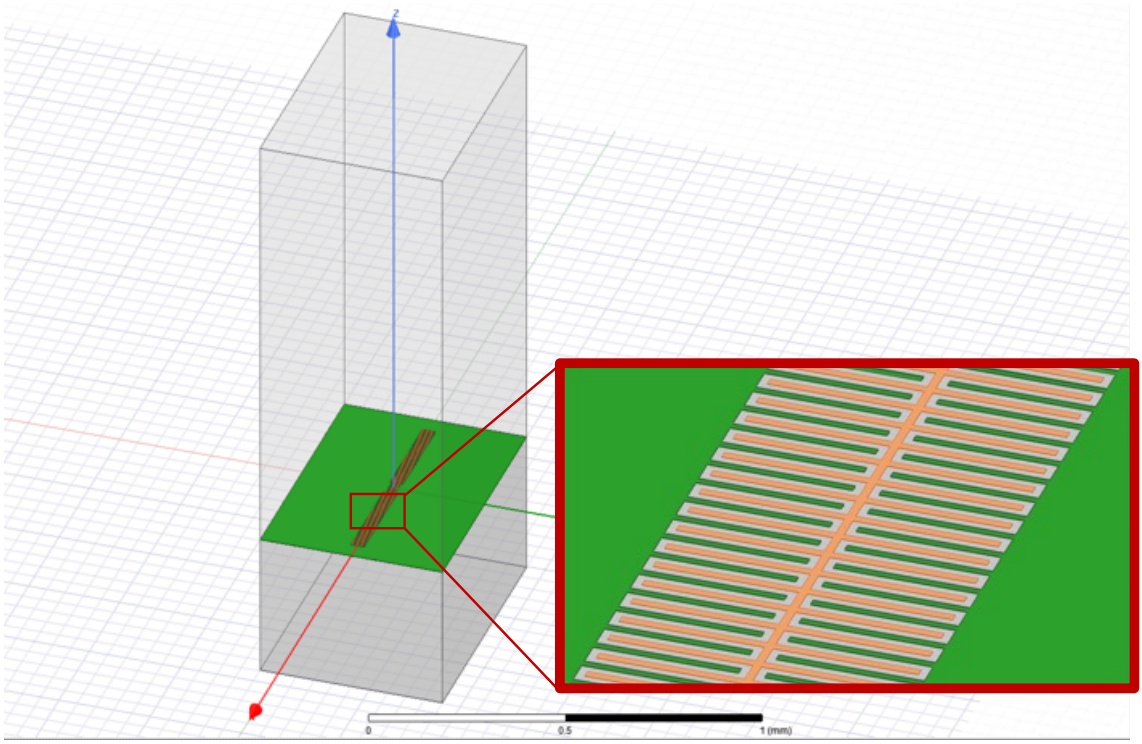

Figure 3.2: Image of a fishbone CPW transmission line model drawn using HFSS, with the centrestrip coloured orange and the ground plane coloured green. The darker transparent region below the ground plane is the substrate, and the lighter transparent region above the ground plane is vacuum.

which can be achieved by assigning an impedance boundary condition on a structure within the CAD model. This technique is explained in detail in [103].

The two most important electrical parameters needed to design a transmission line for a KITWPA are the characteristic impedance, Z_0, and the effective wavelength of the line. The methodology described in the following makes use of a fishbone-style CPW transmission line as an example, although the principle applies to any transmission line type. The CPW model in Fig. 3.2 contains a lumped-port at each end of the line, with each port having a fixed, user-assigned characteristic impedance.[1] The power transfer is maximised (and accordingly the reflection is minimised) when the characteristic impedance of the transmission line matches that of the ports.

[1]HFSS also supports waveports, which automatically match their characteristic impedance to that of the transmission line, however, this technique gives inaccurate results for a fishbone transmission line as the cross section used to calculate the impedance does not taken the length of the stubs into account.

For example, as previously discussed, the additional stubs in a fishbone-style CPW generate additional capacitance, which allows the line to be matched to 50 Ω. The capacitance of the line is proportional to the length of the stubs, so by controlling the length of the stubs, we are able to achieve a 50 Ω line. Fig. 3.3(a) shows the $|S_{11}|$ reflection as a function of stub length. We can see immediately that there is a minimum in the reflection for a stub length of 72 µm, which implies that our transmission line is impedance matched to the 50 Ω ports in the model at this stub length.

In Fig. 2.6, we discussed how introducing periodic loadings to the transmission line after every electrical length, $\frac{\lambda_{\text{per}}}{2}$, produces band-gaps in the dispersion and the transmission spectra at integer multiples of f_{per}. To place these band-gaps at the desired positions, we need to convert the electrical length of the transmission line into physical length, in order to know how far the periodic loadings should be placed in the physical model. There are several ways of achieving this. In our case we calculate the B element of the $ABCD$ matrix in (2.41) and take its imaginary component, which is the wavevector of the transmission expressed in Ω. The B element can be calculated from the S-parameters in (2.44) using,

$$B = Z_0 \frac{(1 + S_{11})(1 + S_{22}) - S_{12}S_{21}}{2S_{21}}, \tag{3.2}$$

which are readily obtained from HFSS. Fig. 3.3(b) shows $\Im[B]$ as a function of frequency for a transmission line of the form in Fig. 3.2. We notice immediately that the curve is sinusoidal and that its first crossing of the x-axis occurs at approximately 6.5 GHz, indicating that the physical length of this model corresponds to an electrical length of half a wavelength at 6.5 GHz. In other words, if we were to place our periodic loadings with this particular physical separation, we would create band-gaps at integer multiples of 6.5 GHz. If instead we wanted our periodic loadings at a different frequency, say integer multiples of 10 GHz, we would simply need to decrease the physical length of the transmission line until the first non-zero x-axis crossing occurred at 10 GHz.

As stated previously, the power of using HFSS is the ability to model many of the subtle effects of a real transmission line that are usually neglected in analytical models, such as the geometric inductance. The total inductance of a transmission line is the sum of the kinetic inductance and the geometric inductance, and it is important to model both contributions as they both affect the characteristic impedance and phase velocity of the line. As shown in (2.19), however, only the kinetic inductance contributes to the non-linearity of the transmission line and hence wave

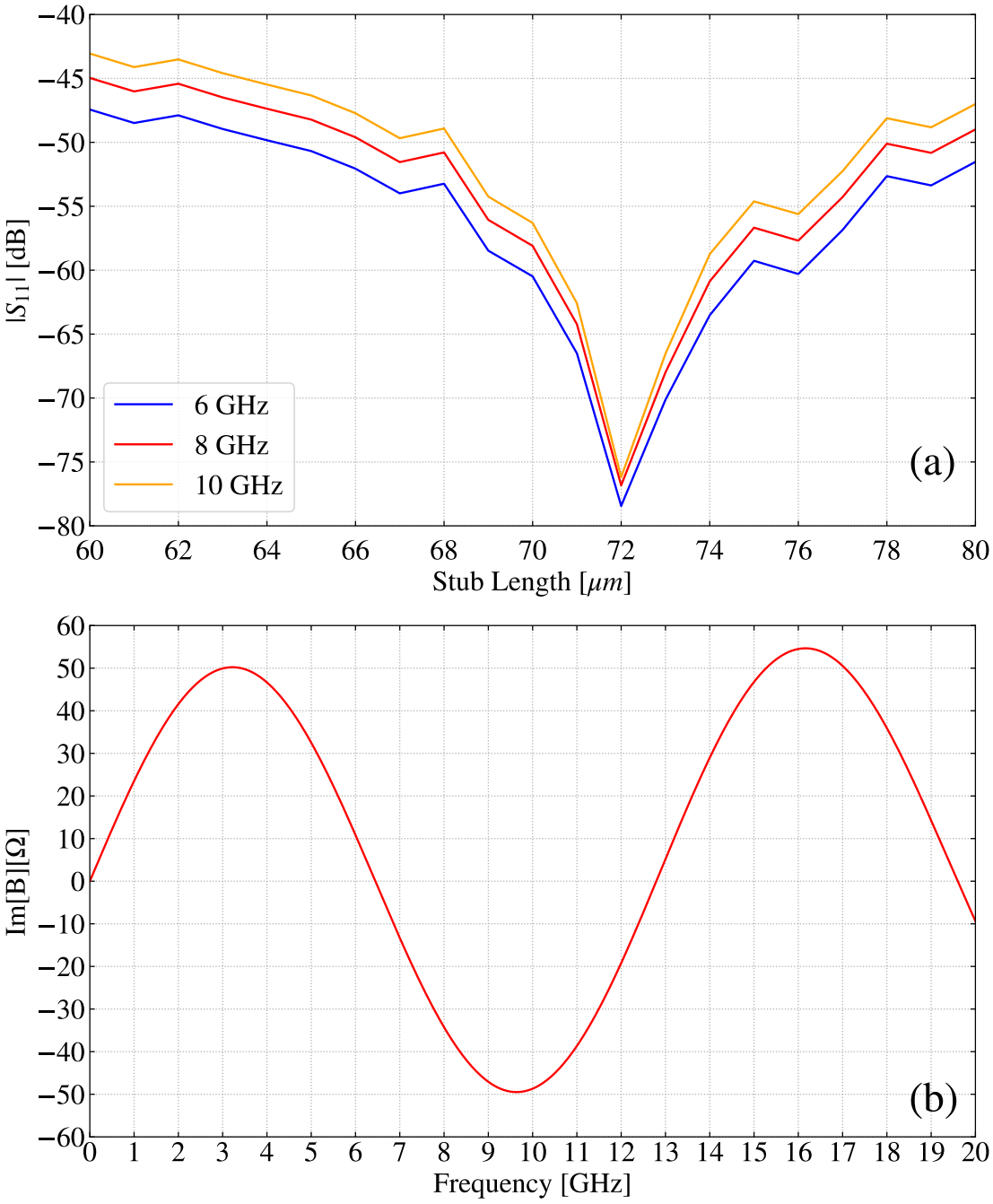

Figure 3.3: (a) Utilising $|S_{11}|$ to determine the transmission line dimensions, in this case, optimising the length of the capacitive stubs to achieve $Z_0 = 50\,\Omega$. (b) Utilising $\Im[B]$ to determine the electrical length of the transmission line.

mixing, therefore, the effects of the geometric inductance need to be removed when calculating the gain of a KITWPA using the CMEs.

For a transmission line in the low-loss limit and where $I \ll I_*$, we can equate the two definitions of the phase velocity and write down an expression for the dispersion

relation in terms of the inductance and capacitance,

$$\frac{\omega}{k} = \sqrt{\frac{1}{(L_{k0} + L_g)\, C}}, \tag{3.3}$$

where L_{k0} is the zero-current kinetic inductance per unit length, L_g is the geometric inductance per unit length, and C is the capacitance per unit length. During the derivation of the CMEs in the low-loss limit, we make the substitution, $k^2 = \omega^2 L_{k0} C$, in (2.28), which removes the remaining $RLGC$ values and allows the direct substitution of the complex propagation constant, γ, into the CMEs. In the subsequent step, we assume that $L_{k0} \gg L_g$, however, if we want to include the effects of L_g, we can see from (3.3) that this substitution is not valid if L_g is large. Rearranging (3.3), we can see that the appropriate substitution should be,

$$\omega^2 L_{k0} C = k^2 - \omega^2 L_g C. \tag{3.4}$$

In a single HFSS model, it is not possible to distinguish between the contributions from L_{k0} and L_g, so to remove L_g, it is necessary to re-simulate the HFSS model without the superconducting surface impedance boundary, and instead with the line material set as PEC. This removes all effects of superconductivity, including the kinetic inductance, meaning that the dispersion relation becomes,

$$\frac{\omega}{k^{\mathrm{PEC}}} = \sqrt{\frac{1}{L_g C}}, \tag{3.5}$$

where k^{PEC} is the wavenumber in the absence of superconductivity. Substituting (3.5) into (3.4) produces,

$$\begin{aligned} \omega^2 L_{k0} C &= k^2 - (k^{\mathrm{PEC}})^2 \\ &= k'^2, \end{aligned} \tag{3.6}$$

where the corrected wavenumber,

$$k' \equiv \sqrt{k^2 - (k^{\mathrm{PEC}})^2}, \tag{3.7}$$

can be considered as an effective propagation constant that only includes contributions from the kinetic inductance.

Fig. 3.4 shows an example of this effect, where we plot the gain versus film resistivity for an arbitrary KITWPA device when simulated with and without the removal of L_g. For all resistivities, failure to remove L_g leads to an overestimation of the gain, although the overestimation is smaller at higher resistivity, where the kinetic inductance is higher. Additionally, we see that for the curve with L_g removed,

the gain goes to zero as the resistivity goes to zero, which makes sense, as this is the case where only L_g is present, hence there should be no wave mixing and, therefore, no gain. This is in contrast to the curve without L_g removal, which implies that a transmission line with zero kinetic inductance would achieve $\sim 3\,\mathrm{dB}$ gain, which is not physical. This highlights the importance of appropriate L_g removal from the HFSS model for an accurate gain calculation, although for higher kinetic inductances the effect becomes more marginal.

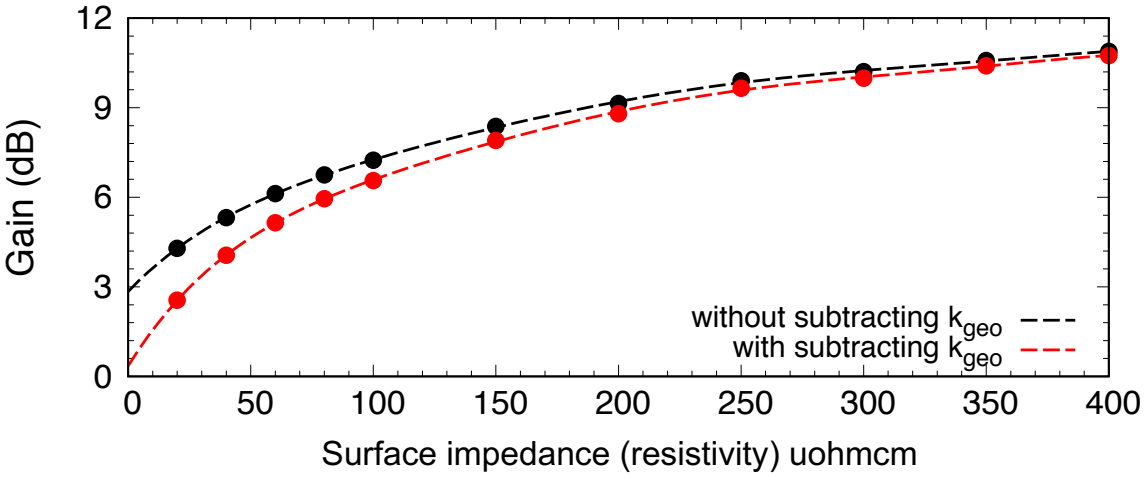

Figure 3.4: Simulated gain as a function of superconducting film resistivity with (red) and without (black) the removal of the geometric inductance.

Having calculated the physical parameters of our transmission line model, we are now able to simulate a KITWPA device. Owing to the relatively intense computational requirements of HFSS, we only simulate a single unit cell using this method. We then extract the S-parameters of the unit cell and convert them to $ABCD$ parameters using the conventional conversion formulae in [109], or we can export the unit cell model as a Touchstone file (or another file format) into a complementary software package, ANSYS Designer (or any other circuit modelling software), which calculates the $ABCD$ parameters. The $ABCD$ matrix for the unit cell is then cascaded using translation symmetry via Floquet Theorem and converted back to the S-parameters of the full transmission line, from which the complex propagation constant, $\gamma = \alpha + i\beta$, can be extracted. This can then be inserted into the CMEs to calculate the gain of the KITWPA, a process which is discussed further in the next section.

It should be emphasised that the power in using this cascading technique is that any arbitrary component, such as filters, tapers, antennae, etc, can be added to the

KITWPA model by simply multiplying the *ABCD* matrix of that component to the rest of the line, allowing its effect on the gain curve to be modelled.

3.2.3 SuperTWPA

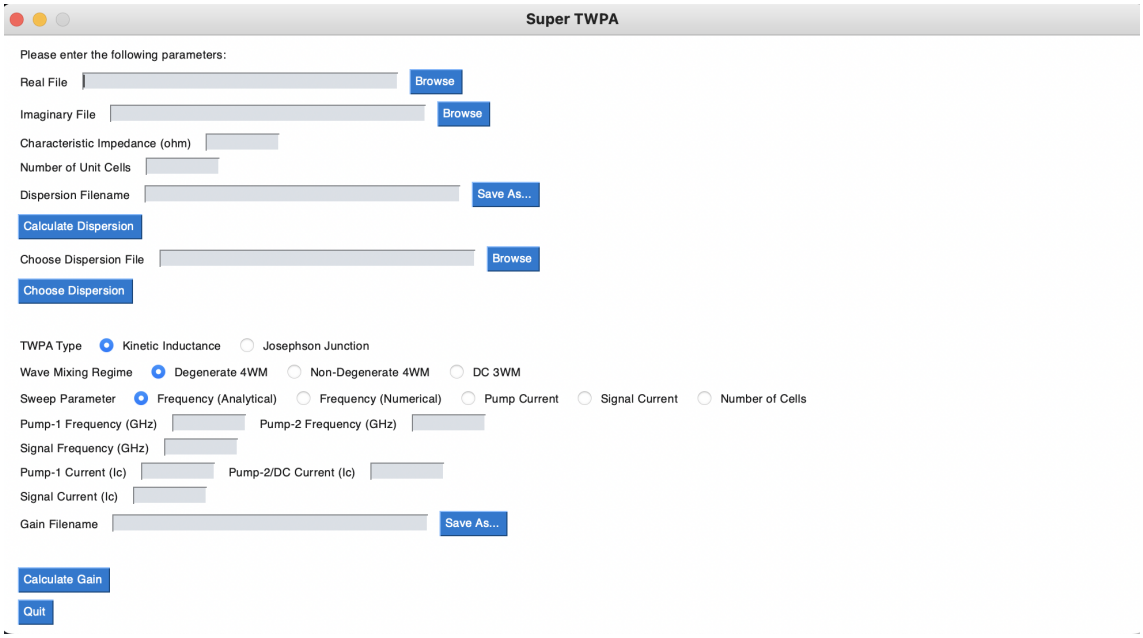

Figure 3.5: SuperTWPA graphical user interface (GUI) used to import transmission line matrix data and subsequently solve the CMEs to calculate the gain of a KITWPA.

In order to quickly and easily calculate the gain performance of a KITWPA device, I have developed a software package in Python called SuperTWPA, which allows the user to import the ABCD matrix of a unit cell from HFSS (or another source for that matter) and cascade the unit cells via matrix multiplication to produce the S-parameters for a full KITWPA. The gain can then be calculated by solving the CMEs, which is either done numerically using numerical integrator function in the SciPy module, or analytically using the expression derived in (2.37).

This code is extremely flexible, as it is able to calculate the gain for any imported transmission line structure operating in any of the three different wave-mixing regimes discussed in § 2.5. Furthermore, the gain can be calculated as a function of different parameters, including the frequency, pump current, signal current, and position along the KITWPA, which allows for gain-bandwidth calculation, the determination of the 1 dB compression point, and the pump saturation point,

etc. SuperTWPA also comes with a convenient graphical user interface (GUI), as shown in Fig. 3.5, which allows the user to easily select the files to import and which calculations to perform.

Finally, I summarise the full design methodology for simulating a KITWPA device in Fig. 3.6, using all of the mathematics and procedures that I described in Chaps. 2-3, except now presented in a more concise manner.

3.3 Design Considerations

Having presented our design methodology, I shall now highlight the versatility of the combined HFSS and bespoke Python package suite by embarking on an investigation into the various design considerations that must be examined when designing a KITWPA device. Tab. 1.1 summarises the successful KITWPAs, which have been reported in the literature, however, on initial inspection of the devices, the various design choices that have been made are seemingly arbitrary, with no obvious reason for their selection. In this section, therefore, we aim to better understand why certain design choices have been made, beginning with the choice of superconducting film.

3.3.1 Thin Film Considerations

When developing a KITWPA, it is crucial that consideration is given to the choice of superconducting film from which the device is constructed, since for a successful KITWPA, it is desired that the film has a high kinetic inductance to promote wave mixing but a low resistive loss to limit the noise and to achieve high gain with a shorter line. Here, I will investigate the properties of a number of commonly used BCS superconducting films to better understand their properties and to ascertain which is most suitable for KITWPA applications, i.e., is there any film that has a higher kinetic inductance but lower resistance compared to the others.

Tab. 3.1 summarises the critical parameters for the BCS films under investigation, which are associated with high resistivity, ρ_N, i.e., niobium nitride (NbN), niobium titanium nitride (NbTiN), titanium (Ti), and titanium nitride (TiN). All the materials listed in Tab. 3.1 have been extensively researched in the literature, either for KITWPA or similar applications, such as MKIDs, which require similar film properties.

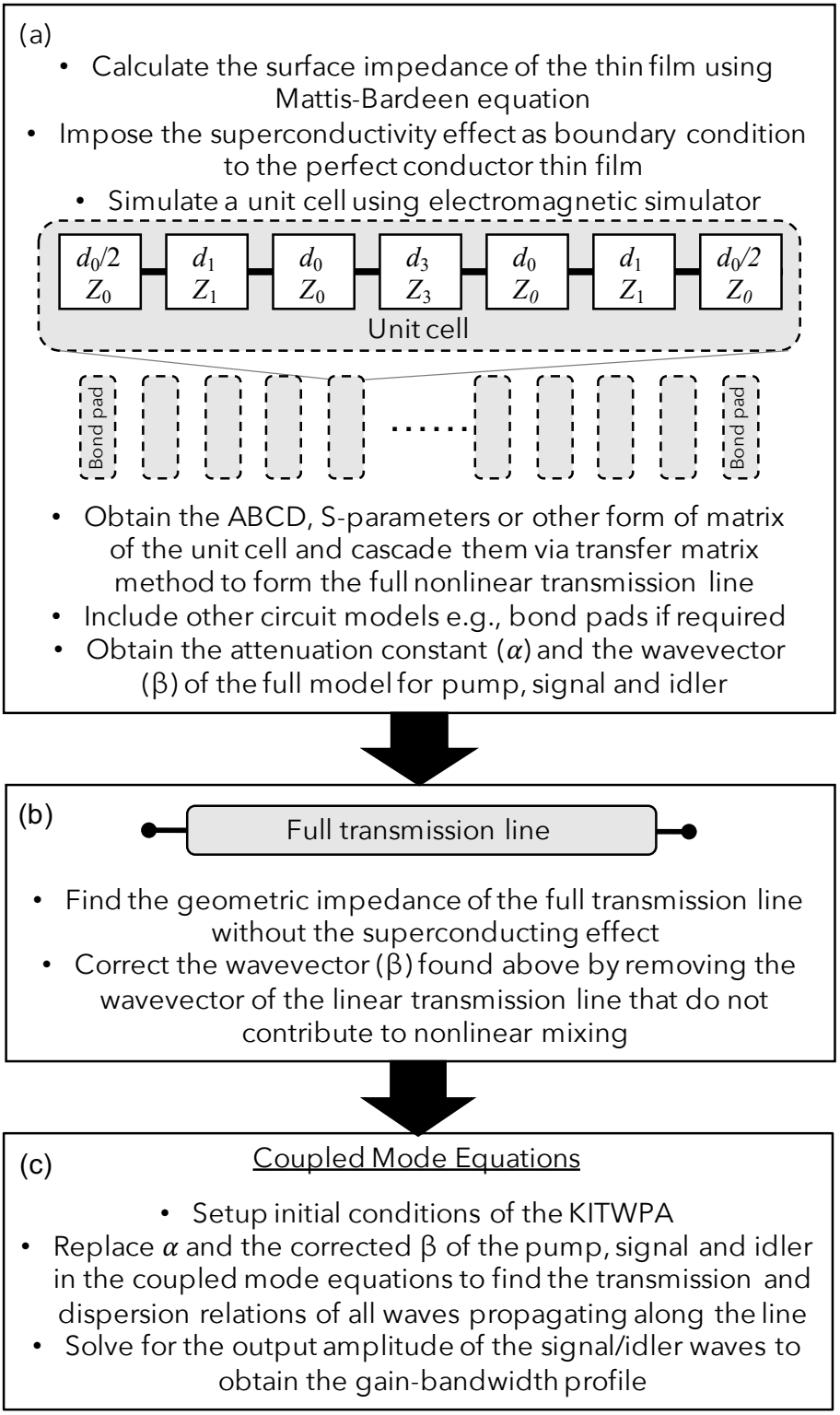

Figure 3.6: Full KITWPA design methodology, highlighting the sequence of computational procedures used to simulate the behaviour of a KITWPA.

Fig. 3.7(a) shows the surface resistance, R_s, and the surface inductance, L_s, as a function of frequency, when normalised by the gap frequency, f_{gap}, of each material.

Film	T_c (K)	V_{gap} (mV)	f_{gap} (GHz)	f_{frac} (at 10 GHz)	ρ_N (μΩ cm)
NbN [116]	14.63	4.44	1073	0.01	220
NbTiN [21]	14	4.25	1027	0.01	100
Ti [117]	0.588	0.17	41	0.24	59
TiN [118]	4.39	1.33	321	0.03	140

Table 3.1: Summary of critical parameters for the generic BCS films under investigation, where $V_{\text{gap}} = \frac{\Delta}{e}$ and $f_{\text{gap}} = \frac{\Delta}{h}$, where e is the elementary charge and h is Planck's constant.

In this instance, we choose to normalise the frequency by f_{gap} to visualise the effect that ρ_N has on the R_s and L_s values of the films, as from the Mattis-Bardeen equations in (2.3a)-(2.3b), and the surface impedance in (2.13), we expect that a large ρ_N will lead to high kinetic inductance and high resistive losses. As expected, the curves in Fig. 3.7(a) show R_s increasing as ρ_N increases, however, L_s does not appear to follow the same trend, with Ti having a relatively large L_s for it's R_s value, compared to the other films. This analysis would, therefore, indicate that Ti would be the ideal film to construct a KITWPA from, due to it's high L_s and low R_s, which is in stark contrast to NbN, which shows a very high R_s and a comparatively low L_s.

This analysis must be taken with care, however, as one must consider the operational frequency range of the KITWPA device, since operating close to f_{gap} is known to substantially increase the resistive losses of the superconducting material. From Tab. 3.1, we can see that for Ti, $f_{\text{gap}} = 41\,\text{GHz}$, and for NbN, $f_{\text{gap}} = 1.073\,\text{THz}$, so a NbN-based KITWPA operating at 10 GHz would be at approximately 1% of f_{gap}, whereas a Ti-based KITWPA operating at 10 GHz would be almost at a quarter of f_{gap}, which is a significant fraction. In Fig. 3.7(b), we again plot R_s and L_s but now as a function of absolute frequency. In contrast to Fig. 3.7(a), we now see a correlation between L_s and R_s for all of the superconducting films under study, which suggests that it may not be possible to achieve a high L_s whilst simultaneously achieving a low R_s value, at least not just by simply choosing the film material, based purely on BCS theory. Another interesting observation from Figs. 3.7(a)-(b) is that L_s stays relatively flat in the simulated range, whereas R_s increases quadratically with frequency.

Figs. 3.8(a)-(b) show L_s and R_s, respectively, as a function of film thickness, which show that both L_s and R_s tend asymptotically towards ∞ is the film thickness

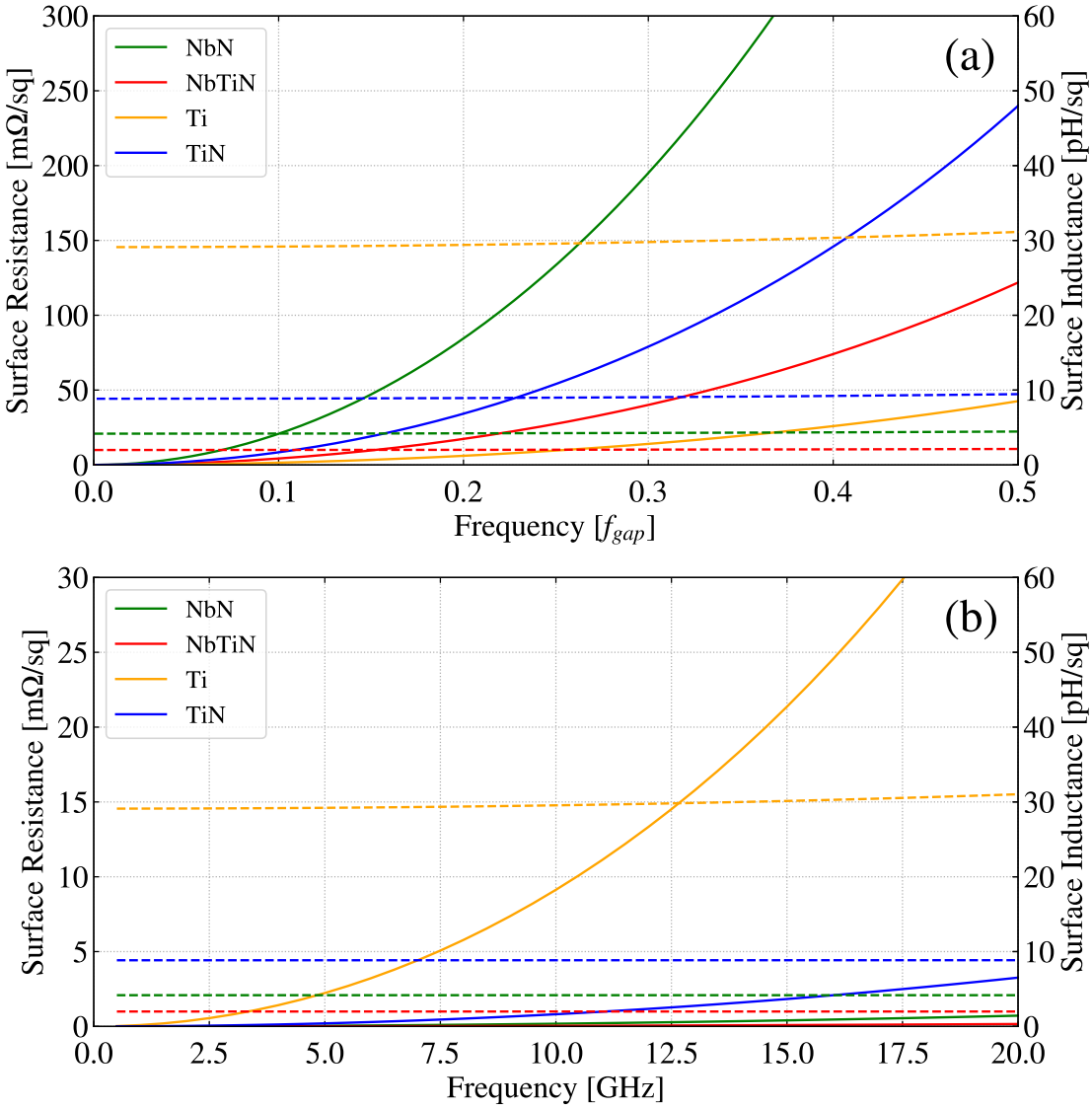

Figure 3.7: Surface resistance (R_s) and surface inductance (L_s) versus frequency for different 50 nm thick BCS superconducting films (a) with and (b) without normalisation to f_{gap}. The solid lines are R_s and the dashed lines are L_s.

approaches 0, and then asymptotically decays as the thickness increases. The grey shaded regions on each plot highlight the L_s and R_s values for the superconducting films that have been used to make successful KITWPA devices to date, as reported in the literature. Whilst this grey region is by no means fundamental, it could give an indication as to which L_s and R_s values are most conducive for KITWPA operation. Initially, it seems that only NbN, NbTiN, and TiN, intersect the grey region, however, looking at the extremes, we can see that Ti intersects the grey region for thicknesses above 210 nm. This suggests, perhaps, that most of these superconducting films could be used to construct a KITWPA, provided the thickness

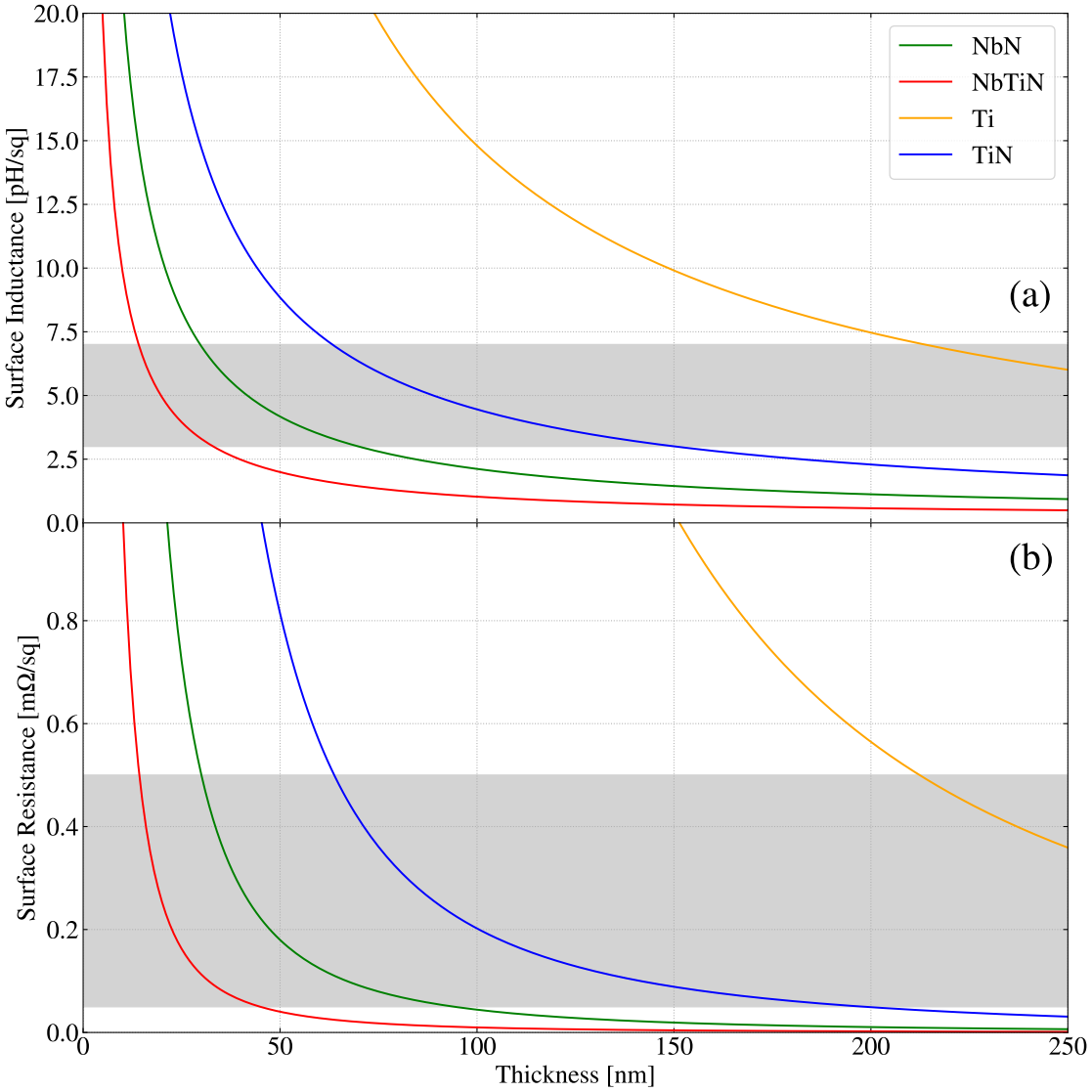

Figure 3.8: (a) Surface inductance (L_s) and (b) surface resistance (R_s) versus film thickness for different BCS superconducting films. The grey shaded regions highlight the range of L_s and R_s values for superconducting films the have been used to make successful KITWPA devices. All values were calculated at 10 GHz.

of the film can be appropriately engineered.

Of course, this analysis assumes that we can simply equate R_s with transmission loss and noise, and L_s with non-linear kinetic inductance that promotes gain. Indeed, the optimum properties are also dependent upon the physical geometry of the KITWPA device and the microscopic physics of the film, since here we have assumed the use of homogeneous superconductors. Additionally, both L_s and R_s are dependent on the strength of the supercurrent passing through the superconduct-

ing material, and whilst the current-dependence of L_s is essential, it is imperative that any potential superconducting film for KITWPA applications minimises the current-dependence of R_s. Nevertheless, the previous analysis still provides a useful insight from a design perspective of which superconducting materials and thickness may lead to a successful KITWPA design.

It has been established that a good film for a KITWPA would have a high L_s and a low R_s, so it is important to find the $\frac{L_s}{R_s}$ ratio for the superconducting films. This ratio is shown in Fig. 3.9 for the BCS films in this study. Fig. 3.9 tells us two important things about the superconducting films. First, a higher operating frequency results in a lower $\frac{L_s}{R_s}$ ratio, which implies that successful high frequency KITWPA operation would require a high V_{gap} superconductor, which is as expected. Second, there is no clear trend between $\frac{L_s}{R_s}$ and ρ_{N}. As with Fig. 3.7(a), Fig. 3.9 implies that Ti is the best film to use compared to the other materials as it has the highest $\frac{L_s}{R_s}$ ratio. Once again, however, we must consider the operational frequency of the KITWPA before making a conclusion on the most suitable superconducting film, as at 10 GHz the $\frac{L_s}{R_s}$ ratio for Ti will in fact be in a similar range to that of NbN. This implies that the use of $\frac{L_s}{R_s}$ as a measure of the films suitability will lead to unexpected results that are not indicative of the actual KITWPA performance.

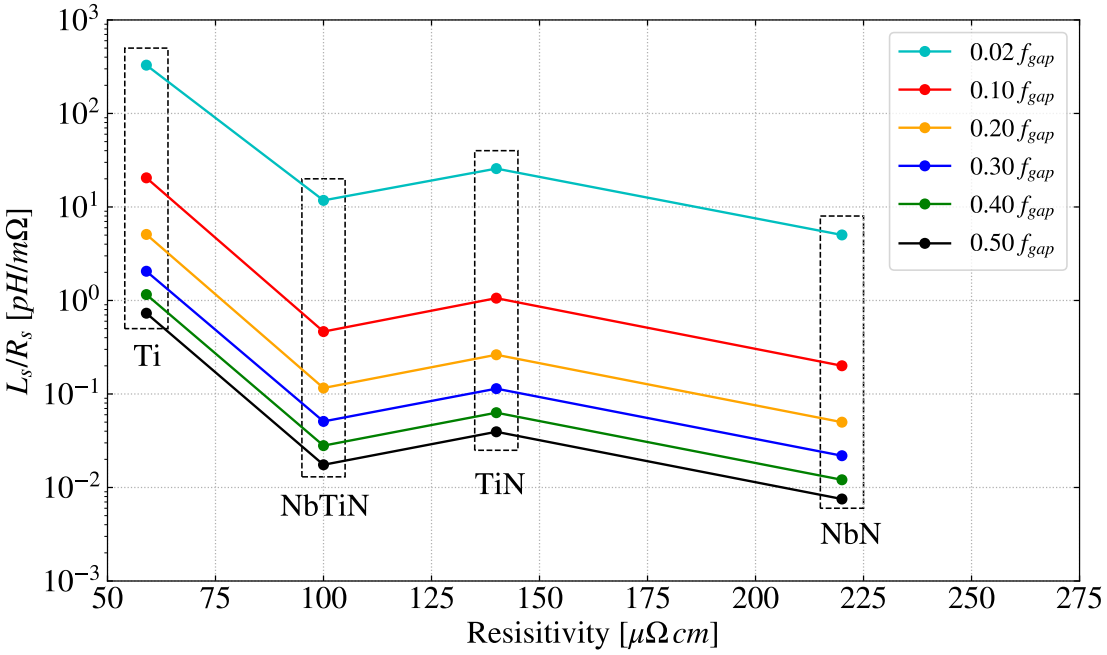

Figure 3.9: Ratio between surface inductance and surface resistance as a function of resitivity for the superconducting films under study at different normalised frequencies. The thickness of each of the films is 50 nm.

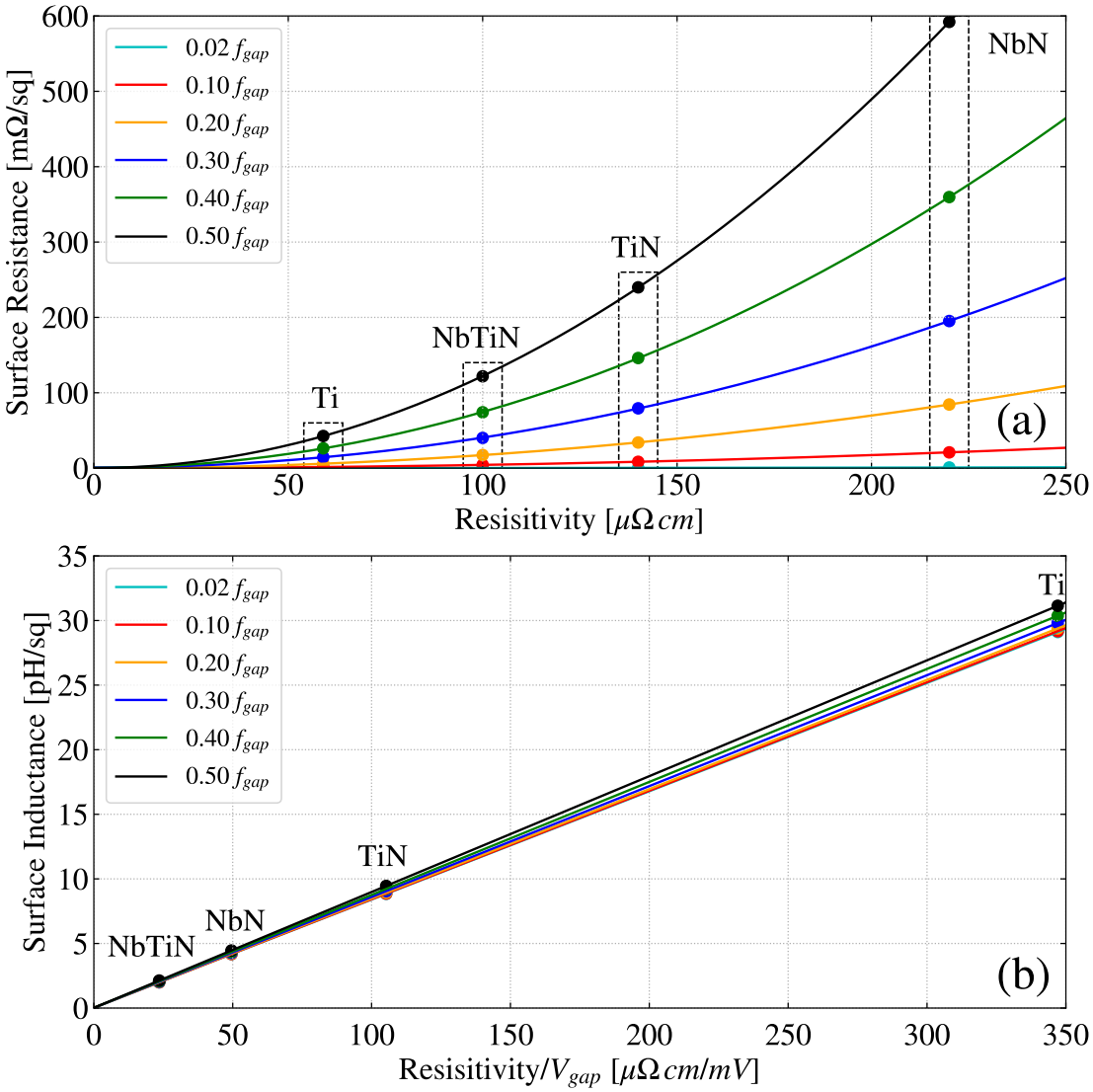

Figure 3.10: (a) Surface resistance versus resitivity and (b) surface inductance versus $\frac{\rho_N}{V_{gap}}$ for the BCS films under study. For both plots, each film under consideration has a thickness of 50 nm.

Whilst Figs. 3.7-3.9 provide a good insight into the dependence of R_s and L_s on frequency and film thickness, it remains inconclusive as to which materials or thicknesses are optimal for KITWPA applications. In Fig. 3.10(a), we relate R_s to ρ_N for different materials at different frequencies, and as expected a higher ρ_N results in a higher R_s. L_s, however, displays no such relationship with ρ_N, nor V_{gap}. Plotting L_s versus $\frac{\rho_N}{V_{gap}}$, however, as shown in Fig. 3.10(b), we see that L_s is in fact linearly proportional to the ratio $\frac{\rho_N}{V_{gap}}$. This result is surprising, as it implies that one can control the surface resistance and surface inductance of the film independently by separately engineering the gap voltage and resistivity values of the film. For example,

lowering ρ_{N} of the film would reduce R_s, then similarly reducing V_{gap} would result in L_s remaining rather constant. This procedure is doable, since V_{gap} is independent of film thickness, hence the thickness of the film can be altered to control ρ_{N} and, hence, R_S once a lower V_{gap} has been engineered. This should be possible for high gap superconductors, such as NbN, NbTiN, or TiN, when the operational frequency is well below f_{gap}.

Another way of assessing the suitability of a superconducting film is to study the following dimensionless parameters: $\frac{hf}{\Delta}$, $\frac{\Delta}{k_BT}$, and $\frac{hf}{k_BT}$. The quantity $\frac{hf}{\Delta}$, which is equivalent to $\frac{f}{f_{\mathrm{gap}}}$, has previously been explored in Fig. 3.9 and Figs. 3.10(a)-(b) and shows that operating the KITWPA closer to the gap, i.e., a larger $\frac{hf}{\Delta}$, leads to a greater number of quasiparticles in the superconducting film, hence more losses. This can be seen from the Mattis-Bardeen equations in (2.3a)-(2.3b), as increasing $\frac{hf}{\Delta}$ leads to an increase in $f(E)-f(E+\hbar\omega)$ at the lower integral limit in (2.3a), hence a larger σ_1, which is the resistive part of the conductivity. In the case where $kT \ll \Delta, hf$, i.e., $\frac{\Delta}{k_BT}$ and $\frac{hf}{k_BT}$ are very large, the substitution of the integration limits in (2.3a)-(2.3b) into (2.4) make it very small, hence we can see that σ_1 exponentially tends to zero. Additionally, the ratio $\frac{hf_p}{k_BT}$ determines the magnitude of the overall thermal noise of the TWPA [119]. In principle these three variables should govern most of the behaviour of the superconducting film, since all of the rest is in the Mattis-Bardeen equations. Hence the ideal superconducting film would minimise $\frac{hf}{\Delta}$ whilst maximising $\frac{\Delta}{k_BT}$ and $\frac{hf}{k_BT}$.

3.3.2 Engineered TiN Films

The analysis in § 3.3.1 suggests that it may be possible to engineer a superconducting film to exhibit the properties of high L_s and low R_s by tuning the values of ρ_{N} and V_{gap}. To experimentally test this, we have fabricated several batches of TiN films onto sapphire substrates, where the T_c of each film has been varied by altering the nitrogen flow rate during the sputter-deposition process. (Our fabrication process is discussed further in Chap. 4.) We assume that varying T_c proportionately varies V_{gap} through,

$$eV_{\mathrm{gap}} = 1.764 k_B T_c, \tag{3.8}$$

which we assume to hold for all $T < T_c$. We then measured the resistivity of each of the films to obtain a relationship between ρ_{N} and V_{gap}, the result of which is shown in Fig. 3.11(a). From this plot, we see that ρ_{N} only decreases gradually as

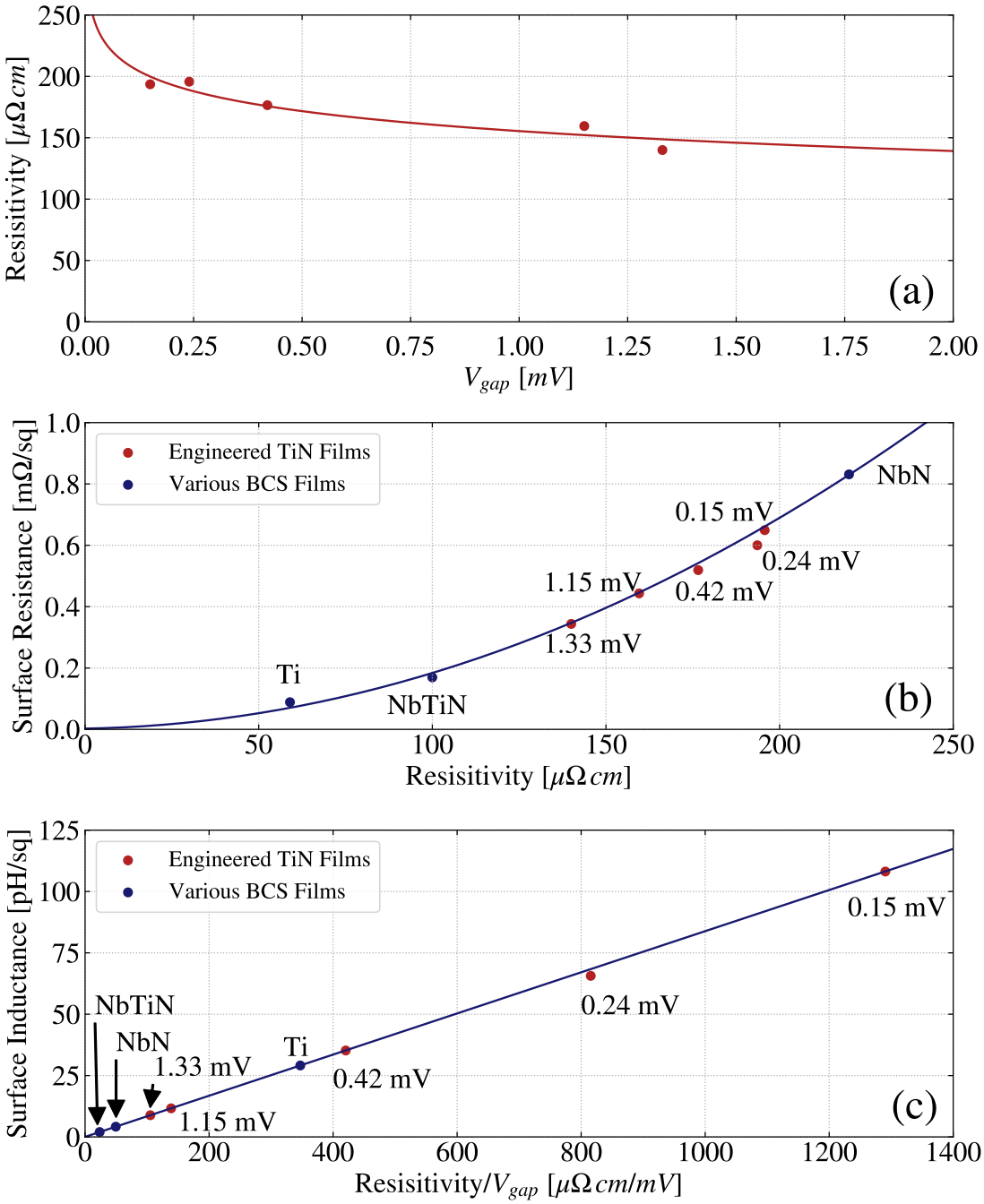

Figure 3.11: (a) Measured resistivity of various engineered TiN films with different gap voltage (V_{gap}). (b) Surface resistance versus resistivity at 0.02 f_{gap} for the various BCS thin films under study as well as the engineered TiN films. All the films in this plot have a thickness of 50 nm. (c) Surface inductance versus $\frac{\rho_{\mathrm{N}}}{V_{\mathrm{gap}}}$ for the same BCS thin films under study in (b).

V_{gap} increases significantly, implying that it is reasonable to assume that ρ_{N} remains rather constant for a large change in V_{gap}. More precisely, we see that ρ_{N} only drops

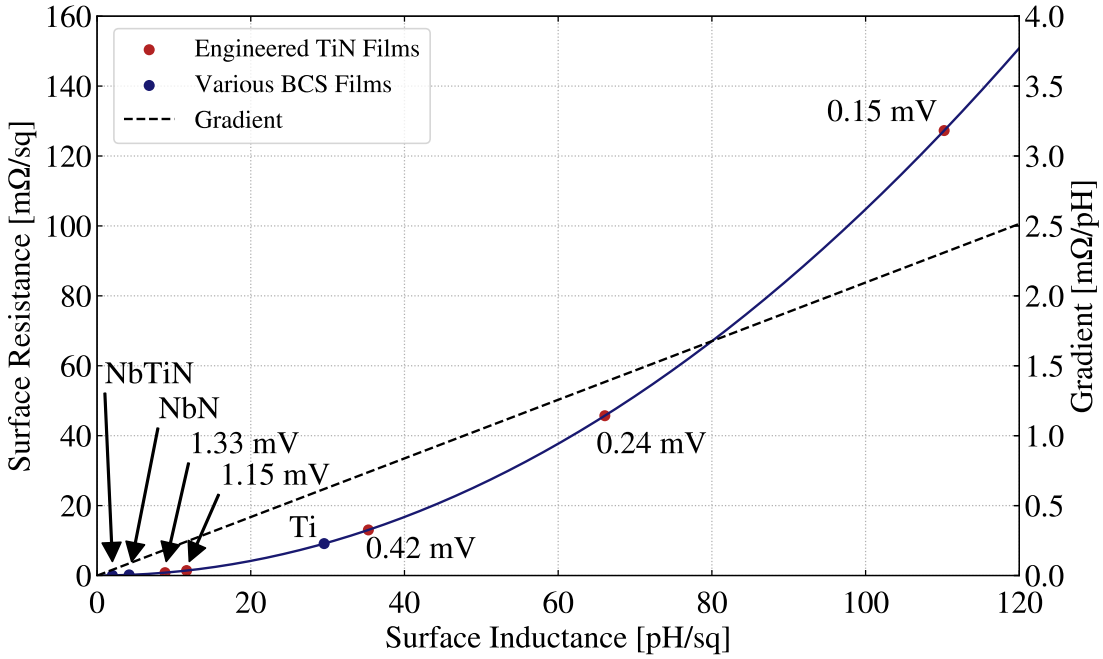

Figure 3.12: Surface resistance (R_s) versus surface inductance (L_s) at 10 GHz for various BCS thin films under study, along with the engineered TiN films, all at 50 nm thickness. The graph shows a quadratic relation between R_s and L_s, with the dashed line plotting the derivative of the quadratic relation.

by a factor of about $\frac{1}{3}$ as V_{gap} is increased by an order of magnitude. This result suggests that we may be able to break the strong correlation between L_s and R_s due to the fact that whilst decreasing V_{gap} will increase ρ_{N} slightly, it will significantly increase L_s whilst resulting in a similar R_s value.

In Figs. 3.11(b)-(c), we reproduce the $0.02\,f_{\text{gap}}$ curves from Figs. 3.10(a)-(b), respectively, but now including the L_s and R_s values from the engineered TiN films. In both plots, we see that the TiN films with the lower V_{gap} have both higher R_s and L_s, although the increase is not the same. In Fig. 3.11(b) for example, we see we see that decreasing V_{gap} from $1.33 \rightarrow 0.15$ mV increases R_s by a factor of ~ 1.9, whereas in Fig. 3.11(c), the same decrease in V_{gap} increases L_s by a factor of ~ 12.3. This corresponds to an increase in the $\frac{L_s}{R_s}$ ratio by a factor of ~ 6.5, which suggests that this film engineering scheme may be feasible in achieving a superconducting film with high L_s and low R_s.

As discussed previously in § 3.3.1, however, lowering the V_{gap} value inevitably lowers the operational frequency range and bath temperature of a KITWPA device. The analysis in Fig. 3.11 assumed operation at a constant fraction of f_{gap}, hence,

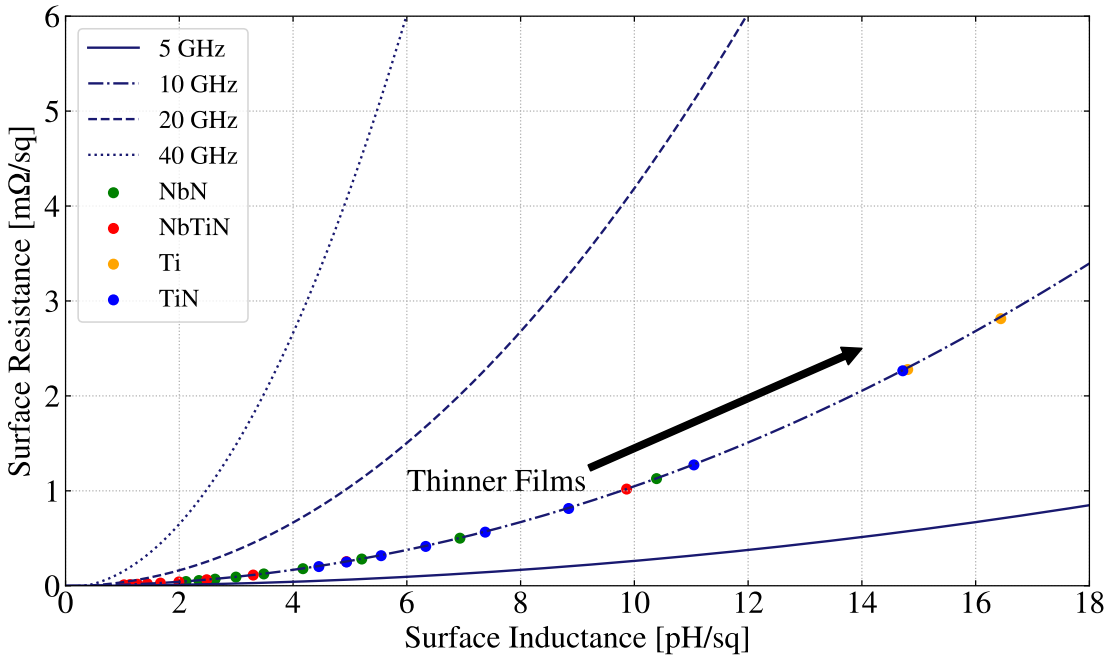

Figure 3.13: Surface resistance (R_s) versus surface inductance (L_s) for different films with different thicknesses at different operating frequencies (data for TiN shown here refers to the TiN with $V_{\text{gap}} = 1.33\,\text{mV}$). The surface impedances were calculated from 10 nm up to 100 nm with 10 nm interval shown in dots.

a more realistic approach is to assume operation at a fixed operational frequency. Fig. 3.12 plots R_s versus L_s for the engineered TiN films as well as the various BCS films under study at a fixed operational frequency of 10 GHz, and shows a quadratic relation between R_s and L_s for all of the films under study. Contrary to the conclusions drawn from Fig. 3.11, we see that whilst decreasing V_{gap} increases L_s, it in fact induces an even larger increase in R_s for a fixed operational frequency. The fact that the quadratic relation seems to hold for all materials, i.e. it is independent of ρ_{N} and V_{gap}, implies that it may not be possible to simultaneously achieve the properties of high L_s and low R_s for a standard BCS superconducting film.

Fig. 3.13 extends on Fig. 3.12 and plots R_s versus L_s for the various BCS films under study at various film thicknesses and at different operational frequencies. As we have established that engineering the V_{gap} of a film has no effect on this relation, we omit the engineered TiN film data points to prevent the plot from being too crowded. Once again, the plot reveals the quadratic relation between R_s and L_s, with resistance increasing much faster for higher operating frequencies. This is understandable, as at higher operating frequencies, the KITWPA is operating closer to the gap; although it implies that high-frequency KITWPA operation, for

example at mm-wave regime, may be severely limited by the high losses. Obviously, one can opt for a low R_s by lowering the L_s of the film, but this may result in a weak kinetic inductance and an amplifier that may not be able to amplify sufficiently or an extremely long device that may not be feasible to fabricate.

The findings presented in this section appear to suggest that most BCS thin films could work as a KITWPA provided the correct thickness is used. Of course, the previous analysis as assumed the dependence of R_s on current to be negligible for all materials and thicknesses, which may not be the case in reality, as certain materials may exhibit a greater R_s current-dependence than others, or the R_s current-dependence may vary as a function of film thickness, which may indicate additional microphysical behaviour that could determine the optimum superconducting film for KITWPA applications. For subsequent KITWPA designs discussed in this thesis, however, I shall focus on the use of 100 nm TiN film with $V_{\mathrm{gap}} = 1.33\,\mathrm{mV}$ ($T_c = 4.39\,\mathrm{K}$) as it has similar R_s and L_s values to most of the successful KITWPA examples reported in the literature, as highlighted in Fig. 3.8. Moreover, this is a film that we are able to fabricate using our collaborator's current fabrication capabilities and it has been proven to work for the MKID devices produced by them [118].

3.3.3 Substrate and Topology Considerations

The choice of superconducting thin film forms only part of the design consideration for an optimal KITWPA device. The planar circuit, from which a KITWPA is constructed, can in principle be formed using any type of transmission line topology fabricated onto different supporting substrate materials. In this section, we explore how transmission line topology and substrate material choices affect the performance of a KITWPA, focusing on the conduction and dielectric losses, the compactness of the device, and the feasibility of fabrication in terms of circuit dimensions.

Figs. 3.1(a)-(d) show the four different types of STL topologies, which form part of this investigation: coplanar waveguide (CPW), inverted CPW, microstrip, and inverted microstrip line. The inverted transmission line architectures, shown in Figs. 3.1(b) and 3.1(d), have the advantage of protecting the long transmission line since the wiring layer is covered by the dielectric and the top ground layer, meaning it is better shielded from potential physical damage during post-fabrication handling of the device such as chip dicing, device mounting, wire bonding, etc. This protection helps to avoid potential open- and short-circuits from scratches to the wiring layer

or debris between the strip and the ground plane. The downside of such protective layer is that the wiring layer is now sandwiched between two non-conductive layers, namely the thin dielectric layer and the supporting substrate, which could lead to increased dielectric losses and induce higher noise due to the two level system (TLS) noise mechanism. Conversely, conventional CPW and microstrip transmission lines only have a single contact interface between the wiring layer and the dielectric or the substrate, hence a potential reduction in TLS and dielectric loss effects. Furthermore, the single layer structure of the CPW means only one deposition step during fabrication is required, which greatly reduces the complexity of the fabrication process. The downside to these transmission lines, of course, is that they may be prone to mechanical damage as the transmission line is now completely exposed. Additionally, the CPW line is susceptible to a parasitic propagation mode, which can be suppressed by employing additional structures, such as equipotential bridges [120], although these require additional fabrication steps, which detract from the simple single-layer fabrication process of the CPW.

As § 3.3.1 suggests that the choice of superconducting thin film is not so critical as long as the thickness of the film can be controlled accurately, we make the choice to focus the following analysis on the TiN film with a $T_c = 4.39\,\mathrm{K}$ and thickness of 100 nm. For all of the STL topologies under study here, we assume that the dielectric layer is formed using silicon monoxide (SiO) with a resistivity $\rho = \infty$, a dielectric loss tangent $\tan\delta = 0.004$, and relative permittivity $\epsilon_r = 5.8$, as this is the commonly used dielectric material by our collaborator who fabricates our devices. We shall explore three different types of commonly used substrate: high resistivity silicon, sapphire, and quartz (the characteristics of these substrates are listed in the footnote of Tab. 3.2), each with the same thickness of 500 µm. The dimensions of all of the transmission line topologies are optimised to achieve $Z_0 = 50\,\Omega$ to match to the impedance of the external circuitry. As discussed previously in § 3.2.1, a $50\,\Omega$ STL with a high kinetic inductance is extremely difficult to achieve with a conventional CPW, hence we omit this line type in favour of a CPW with additional stubs is depicted in Fig. 3.1(e).

Tab. 3.2 shows the EM properties of several transmission line structures simulated using HFSS, and one immediately notes that the $|S_{21}|$ transmission (insertion) loss of the fishbone CPW with additional stubs (henceforth referred to simply as CPW) is much lower when compared to the other three STL topologies for all three substrate types. This is because the effective dielectric loss seen by the CPW electric field lines is half of that the substrate dielectric constant, as the top half of the

Silicon [1]				
	Fishbone	Inv. CPW	Microstrip	IMS
Width (µm)	10	5.06	2.16	1.93
Gap (µm)	5	5	N/A	N/A
L_{stub} (µm)	50	N/A	N/A	N/A
$L_{\frac{\lambda}{2}}$ (mm) [4]	1.27 (42 stubs)	1.19	0.65	0.60
$\lvert S_{21}\rvert$ @ 10 GHz (dB) [5]	-0.91	-2.00	-3.47	-3.07
$\lvert S_{21}\rvert$ @ 30 GHz (dB) [5]	-2.17	-7.36	-13.03	-11.58
Sapphire [2]				
	Fishbone	Inv. CPW	Microstrip	IMS
Width (µm)	10	5.18	2.16	2
Gap (µm)	5	5	N/A	N/A
L_{stub} (µm)	74	N/A	N/A	N/A
$L_{\frac{\lambda}{2}}$ (mm)	1.14 (38 stubs)	1.2	0.65	0.61
$\lvert S_{21}\rvert$ @ 10 GHz (dB)	-0.14	-1.87	-3.47	-3.04
$\lvert S_{21}\rvert$ @ 30 GHz (dB)	-1.26	-7.66	-13.03	-11.79
Quartz [3]				
	Fishbone	Inv. CPW	Microstrip	IMS
Width (µm)	10	5.48	2.16	2.1
Gap (µm)	5	5	N/A	N/A
L_{stub} (µm)	235	N/A	N/A	N/A
$L_{\frac{\lambda}{2}}$ (mm)	0.84 (28 stubs)	1.25	0.65	0.625
$\lvert S_{21}\rvert$ @ 10 GHz (dB)	-0.10	-2.55	-3.42	-3.21
$\lvert S_{21}\rvert$ @ 30 GHz (dB)	-0.98	-9.71	-12.87	-12.20

[1] $\epsilon_r = 11.9$, $\rho = 15\,\text{k}\Omega\,\text{cm}$, $\tan\delta = 1.2 \times 10^{-5}$.

[2] $\epsilon_r = 9.4$, $\rho = \infty$, $\tan\delta = 8.0 \times 10^{-8}$.

[3] $\epsilon_r = 3.78$, $\rho = \infty$, $\tan\delta = 0$.

[4] At 24 GHz.

[5] 70 wavelengths at 24 GHz.

Table 3.2: Electromagnetic characteristics of different types of transmission lines on different substrates for a 100 nm thick TiN with $T_c = 4.39\,\text{K}$. The SiO thickness is increased to 200 nm for easier match to $Z_0 = 50\,\Omega$ to avoid need for narrow strip line in the microstrip devices.

field is above the CPW and travels in the free space. In other words, the filling factor is about 50% because the field lines are divided between the free space and

the substrate. This is in contrast to the ICPW, where the majority of the field lines are enclosed between the top ground plane and the substrate, i.e., in the dielectric. Likewise for the MS and IMS lines, the field lines are tightly confined within the thin dielectric layer, hence the losses from these lines are inevitably higher.

The benefit of the MS and IMS lines, however, is that they have a shorter physical length (due to higher geometrical shunt capacitance) compared to CPW lines, which allows for a more compact KITWPA design and a potentially increased yield due to a smaller footprint area for damage and defects. From the point of view of insertion loss, it can be easily concluded that the ICPW line offers no advantage compared to the other transmission line types, as it exhibits comparable losses to the microstrip family, whilst having a comparatively long electrical length like the CPW. Comparing the microstrip with the inverted microstrip, it can be easily noted that the performances are relatively similar, although the inverted microstrip offers an additional protective layer in terms of the top ground plane, with the only downside being that it may induce higher TLS losses.

In terms of the substrate choices, one notes immediately from Tab. 3.2 that the characteristics of the MS family are relatively unaffected by the choice of the substrate, since the field lines are concentrated in the dielectric layer rather than the substrate. For the case of CPW lines, however, silicon, which is a semiconductor that can partially conduct current, generally induces higher loss than sapphire and quartz, which are ceramic in nature ($\rho = \infty$), hence even with a very high substrate resistivity of $\rho = 15\,\mathrm{k\Omega\,cm}$, the losses are still visibly higher due to the long transmission line length. Here, we assume that the cryogenic resistivity of silicon is similar to the room temperature resistivity. Whilst in reality, the resistivity should increase at cryogenic temperature, there is relatively little information regarding the magnitude of this measurement in the literature. Between sapphire and quartz, the latter induces the lowest loss because it has the lowest loss tangent, although the use of quartz results in the length of the capacitive stubs (L_{stub}) being substantially increased compared to silicon and sapphire because of the low relative permittivity. The effective wavelength of both ceramic substrates also decreases compared to silicon, hence a shorter physical STL is required. We can conclude, therefore, that for a CPW transmission line, sapphire is the optimal choice as it is less lossy than silicon and requires significantly shorter stubs than quartz, hence reducing the footprint of the amplifier chip.

In summary, the CPW has the lowest insertion loss among all STL topologies,

especially when sapphire or quartz substrates are employed, although the inconveniently long stub length for using quartz means the use of sapphire substrate is a better option. An ICPW may produce more compact amplifier design as it can achieve 50 Ω characteristic impedance without the need for capacitive stubs, however, the high induced losses, which are at a level similar to that of the MS family, means this topology offers no added advantage here. For the MS and the IMS lines, their characteristics are largely similar and are unaffected by the choice of substrate, however, the IMS line allows for protection of the main transmission line from potential physical damage, as well as better thermalisation as the wiring layer is now directly in contact with the substrate. We identify, therefore, that to achieve the lowest loss (hence least resistive heating) design with relatively small footprint, one should opt for using the 100 nm film forming a CPW with capacitive stubs on top of sapphire.

3.4 An Optimised TiN CPW KITWPA Design

In this section, we focus on the design and optimisation of a stub-shunted CPW KITWPA, which is formed from 100 nm TiN deposited onto a 500 µm sapphire substrate and operated in the D-4WM regime. Here we use the discrete periodic loading structure, with the physical dimensions of the 50 Ω, the primary-loading and the third-loading sections highlighted in Tab. 3.3. The investigations in this section focus on the case of D-4WM as this is the simplest case of wave mixing, however, the same analysis can of course be generalised to other wave mixing regimes.

It is desirable for a KITWPA device that the pump power is minimised whilst achieving the target gain, as this reduces the amount of resistive losses along the line. We, therefore, begin with an investigation into the effect that the pumping level has on the gain performance of a KITWPA. Fig. 3.14(a) plots the signal and idler gains as a function of pump current, I_p, for different KITWPA lengths. One notices immediately that the gain values do not rapidly increase until $I_p > 0.3I_*$, and that the longer KITWPAs exhibit a much sharper gain increase. In other words the longer a KITWPA is, the faster it will reach its maximum gain at lower pump power, however, the onset of rapid signal gain occurs at much higher I_p values compared to a shorter KITWPA. This behaviour is consistent with that of the total phase mismatch, Δ_k, which is plotted in Fig. 3.14(b) as a function of I_p for the same amplifier lengths as in Fig. 3.14(a). We can see from Fig. 3.14(b) that for low pump

CPW with 100 nm TiN Film			
Parameter	Primary Line	1st Loading	3rd Loading
Z_0	50 Ω	60 Ω	90 Ω
Width	10 µm	10 µm	5.7 µm
Gap	5 µm	5 µm	5 µm
L_{stub}	74 µm	36 µm	N/A
Length	34 stubs	4 stubs	200 µm†

† Third loading section has no stubs, hence is quoted as a length rather than number of stubs.

Table 3.3: Dimensions of the transmission line that form a single unit cell for the CPW KITWPA on a sapphire substrate, where Z_0 is the characteristic impedance and L_{stub} is the length of the shunted stubs.

powers, Δ_k for longer transmission lines diverges further from 0, hence it is not until higher I_p that the condition, $\Delta_k = 0$, is met, hence longer transmission lines require higher pumping levels before phase matching and maximum wave mixing occurs. The results from this are intriguing, as they suggest that it may not be completely necessary to use a long transmission line to achieve a moderate gain of 20 dB. For example, a 100 unit cell KITWPA can achieve ~ 20 dB gain at $I_p \approx 0.4I_*$, which is roughly the same gain that the 125 and 150 unit cell KITWPAs can achieve for the same pumping level. Not only does it suggest that it is unnecessary to make the KITWPA longer than 100 cells, it is actually advantageous to keep the line shorter, as it will be more compact for fitting onto a single chip and will be less prone to physical damage. This suggests that the optimal design for this case would comprise 100 unit cells.

From (2.37), one would expect the gain to increase exponentially for all values of I_p, however, this is clearly not the case in Fig. 3.14(a), where the maximum gain plateaus at around 55 dB. Unlike the case in (2.37), where we assumed the undepleted pump approximation, in reality the pump power is a finite value, hence after some amplifier length the signal amplitude becomes higher than the pump amplitude. At this point, energy will flow from the signal back to the pump, which prevents any further amplification. This depletion in the pump tone is clearly shown in Fig. 3.14(c), which plots the normalised amplitudes of the pump, signal, and idler tones. In this plot, depletion begins at $I_p \approx 0.56I_*$, which is followed by a minimum in the pump tone at $I_p \approx 0.67I_*$, before the signal and idler start to deplete and the

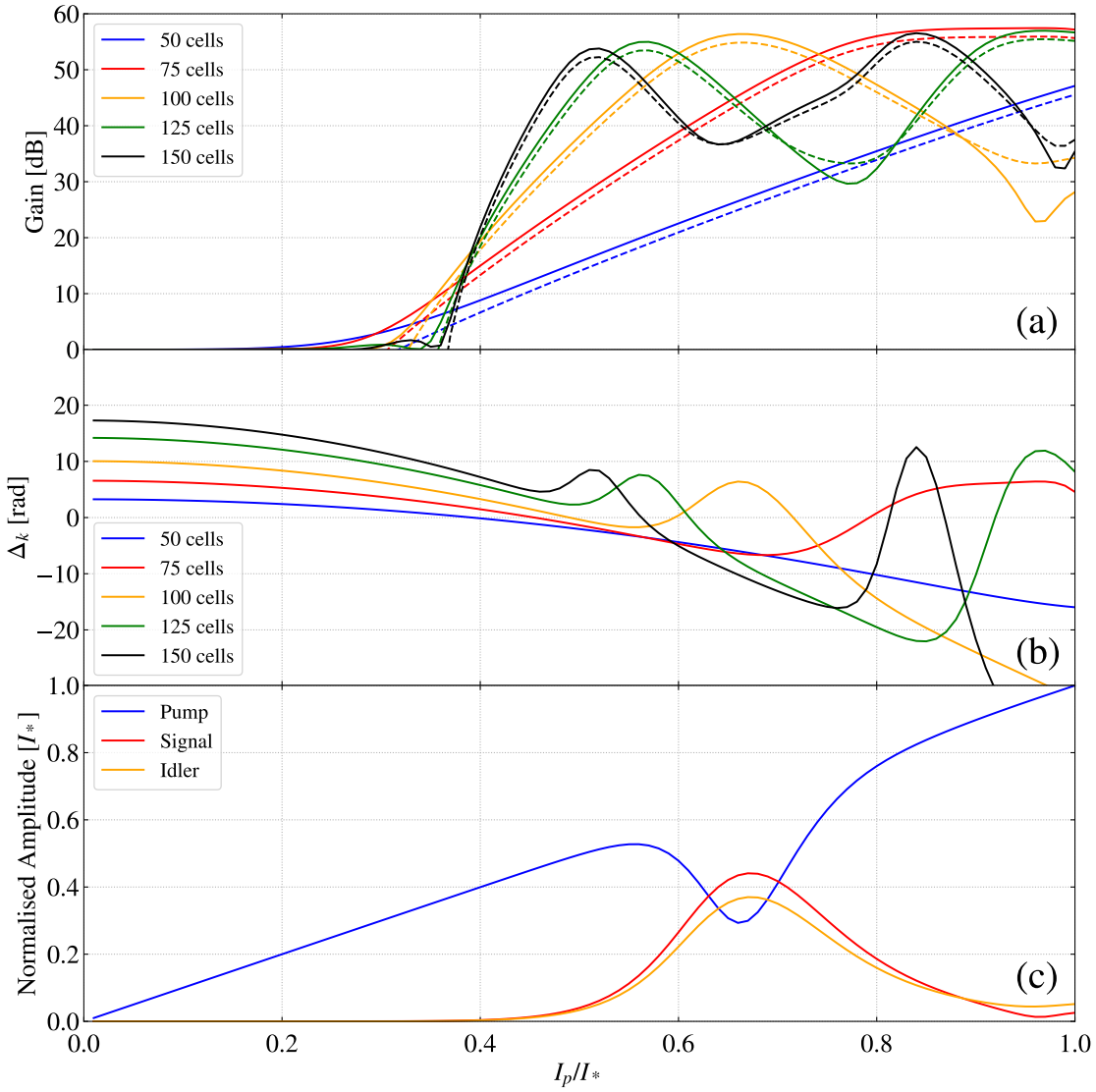

Figure 3.14: (a) The signal gain (solid) and idler conversion gain (dashed) plotted against the pump current for different KITWPA lengths. (b) The total phase mismatch plotted against the pump current for different KITWPA lengths. (c) Amplitudes of the pump, signal, and idler tones normalised to I_* plotted against pump current for KITWPA device with 100 unit cells. All curves were plotted with a signal frequency of 9 GHz and a pump frequency of 7.649 GHz.

pump slowly increases again. This results in an oscillatory behaviour between the pump, signal, and idler tones, which is shown more clearly for the longer KITWPAs presented in Fig. 3.14(a). One can see from Fig. 3.14(b) that the position of the maximum gain is dependent on Δ_k, since this is dependent on the pump power.

An important observation from Fig. 3.14(b) is that at the I_p value that gives the

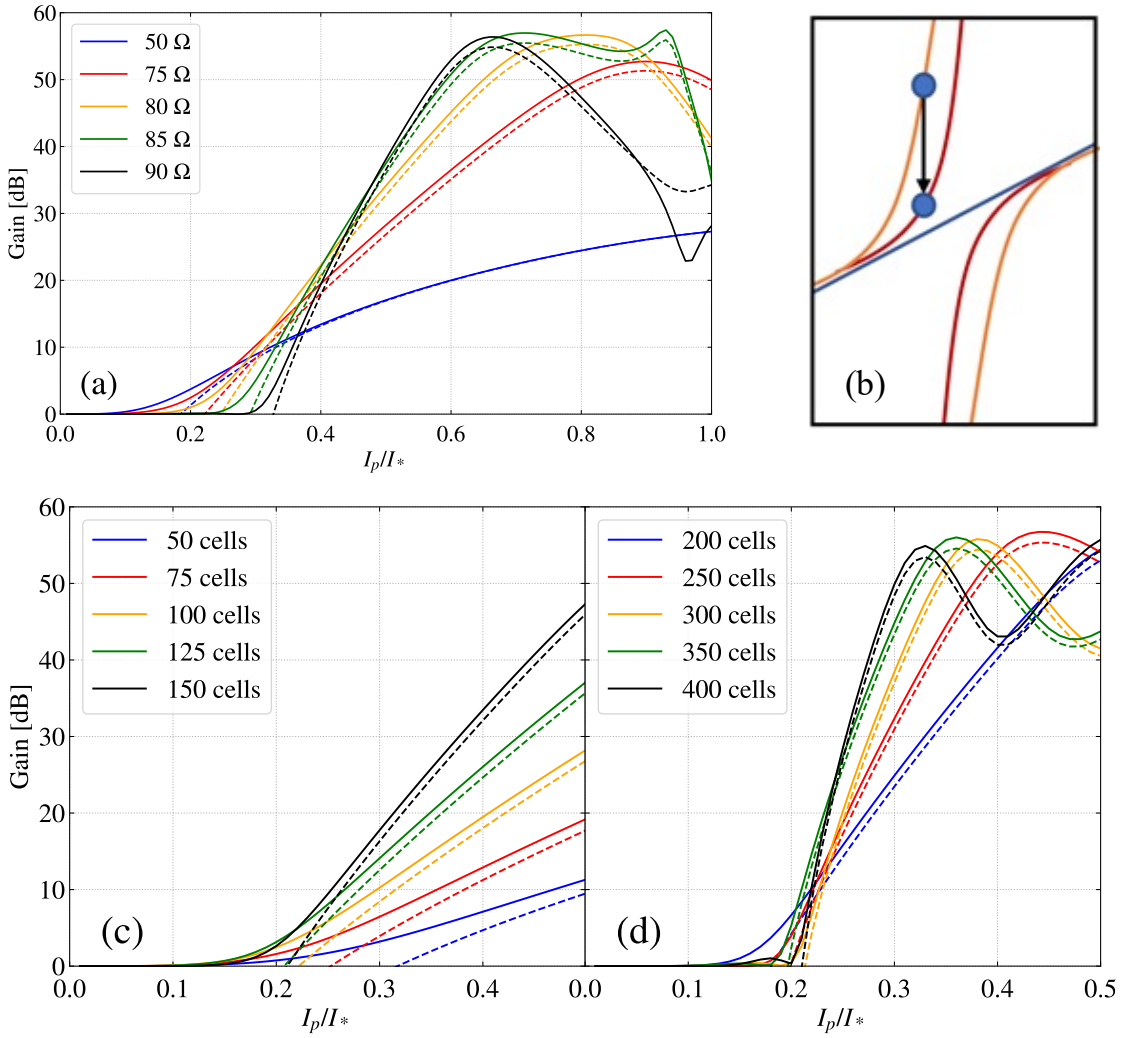

Figure 3.15: (a) The parametric gain plotted against pump current for a 100 unit cell KITWPA with different impedance values for the third loading. The gain onset starts earlier with a lower pump current if the third loading impedance is closer to the primary loading impedance. (b) Sketch illustrates how the dispersion relation changes if the third loading impedance is decreased from 80 Ω (orange) to 75 Ω (red), showing a reduction in the extra dispersion acquired by the pump tone if it remains at the same frequency. (c) & (d) Gain versus pump current for different KITWPA lengths with the impedance of the third loading being set to 75 Ω. All curves were plotted with signal frequency of 9 GHz and pump frequency of 7.649 GHz.

target gain of 20 dB, the phase mismatch $\Delta_k \neq 0$, which suggests that we may have overcompensated the phase shift that has been applied to the pump. The amount of phase shifting applied to the pump is proportional to the strength of the smaller band gaps, which is given by the ratio between the primary loading and third loading impedance values. We would like to explore, therefore, what effect changing the

ratio between the impedance values has on the gain and whether it might be possible to achieve the same gain performance whilst reducing I_p. Fig. 3.15(a) plots the signal and idler gains as a function of I_p for different third periodic loading impedance values, where the $50\,\Omega$ curve denotes a pure $50\,\Omega$ transmission line without periodic loadings. As with Fig. 3.14(a), we see that to achieve 20 dB, all the curves converge at $I_p \approx 0.4I_*$, however, recalling from the same figure, we also see that a longer KITWPA produces a steeper gain curve. To reduce the I_p for our KITWPA, therefore, we can first reduce the impedance of the third loading section from $90\,\Omega$ to $75\,\Omega$, which reduces the phase shift applied to the pump tone, as illustrated in Fig. 3.15(b) and then plot the gain versus I_p for different KITWPA lengths to see which gives us 20 dB. This is shown in Figs. 3.15(c)-(d) and we see that 300 unit cells allows us to achieve 20 dB with $I_p \approx 0.25I_*$. From this, we see that it is indeed possible to decrease I_p whilst retaining the same gain, however, this comes at the expense of tripling the length of the transmission line.

Another way that we can reduce the overcompensation of Δ_k is to change the frequency of the pump tone such that it is now further away from the band gap, which reduces the additional phase that is added to the pump tone. Fig. 3.16(a) shows the $|S_{21}|$ transmission spectrum focused just to the left of the first band gap for a KITWPA with different numbers of unit cells, where the inset shows the same spectrum over a broader frequency range. One notices from this plot that there are ripples in the $|S_{21}|$ close to the band gap that create local maxima, denoted as 1^{st} peak, 2^{nd} peak, etc, where the pump will experience a strong phase shift but its attenuation is minimised. Here, we investigate the effect that placing the pump at the different peaks has on the gain performance of the KITWPA, as whilst it allows us to control the phase shift of the pump, placing the pump further from the band gap would inevitably increase the zero-gain gap in the centre of the gain profile.

As illustrated in Fig. 3.16(b), moving the pump away from the band gap reduces the additional phase that it acquires. Figs. 3.16(c)-(d) plot the gain and Δ_k, respectively, as a function of I_p for when the pump tone is placed at the different peaks. From Fig. 3.16(c), we see that moving the pump to the second peak does reduce the I_p value required to achieve 20 dB gain, but only by about 5%. We can see from Figs. 3.16(c)-(d), though, that pumping at the second gap is in fact optimal, as we need $I_p \approx 0.4I_*$ to achieve ~ 20 dB, and at this point $\Delta_k = 0$. If we were to move the pump further away from the band gap to even higher peaks, we would see that the gain would decrease as the total phase mismatch once again deviates from zero. To counter the disadvantage of this technique mentioned earlier, the 1^{st} peak is only

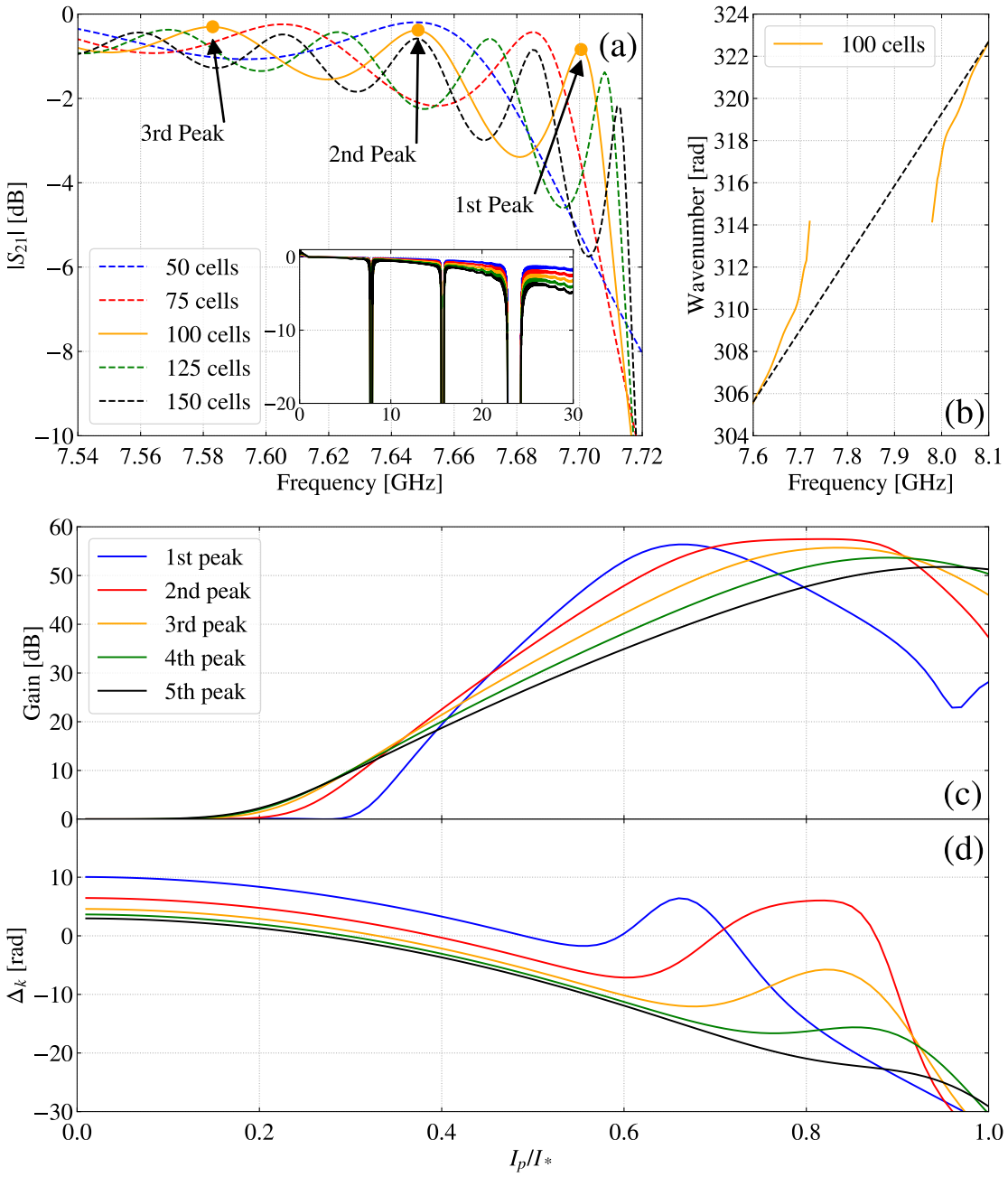

Figure 3.16: (a) The insertion loss versus I_p for a KITWPA with different lengths near the first band gap around 8 GHz, showing the peaks with lowest loss. (b) The dispersion relation of the 100 unit cells KITWPA around the first band gap. (c) The parametric gain and (d) total phase mismatch of the 100 unit cell KITWPA with the pump frequency fixed at different peak positions. All curves were plotted with signal frequency of 9 GHz.

0.05 GHz from the 2nd peak, so moving the pump from the 1st peak to the 2nd peak will only have a small effect on the width of the zero-gain gap.

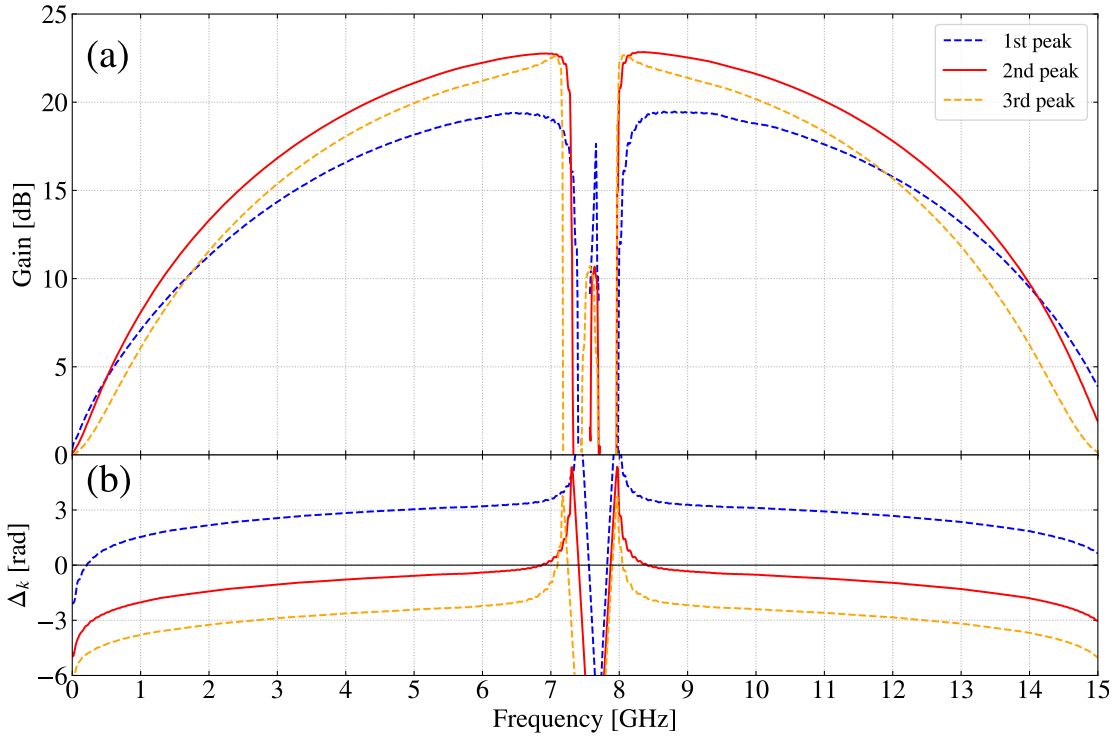

Figure 3.17: (a) The gain-bandwidth profile of a 100 unit cells KITWPA with pump frequency placed at first, second and third peak of the insertion loss curve for $I_p = 0.4I_*$. (b) the total phase mismatch corresponding to (a). The gain bandwidth is broadest with pump frequency placed at the second peak, where the total phase mismatch is closest to zero over the broadest bandwidth.

The gain-bandwidth relation and phase-mismatch for this optimal KITWPA design are shown in Figs. 3.17(a)-(b), respectively, where the KITWPA comprises 100 unit cells and is pumped at $I_p = 0.4I_*$. From Fig. 3.17(a), we can clearly see that pumping at the 2^{nd} peak not only produces the highest maximum gain, but also achieves a gain higher then 20 dB over the widest bandwidth.

3.5 Summary

This section has introduced a powerful design methodology that enables the behaviour of a superconducting transmission line to be accurately captured by taking into account subtle EM effects that could become significant when designing a KITWPA comprising hundreds of repeated unit cells. The flexibility offered by HFSS and the complementary python package provides a fast and simple way to explore and analyse the behaviour of different KITWPA variants, allowing a bespoke

KITWPA to be designed with optimal performance for a particular application. It also allows for an easy way to explore more complex schemes such as the use of multi-layer superconductors [117] for future KITWPA improvement, opens up the possibility to include more complicated designs that incorporate other circuit elements like filters, and potentially allows for other functionality apart from amplification such as frequency conversion [121].

I have also presented an investigation into the numerous design considerations that must be explored before designing a KITWPA device, and have arrived at an optimised KITWPA design.

3.5.1 Note on Other Non-EM Related Considerations

In subsequent chapters, we will experimentally characterise KITWPA devices that have been designed using the philosophy described in this section, which will potentially provide further insights into the design considerations that may be overlooked when designing a KITWPA purely from an EM perspective.

It is important to stress that this chapter focused on the design considerations of a KITWPA purely based on an EM perspective and assuming an ideal BCS film. Whilst it is apparent that KITWPAs function due to effects that deviate from standard BCS theory for a homogeneous superconductor, the root causes and underlying physics of KITWPA operation are still under investigation and beyond the scope of this thesis.

It should be noted that the main aim of § 3.3.1 was to study, using the available BCS and EM theories, the pros and cons of various BCS films to identify a specific film with the best properties for KITWPA operation, as this study has not been previously reported in the literature. Whilst our conclusion that any film may work is not as exciting as being able to single-out a specific film, we believe it is still a valuable investigation worth reporting here. This lengthy investigation was one of the first investigations carried out during my DPhil, hence was carried out without experimental work to guide us and without any related devices to measure and confirm our findings.

In practice, the R_s value should be significantly less than the value derived from BCS theory for a KITWPA to work properly, hence the analysis presented here can be viewed as a worst-case scenario. In a subsequent investigation by other

members of the group at a later date, we successfully recovered the unpumped transmission and gain profiles for a NbTiN KITWPA device reported in [82] using the design methodology described in this chapter, with the results of this shown in Figs. 3.18(a)-(b).

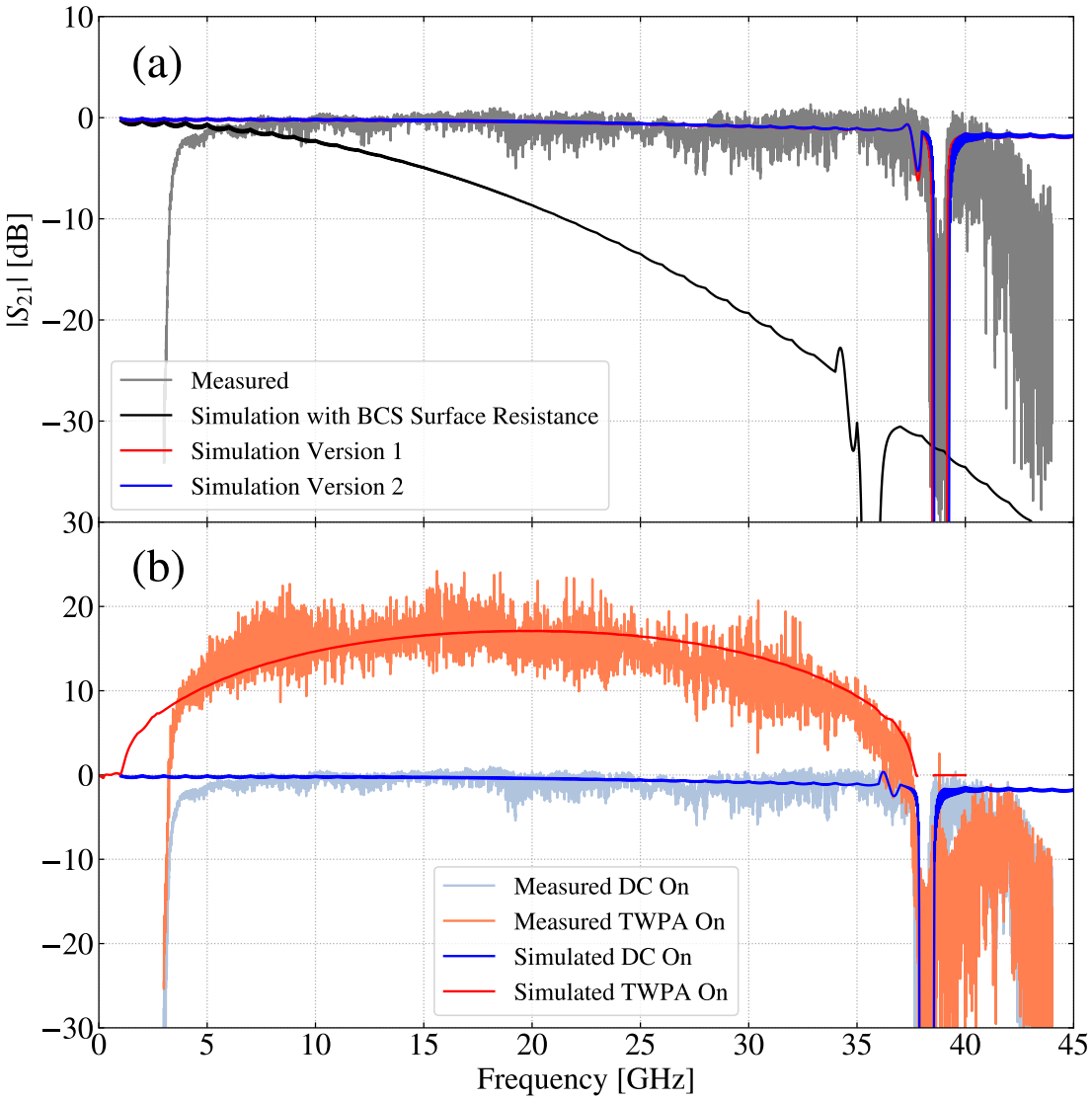

Figure 3.18: Comparison between our design methodology and experimental data for a KITWPA design reported in [82]. KITWPA comprises a stub-shunted IMS line with a single sinusoidal loading structure. (a) $|S_{21}|$ transmission, comparing the measured data (dark grey) with the simulated transmission using the BCS surface resistance (black) and with $n_{\text{loss}} = 5\%$ (red and blue). (b) DC-3WM gain measurement and simulation comparison.

Using our methodology, we are able to reproduce the position of the band gap in the $|S_{21}|$ curve, shown in Fig. 3.18(a) using the combinations of $\rho_{\text{N}} = 168\,\mu\Omega\,\text{cm}$,

$T_c = 12.5\,\mathrm{K}$ (simulation version 1), and $\rho_\mathrm{N} = 200\,\mu\Omega\,\mathrm{cm}$, $T_c = 15.0\,\mathrm{K}$ (simulation version 2), which are both reasonably close to the reported values [82], since there is some uncertainty in the measurements of ρ_N and T_c. The magnitude of the transmission curve, however, is much lower in the simulated case with BCS theory than the measured case, suggesting that we have overestimated the resistive part of the film's surface impedance. In order to successfully reproduce the measured transmission, we have to calibrate the BCS-calculated surface resistance by a factor of $n_\mathrm{loss} \leq 5\%$, where we define n_loss as,

$$n_\mathrm{loss} = \frac{R_s^{(\mathrm{Measurement})}}{R_s^{(\mathrm{BCS})}}, \tag{3.9}$$

where $R_s^{(\mathrm{Measurement})}$ is the surface resistance deduced from measurements of the superconducting device and $R_s^{(\mathrm{BCS})}$ is the surface resistance calculated from BCS theory. We should emphasise that this $n_\mathrm{loss} \leq 5\%$ factor is not fundamental and is not necessarily general for all films; we simply use it for this particular film to correct our BCS simulations to recover the measured behaviour of the transmission line. Whilst the reasons for this discrepancy in the transmission line losses is unclear and are currently being investigated, it is indicative that the microphysics of the film deviates in its behaviour from that predicted by BCS theory. We observe this same effect later in Chap. 5 for our TiN KITWPA devices.

Fig. 3.18(b) shows the measured and simulated DC-3WM gain profiles, and shows that the simulated gain curve is in very good agreement with the measured curves when a $n_\mathrm{loss} = 5\%$ correction factor is applied. In all curves, the DC bias along the transmission line was 0.57 mA, however, the simulated curves use a slightly higher pump power value at -27.5 dBm, compared to -29.3 dBm for the measured curves, although this is still within a reasonable margin.

This revelation also solves another conundrum of this chapter, namely that a very high I_p value is required to achieve the target gain, and that the gain does not take off until a relatively high I_p is applied. Both effects are because we are using the BCS R_s value. If we instead reduce this value to around 5%, as with the previous NbTiN device, we are still able to obtain a relatively high gain using a significantly reduced I_p. Furthermore, we assume that the resistivity of silicon remains unchanged at cryogenic temperatures relative to the room temperature value, hence we are likely overestimating the substrate losses in the silicon design. In experiments shown in subsequent chapters, we clearly notice that the silicon resistivity increases at cryogenic temperatures, with the devices exhibiting very little frequency-independent loss.

Nevertheless, much of the analysis here remains valid, such as the optimisation of f_p and the device length, since this behaviour remains unchanged even when the actual loss is much smaller than the value we expected here. Similarly, the investigation of device topology remains valid and valuable for design consideration.

Chapter 4

Fabrication and Experimental Setup

4.1 Introduction

The successful operation of a KITWPA is hugely dependent upon high-quality fabrication techniques, including the deposition and patterning of superconducting thin films such as titanium nitride (TiN). The superconducting nature of these films, and by extension the KITWPA devices themselves, necessarily requires their placement in a cryogenic environment in order to cool them to temperatures well below the critical temperature, T_c, of the superconducting film.

In this chapter, I present the fabrication techniques and experimental setups, which are used to construct and characterise our KITWPA devices, respectively. I will begin with a description of how I draw the full KITWPA device masks before describing the fabrication process for depositing and patterning TiN thin films, a process carried out by our collaborators Dr Faouzi Boussaha and Dr Christine Chaumont in the clean-room facilities at the Observatoire de Paris, where they have spent considerable time developing TiN films for MKID applications. I shall then proceed to a discussion of cryostats before concluding the chapter with a summary of the various cryogenic experimental setups that were used for experimental characterisation of the KITWPA devices presented later in this thesis.

4.2 Drawing of the Wafer Photomask

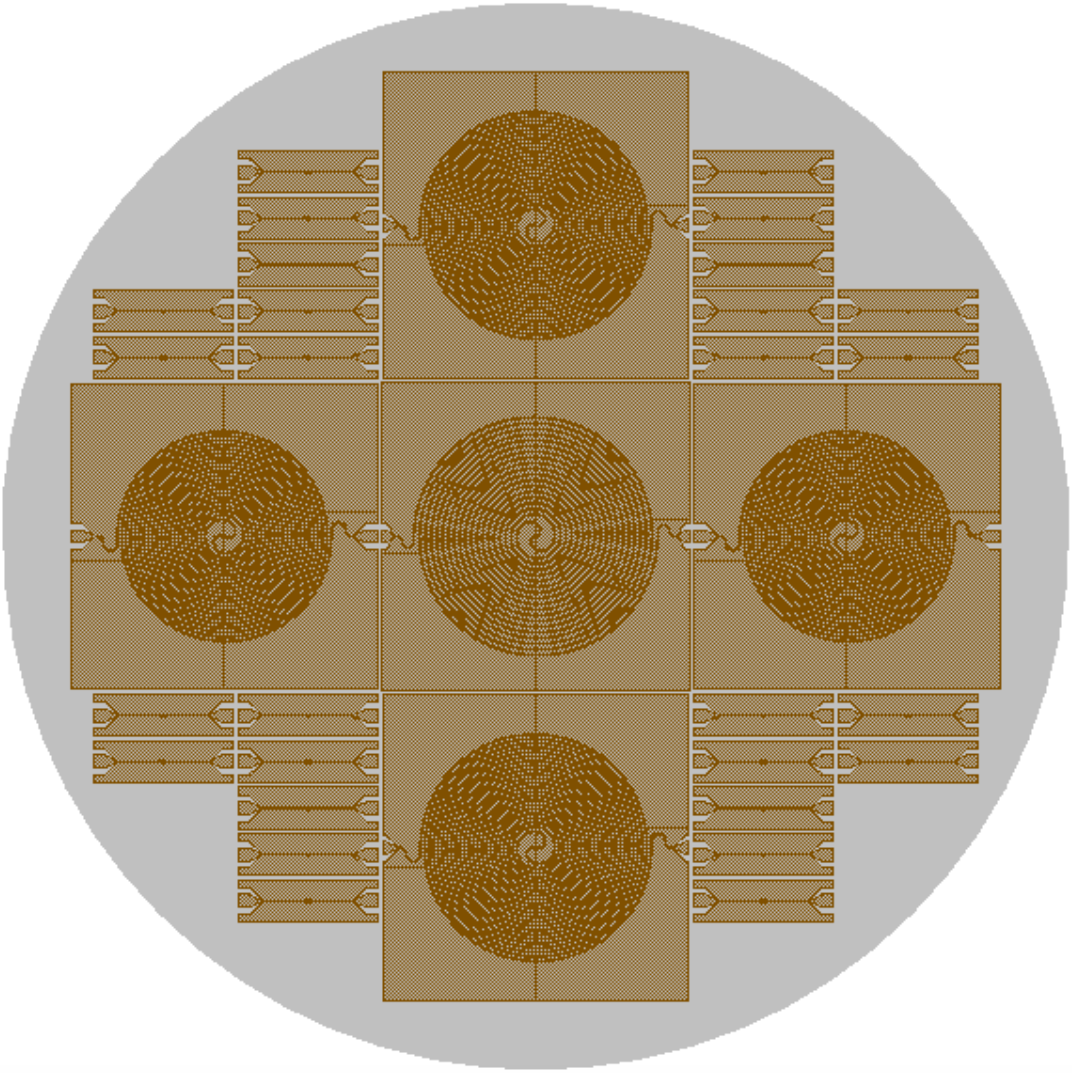

Figure 4.1: Computer aided design (CAD) image of KITWPA mask, highlighting the five full KITWPA devices and the smaller test devices located in the corners of the wafer. The regions coloured in brown are areas where TiN is deposited and the grey regions are areas of exposed substrate.

The KITWPA devices reported in this thesis were patterned using photolithography techniques, which are discussed further in the next section. Photolithography requires a photomask to be drawn, which is a plate with opaque and transparent regions that allows light to be transmitted in the image of a pattern to be fabricated, such as that in Fig. 4.1, which shows a CAD image of a full KITWPA wafer mask. This mask has been drawn using a python package called gdspy, which allows the user to easily draw arbitrary transmission line structures in the form of GDSII files.

The GDSII files can subsequently be read and viewed using one of a number of viewers and editors, such as KLayout. I have developed a number of gdspy scripts, which I use as templates for generating the masks of the various KITWPA and test devices that are presented in this thesis. This includes the CPW structure compacted into a double spiral and hairpin style layouts, MS/IMS variants, and both discrete and sinusoidal periodic loading structures.

4.3 Device Fabrication

TiN is a ceramic material, which has found applications as thin films in superconducting micro-resonator detectors [122], such as MKIDs [118, 123], due to their high kinetic inductance, controllable T_c and physical robustness [122]. TiN films have additionally been shown to display extremely low losses compared to other superconducting films [104]. The ideal film properties suited for MKID development are very similar to those that are sought after for KITWPA development, hence we make use of these developed TiN films in our KITWPA designs.

The fabrication process for our KITWPA devices involves the use sputter deposition, photolithography, and lift-off techniques and is described graphically in Figs. 4.2(a)-(f). This process has previously been described in [118, 123]. The first step in Fig. 4.2(a) is to thoroughly clean the substrate of the device, which is typically either high resistivity (>15 kΩ cm), <100>-oriented silicon or 99.999% high-purity, c-plane mono-crystalline sapphire. A photoresist, which is sensitive to UV light, is then spin-coated onto the wafer and baked, as shown in Fig. 4.2(b). We used either a bilayer of LOR1A resist and SPR700 resist or a single layer of SPR700 resist. In the next step, shown in Fig. 4.2(c), a photomask, as discussed in § 4.2, is placed on top of the wafer and UV light is shone through the mask and on to the wafer. The UV light breaks down the bonds in the resist molecules that are exposed to the light, which leaves the resist soluble, allowing the exposed areas to be removed using a development solvent, as shown in Fig. 4.2(d). These four steps result in an optically patterned photo-resit.

Following the patterning of the resist, the next step, as shown in Fig. 4.2(e), is to transfer the substrate to a sputtering machine, where the TiN layer is applied. Sputtering is a process where atoms are broken off or 'sputtered' from a target material onto a substrate in the presence of a high voltage/temperature and a career gas, such as argon (Ar) or nitrogen (N_2). Typical sputter-deposition parameters for

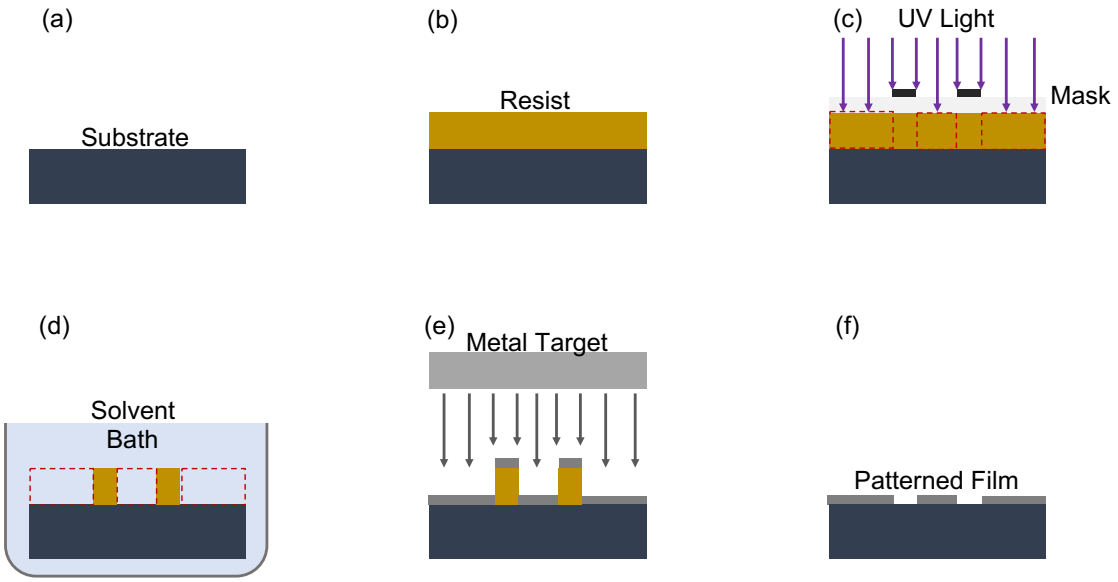

Figure 4.2: Simplified schematic of patterned TiN film fabrication process, similar to that described in [123].

our KITWPA devices are a 99.995% titanium target with a N_2 flow rate of 5.2 sccm[1], an Ar flow rate of 50 sccm at a total pressure of 0.6 Pa with 700 W DC power, although tuning the parameters of the sputtering process influences the properties of the deposited film, allowing them to have the desired properties for a particular application. The films produced for our KITWPA devices have target parameters of a normal-state resitivity, $\rho_N \approx 140\,\mu\Omega\,\text{cm}$, a critical temperature, $T_c \approx 4.39\,\text{K}$, and a film thickness, $t = 100\,\text{nm}$.

Following the sputtering process, the lift-off procedure occurs, which is shown in Fig. 4.2(f), whereby the remaining resist is dissolved in an acetone bath, taking the TiN patterned on top of it with it. This results in a patterned TiN wafer, which can be subsequently diced into individual devices with a dicing saw.

Another process involved using an etching technique instead of a lift-off process to pattern the TiN films, but since the majority of the devices reported in this thesis were patterned using lift-off techniques, I do not include this etching process here, although it is described in [123].

[1]Standard cubic centimetres per minute (sccm), where 1 sccm $\equiv$ 1 cm^3_{STP}/min, where 1 cm^3_{STP} denotes 1 cm^3 at standard temperature and pressure.

4.4 Device Mounting

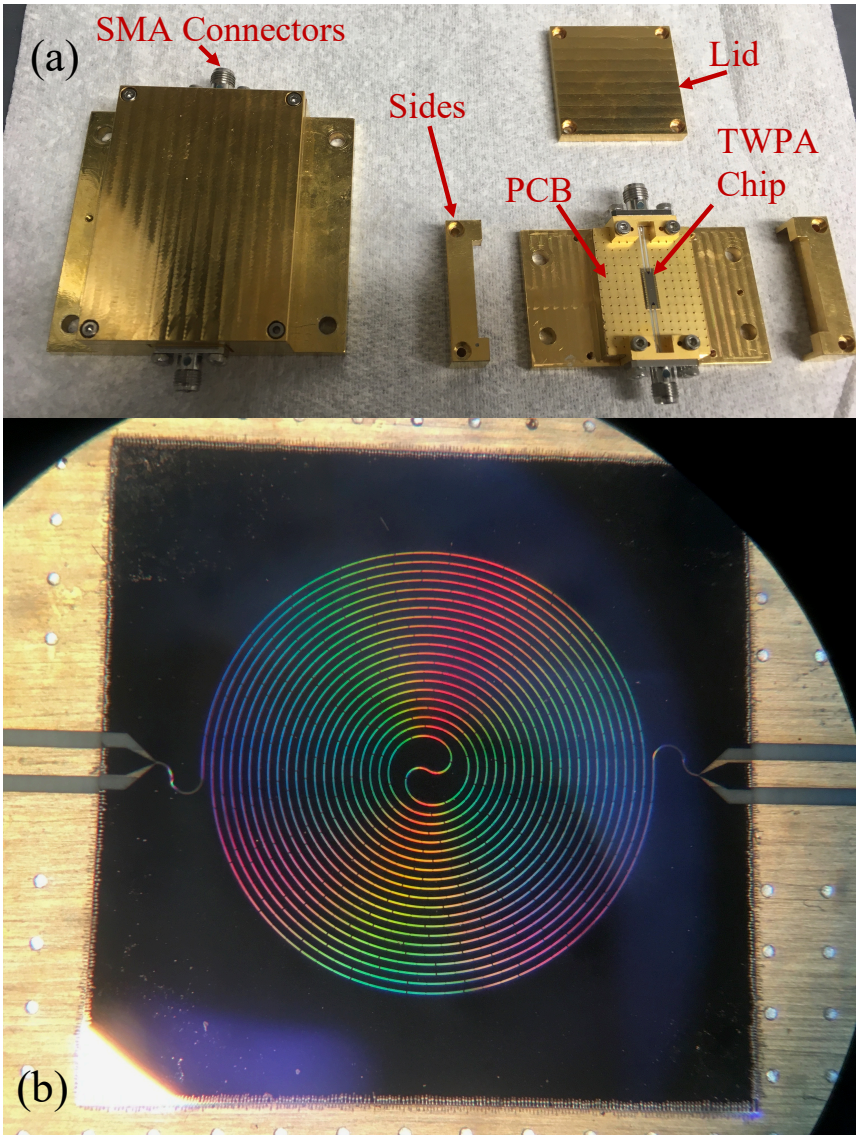

Figure 4.3: (a) Gold-plated copper sample holders used to mount KITWPA devices and connect them to external circuitry via SMA end-launch connectors. (b) KITWPA chip mounted on PCB within sample holder. Chip is electrically connected to PCB via numerous aluminium bond wires around edge of chip.

Fig. 4.3(a) shows an example of the gold-plated[2] copper sample holder design, which is used to house our KITWPA devices. The sample holder comprises a bottom block, upon which the KITWPA devices and PCBs sit to provide good thermalisation of the chip to the base plate of the cryostat. The chip is held with superglue

[2]Note that not all fabricated sample holders were gold-plated.

around the corners. The PCB is clamped down with two side bars which also provide the means for attaching the covering lid. The sample holder is designed such that it can be used with or without the lid, and the copper PCB can be replaced with different sizes to accommodate various sized KITWPA chips.

Fig. 4.3(b) shows a zoomed-in image of a fabricated KITWPA sample mounted within the sample holder. The KITWPA sample is wire bonded to a copper-clad and gold-plated[3] PCB, which comprises a grounded CPW etched into a 0.51 mm thick Rogers Duroid ® RO4350b board using standard photolithography techniques. The PCB is connected to SMA end-launchers for integration to the external circuitry. Aluminium bond wires of 75 µm diameter are used to provide an excellent electrical connection and are installed using an ultrasonic wedge-bonder. The two grounding patches of the CPW lines fabricated on top of the PCB are connected to the bottom ground plane through a grid of plated via holes.

4.5 Cryogenic Systems Setup

The development of cryogenic systems has advanced rapidly over the last few decades, with it now being possible to purchase a complete off-the-shelf dilution refrigerator (DR) system capable of reaching base temperatures below 10 mK, albeit with a hefty price tag. To circumvent the high price tag, we decided to build our own cryostat.

Figs. 4.4(a)-(b) shows the cryostat that we built, which we named OX300. OX300 is an absorption cryostat, which uses a commercial cryocooler from Chase Research Cryogenics ® to reach a base temperature as low as 280 mK[4], which is sufficiently cold to experimentally characterise TiN KITWPA devices. The cryocooler is precooled to <4 K by a mechanical Gifford-McMahon (GM) cold head from Sumitomo Heavy Industries ®. The remainder of the cryostat was designed by my supervisor, Dr Boon Kok Tan, with help from the in-house design office and the metalwork was fabricated by the in-house mechanical workshop. During the first 18 months of my DPhil, I assembled and commissioned OX300, which included troubleshooting and populating it with the various components and cables required to experimentally characterise our KITWPA devices. We initially struggled to cool OX300 to the expected base temperature, although this was eventually solved after many months of troubleshooting by myself and postdoc Dr Kitti Ratter, where we identified and

[3]Note that not all fabricated PCBs were gold-plated.

[4]When the cryostat is empty.

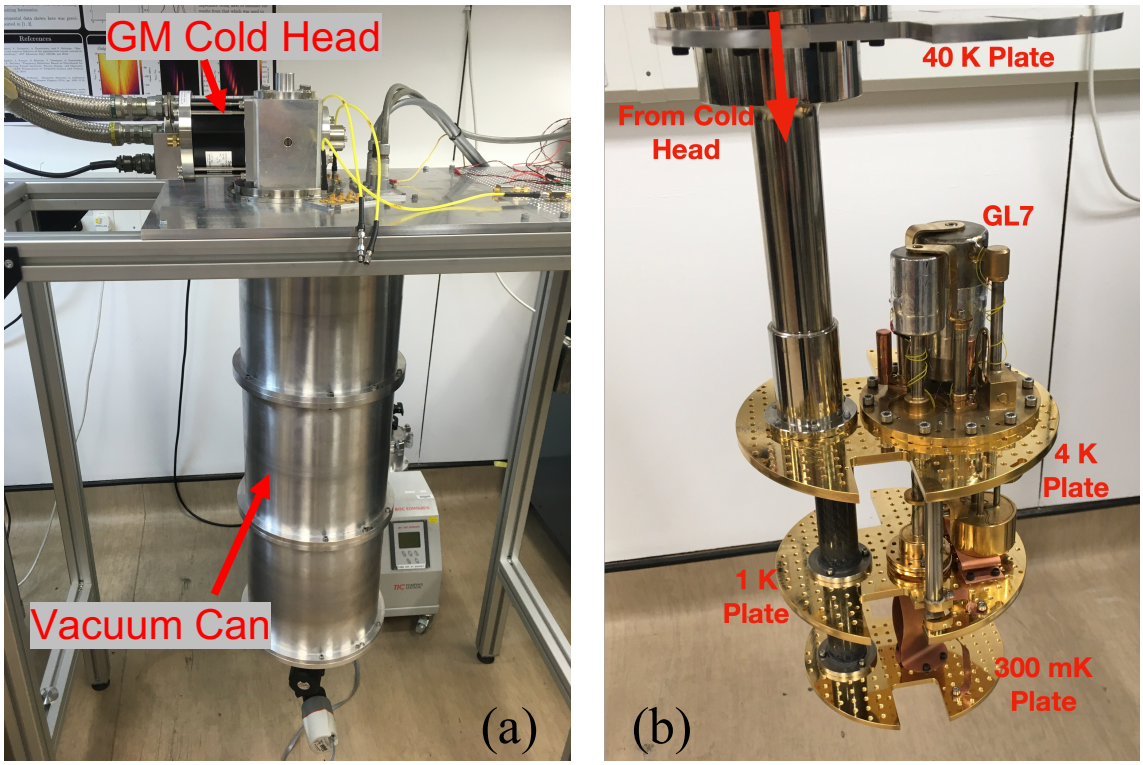

Figure 4.4: (a) Photograph of OX300; a 300 mK absorption cryostat designed and built by the group at the University of Oxford. Images shows a GM cold head from Sumitomo Heavy Industries®, which is used to precool the system to 4 K. (b) Inside of empty OX300, which is designed around a GL7 helium absorption cooler from Chase Research Cryogenics®. Cutaways in the cryogenic plates are spaces where RF coax flanges were later installed.

corrected several unexpected fabrication issues. The system is now running well and is used regularly to characterise various TWPAs designed by the group, including some of those reported in this thesis.

Later grant awards meant that we were able to purchase an additional cryostat for KITWPA characterisation. This cryostat is shown in Figs. 4.5(a)-(b) and is a BlueFors LD250 DR capable of reaching base temperatures of < 9 mK. This DR, which was commissioned in August 2021 has also been used to characterise most of the KITWPAs reported in this thesis, providing a performance comparison between different base temperatures. It's larger size also allows for multiple KITWPA devices to be characterised during a single cooldown. In this DR, I have developed several experimental setups from scratch, with the purpose of measuring the transmission, gain, and, in future, the noise performance of the KITWPA devices, as well as characterising the yield of the devices and diagnosing unexpected behaviour. These

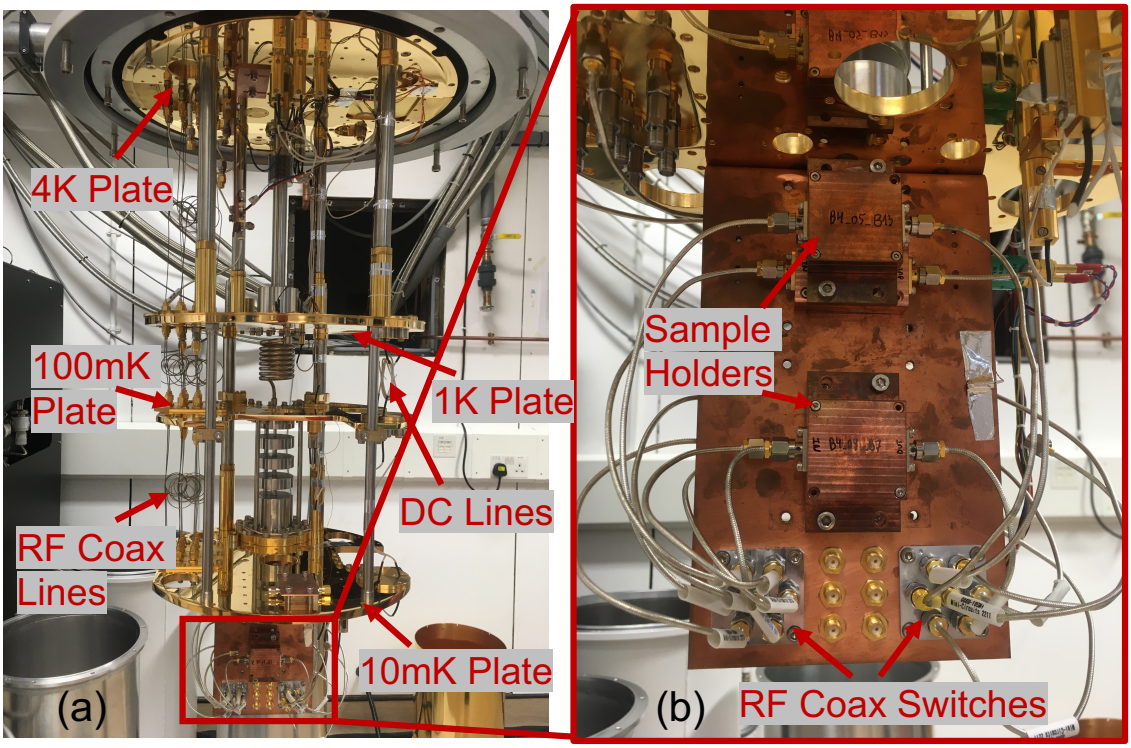

Figure 4.5: (a) Inside of our BlueFors LD250 dilution refrigerator. (b) Zoom-in of some of the 10 mK stage of Experimental Setup A in Fig. 4.7, showing the sample holders introduced in Fig. 4.3(a) and RF coax switches, which are used to switch between KITWPA devices for characterisation as well as for measurement calibration. Note that the cryogenic bias tees are located on the rear of the copper bracket, hence are not visible here.

experimental setups are presented in the following sections.

4.6 DC Screening Setup

A fabricated wafer will often contain several KITWPA devices as well as numerous test structures, so complete characterisation of the full wafer could be very time consuming. To identify which devices have the most desirable properties for KITWPA operation, a DC screening setup has been developed, with a schematic shown in Fig. 4.6. A programmable Keithley 6221 current source at room temperature is used to provide a DC signal, which is transmitted to the device under test (DUT) at the mixing chamber of a DR via twisted-pair wiring. A Keithley 2182A Nanovoltmeter at room temperature, which allows for extremely precise voltage measurements across an ultra-low resistance, then measures the voltage across the

DUT. A 3.5 mm headphone plug and a switchboard-style interface, designed and built by Mr. Rik Elliot, allows for switching between DUTs in the DR.

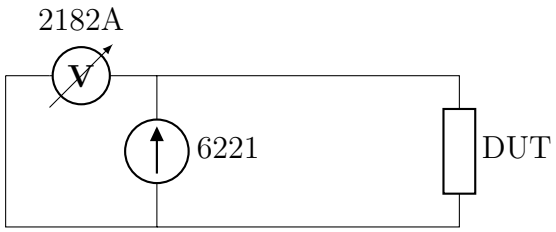

Figure 4.6: Schematic of DC screening setup. The Keithley 6221 provides a current to the DUT whilst the Keithley 2182A measures the voltage across the DUT.

A single current measurement allows for the identification of an open- or short-circuit in the DUT, a useful measure of the yield of the wafer. Alternatively, a swept current measurement can be used to produce an IV curve of the DUT, which allows the I_c of the DUT to be measured and enables hot-spots in the DUT to be identified. Hot-spots, in the context of a KITWPA, are small regions along the superconducting transmission line where the I_c is significantly lower than the rest of the line and are associated with higher losses along the transmission line. Hot-spots can easily be identified from voltage steps the IV curve of a KITWPA, which are significantly smaller than the voltage jump when bulk superconductivity is broken, as shown in [86].

This rapid DC testing capability allows for the identification of functional KITWPA devices before proceeding to full RF testing.

4.7 Experimental Setup A: Gain Measurements

Once DC screening has been performed to identify the best KITWPA devices, work can proceed to RF characterisation. The first RF characterisation that is typically performed is measurements of the transmission, S_{21}, and gain. To perform these measurements, a 'passive' experimental setup has been developed, which is intentionally designed to use as few components as possible and to have most of them outside of the cryostat at room temperature, which makes the setup more versatile and easy to configure.

4.7.1 Passive Experimental Setup

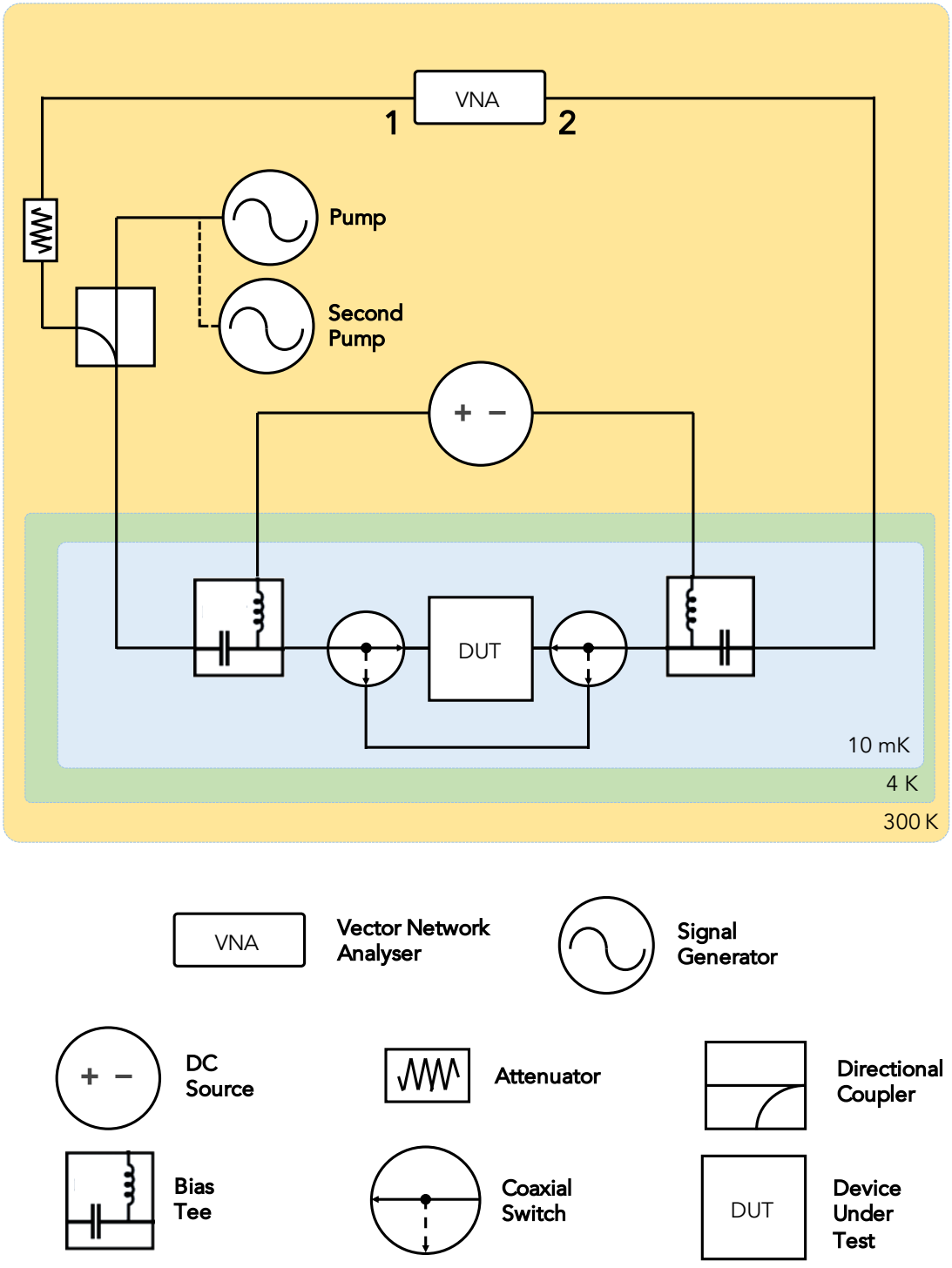

Figure 4.7: Experimental Setup A used for measuring S_{21} and gain.

A schematic of the setup, henceforth referred to as Experimental Setup A, is shown in Fig. 4.7 and comprises an Anritsu Vectorstar MS4644B vector network analyser (VNA) at room temperature, which is used to provide a swept-frequency

signal tone, which after warm attenuation is injected into the DUT at the 10 mK stage of the DR, as shown in Fig. 4.5(b). The output signal is then routed back via a low-loss RF line to the VNA. A pump tone (or multiple pump tones) is generated by an Anritsu Rubidium MG36241A signal generator (SG) (or multiple signal generators) at room temperature, which is coupled to the signal tone via a room temperature RF-Lambda RFDC5M18G10 directional coupler. A DC current can also be provided by a Keithley 6221 programmable current source and injected along the length of the transmission line using a pair of Sematron 8810SMF2-26 cryogenic bias tees. Additionally, a pair of Radiall R591762600 6-way actuator-operated coaxial switches at the cryogenic stage are utilised to switch between multiple DUTs and a through line, to allow for in-situ cryogenic calibration.

4.7.2 Passive Measurement Techniques

With this configuration, a frequency sweep of the signal can be performed with the VNA, allowing the S_{21} of the KITWPA to be obtained as a function of frequency. Taking the magnitude of this, $|S_{21}|$, gives the transmission spectrum of the KITWPA. Subsequently using the definition of the gain,

$$G_{\text{para}} = \left|S_{21}^{(\text{Pump on})}\right| - \left|S_{21}^{(\text{Pump off})}\right| \ (\text{in dB}), \tag{4.1}$$

means that the gain of the KITWPA can simply be obtained with two measurements of the S_{21}. It should be clarified that (4.1) gives the parametric gain, G_{para}, i.e., the rise in signal power due to parametric processes in the presence of a strong pump tone. In the field of KITWPAs, G_{para} is the gain value that is typically quoted in the literature, with all of the gain values quoted in Tab. 1.1 being calculated in this way. The reasons that G_{para} is typically quoted as the KITWPA gain is because it is easy to measure, since it does not require cryogenic S-parameter calibration, and it is also assumed that the unpumped $|S_{21}|$ of a KITWPA is close to 0 dB, which for a superconducting material on a high-resistivity substrate is a reasonable assumption.

From an end user point of view, however, this is not a particularly helpful definition, since it does not say how much the signal will be amplified with respect to a through line in the absence of an amplifier. The 'true' gain of the amplifier is given by,

$$G_{\text{true}} = P_{\text{out}} - P_{\text{in}} \ (\text{in dB}), \tag{4.2}$$

where P_{out} is the signal power (in dBm) at the output of the device and P_{in} is the signal power (in dBm) at the input of the device. For the purposes of this thesis,

however, the low insertion loss of the unpumped KITWPA means we assume that G_{para} is a sufficiently good approximation to G_{true}.

The parametric gain definition in (4.1) holds for D-4WM where there is only a single pump tone, however, for other wave mixing regimes, such as DC-3WM, there are other definitions we can use. The most obvious of these is given by,

$$G_{\text{para}}^{(\text{Pump,DC})} = \left|S_{21}^{(\text{Pump on, DC on})}\right| - \left|S_{21}^{(\text{Pump off, DC off})}\right| \text{ (in dB)}, \tag{4.3}$$

which gives the increase in signal power in the presence of a strong pump and DC. Another commonly used parametric gain definition for DC-3WM is given by,

$$G_{\text{para}}^{(\text{Pump})} = \left|S_{21}^{(\text{Pump on, DC on})}\right| - \left|S_{21}^{(\text{Pump off, DC on})}\right| \text{ (in dB)}, \tag{4.4}$$

where the DC current is kept switched on for both $|S_{21}|$ measurements and the pump is switched on and off. The reason why this gain definition is so useful is because it minimises the effects of gain ripples in the gain profile, which may shift in frequency and constructively interfere when a DC current is applied. For completeness, we can also define the parametric gain as,

$$G_{\text{para}}^{(\text{DC})} = \left|S_{21}^{(\text{Pump on, DC on})}\right| - \left|S_{21}^{(\text{Pump on, DC off})}\right| \text{ (in dB)}, \tag{4.5}$$

where the pump is kept switched on for both $|S_{21}|$ measurements and the DC is switched on and off. These definitions can naturally be extended to ND-4WM and other parametric processes.

The dispersion relation of the KITWPA device can simply be calculated by unfolding the phase of the S_{21} according to,

$$k = -\frac{\text{unfold}\left[\arg\left(S_{21}\right)\right]}{n} \text{ (per unit cell)}, \tag{4.6}$$

where n is the number of unit cells in the KITWPA transmission line [74]. The phase behaviour of the KITWPA device is an extremely useful probe of other behaviour of the device, such as the kinetic inductance. By equating the two expressions for the phase velocity along the KITWPA (in the low loss regime),

$$\begin{aligned} v_{ph} &\equiv \frac{\omega}{k} \\ &\equiv \frac{1}{\sqrt{LC}} \\ \implies L &\propto k^2, \end{aligned} \tag{4.7}$$

it can be shown that the (kinetic) inductance is proportional to the phase of the KITWPA squared. It is known from (2.8) that the kinetic inductance of the device

varies quadratically with the applied current to it. We can, therefore, measure the dispersion of the KITWPA at different applied DC current values and equate to the kinetic inductance using,

$$\frac{L\left(I\right)}{L\left(0\right)} = \left(\frac{k\left(I\right)}{k\left(0\right)}\right)^2, \tag{4.8}$$

to obtain the measured fractional kinetic inductance change as a function of applied DC current. We can then fit these data with the (2.8) to estimate the I_* of the KITWPA, which is an important measure of the non-linearity of the device.

It should be noted that for the definition of the gain in (4.1), the user need not perform a full S-parameter calibration for the S_{21} measurements, as both $\left|S_{21}^{\text{Pump on}}\right|$ and $\left|S_{21}^{\text{Pump off}}\right|$ values will contain contributions from the cables and other components, which subsequently cancel when the two values are subtracted from each other.

4.8 Experimental Setup B: Noise Measurements

Experimental Setup A in § 4.7 was designed to be as easy to configure as possible by placing the majority of the components outside of the cryostat. This is acceptable for simple transmission and gain measurements where the noise of the KITWPA is not important. For noise measurements, however, an alternative 'active' experimental setup is required, which places many of the components at cryogenic temperatures in order to minimise the thermal noise of the system. This experimental setup is shown in Fig. 4.8 and is referred to as Experimental Setup B from here onwards. It should be noted here that whilst we never actually performed noise measurements on any of my KITWPA devices due to time constraints, the experimental setup described here was initially set up in anticipation of noise measurements once we had identified a high gain device.

A VNA is used to provide a swept signal tone, which after warm and cold attenuation, and filtering is injected into the DUT. The output from the DUT is routed via a low-loss RF line and cryogenic circulators to a cryogenic low-noise amplifier (LNA) located at the 4 K stage of the DR. The circulators are used to prevent back radiation from the LNA from disturbing the DUT. The 4 K amplification is followed by room temperature amplification before the signal re-enters the VNA. A pump tone (or multiple pump tones) is generated by a SG (or multiple SGs), which is then split by an in-phase RF splitter. One of the branches is warm and cold attenuated

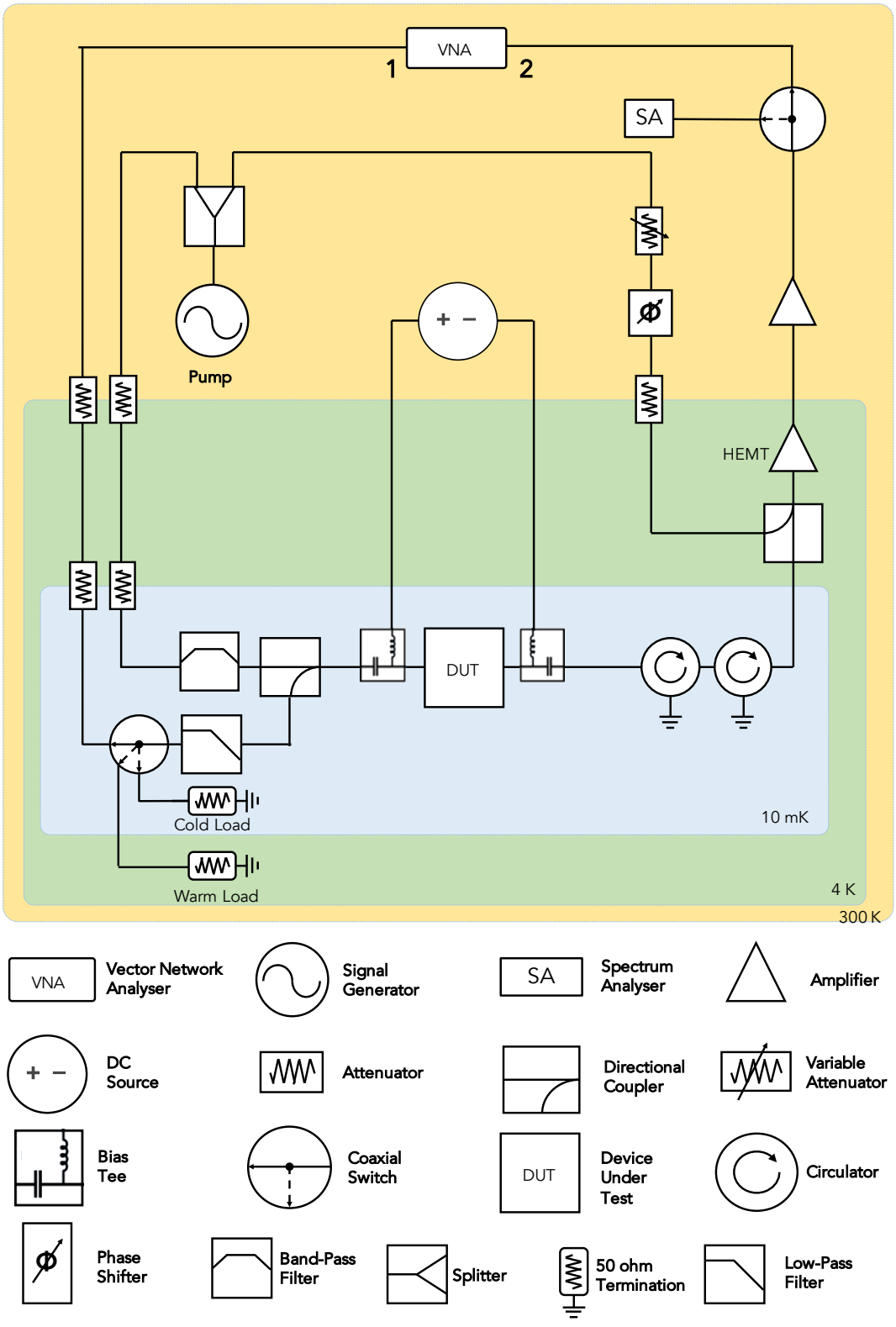

Figure 4.8: Experimental Setup B used for noise temperature measurements.

and filtered, before being coupled to the signal tone at the mixing chamber stage of the DR via a cryogenic directional coupler. The second branch is phase shifted

and attenuated before being coupled to the output signal tone at the 4 K stage just before the LNA. The injection of this second pump tone is used to cancel the strong pump before it enters the LNA, thus preventing the LNA from being saturated. A DC current can also be provided by a programmable current source and injected along the length of the transmission line using a pair of cryogenic bias tees. For standard hot-cold noise figure measurements, an RF coaxial switch before the DUT allows the input to be switched between the signal, a cold load at 10 mK, and a warm load at 4 K. A further RF coaxial switch at the output allows the user to switch between the VNA and a spectrum analyser (SA), if needed.

4.9 Other Measurement Techniques

In this section, I present two more experimental setups, which, whilst were used for some of the measurements presented in this thesis, are just variations to Experimental Setup A, hence are described more briefly.

4.9.1 Experimental Setup C1: Intermodular Distortion

Intermodular distortion (IMD) measurements are commonly used in RF characterisation to probe the non-linearity of a DUT. It is a multi-tone distortion product, which typically involves injecting two different frequency tones into a DUT and measuring the spurious harmonic products, which are generated by the non-linearity of the DUT [124]. For KITWPA applications, IMD is a useful probe of the non-linearity of the superconducting film, since it is a Kerr-3 non-linear material and, therefore, expected to generate 3^{rd}-order spurious products, the absence of which could suggest that our TiN film may not be behaving as expected.

The experimental setup used for IMD measurements is shown in Fig. 4.9 and, as stated, is essentially a variation on Experimental Setup A. The difference with this setup is that no VNA is used, with two RF tones instead being provided by a pair of SGs and the output spectrum being read out with an SA. Again, a pair of RF coaxial switches at the cold stage allows for calibration of the DUT.

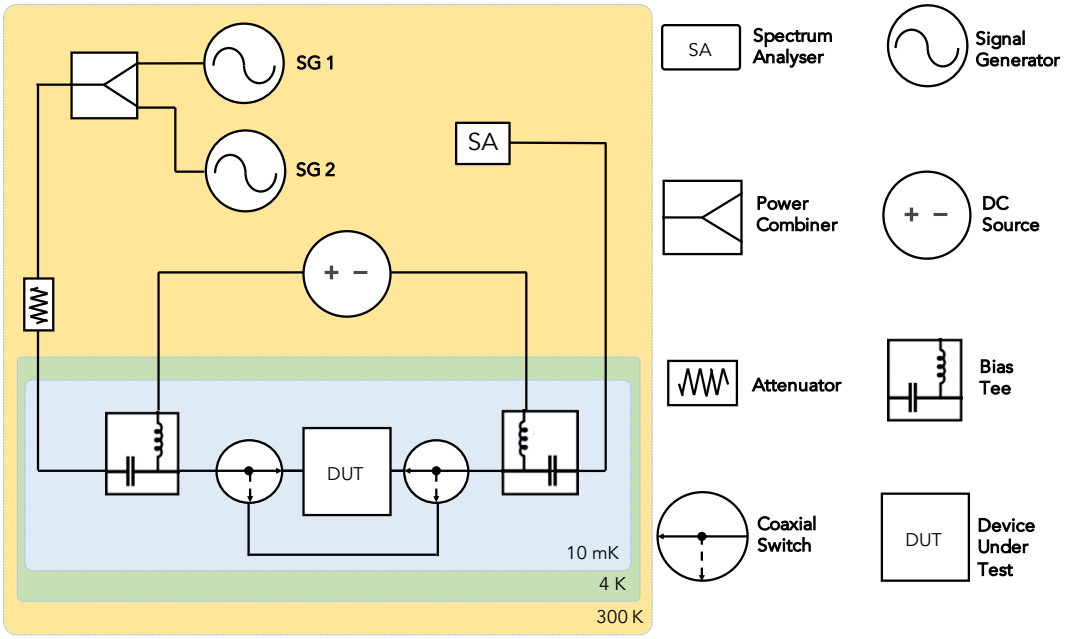

Figure 4.9: Experimental Setup C1 used for intermodular distortion measurements.

4.9.2 Experimental Setup C2: Time-Domain Reflectometry

Another diagnostic experimental technique that can be useful for KITWPA characterisation is time-domain reflectometry (TDR), a process that involves sending a pulse to the DUT and measuring the reflected waveform from it. Specifically, TDR can be used to characterise the transmission line properties of a KITWPA device, such as the characteristic impedance.

A boundary between two transmission line sections with different characteristic impedances will lead to reflections of an incoming signal, with the strength of the reflection being dependent on the ratio between the characteristic impedances. Defining the reflection coefficient, Γ, of the reflected pulse as the ratio between the reflected pulse amplitude and the sent pulse amplitude, the characteristic impedance of the KITWPA line, Z_L, can be inferred using,

$$\Gamma = \frac{Z_L - Z_0}{Z_L + Z_0}, \tag{4.9}$$

where Z_0 is the characteristic impedance of the input line and is normally $50\,\Omega$. In the extreme case, this technique is able to identify whether the KITWPA is open-circuited (for $\Gamma = 1$) or short-circuited (for $\Gamma = -1$). Additionally, the measured response can in principle be used to identify the positions of defects along the transmission line.

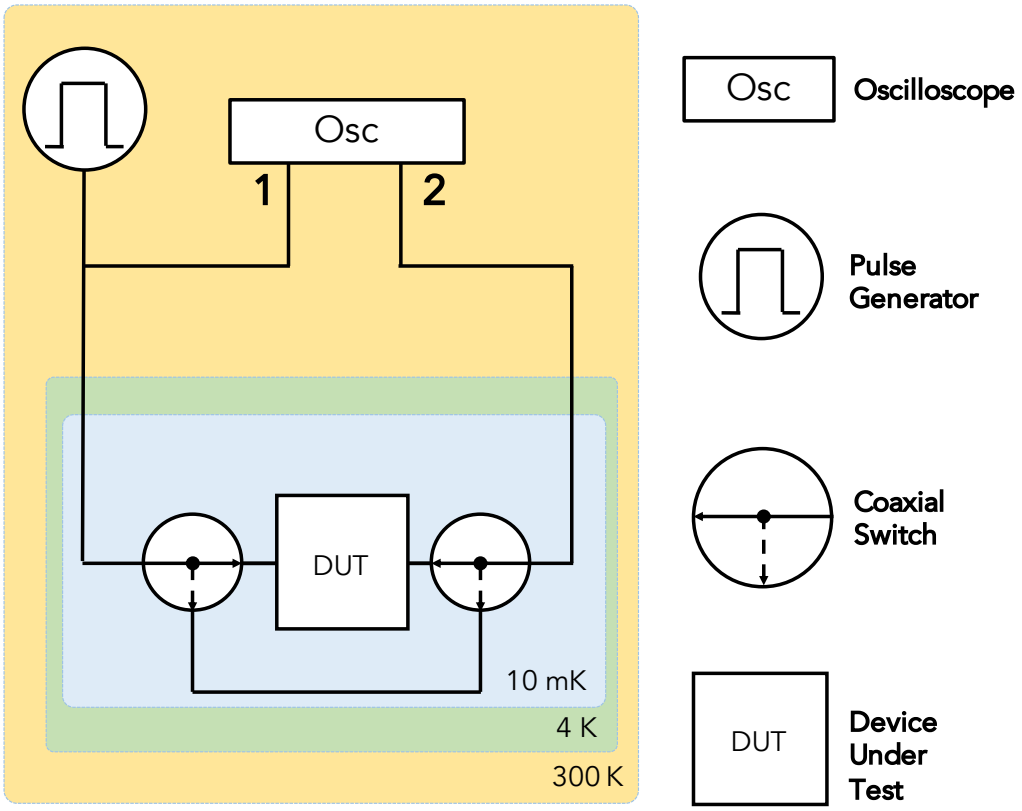

Figure 4.10: Experimental Setup C2 used for time-domain reflectometry measurements.

The experimental setup used to perform TDR measurements is shown in Fig. 4.10. A synthesiser is used to provide a pulsed signal, half of which is routed to port 1 of an oscilloscope and half is routed to the DUT at the mixing-chamber stage of the DR. At the DUT, a portion of the signal will be reflected back out of the cryostat to port 1 of the oscilloscope and the rest will propagate through the DUT before being routed to port 2 of the oscilloscope. The amplitude of the reflected pulse is dependent on the size of the impedance mismatch between two sections of the transmission line.

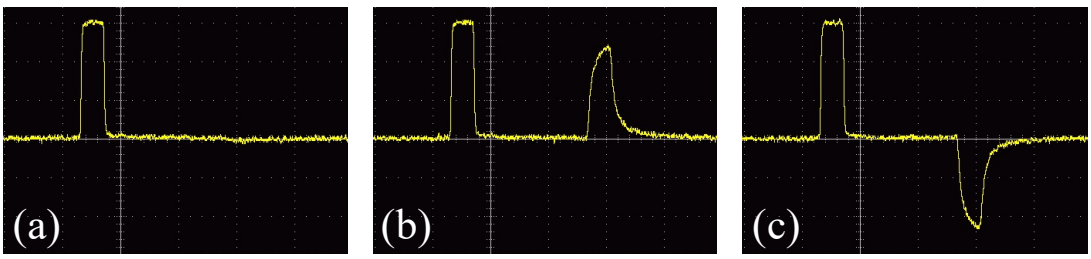

Figure 4.11: Example time-domain reflectometry (TDR) traces at port 1 of oscilloscope. (a) 50 Ω termination. (b) Open circuit. (c) Short circuit.

The TDR response at port 1 of the oscilloscope allows the reflection coefficient to be determined by taking the ratio between the peak of the reflected pulse and the peak of the original transmitted pulse, with some examples shown in Figs. 4.11(a)-(c). Fig. 4.11(a) shows the TDR spectrum for a $50\,\Omega$ termination, which clearly shows no reflected pulse, hence $\Gamma = 0$ for this. Fig. 4.11(b) displays the TDR spectrum for an open termination, which clearly shows a reflected pulse. Due to losses in the coaxial transmission cable, the reflected pulse has a peak smaller than the original transmitted pulse even though $\Gamma = 1$, which demonstrates the importance of ensuring the setup is properly calibrated. Fig. 4.11(c) displays the TDR spectrum for an short termination, which is much the same as in Fig. 4.11(b) except the reflected pulse is now inverted, giving $\Gamma = -1$

Measuring the response at port 2, known as time-domain transmitometry (TDT), gives the transmission through the device, providing a further useful indication as to whether the transmission line is physically broken.

Note that is important for TDR/TDT measurements that any bias tees along the signal path are removed before commencing measurements, as these will cause additional reflections that make the TDR/TDT trace much more difficult to interpret.

4.10 Summary

In this chapter, I have briefly described the fabrication techniques used by our collaborators to construct the KITWPA devices that are presented in this thesis, including how I draw the photomasks in preparation for fabrication. I have also introduced several experimental setups used to characterise our KITWPA devices, displaying the range of experiments that can be performed and the flexibility of the setups. These experimental setups will be referred back to in subsequent chapters of this thesis, where experimental characterisation of our KITWPA devices is presented.

Chapter 5

Experimental Characterisation of TiN KITWPA Devices

5.1 Introduction

In this chapter the experimental characterisation of TiN CPW KITWPA devices is presented. These KITWPA devices have been designed using the principles discussed in Chap. 3 and experimentally tested using the experimental setups described in Chap. 4. We begin with a description of the KITWPA design, detailing the physical dimensions of the device, justifying the design choices, and presenting the simulated transmission and gain profiles. Once the designs were finalised, we first scaled down the full design into a set of test structures, to characterise the behaviour of our TiN film. We present the results of these smaller scale chips before progressing to the characterisation of the full KITWPA devices. The chapter finishes with a discussion of the implications of the results, the conclusions that can be drawn, and how to proceed with further characterisation and subsequent design alterations.

5.2 TiN CPW Design

Fig. 5.1(a) shows a CAD image of the KITWPA design that has been characterised in this section. The device comprises a 42 cm long CPW transmission line containing 300 unit cells on a 22 mm by 22 mm chip. The transmission line is patterned into 100 nm thick TiN deposited onto a 500 µm thick sapphire substrate, using the

techniques described in § 4.3. Fig. 5.1(b) shows a zoom-in of a section of the CAD image, highlighting the spacing of 175 µm between adjacent lines, and the periodic loading structure. The transmission line has a nominal characteristic impedance of 50 Ω with perturbations to the impedance made every 460 µm with lengths of 48 µm. Most of the perturbations have a characteristic impedance of 60 Ω to create a large band gap near 20 GHz and integer multiples thereof. Every third loading has a characteristic impedance of 70 Ω to create a smaller band gap near 6. GHz and integer multiples thereof. Fig. 5.1(c) shows a zoom-in of the 50 Ω section of the transmission line, which has a centre-strip width of 2 µm, a gap width of 2 µm, and a finger length of 71 µm. The device dimensions are summarised in Tab. 5.1.

Parameter	Symbol	Unit	Value
Chip width	a	mm	22
Chip Length	b	mm	22
Bond pad width	p	µm	960
Periodic loading separation	d	µm	460
Spiral arm separation	s	µm	175
Main line impedance	Z_0	Ω	50
Primary loading impedance	Z_1	Ω	60
Third loading impedance	Z_3	Ω	70
Centre-strip width	w	µm	2
CPW gap width	g	µm	2
Finger length	l_f	µm	71

Table 5.1: Physical dimensions of fabricated TiN CPW KITWPA devices.

Fig. 5.2(a) shows the simulated $|S_{21}|$ transmission profile, highlighting the first three band gaps. Fig. 5.2(b) shows the simulated gain-bandwidth profile for different I_p values for $f_p = 6.41$ GHz, and Fig. 5.2(c) shows the gain as a function of input signal current, I_s, for different I_p values for $f_p = 6.41$ GHz and $f_s = 5$ GHz.

5.3 Test Structures

The analysis performed in § 3.3.1 provided a valuable insight into the necessary requirements for a superconducting film to be used for KITWPA applications. It remains the case, however, that this work is purely theoretical and based on the

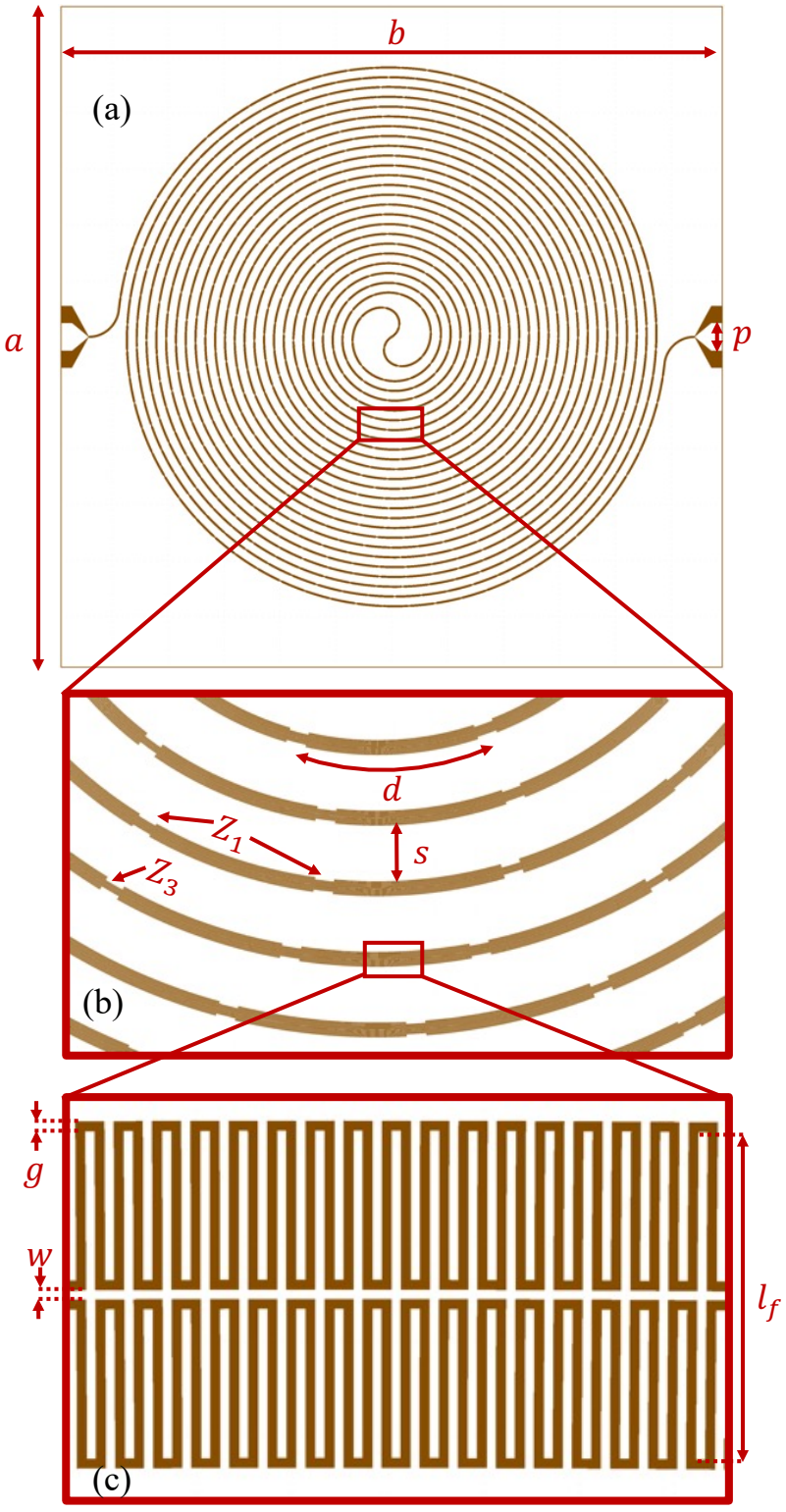

Figure 5.1: Design layout of the 100 nm TiN KITWPA chip. (a) CAD image of the full KITWPA device, including bonding pads. (b) Zoom-in of spiral winding structure, highlighting the spacing between the spiral arms and the positions of the periodic loadings. (c) Zoom-in of the 50 Ω section, highlighting the fishbone structure of the transmission line. The coloured regions indicate the areas where the TiN film has been removed.

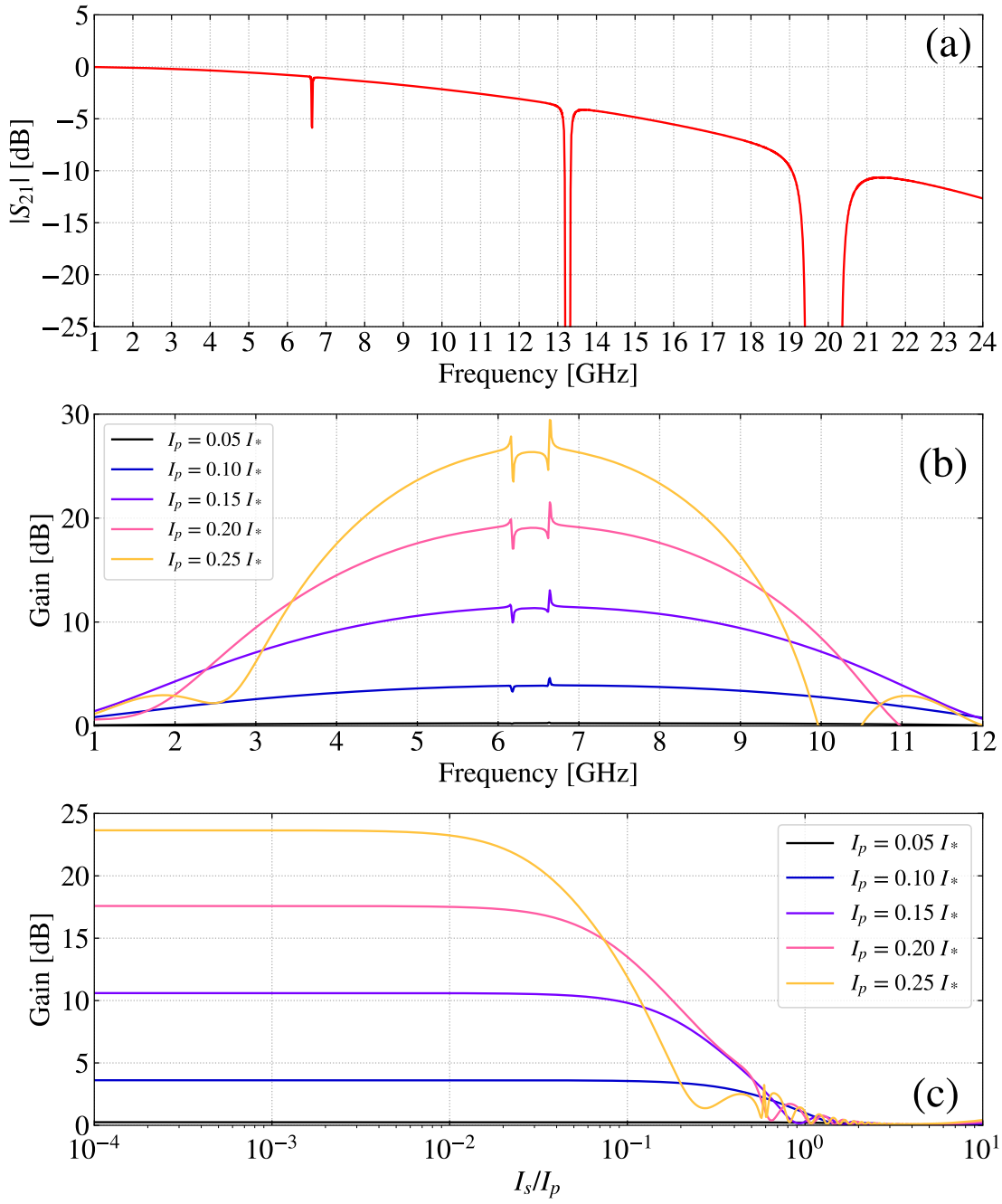

Figure 5.2: Simulation results of the 100 nm TiN KITWPA device. (a) Simulated transmission spectrum for a KITWPA device comprising 300 unit cells. (b) Gain versus signal frequency for various I_p values for $f_p = 6.41$ GHz. (c) Gain versus I_s for various I_p values for $f_p = 6.41$ GHz.

assumption of an ideal BCS superconducting film. It is crucial, therefore, to experimentally characterise our superconducting film to verify that we would observe the expected behaviour and that our conclusions from § 3.3.1 are justified. Before fabricating the full KITWPA devices in Fig. 5.1, therefore, we first designed and fabricated a set of 'test structures' using the same 100 nm TiN superconducting film, which we expected to use for the actual KITWPA.

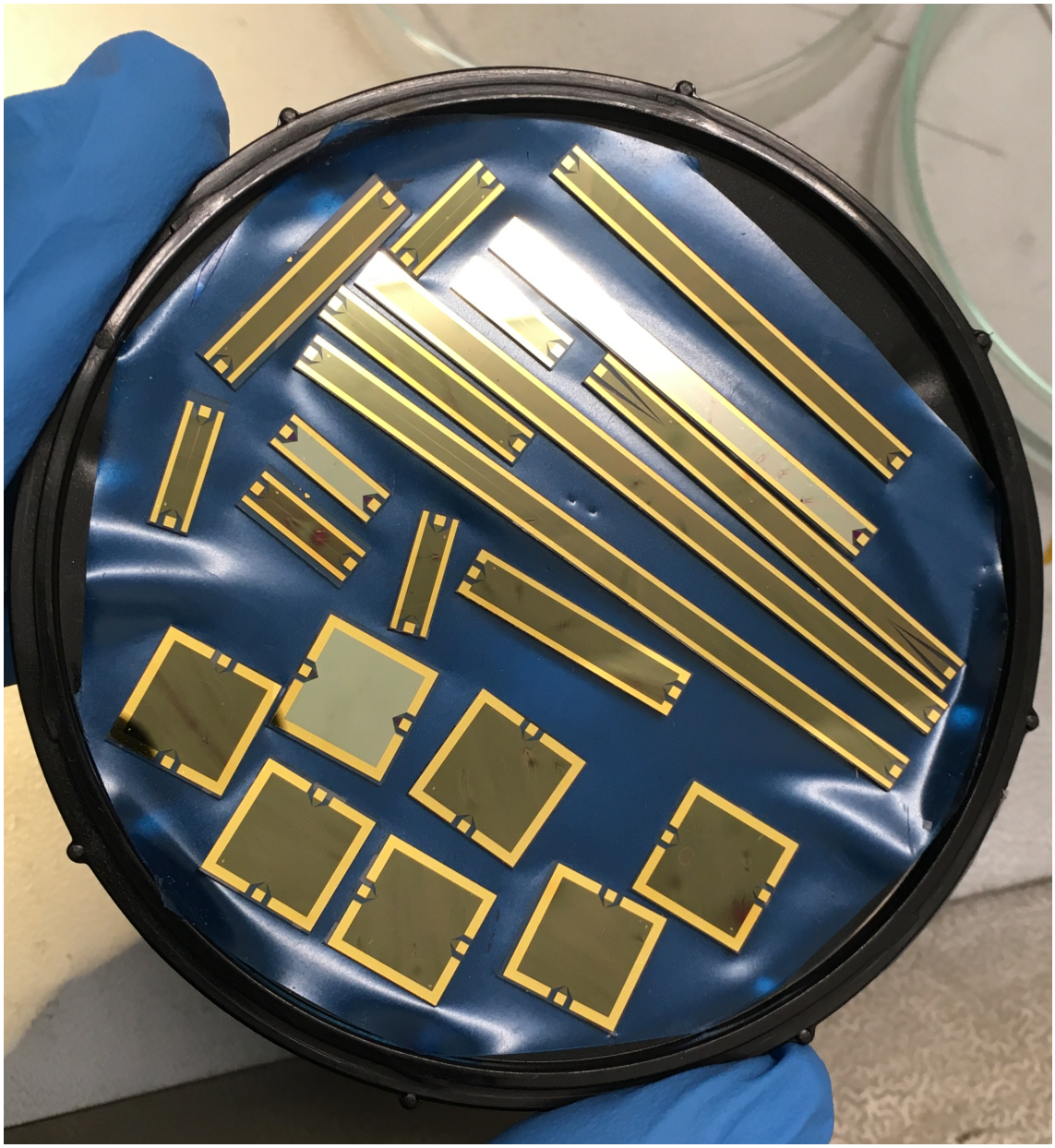

Figure 5.3: Photograph of test mask wafer, showing the various test devices. Note that during this particular fabrication run, an additional gold layer was deposited on top of the TiN to assist with wire bonding, and can be clearly seen around the edge of each chip.

Fig. 5.3 shows a photograph of the different test devices, which comprise various basic transmission line structures, such as short 50 Ω transmission lines comprising 10 unit cells and transmission lines shunted with lumped-element LC resonators, etc. The test structures are of the same nominal design as the KITWPA in Fig. 5.1 but with varying CPW centre-strip and gap dimensions, and different geometries, e.g. spiral or hairpin winding patterns. Probing these devices with DC and RF techniques allows us to investigate whether our TiN film displays the behaviour we expect for KITWPA operation, and to refine our design process for fabricating the full KITWPA devices.

5.3.1 Non-linearity Measurements

The first investigation I performed on the test devices was to confirm that the superconducting film displayed the appropriate non-linearity that is required for KITWPA operation. From [105], we see that measuring the S_{21} transmission of a KITWPA device whilst increasing the DC current flowing along the centre-strip of the line should result in a change in the phase of the S_{21} whilst leaving the magnitude relatively unchanged. This implies that the film would provide the required high non-linear kinetic inductance with minimal conduction losses.

The results of this investigation for a 50 Ω TiN fishbone CPW line, such as that shown in Fig. 5.4(a), are presented in Fig. 5.4(b), which clearly shows the phase of the transmission varying with applied current, whilst the magnitude remains relatively constant within a small current range. This result, which is in qualitative agreement with [105], suggests that the TiN CPW is operating as a low-loss, non-linear transmission line as expected.

The verification of the non-linearity in our TiN transmission line means that wave mixing should be observable along it. As a Kerr-3 non-linear material with a power-dependent kinetic inductance relation, it is expected that injecting a strong tone into the device will produce a third harmonic of the input tone, as well as subsequent odd harmonics of it. We experimentally reproduce this result in Fig. 5.4(c), where a 4 GHz tone from a signal generator was injected into the transmission line and the amplitude of the third harmonic at 12 GHz was measured with a spectrum analyser. As shown in this figure, we found a linear relation between the input power (in dBm) and the third harmonic's output power (in dBm) within the uncertainties of the spectrum analyser. The gradient of the linear fit of this log-log plot

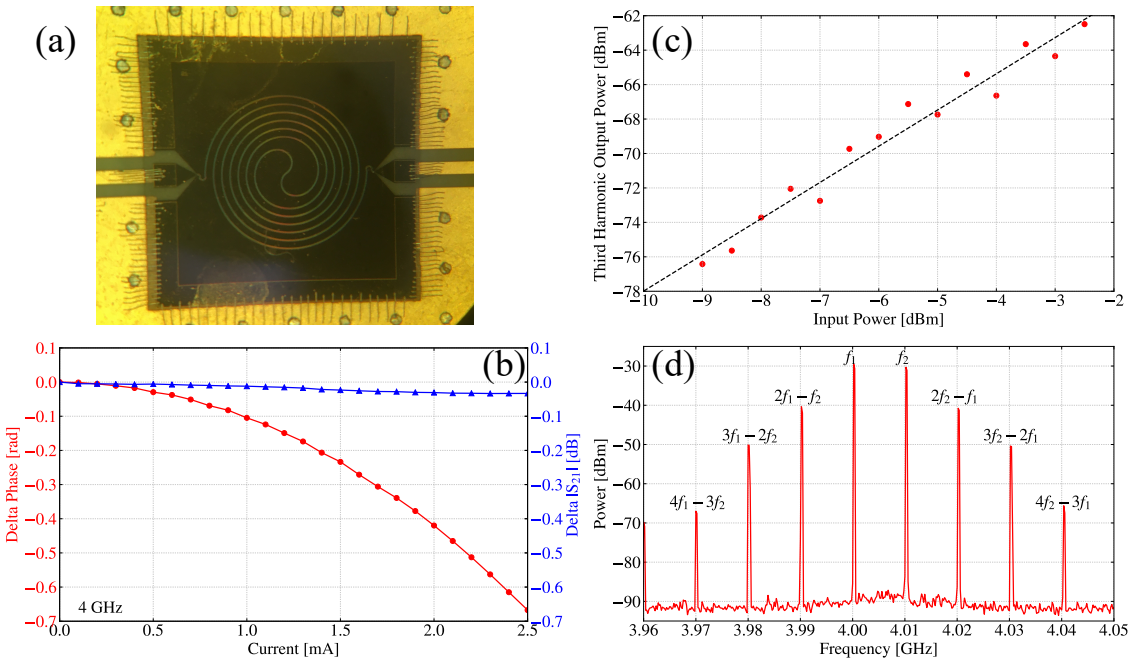

Figure 5.4: (a) Photograph of test device, comprising a 14.4 cm long CPW transmission line with dimensions of $w = 10\,\mu m$ and $g = 5\,\mu m$. Structure was designed to have a transmission line length of approximately one third of the full KITWPA design. (b) S_{21} measured at 4 GHz as a function of applied DC current. The phase of the S_{21} is shown in red and the magnitude in blue. (c) Output power of the third harmonic as a function of the input power of the primary tone set at 4 GHz. (d) Output inter-modular distortion (IMD) spectrum with two input tones at $f_1 = 4.00\,GHz$ and $f_2 = 4.01\,GHz$, respectively.

is approximately 2, meaning that the absolute power of the third harmonic in fact depends quadratically on the absolute input power. For this experiment, I removed all the room-temperature amplifiers and other active components from the experimental setup to ensure that the superconducting transmission line was the only non-linear component in the setup. This was further confirmed by swapping the test device out for a blank cooper CPW line, which resulted in the disappearance of the generated harmonics, confirming the TiN transmission line ito be the source of the non-linearity. A second harmonic was also observed if a DC current was concurrently passed along centre conductor, again in agreement with the expected non-linearity behaviour of the film.

To further explore the wave mixing properties of the superconducting transmission line, we subsequently performed inter-modular distortion (IMD) measurements, which involved simultaneously injecting two RF tones at different frequencies into

the device and measuring the output with a spectrum analyser, as discussed in § 4.9.1. If the transmission line exhibits purely linear behaviour, one would expect to observe only the two input frequencies, f_1 and f_2, at the output. In contrast, if the transmission line exhibits non-linear behaviour consistent with a current-dependent kinetic inductance, then one would expect to see 3^{rd}-order wave mixing terms at the output, as well as the input frequencies. One example of the IMD measurements is shown in Fig. 5.4(d), which clearly shows the output spectrum of the device containing many wave mixing products, which comprise all the expected 3^{rd}-order cross-harmonics consistent with a non-linear material exhibiting a four-wave mixing behaviour. Once again, swapping out the TiN transmission line for a blank copper CPW resulted in the generated harmonics disappearing, confirming the TiN line to be the only non-linear inductor in the experiment.

Another way of verifying the expected lossless non-linearity of the superconducting film is to measure the change in the behaviour of a resonator made from that particular material, such as that shown in Fig. 5.5(a), in response to an applied RF power. From [105], it is expected that increasing the power through the superconducting resonator will shift the resonance to lower frequencies, and for some films, such as TiN and NbTiN, the depth of the resonance (or the quality factor, Q) remains unchanged up to some power value (P_{lossless}), which is indicative of a dissipationless non-linearity. Above this power, the depth of the resonance will decrease as the film starts to become dissipative and lossy. Fig. 5.5(b) shows the shift in the resonance of one of the lumped-element TiN LC resonators that I tested as the power from the VNA is varied. For VNA powers below –20 dBm, we can see that the resonant frequency shifts with increased power without a change in the depth of the resonance, indicating that the film is exhibiting the expected lossless non-linearity. Above this power, the depth of the resonance rapidly decreases, implying a sudden onset of lossy behaviour, again in qualitative agreement with [105].

The results in Figs. 5.4-5.5 demonstrate that our TiN film displays the necessary non-linear behaviour to promote wave mixing and to achieve gain in a proper KITWPA configuration. From Fig. 5.5(b), we additionally see that this non-linearity is lossless below P_{lossless}, which implies that our TiN film should be suitable for KITWPA operation.

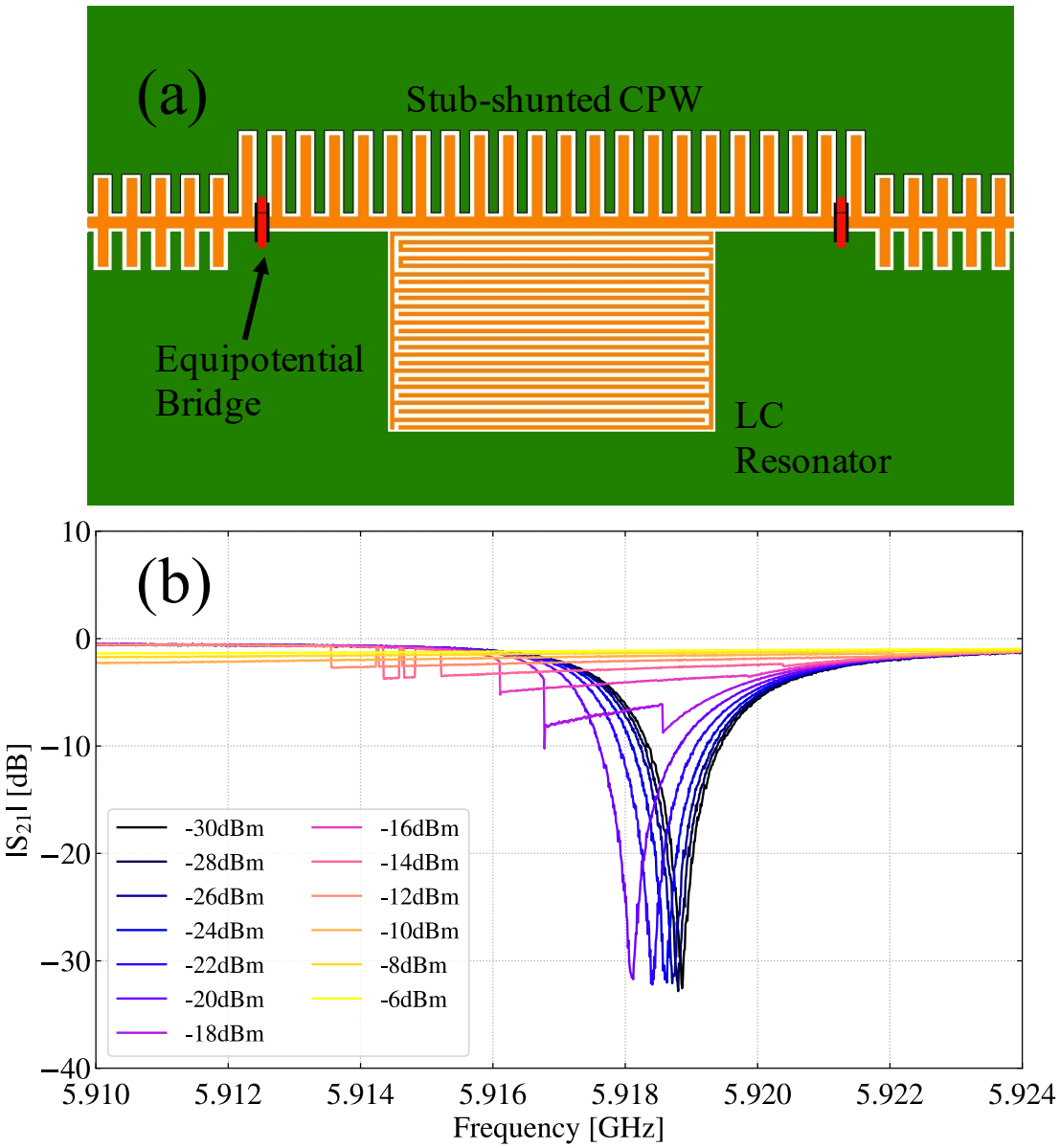

Figure 5.5: (a) CAD image of lumped element LC resonator shunted to a 50 Ω transmission line. Note that the red equipotential bridges [120] are not included on the fabricated chip. (b) Shift in the resonance frequency and depth as the input power from the VNA is increased.

5.3.2 Dimension Comparison

Having verified the non-linear behaviour of our TiN film, we can now proceed to further analysis of the geometry of the transmission line structures. The minimum dimensions of the transmission line are limited by the UV photo-lithography step in our fabrication process, since we do not currently have access to E-beam lithography capabilities that could allow us to achieve much smaller features.

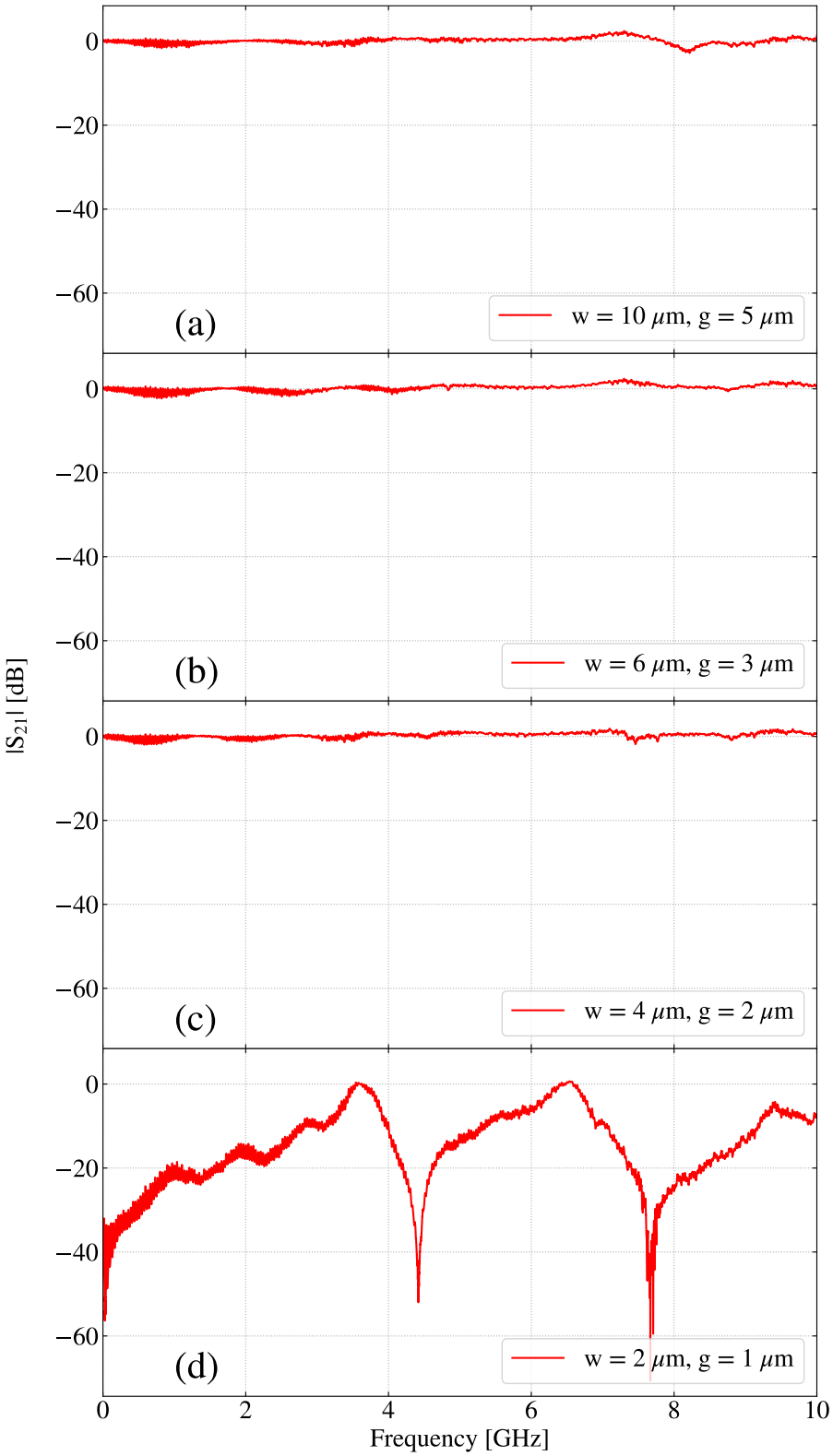

Figure 5.6: $|S_{21}|$ transmission spectra for different CPW transmission line dimensions. Input power to the devices was levelled at approximately –50 dBm.

It is desired that the dimensions of the transmission line be as small as possible in order to maximise the compactness of the KITWPA device and to ensure uniformity of the TiN film across it. A transmission line with smaller dimensions, specifically the CPW gap, however, is also more prone to fabrication defects, which can lower the yield of KITWPA fabrication. To ascertain the limitations of our photo-lithographic fabrication capabilities on the smallest features we can comfortably fabricate, we fabricated a set of CPW lines with several different w and g dimensions to measure and compare their $|S_{21}|$ behaviour.

Figs. 5.6(a)-(d) show the $|S_{21}|$ transmission spectra for four fishbone-style 50 Ω CPW lines with the same physical length of 10 mm, where the lengths of the stubs are optimised for each line to achieve a 50 Ω impedance. For the devices with CPW $w : g$ ratios of 10:5, 6:3, and 4:2 µm in Figs. 5.6(a)-(c), respectively, we observe a close to 0 dB transmission up to approximately 10 GHz, with relatively small ripples in the spectrum, indicating that the devices are reasonably defect-free and the characteristic impedance is well matched to 50 Ω, in agreement with our simulations. This is in stark contrast to the $|S_{21}|$ of the 2:1 µm CPW, in Fig. 5.6(d), which is found to be much less than 0 dB and displays significant variation with frequency. Subsequent time-domain reflectometry (TDR) and DC measurements on this device revealed it to be short-circuited. We repeated these measurements for longer transmission lines, where we observed the same behaviour. These results suggest that a KITWPA made with a CPW gap of 1 µm or smaller using our photo-lithography techniques would result in a very low yield. Following this investigation, we, therefore, decided to construct our KITWPA with the 2 µm CPW centre-strip and gap width dimensions used in § 5.2 as it presents a good compromise between a compact KITWPA design whilst achieving a reasonable yield.

5.4 TiN CPW KITWPA Characterisation

From § 5.3, we concluded that our TiN superconducting film displays the necessary non-linear behaviour to promote wave mixing, and we have identified the optimum CPW dimensions for our fabrication capabilities, which comply with the KITWPA design presented in Fig. 5.1. This section details the experimental characterisation of this KITWPA design. The devices were fabricated using a 3 inch substrate, which allowed for a maximum of five KITWPA devices to be allocated per wafer. At the edges of the wafer, where space was limited, we include a set of smaller test

devices, similar to that presented in Fig. 5.5(a). These devices comprise a 10 mm long fishbone CPW line with the same centre-strip and gap widths as for the full KITWPA designs. Additionally, these devices are shunted with a lumped-element LC resonator, with a simulated resonance at 6.5 GHz. These additional test devices were included so that we can check the quality of the film for each fabrication run to ensure that the film has similar properties to the test mask presented in § 5.3.

5.4.1 Summary of Batches

At time of writing, we have fabricated seven different batches of 100 nm TiN KITWPA devices in total, with the key properties of each batch summarised in Tab. 5.2.

Batch	Substrate	ρ_N (μΩ cm)	Number of Surviving Devices (/5)	Measured Thickness (nm)	Recalculated Impedance (Ω)	n_{loss}
1	Sapphire	-	0	97	-	-
2	Sapphire	-	0	97	-	-
3	Sapphire	380	1	96	85	5%
4	Sapphire	380	2	106	81	5%
5	Sapphire	200	2	106	63	10%
6a	Sapphire	120	1	95	55	50%
6b	Silicon	120	1	95	51	40%

Table 5.2: Summary of fabricated TiN CPW KITWPA batches. For each batch, the film is 100 nm thick stoichiometric TiN with an expected T_c of 4.39 K, based on previous measurements of the same film.

In the first two batches, the fabrication yield was found to be 0%, with all 10 KITWPA devices being either short- or open-circuit. Close inspection of the devices under a microscope subsequently revealed numerous defects per chip, such as anomalies to the width of the CPW centre-strip leading to hotspots, as shown in Fig. 5.7(a), and white debris in the CPW gap, which is likely to be TiN residue left behind after the lift-off step during fabrication, leading to a short-circuit in the transmission line as shown in Fig. 5.7(b). Whilst these fabrication defects appear to be random, the 0% yield of the first two batches suggests some systematic error in the fabrication process. We, therefore, made a small modification to our fabrication

process, which was to reduce the wavelength of the UV light used in the photolithography process from 365 nm to 320 nm. The adoption of this shorter wavelength for subsequent batches led to a fabrication yield of 20-40%, which whilst still low, was sufficient to characterise the KITWPA devices. It should be clarified here, however, that whilst the reduction in UV wavelength appears to have improved the fabrication yield, the small number of devices that have been tested are not statistically significant, hence we cannot make any strong conclusions as to the effectiveness of reducing the UV wavelength.

The KITWPA shown in Fig. 5.1 was designed and simulated using an assumed film resistivity of $\rho_{\mathrm{N}} = 140\,\mu\Omega\,\mathrm{cm}$, however, subsequent measurements of the film resistivity of each batch using a four-point probe revealed a considerable variation in ρ_{N} between each batch. This variation is shown in Tab. 5.2, highlighting how ρ_{N} for batches 3 and 4 deviates from the design value by a factor of over 2.5. Whilst the reason for this resistivity variation is not completely clear, one possible reason is due to erosion of the Ti target used in the sputtering process, which could lead to drifts in the fabrication parameters used when sputtering TiN films [125]. In subsequent batches, ρ_{N} values closer to the design value were achieved by reducing the pressure in the sputtering machine from 0.6 Pa to 0.4 Pa.

As discussed in § 3.4, we concluded that the optimum substrate to use for a KITWPA is sapphire, as from an EM perspective, it displays much lower losses than silicon but has a much higher relative permittivity, ϵ_r, than quartz, meaning that $50\,\Omega$ can be achieved with much shorter stubs, giving a more compact design. Comparing to most devices reported in the literature, however, we note that they were instead fabricated onto silicon substrates, so to understand if there is any unexpected property of sapphire that we have not considered, we additionally fabricated a batch on silicon during our sixth fabrication run.

Fig. 5.8 shows the un-pumped transmission spectrum for a single device from each batch except batch 2, where the raw data is shown in light grey and the smoothed data is shown in orange, which is averaged every 100 data points. The transmission for the batch 1 chip clearly shows an extremely poor low-frequency transmission, which is characteristic of a capacitive open or an inductive short as highlighted in Figs. 5.7(a)-(b). For the remaining batches, the transmission is much better, as we see that the 'envelope' of the transmission is much closer to 0 dB, and we also observe the presence of periodic band gaps. The positions of the band gaps, however, are different to those simulated in Fig. 5.1, which can be explained by the deviation in

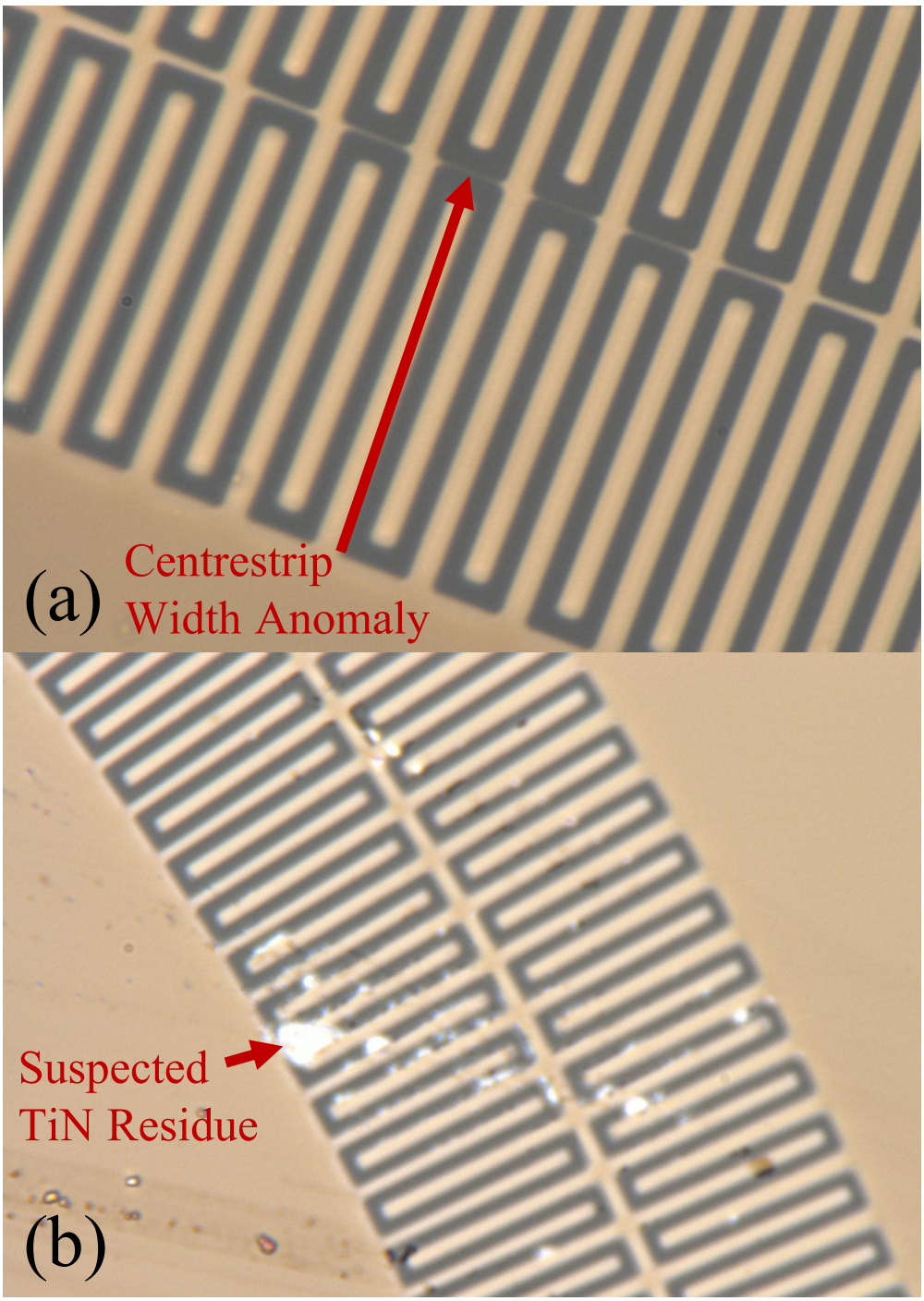

Figure 5.7: (a) Possible hotspot/open-circuit in transmission line. (b) Possible short-circuit in transmission line, with the white debris likely do be residual TiN. Gold coloured areas highlight the regions were the TiN film is deposited.

ρ_N and thickness from the simulated parameters. This variation additionally means that the characteristic impedance of each transmission line will have deviated from the 50 Ω design value, causing an impedance mismatch at the ends of the KITWPA.

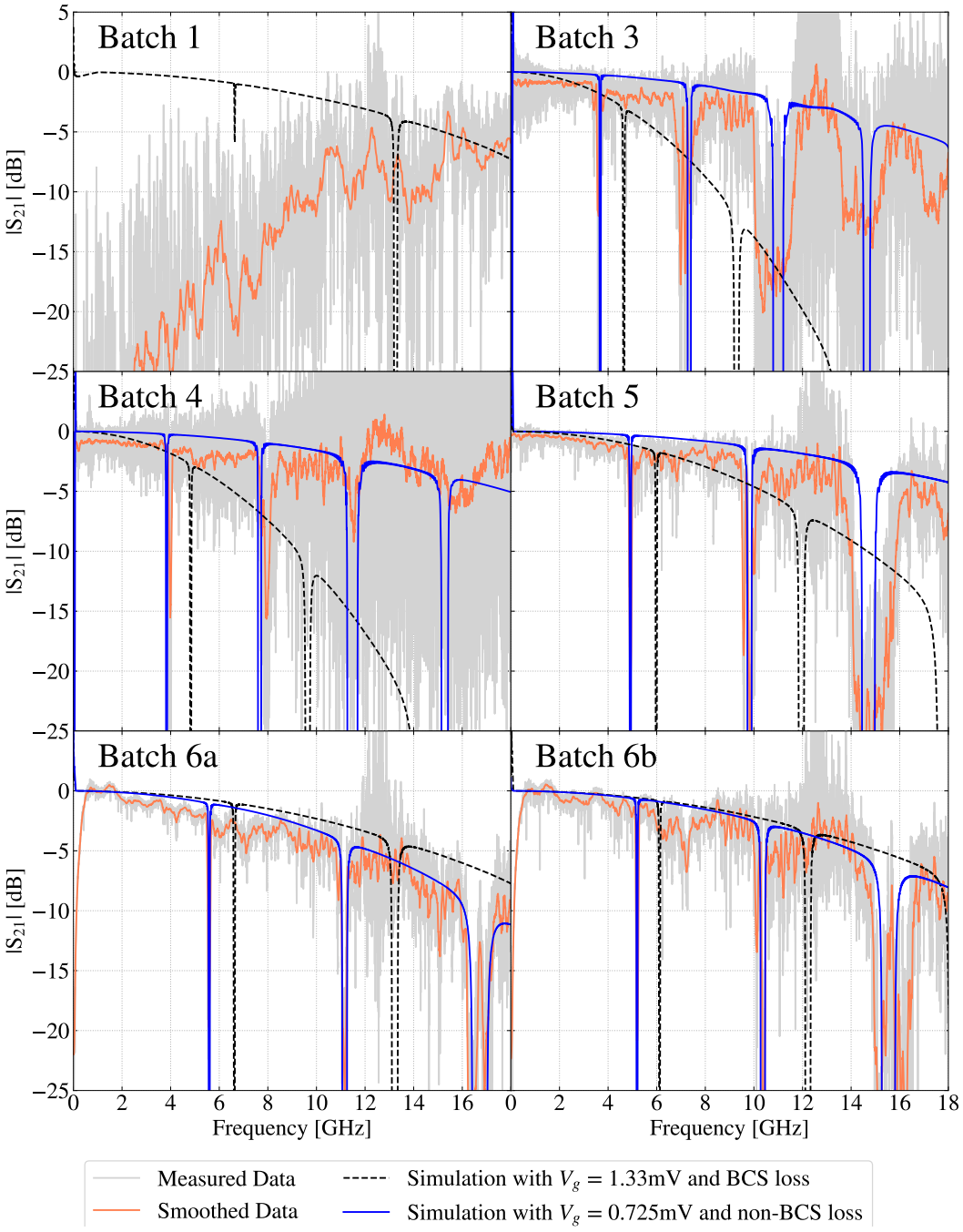

Figure 5.8: Un-pumped transmission spectra of KITWPA devices from different fabrication batches as summarised in Tab. 5.2. The simulated transmission curves for each batch were calculated using the methodology in Chap. 3.

This is evident from the ripples in the raw transmission spectra in Fig. 5.2(a), which are largest for batches 3 and 4 since they have the largest deviation in measured ρ_N, hence have the largest mismatch to 50 Ω.

For batches 3-6b, we re-simulated the transmission spectra using the measured

ρ_N and thickness parameters given in Tab. 5.2, and the assumed gap voltage, $V_{\text{gap}} = 1.33\,\text{mV}$. The results of this are given by the dashed black curves in Fig. 5.8, which show that for each batch, the frequency of the first band gap is still approximately 1 GHz higher in the simulated transmission compared to the measured transmission, despite using the measured ρ_N and thickness values. This discrepancy means that the inductance, and hence the phase velocity of the line, is larger than the values expected from the simulations. Re-simulating with the measured ρ_N and thickness parameters given in Tab. 5.2, however, one would expect the simulations to match more closely to the measured spectra, suggesting that one or more of our simulation parameters may be inaccurate.

Arguably the most interesting feature of these re-simulations, however, is how the 'envelope' of the spectrum compares between the measured and simulated data. For batches 3 and 4, which have the highest resistivity, the measured transmission is much higher than the transmission simulated using BCS theory; behaviour which is very similar to the NbTiN KITWPA spectrum displayed in Fig. 3.18(a). This implies that the film is much less lossy than expected for a BCS film, suggesting it would be suitable for use as KITWPA. If we look at the batches with lower film resistivity values, however, we see that the BCS simulated and measured data gradually match each other more closely as the resistivity is reduced, with the simulated 'envelope' for batch 6b being in very good agreement with the measured data. This implies that the n_{loss} coefficient, which we use to 'correct' for the R_s value calculated by BCS theory, is dependent on the resistivity of the film; further indicative of some microphysics beyond standard BCS theory.

To try and better understand the true properties of our TiN film, we further re-simulated the transmission spectra using the measured ρ_N and thickness parameters given in Tab. 5.2, except this time we altered the V_{gap} and n_{loss} parameters until the simulations matched the measured spectra. These further re-simulations are shown by the blue curves in Fig. 5.8, where for each batch we reduced the simulated gap voltage of the film to $V_{\text{gap}} = 0.725\,\text{mV}$, which, assuming the relation in (3.8) still holds, implies a T_c of 2.39 K. Using these V_{gap} and T_c values bring all of the simulated band gaps into very good agreement with the measured band gaps, suggesting that V_{gap} and T_c of our TiN film are much lower than expected. One possible reason for this could be a systematic error in our fabrication process, as recalling from Fig. 3.11(a), we see that V_{gap} of our TiN film can be tuned quasi-independently of ρ_N by altering the nitrogen flow rate in the sputtering machine. As we did not explicitly measure the T_c of our KITWPA devices, it is possible that the nitrogen

flow rate for all batches was set lower than expected, leading V_{gap} and, hence, T_c to be much lower than we assumed in our original simulations. This reason does not completely make sense, however, as we are dealing here with stoichiometric TiN, which should have a T_c of 4.39 K. Another possibility, therefore, is that this behaviour is indicative of some microphysical behaviour that we have not taken into account, such as the smearing of the superconducting gap [106, 107, 126], which could lead to the prefactor in (3.8) no longer being 1.764. The significant shift in V_{gap}, however, appears to be much too large to be completely explained by gap smearing alone. A simpler explanation could simply be that V_{gap} and T_c remain at 1.33 mV and 4.39 K, respectively, and that there is some systematic error in the ρ_N or thickness measurements of our TiN films, such that ρ_N has been consistently underestimated or the thickness has been consistently overestimated. An increased ρ_N or a decreased thickness would lead to a decreased phase velocity, hence lower frequency band gaps, however, more study is required to ascertain the true properties of our TiN KITWPA films.

Recalling from Fig. 3.10(b), re-simulating our TiN film with a reduced V_{gap} increases the inductance of the line, which reduces the cut-off frequency of our KITWPA transmission line and in turn increases the losses of the line. To recover the measured transmission 'envelope' of our devices, therefore, we need to include the n_{loss} coefficient in our simulations. The n_{loss} values used for each re-simulation are summarised in Tab. 5.2, and from this we see a clear ρ_N-dependence on the value of n_{loss}, with the films with higher ρ_N resulting in a lower n_{loss}. For all batches, we notice that $n_{\text{loss}} < 100\%$, meaning they are all less lossy than expected from BCS theory. As we stated previously, the value of n_{loss} is not fundamental, it is simply a fit parameter used to 'correct' the calculated R_s value from BCS theory. From the values used in Tab. 5.2, however, the clear dependence of n_{loss} on ρ_N is indicative of some microphysics beyond standard BCS theory.

5.4.2 DC Characterisation

Having summarised the fabricated batches of the KITWPA devices, I proceed to report the DC characterisation results of the KITWPA devices, which allows a number of important values to be extracted, such as I_c and I_*.

I_c can be determined by taking an IV curve of the KITWPA device, as illustrated in Fig. 5.9(a), which shows a pair of example IV curves for two different KITWPA

devices that have been measured using the DC screening setup presented in Fig. 4.6. I_c can be extracted from this plot by simply reading the current value at which the voltage rapidly increases. The blue and the red curves in Fig. 5.9(a), which represent two different devices, give similar I_c values, however, the curves themselves have different shapes, with the red curve containing several steps in the voltage, whereas the blue curve has a single, sharp increase in the voltage. From [86], these steps can be ascribed to 'hotspots', which are areas of the transmission line where I_c is much lower than the majority of the line and can be caused by defects such as that shown in Fig. 5.7(a). In practice, the presence of 'hotspots' limits I_c of the entire KITWPA device, which reduces the maximum I_p that can be provided to the line. This lowers the gain of the KITWPA, as exceeding I_c of one of the 'hotspots' leads to significant losses in the transmission line. This highlights the importance of the uniformity of the film and the transmission line that comprise a KITWPA, as even a small defect can severely limit the operational performance of a KITWPA and drastically reduce the yield of a batch of devices.

I_* for a superconducting transmission line can be obtained by measuring the change in transmission in response to an applied current. For example, Fig. 5.9(b) shows the phase of the S_{21} as a function of applied DC current along the central conductor of the KITWPA transmission line, which was measured using experimental setup A from Fig. 4.7. It is clear from this plot that the phase shifts with applied current, with a stronger shift being observed for stronger DC currents. This is expected as recalling from (2.7), we see that the L_k, and hence v_{ph}, of the transmission line is dependent on the strength of the current flowing along it. Equating the fractional change in phase with the fractional change in L_k using (4.8) allows us to plot the fractional change in L_k versus applied DC. If we then fit these data with the quadratic expression for the current-dependent inductance,

$$\frac{L_k(I)}{L_{k0}} = 1 + \left(\frac{I_{\mathrm{DC}}}{I_*}\right)^2, \tag{5.1}$$

we can estimate the value of I_*.

Figs. 5.10(a)-(c) plot the measured I_c and I_* values for all the KITWPA devices from batches 3-6b. Fig. 5.10(a) presents I_c versus ρ_N, for the KITWPA devices as well as the small test structures, which were fabricated on the same wafer as the KITWPA device. The data show a variation in the maximum I_c value per batch versus film resistivity, as well as an enormous variation in the measured I_c value within a given batch. The variation in the maximum I_c for different batches is expected, as from (2.1) in Chap. 2, we see that $I_c \propto \rho_N^{-\frac{1}{2}}$. The variation within

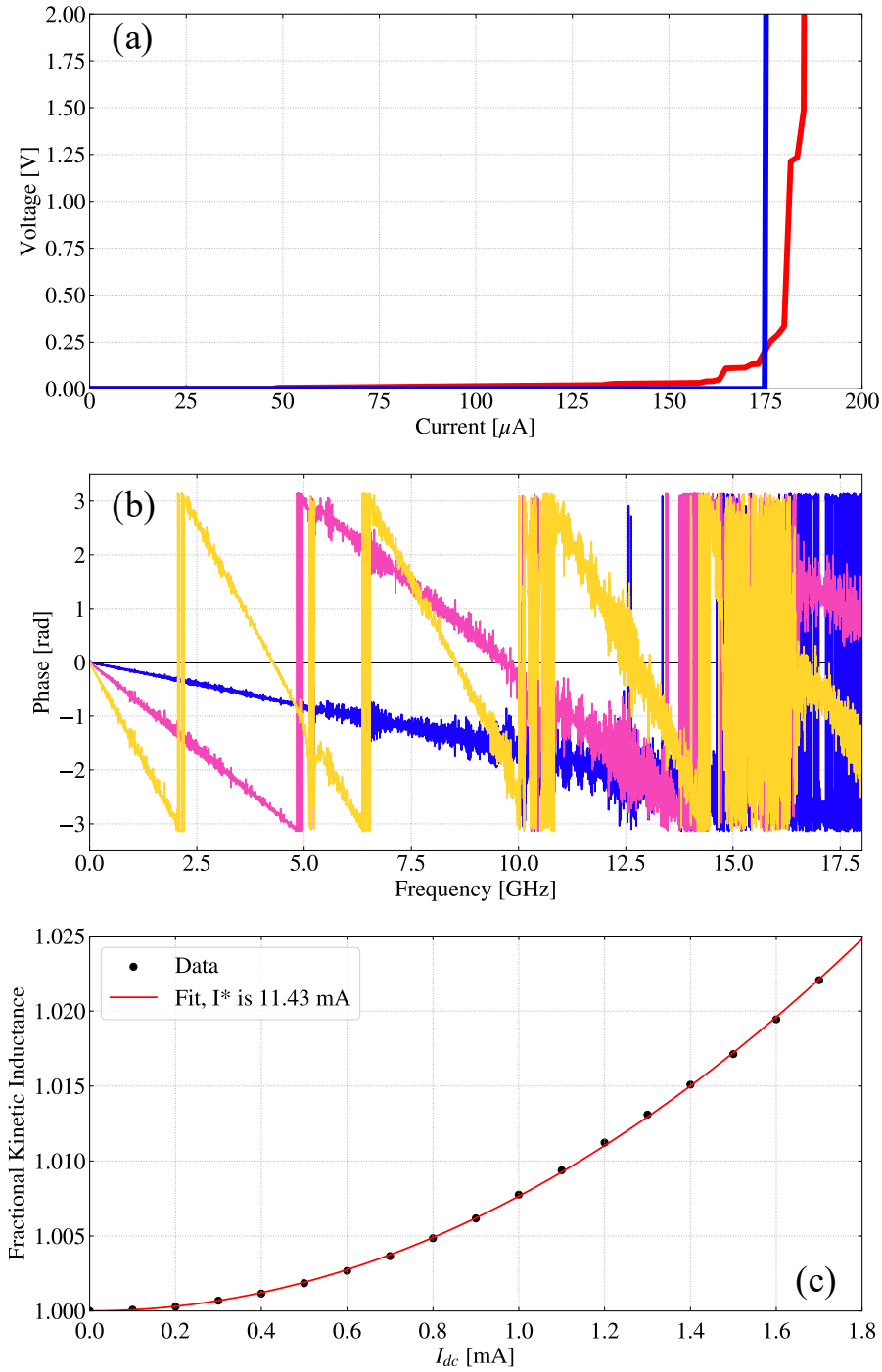

Figure 5.9: (a) IV curve comparison for device with hotspots (red) and without (blue). (b) Relative phase shift for batch 6b device with DC current applied at 0.0 mA (black), 0.5 mA (blue), 1.0 mA (pink), and 1.5 mA (yellow). (c) Fractional kinetic inductance as a function of applied DC current for batch 6b device. The data was fitted with $\frac{L}{L_0} = 1 + \frac{I_{\mathrm{DC}}}{I_*}$ to give an estimated $I_* = 11.43\,\mathrm{mA}$ and $\frac{I_c}{I_*} = 0.149$.

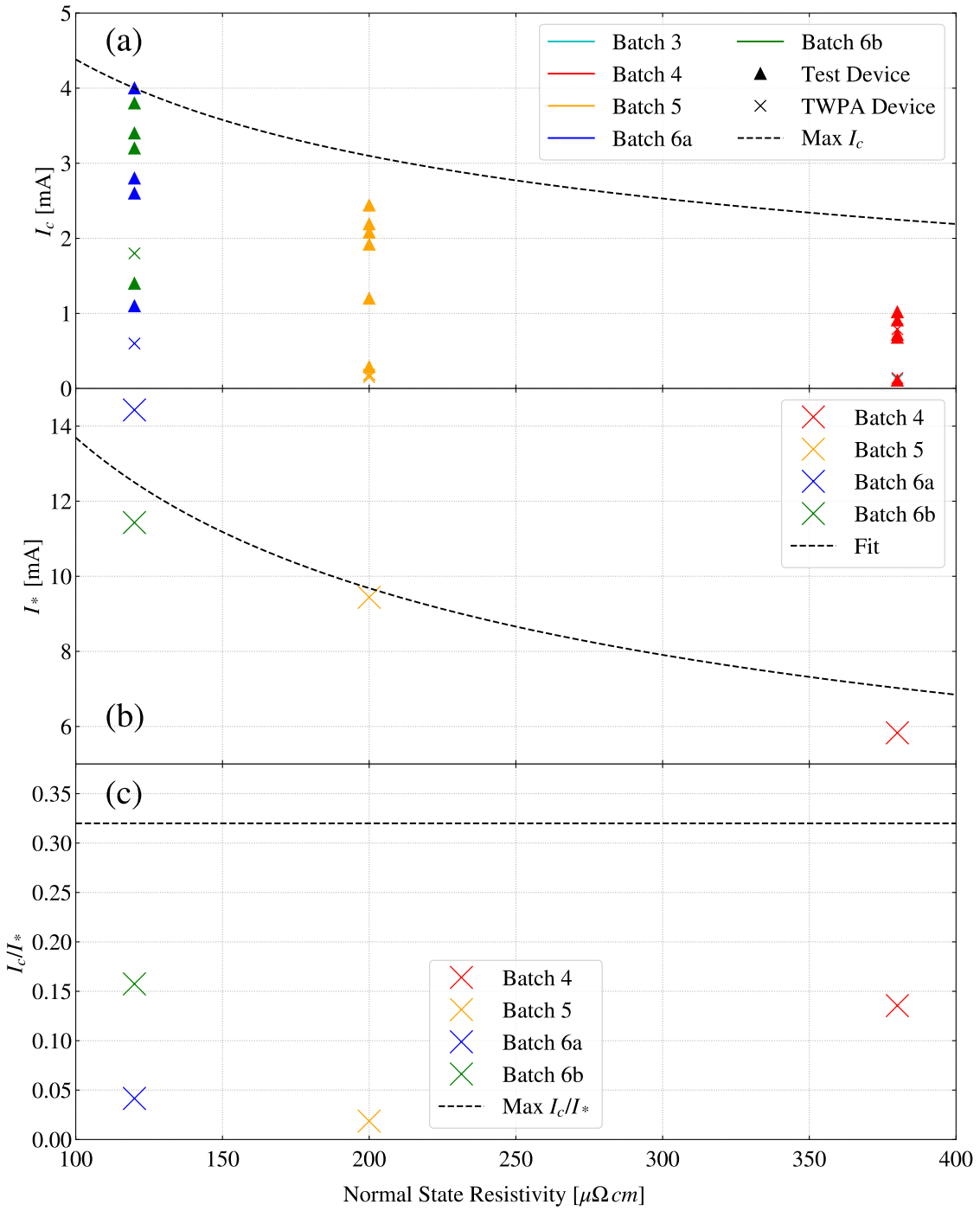

Figure 5.10: (a) I_c versus ρ_N for different batches, including both full KITWPA devices and test structures. (b) I_* versus ρ_N for different batches. (c) $\frac{I_c}{I_*}$ versus ρ_N for different batches.

particular batches is not expected, however, as all the devices from a particular batch are fabricated on the same wafer with the same processing steps, hence should have exactly the same superconducting film properties.

One possible reason for this variation in measured I_c values could be due to random fabrication defects such as those presented in Fig. 5.7(a)-(b). This hypothesis is supported by the fact that the majority of the test structures exhibit a higher measured I_c value than the full-length KITWPA devices from the same batch, since the test devices are much shorter and, therefore, have a smaller chance of suffering from a fabrication defect. Another possibility is that the variation in I_c is due to non-uniformities in the resistivity of the deposited film. From [127] we can see that the resistivity in their deposited NbTiN films varies by a factor of $\sim$2 across the surface of their wafer, which demonstrates how significant non-uniformities in a sputter-deposited superconducting film can arise. On our fabrication masks, the test devices are physically located towards the edge of the wafer, which is typically more prone to variation in ρ_N, hence the ρ_N value for each of these devices may be subject to large uncertainty. Whilst further investigation is required to confirm the exact source of this variation, it is clear that it is affecting the performance of our KITWPA devices and lowering the fabrication yield.

For now, let us assume that there is negligible ρ_N variation across the wafer. Recalling from (2.1), it is expected that the critical current of a superconducting transmission line is proportional to the inverse square root of the resistivity, i.e.,

$$I_c = \frac{A}{\sqrt{\rho_N}}, \tag{5.2}$$

where $A = \frac{3}{4} wt\Delta^{\frac{3}{2}} \sqrt{\frac{N_0}{\hbar}}$. It is desirable to find the maximum possible I_c as a function of ρ_N, as this gives a truer indication of the real I_c of the film and allows the performance of the KITWPA devices in the absence of defects to be estimated. As we want to find an upper bound for I_c, (5.2) is overlaid onto the data in Fig. 5.10(a) as the dashed black line, such that it intersects with the maximum measured I_c value, which is achieved for a fit parameter of $A = 44 \pm 8\,\mathrm{mA}\,\mu\Omega^{\frac{1}{2}}\,\mathrm{cm}^{\frac{1}{2}}$.

Fig. 5.10(b) presents the measured I_* values as a function of resitivity for the KITWPA devices from batches 4-6b using the technique presented in Figs. 5.9(b)-(c). I_* was calculated for the full KITWPA devices only, as the test structures are to short to observe a noticeable current-dependent phase shift. As described in (2.9)

similar to I_c, I_* is also proportional to the inverse square root of ρ_N,

$$I_* = \frac{A'}{\sqrt{\rho_N}}, \tag{5.3}$$

where $A' = wt\kappa_*\Delta^{\frac{3}{2}}\sqrt{\frac{\pi N_0}{\hbar}}$. Fitting (5.3) to the data in Fig. 5.10(b) gives an estimate for I_* as a function of film resistivity for a fit parameter of $A' = 137 \pm 9\,\mathrm{mA}\,\mu\Omega^{\frac{1}{2}}\,\mathrm{cm}^{\frac{1}{2}}$. Due to the low yield of the KITWPA devices, only four data points can be fitted to, hence there is a reasonably large uncertainty on the fit parameter.

With the ρ_N-dependent I_c and I_* values obtained, we can take the ratio of the fit parameters A and A' to give an upper bound on the maximum achievable ratio of $\frac{I_c}{I_*} = 0.32 \pm 0.06$ for the devices made from this TiN film, which is in agreement with the value reported in [128], within error margins. Overlaying this value on top of the measured $\frac{I_c}{I_*}$ ratios for the KITWPA devices, as shown in Fig. 5.10(c), demonstrates that our KITWPA devices display a ratio significantly less than the maximum, with the best performing device having a ratio of approximately half of the maximum. The $\frac{I_c}{I_*}$ ratio also allows for an estimation of $\kappa_* = 0.7 \pm 0.1$, which is of order unity as expected, although it is approximately half of the value $\kappa_* = 1.37$ as reported in [82].

Due to the low yield of our KITWPA devices, we only have four data points for the I_* and $\frac{I_c}{I_*}$ values, which makes it hard to draw any definitive conclusions, hence more testing needs to be performed. To truly understand the behaviour of the TiN films, however, a more detailed mapping of ρ_N over the surface of the wafer also needs to be performed, which would hopefully reveal the extent to which the film varies across the wafer.

5.4.2.1 AC Noise from Current Source

For a superconducting transmission line, it is expected that injecting a DC signal along the centre-strip of the line would have no effect on the $|S_{21}|$, provided the DC current is less than I_c. When performing measurements on our KITWPA devices, however, it was found that injecting a DC current would result in severe transmission line losses, as illustrated by the red curve in Fig. 5.11(a). It was further observed, as displayed in Fig. 5.11(b) that the amount of loss was dependent on the strength of the DC current. It appeared, therefore, that the presence of DC resulted in an unknown loss mechanism in the TiN film, which could not be explained by wave mixing as this is not promoted by a DC tone. This behaviour was in complete contradiction

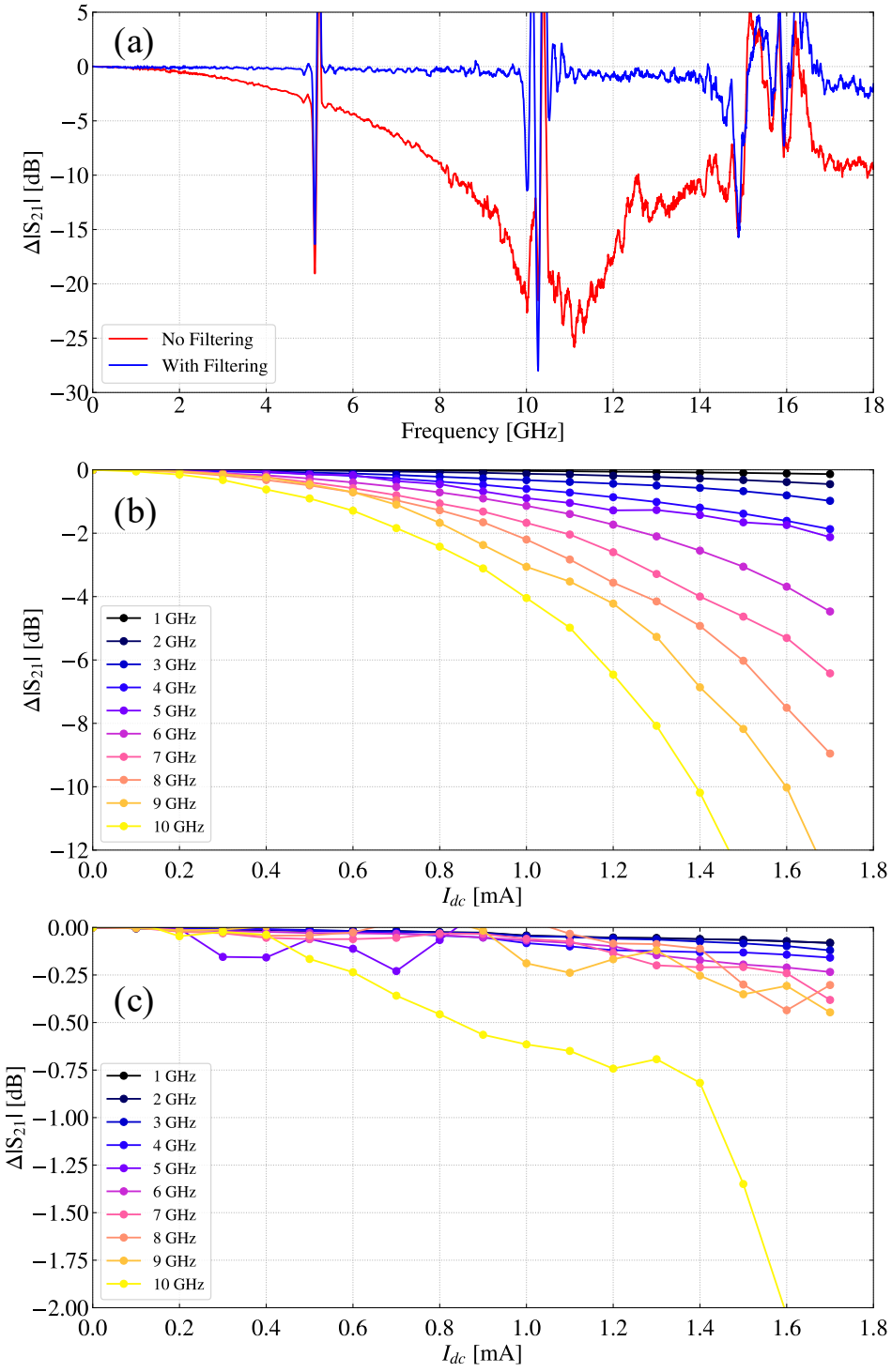

Figure 5.11: (a) $|S_{21}|$ spectrum for DC-on vs DC-off for batch 6b chip with and without DC - 2 kHz low-pass filters installed. Applied DC current was 1.7 mA. Change in $|S_{21}|$ as a function of applied DC current for batch 6b device (b) without and (c) with DC - 2 kHz low-pass filters installed.

with that seen in the early test devices, although the KITWPA devices presented here are much longer than the early test devices, so a small effect in the shorter devices may appear as a much larger effect in these longer devices.

Subsequent modifications to the experimental setup, however, revealed that the installation of DC-2 kHz low-pass filters between the current source and voltmeter and the DUT dramatically improved the DC response. Connecting the current source and the voltmeter individually to a spectrum analyser without the low-pass filters revealed that they both produce a significant amount of unwanted AC signal up to a few MHz in frequency, which are seemingly responsible for the observed 'DC' losses since the inclusion of the filters results in the almost complete elimination of DC-induced losses. These findings are demonstrated by the blue curve in Fig. 5.11(a) and the losses versus DC in Fig. 5.11(c). The large loss at 10 GHz in Fig. 5.11(c) is an artefact that arises due to the shifting of the second band gap when DC is applied, as evident in Fig. 5.11(a). The remaining losses at the other frequencies could be ascribed to residual AC signal below 2 kHz, which is not fully attenuated by the filters. I should stress here that all experiments presented previously and performed subsequently were done with these filters installed.

5.4.3 RF Characterisation

Having performed a detailed analysis of the DC behaviour of our KITWPA and test devices, we now proceed to RF characterisation, whereby a strong RF pump tone is injected into the KITWPA devices. Whilst the installation of the low-pass filters to the DC lines dramatically reduced the transmission losses described in Figs. 5.11(a)-(c), it implies that there is some underlying RF loss mechanism, which is dependent on the power propagating through the film. In this section, I investigate these RF-induced losses and attempt to identify their source to understand whether they can be mitigated by using the KITWPA in particular operational modes, by redesigning the KITWPA device, or whether the losses are something more fundamental related to the properties of the superconducting TiN film. The DC analysis in Figs. 5.10(a)-(c) revealed that the KITWPA chips from batches 4 and 6b exhibited the highest $\frac{I_c}{I_*}$ ratio, hence I shall focus on these particular devices in the following section.

Figs. 5.12(a)-(b), show the change in the transmission spectrum for the batch 4 and batch 6b devices, respectively, when pumped at a frequency just below the first band gap at a power level of 1 dB below I_c. Instead of amplifying, the transmission

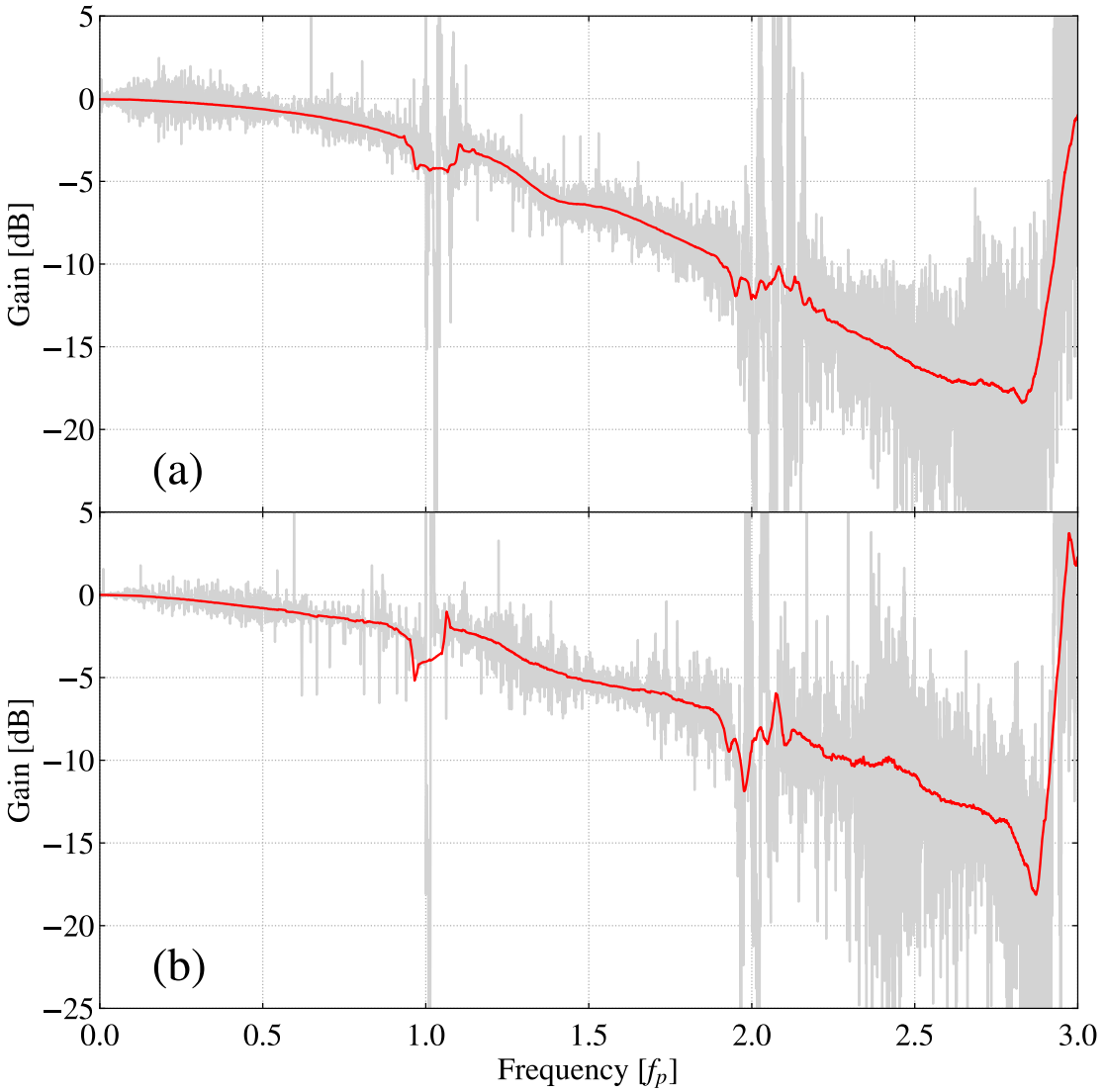

Figure 5.12: (a) Transmission profile for batch 4 device with pump tone at 3.75 GHz and –14.00 dBm. (b) Transmission profile for batch 6b device with pump tone at 5.10 GHz and –7.00 dBm. In both plots, the frequency is normalised by the pump frequency, f_p.

through the devices actually decreases, with the magnitude of the losses in each chip being broadly identical when normalised by the pump frequency, f_p, which takes into account the fact that the electrical lengths of the two chips are different due to the different resistivities. This pump-induced loss is unexpected as from Fig. 5.5(b), an applied RF tone should not induce any losses in the film when it is operating in the desired regime. If we compare the pump powers used in Figs. 5.12(a)-(b) with the RF powers in Fig. 5.5(b), however, we see that the pump powers in the KITWPA devices are much higher than P_{lossless}, implying our KITWPA devices are operating

in a lossy regime. If this is true, it means that the KITWPA devices may not work properly in their designed D-4WM regime, as at the powers required to achieve the simulated gain performance, the unexpected losses would completely negate any possible gain from wave mixing. If we reduce the pump power into the lossless regime, however, the pump is now too weak to promote any sufficient wave mixing to achieve the desired gain.

The spectra in Figs. 5.12(a)-(b) reveal the presence of pump-induced losses in the TiN KITWPA devices, however, the responsible loss mechanism is not completely clear to us at the moment. Whilst the comparison of the pump powers suggests the KITWPA is operating in a dissipative non-linear regime where Cooper pair breaking is leading to quasi-particle generation and, therefore, losses, it is not the only loss mechanism that may be present. Another possible loss mechanism is parasitic wave mixing, whereby unwanted frequency conversion mechanisms steal energy away from the signal frequency by converting it to other frequencies. Fortunately, there is a convenient way in which we can distinguish between the two loss mechanisms. As with parametric amplification, parametric frequency conversion is only expected to occur when the pump and signal tones are co-propagating along the KITWPA in the same direction, whereas Cooper pair breaking will occur independently of the pump propagation direction. An easy way to distinguish between the different mechanisms, therefore, is to compare the response of the magnitude of the forward transmission, $|S_{21}|$, and the magnitude of the reverse transmission, $|S_{12}|$, in the presence of a strong, forward-propagating pump tone. Whilst $|S_{21}|$ would be sensitive to both loss mechanisms, $|S_{12}|$ would only be sensitive to non-wave-mixing processes, hence we can disentangle the effects of both loss mechanisms.

I, therefore, made measurements of both the forward and reverse transmission spectra in the presence of a forward propagating pump, focusing on the batch 6b device as this had the cleanest transmission spectrum. I carried out these measurements over a wide range of pump frequencies and pump powers to ascertain what relationships, if any, the losses displayed relative to these parameters.

Fig. 5.13 plots the change in the forward transmission $\Delta|S_{21}|$, where,

$$\Delta|S_{21}| = |S_{21}|^{\text{Pump On}} - |S_{21}|^{\text{Pump Off}}, \tag{5.4}$$

and change in the reverse transmission $\Delta|S_{12}|$, where,

$$\Delta|S_{12}| = |S_{12}|^{\text{Pump On}} - |S_{12}|^{\text{Pump Off}}, \tag{5.5}$$

for different f_p values using Experimental Setup A. For each f_p, the pump power, P_p, was set to just below I_c to ensure the same amount of power was entering the transmission line at each f_p. Studying the spectra across Fig. 5.13, we observe a huge amount of variation in them. For f_p values of 1 GHz, 2 GHz, 3 GHz, and to a lesser extent 5 GHz, we observe a stark contrast between $\Delta|S_{21}|$ and $\Delta|S_{12}|$, which is strongly indicative that parasitic wave mixing is the primary source of the losses.

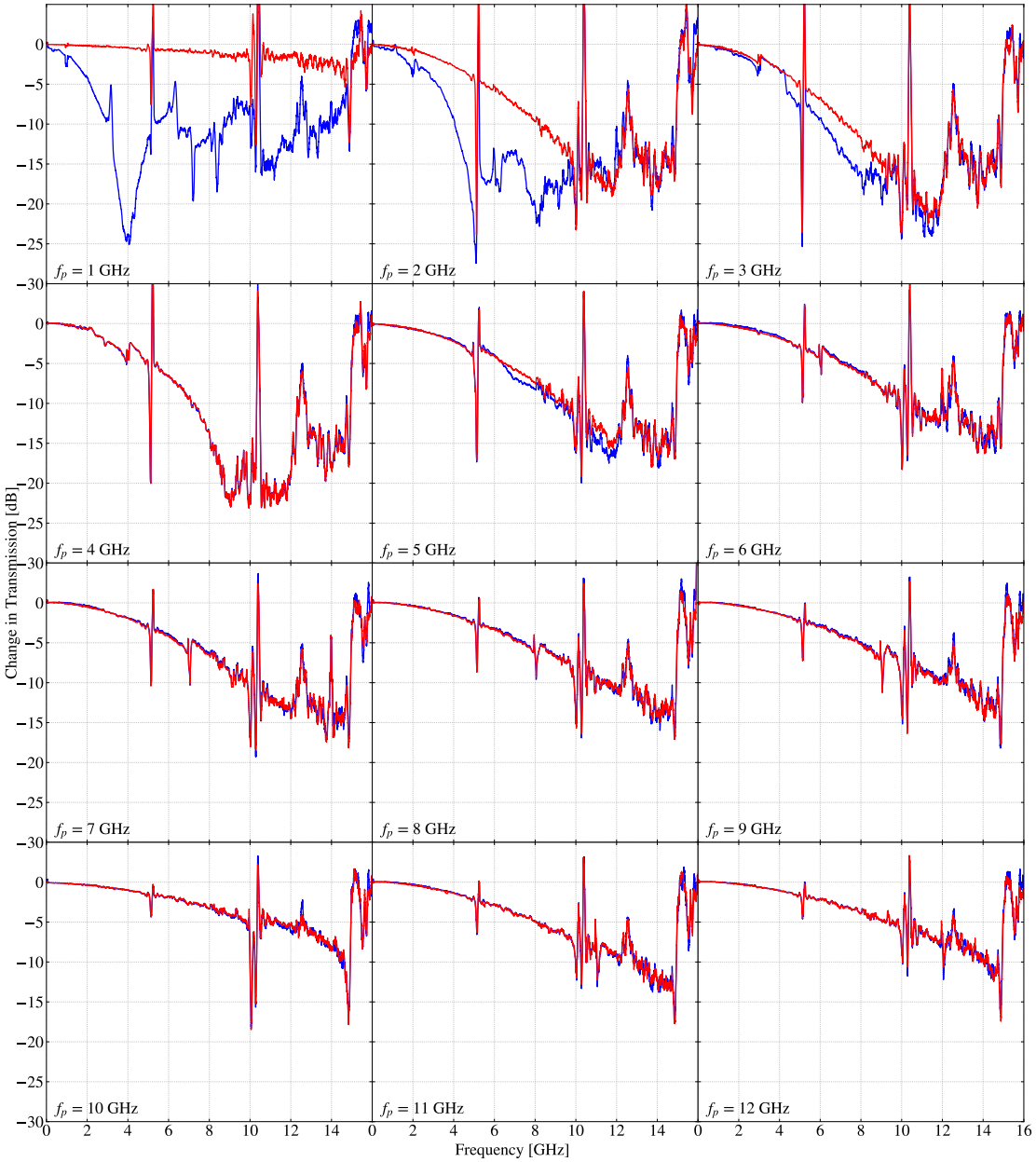

Figure 5.13: $\Delta\,|S_{21}|$ (blue) and $\Delta\,|S_{12}|$ (red) for different f_p values, where for each f_p, P_p was adjusted to be just below the point at which superconductivity is broken. Note that the sharp peaks near 5 GHz, 10 GHz, and 15 GHz are the band gaps.

Inspecting the $f_p = 1\,\text{GHz}$ plot more closely, we observe a minimum in $\Delta|S_{21}|$ at a signal frequency of $f_s = 4\,\text{GHz}$. Assuming that the lowest order up-conversion process is taking place, $f_u = 2f_p + f_s$, this would give an up-conversion product at $f_u = 6\,\text{GHz}$, which is just above the first band gap. Due to the shifts in phase that occur near the band gaps, it is possible that this particular up-conversion process is unintentionally well phase-matched at $f_s = 4\,\text{GHz}$, allowing this process to take place. It should be noted, here that the up-conversion tone is not observed in the plots in Fig. 5.13 as the VNA receiver port only scans a narrow frequency band around f_s for each frequency point, hence the up-conversion tone will be outside of this band and not detected.

We can make the same argument for $f_p = 2\,\text{GHz}$, where the dip at $f_s = 5\,\text{GHz}$ could be indicative of the equivalent up-conversion process to $f_u = 9\,\text{GHz}$, which is just below the second band gap. For $f_p = 3\,\text{GHz}$, the picture is less clear, however, a local minimum around $f_s = 9\,\text{GHz}$ could indicate up-conversion to around the third band gap, although this process is weaker. For f_p values above 5 GHz, the up-conversion is not clearly seen and both the forward and reverse transmission curves are virtually identical, meaning the up-conversion process could be suppressed for higher pump frequencies due to poorer phase-matching caused by the larger non-linear dispersion at higher frequencies.

Another explanation for the observed behaviour in Fig. 5.13 could be due to higher pump harmonics being created and interacting with f_s. This process could create many harmonic tones, which steal energy away from the signal, leading to distortions in the transmission spectra. The reason that this has a stronger effect on the blue curves at lower f_p values in Fig. 5.13 could be that a lower frequency pump can create more harmonics within the f_s bandwidth that is being probed, leading to more unexpected wave mixing processes.

The discrepancy between $\Delta|S_{21}|$ and $\Delta|S_{12}|$ at lower f_p values may be indicative of parametric losses at these frequencies. Focusing on $\Delta|S_{12}|$ only, however, we can see from the spectra in Fig. 5.13 that applying a pump tone in the opposite direction to the signal tone also results in losses, which cannot be explained by parametric processes alone, indicating the presence of Cooper pair breaking. We can see from Fig. 5.13 that $\Delta|S_{12}|$ seems to vary with f_p, so to clarify this relation, I have plotted $\Delta|S_{12}|$ as a function of f_p for various f_s values, which is shown in Fig. 5.14. Rather unexpectedly, we observe a large dip in $\Delta|S_{12}|$ for $f_p = 4\,\text{GHz}$, implying this pump frequency is particularly loss-inducing. This is unexpected because at higher

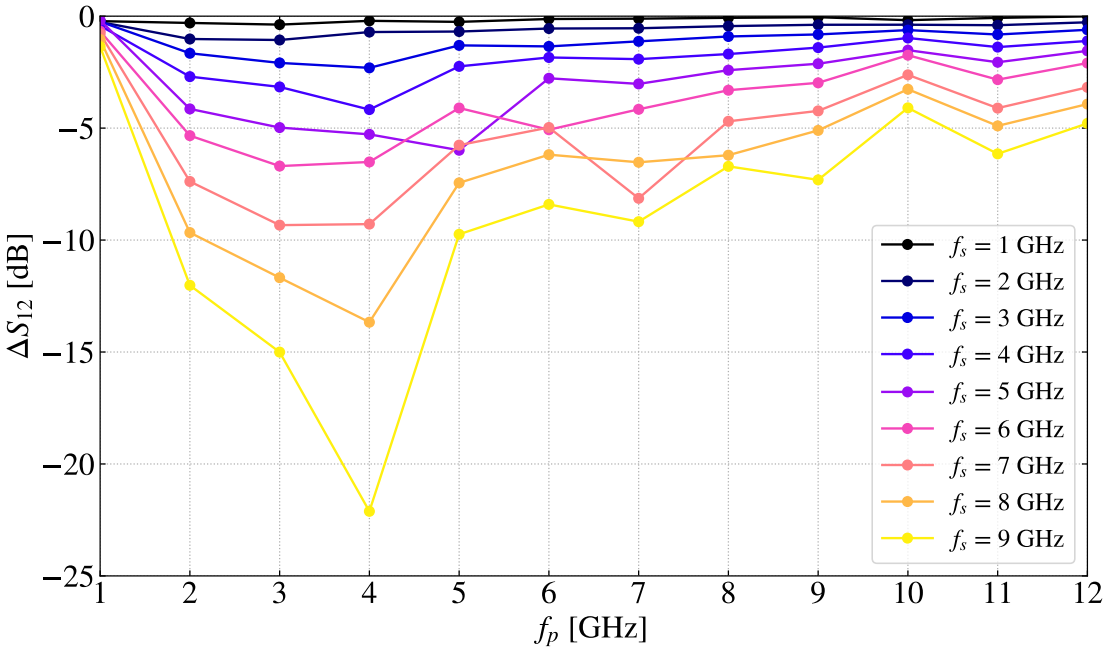

Figure 5.14: $\Delta\,|S_{12}|$ as a function of f_p for different f_S values. For each f_p, the power was adjusted to be just below the point at which superconductivity is broken.

frequencies, hence shorter wavelengths, a given physical length will have a longer electrical length as more wavelengths can fit into the physical length. One would, therefore, expect the higher frequency pump tones to induce more losses, as the KITWPA is effectively longer at these pump frequencies, so the pump has a longer length over which to interact with the other tones propagating along the KITWPA.

Fig. 5.15 again plots $\Delta|S_{21}|$ and $\Delta|S_{12}|$ spectra but this time for different P_p values. I have performed this measurement at a fixed f_p of 5 GHz, just below the first band gap, which is where the design f_p value is. At this frequency, $\Delta|S_{21}|$ and $\Delta|S_{12}|$ are virtually identical, suggesting there is no strong, unwanted parametric loss process occurring. Additionally, we can see from both $\Delta|S_{21}|$ and $\Delta|S_{12}|$ spectra that the losses in both directions vary depending on P_p.

To further clarify the loss dependence on P_p, I have plotted $\Delta|S_{12}|$ as a function of $P_p - P_c$, where $P_c = I_c^2 Z_0$ is the RF power at which superconductivity is broken, for various f_s values, which is shown in Fig. 5.16. We can see from this figure that $\Delta|S_{12}|$ follows a clear trend with P_p, in that the losses increase as the pump power is increased towards I_c of the film. We see that $\Delta|S_{12}|$ at all f_s values displays the same type of relationship with P_p, with the exception of $f_s = 5$ GHz, which seems to become lossier much faster. This can simply be explained, however, by the

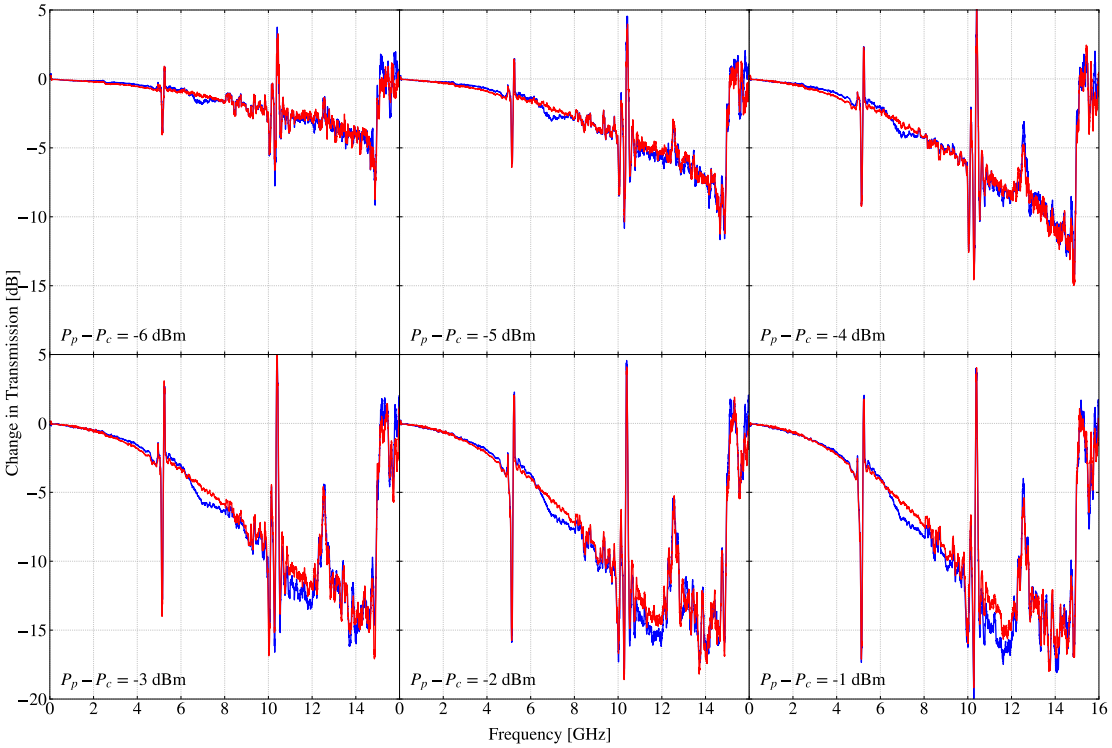

Figure 5.15: $\Delta\,|S_{21}|$ (blue) and $\Delta\,|S_{12}|$ (red) for different pump powers. For each case $f_p = 5\,\mathrm{GHz}$.

frequency shifting of the first band gap to lower frequencies as increasing P_p increases the kinetic inductance of the film. This power-dependent behaviour appears to be consistent with Cooper pair breaking due to the KITWPA device operating in the dissipative non-linear regime, as discussed previously, once again suggesting that this KITWPA design will not achieve the target gain.

Even if our TiN film displays this unexpected Cooper pair breaking that significantly affects the gain performance of our KITWPA devices, we have clearly seen that wave mixing processes are still taking place, hence it may be possible to observe some parametric amplification process taking place underneath the loss mechanisms. This potential parametric gain, $G_{\mathrm{parametric}}$, can be uncovered by using the expression,

$$G_{\mathrm{parametric}} = \Delta|S_{21}| - \Delta|S_{12}|, \tag{5.6}$$

which removes the effects of losses due to Cooper pair breaking from the forward transmission profile, leaving just the parametric effects. This is shown in Fig. 5.17 at $f_p = 5\,\mathrm{GHz}$ for a various P_p values, and clearly shows a small but noticeable D-4WM parametric gain over a bandwidth of approximately 2-6 GHz.

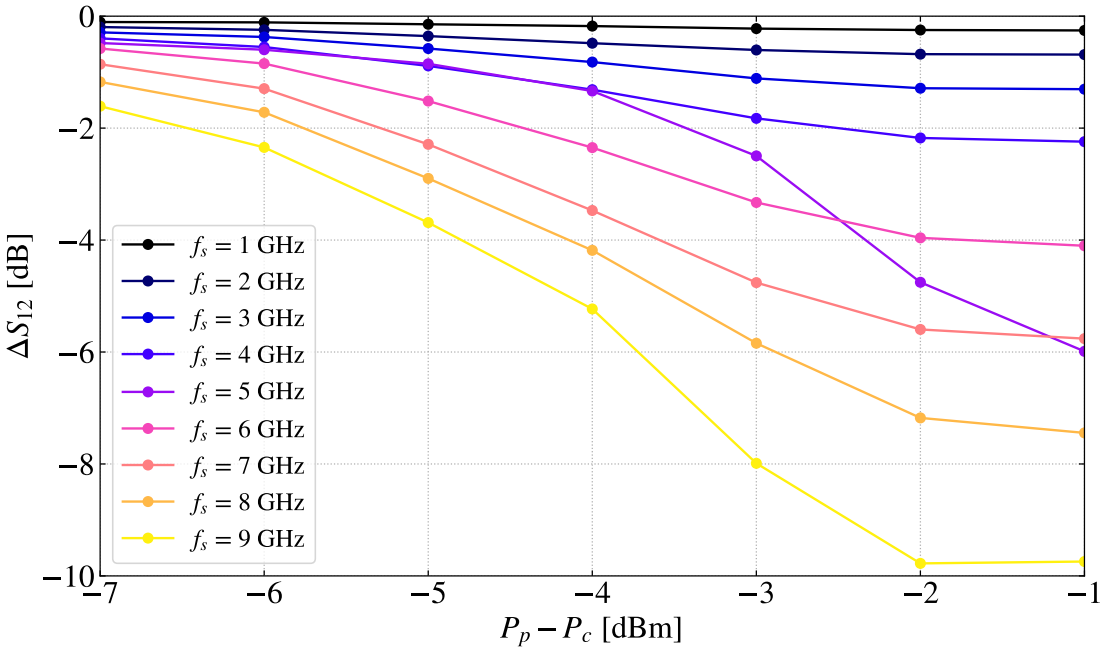

Figure 5.16: $\Delta\,|S_{12}|$ as a function of pump power for different signal frequencies. For each case $f_p = 5\,\text{GHz}$.

At 5 GHz, we clearly see the zero-gain gap, which is commonly seen in D-4WM gain profiles when the pump is placed just to the side of one of the band gaps. From simulations of D-4WM, one would expect the gain profile to be symmetric about this zero-gain gap, however, we clearly observe a large dip in each spectrum around 7 GHz. The likely cause of this dip is parametric up-conversion to $f_u = 2f_p + f_s$, which has not been modelled in our simulations, whereby the signal is converted to a frequency just above the third band gap where the phase-matching condition for this process could be accidentally optimised. The $G_{\text{parametric}}$ performance for this process is very small, with a peak $G_{\text{parametric}} \sim 0.5\,\text{dB}$ observed for $P_p - P_c = -2\,\text{dBm}$, which is far lower than the predicted gain curve showed in Fig. 5.2(b). The most obvious explanation for this discrepancy between the simulated and measured curves is the previously-discussed loss mechanism, meaning the pump power is being dissipated within the KITWPA rather than being transferred to the signal tone. We also notice from these plots that $G_{\text{parametric}}$ generally gets larger as P_p is increased, with the exception of the highest P_p value where $G_{\text{parametric}}$ drops slightly relative to the previous curve. The increase in $G_{\text{parametric}}$ with increased P_p is understandable, as a higher P_p promotes more wave mixing. The decrease at the highest P_p could be caused by the fact that the phase-matching condition for signal amplification at this frequency is no longer optimised or because the pump-induced losses are much

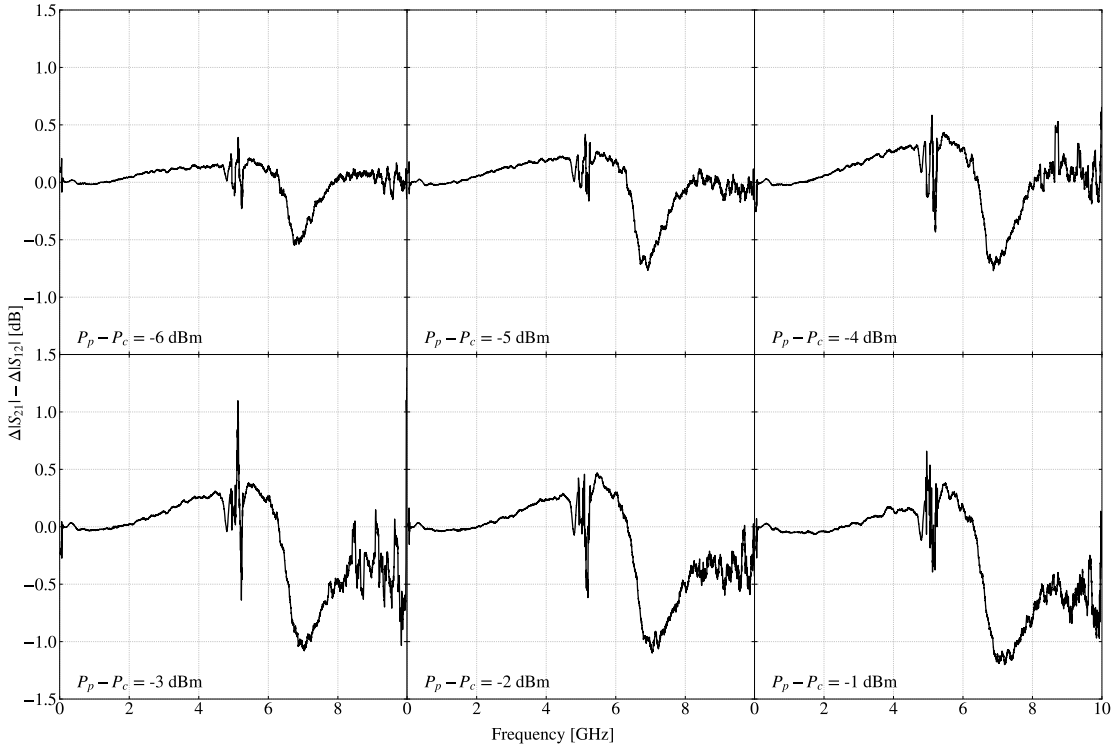

Figure 5.17: $G_{\text{parametric}}$ for different P_p values for $f_p = 5\,\text{GHz}$. The data for both $\Delta\,|S_{21}|$ and $\Delta\,|S_{12}|$ are smoothed every 100 points to more clearly show the underlying behaviour.

higher.

5.4.4 Temperature Variation

The previous section explores the loss mechanisms in our KITWPA devices by probing them with strong RF signals, however, another way to investigate the loss mechanisms is to measure the transmission through the KITWPA devices as a function of bath temperature, T_{Bath}. One such loss mechanism that could be identified through T_{Bath} variation is that caused by two-level system (TLS) losses, which is a quantum mechanical effect that is related to the boundary between different materials. Crucially, as a quantum effect it is strongest at low powers and temperatures, and becomes saturated out at higher powers and temperatures. If TLS was the responsible loss mechanism in our KITWPA device, we would see the transmission increase as T_{Bath} is raised through $0.1T_c$, which for TiN is $\sim 0.4\,\text{K}$, before decreasing again as Cooper pair breaking becomes the dominant loss mechanism. If the loss mechanism is simply due to Cooper pair breaking, however, we would expect the transmission

to decrease as T_{Bath} increases for all $T_{\text{Bath}} < T_c$.

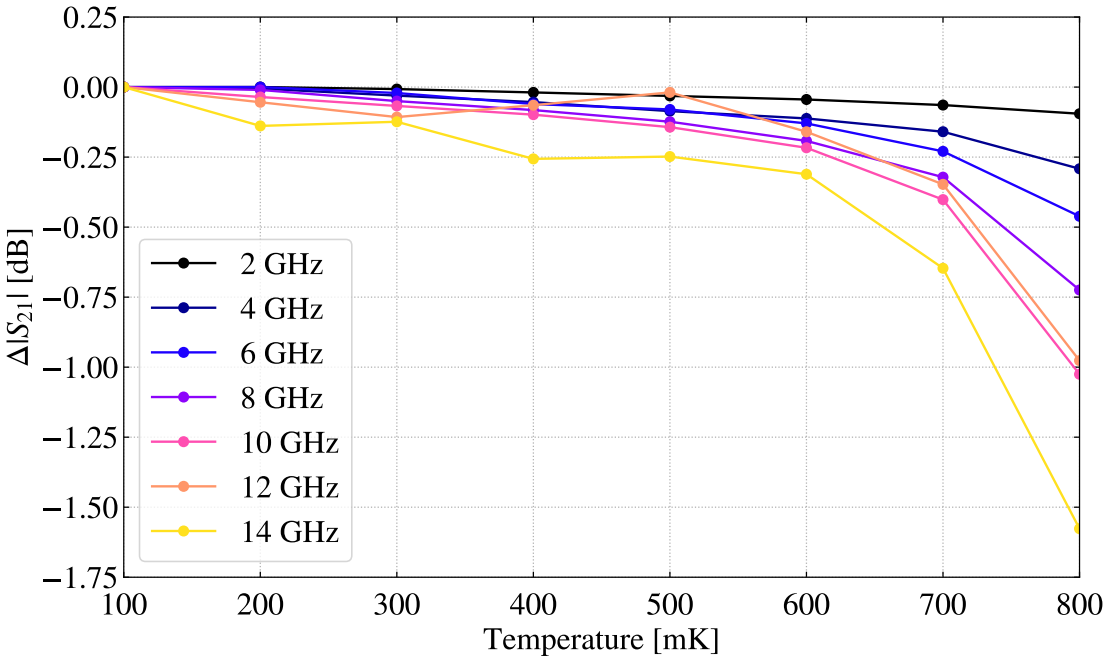

Figure 5.18: $\Delta|S_{21}|$ as a function of temperature for batch 6b device.

Fig. 5.18 shows $\Delta|S_{21}|$ for the batch 6b KITWPA device as a function of T_{Bath} for different f_s values. The graph clearly shows the transmission slowly decreasing as T_{Bath} increases. The results in Fig. 5.18 imply that Cooper pair breaking is the dominant loss mechanism in the KITWPA device and that TLS may only have a very small contribution to the observed losses.

5.4.5 DC-3WM Measurements

The previous sections have investigated the loss mechanisms in our KITWPA devices, with the evidence pointing to the fact that we are operating the KITWPA in a dissipative non-linear regime leading to Cooper pair breaking when the device is operated in its current configuration. From Fig. 5.17, we see that by subtracting the losses from Cooper pair breaking, we can observe some parametric gain, meaning our KITWPA devices do promote wave mixing. From Fig. 5.14, we see that the pump-induced losses exhibit a strange relationship to f_p, with higher f_p values inducing smaller losses, although the origin of this effect is still unclear to us. This relationship, however, suggests that we may be able to find an alternative wave mixing configuration that displays smaller losses and potentially allows us to observe amplification in our KITWPA devices.

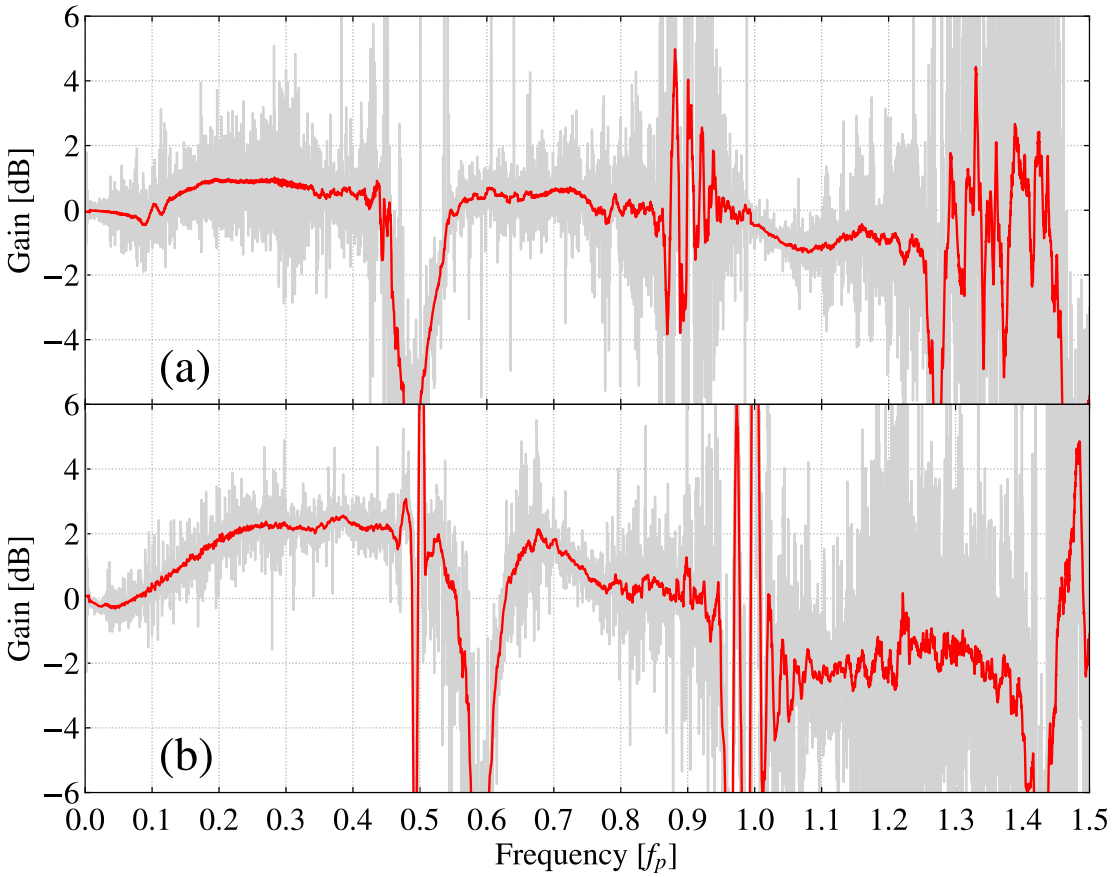

Figure 5.19: (a) DC-3WM gain profile for batch 4 device with $f_p = 8.6\,\text{GHz}$, $P_p = -21.0\,\text{dBm}$, and $I_{DC} = 0.4\,\text{mA}$. (b) DC-3WM gain profile for batch 6b device with $f_p = 10.4\,\text{GHz}$, $P_p = -13.2\,\text{dBm}$, and $I_{DC} = 1.5\,\text{mA}$. In both plots, the devices are pumped just above the second band gap.

The smaller pump-induced loss at higher f_p combined with the low loss DC transmission when biased with a DC current, as shown in Figs. 5.11(a)-(b), means it naturally makes sense to try to operate the KITWPA devices in a DC-3WM mode with f_p set at twice the desired centre frequency of the gain profile. Figs. 5.19(a)-(b) show the gain curves for a chip from both batch 4 and batch 6b, respectively, operating in the DC-3WM mode when pumped just above the second band gap. Remarkably, both devices exhibit a measurable gain, with the batch 4 device having a smoothed gain peak at approximately 1 dB, and the batch 6b device having a smoothed gain peak at approximately 2.5 dB. Pumping at the second band gap brings the central frequency of the gain profile to roughly the first band gap, which is the same as for the original design. By normalising the signal frequency for each device by f_p, as with Figs. 5.12(a)-(b), and plotting both gain curves against this normalised frequency, we observe a remarkable consistency in the behaviour of the

two KITWPA devices, with only a slight discrepancy in the normalised frequency positions of the various features in the curve, which is due to the f_p in the batch 6b device being slightly closer to the band gap than for the batch 4 device. The discrepancy between the gain amplitudes for each device can be explained by the fact that the batch 4 device has a slightly lower $\frac{I_c}{I_*}$ ratio than the batch 6b device, as well as that its characteristic impedance has deviated further from $50\,\Omega$, which is indicated by the much larger gain ripples present in the raw data for the batch 4 device.

Interestingly, both gain curves are asymmetric about their central frequencies, with each having a significant deamplification band just above the first gap. This deamplification is indicative of a parasitic frequency conversion process, such as $f_p + f_s$, taking place, which converts the signal to a frequency just above the third gap, where the phase-matching condition for this process is unintentionally satisfied. This is especially interesting, as for the batch 6b device, the deamplification band is at almost the identical frequency to that in the D-4WM profiles in Fig. 5.17. Looking closely, we can see that it is the same frequency conversion process taking place in each wave mixing regime, with the signal being converted from just above the first band gap to a frequency near the third band gap.

The previous analysis demonstrates how despite that fact that our KITWPA designs are severely limited by Cooper pair breaking losses, we can still observe gain in them by changing the operating regime. This analysis can be extended further by placing f_p at higher band gaps, as not only would this increase the bandwidth of the KITWPA, but it may also lead to higher gain as the effective electrical length of the KITWPA becomes longer at higher frequencies. Figs. 5.20(a)-(b) show the gain curves normalised by f_p for the batch 4 and batch 6b devices, respectively, this time pumped just above the third gap. Once again, both devices exhibit a parametric gain, with the batch 4 device having a peak average gain of approximately 2 dB, and the batch 6b device having a peak average gain of approximately 5 dB.

Aside from the difference in peak average gain, the two plots are again noticeably similar in shape, with dips at roughly $0.3f_p$ and $0.6f_p$, which are caused by presence of the first and second band gaps in the transmission spectrum, respectively. We additionally notice a pair of dips at roughly $0.4f_p$ and $0.7f_p$, which occur when a signal propagating at these frequencies generates an idler, $f_i = f_p - f_s$, that falls into or close to one of the two band gaps at $0.3f_p$ and $0.6f_p$, which suppresses any gain at those frequencies.

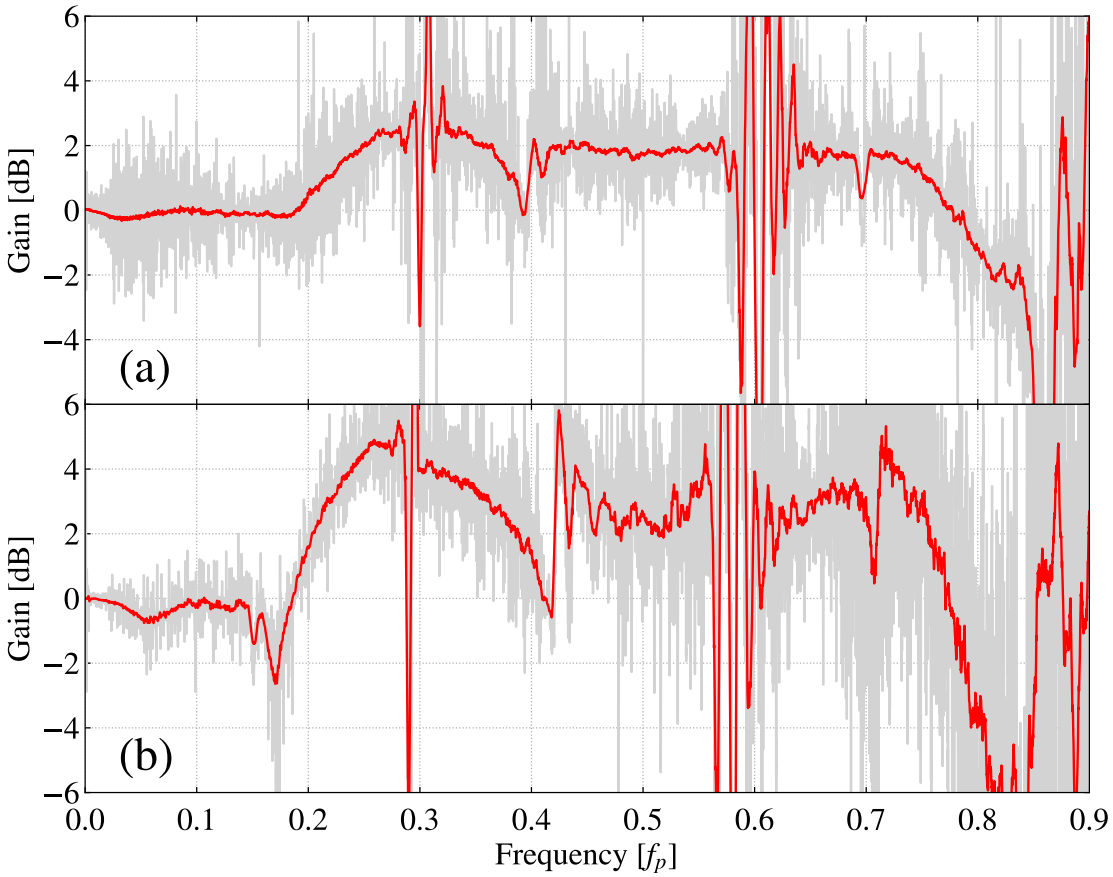

Figure 5.20: (a) DC-3WM gain profile for batch 4 device with $f_p = 12.7\,\text{GHz}$, $P_p = -21.0\,\text{dBm}$, and $I_{DC} = 0.63\,\text{mA}$. (b) DC-3WM gain profile for batch 6b device with $f_p = 17.7\,\text{GHz}$, $P_p = -10.0\,\text{dBm}$, and $I_{DC} = 1.53\,\text{mA}$. In both plots, the devices are pumped just above the third band gap.

We can see by comparing Figs. 5.19(a)-(b) and Figs. 5.20(a)-(b), that pumping the KITWPA devices at the third gap results in a flatter and more symmetric gain profile, without any significant up-conversion. The reason for this is that when pumping at the second gap, any up-conversion will be placed near the third gap, which is very large as it is created by the primary periodic loading sections. This means it will create a stronger phase shift, which will phase match the up-conversion process when pumped at the second gap. When pumping at the third gap, however, any up-conversion will be to a frequency located around the forth and fifth band gaps, which are generally much smaller than the third gap, hence will provide only a small phase shift that will not phase-match the up-conversion process. Nevertheless, I should note that this up-conversion effect is currently being investigated by other members of my research group and we are yet to arrive at a concrete conclusion at the time of writing this thesis.

The gain curves in Figs. 5.19(a)-(b) use the parametric gain definition of $G_{\text{para}}^{(Pump,DC)}$ as described in (4.3), however, this does not factor out the RF-induced losses as previously discussed. One way of removing the effects of the RF losses without requiring a separate measurement of $|S_{12}|$ is to use a different definition of the gain, such as $G_{\text{para}}^{(DC)}$ in (4.5). By measuring the change in transmission when the DC is switched off then on, whilst keeping the pump on, we can remove the effects of the pump-induced losses, and just observe the extent of the parametric gain. Figs. 5.21(a)-(c) plot the three different definitions of the parametric gain from (4.3)-(4.5), respectively, for the batch 6b device when pumped around the second band gap in the same configuration as in Fig. 5.19(b). We notice that all the gain curves are actually very similar, which makes sense as our RF losses when pumping at this frequency are relatively small, hence the observation of gain. Additionally, in Fig. 5.21(b), where the parametric gain definition is $G_{\text{para}}^{(Pump)}$ from (4.4), we notice that the ripples in the gain profile are much smaller when compared to the other two definitions. This is because in this KITWPA configuration, I_{DC} is larger than I_p, meaning that switching the DC on has a much greater effect on the kinetic inductance and, hence, the impedance than switching on the pump tone does. Using this definition where the DC is already on, therefore, has only a limited effect on the impedance, hence the ripples are smaller.

As stated previously, it is expected that wave mixing only occurs when the pump and signal tones are propagating along the KITWPA in the same direction, meaning that any directionally-independent losses can be factored out by measuring the reverse transmission when the pump and DC are applied. In Figs. 5.22(a)-(b), I have plotted the forward and reverse 'gain' for the batch 6b chip when pumped above the second gap and the third gap. In the second of the two plots, where the device is pumped at the third gap, the device behaves as expected, with a clear gain in the forward direction and only a small loss in the reverse direction. If we compare this to the first plot, however, we see that the reverse gain displays the same overall shape as the forward gain, although the peak amplification and deamplification values are smaller in the reverse direction than the forward direction.

There are two likely reasons as to why we observe a gain in the reverse direction. The most obvious reason is that this is a real back-amplification as described in [76], whereby the phase-matching condition for back-amplification is serendipitously achieved for this particular pump frequency and power. The other possibility is that a significant fraction of the pump power that arrives at the end of the KITWPA device is reflected back along the device and subsequently co-propagates with the

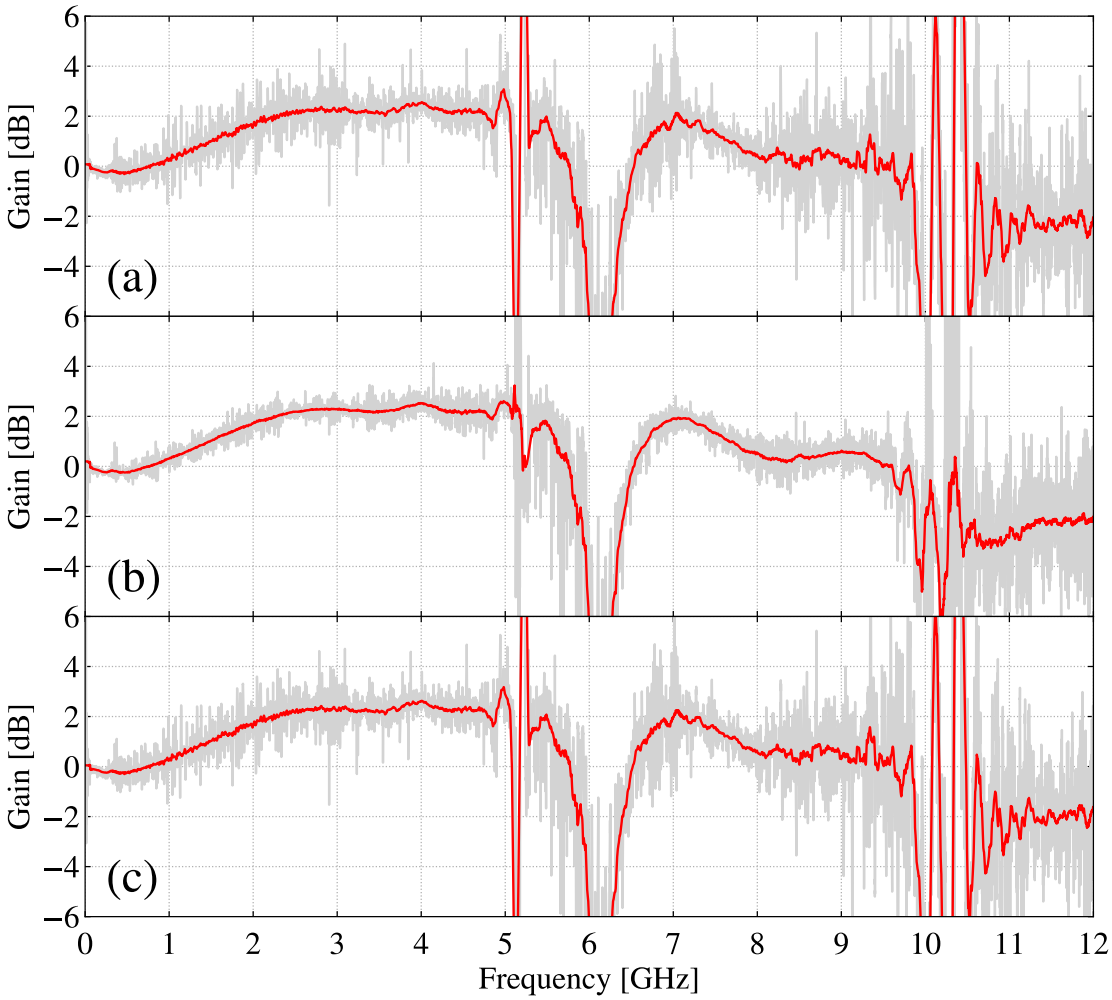

Figure 5.21: DC-3WM gain profile for batch 6b device when pumped just above the second band gap for, $f_p = 10.4\,\text{GHz}$, $P_p = -13.2\,\text{dBm}$, and $I_{DC} = 1.5\,\text{mA}$ using the gain defintions discussed in (4.3)-(4.5). (a) $G_{\text{para}}^{(Pump,DC)}$, (b) $G_{\text{para}}^{(Pump)}$, (c) $G_{\text{para}}^{(DC)}$. For each plot, the raw data is in light grey and the smoothed data is in red.

signal tone, leading to a backward amplification. This reflection mode is dependent on the frequency, as evident by the ripple in the gain profiles. This could explain why the configuration in Fig. 5.22(b) does not display reverse gain, as f_p may be located at $|S_{21}| = 0\,\text{dB}$ at the far end of the line.

5.5 Summary

In this chapter, I have explored and experimentally characterised the behaviour of a limited number of TiN KITWPA devices available to me at cryogenic temper-

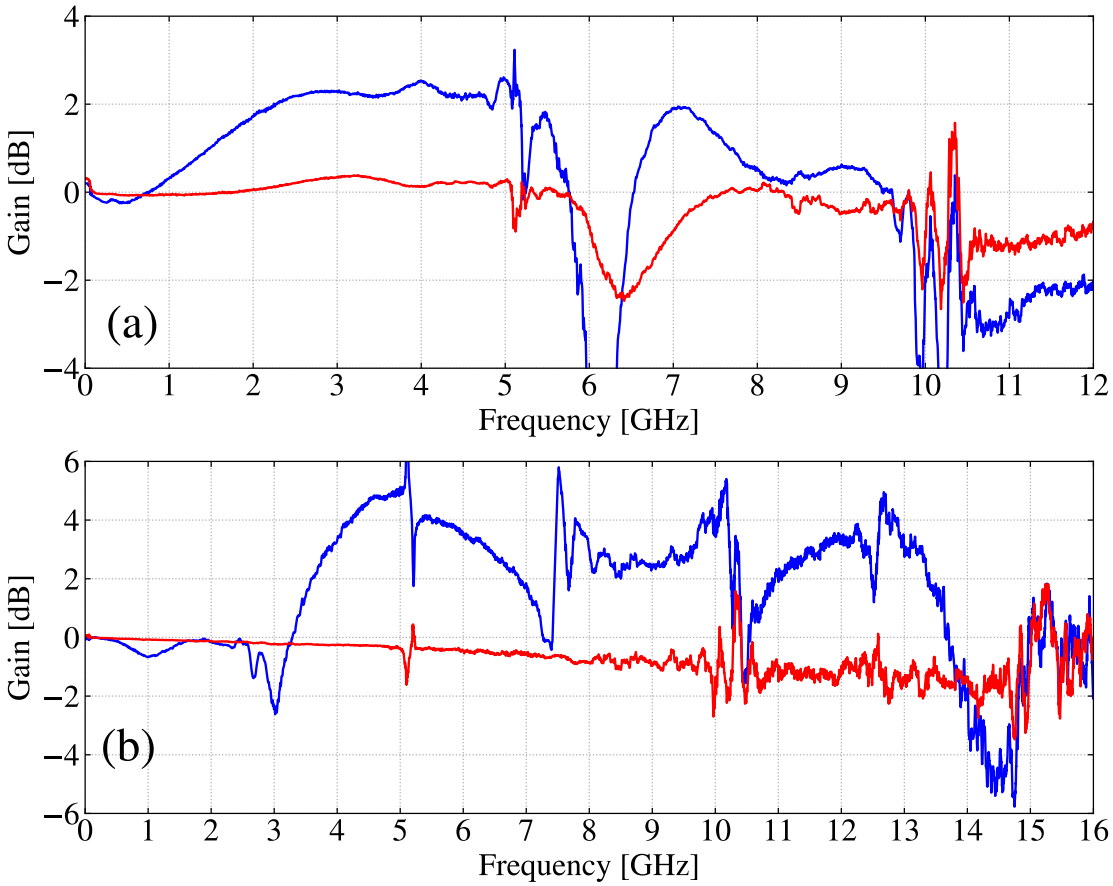

Figure 5.22: DC-3WM gain profiles of the batch 6b device when the pump and signal are co-propagating (blue) and when they are anti-propagating (red) when pumped just above (a) the second band gap and (b) the third band gap.

atures. The initial characterisation of the TiN test structures revealed that the superconducting film demonstrated the required lossless, non-linear behaviour for KITWPA operation, however, subsequent characterisation of the actual KITWPA devices revealed significant losses when trying to operate them as amplifiers as originally designed. It was found that operating the devices in a DC-3WM regime, rather than the design D-4WM regime, however, was able to produce signal amplification, with a peak smoothed gain of 5 dB being achieved, although this is still much smaller than the original expected design value.

It appears from the measured results that there are two distinct superconducting regimes; one at low signal powers where the resistive part of the superconducting film is much smaller than predicted by BCS theory, and one at higher powers where the film displays the losses predicted by BCS theory, with the boundary described by P_{lossless}. This could be explained by the presence of distinct non-linearity mech-

anisms such as those discussed in [129], where the authors discuss two non-linearity mechanisms that are commonly observed in superconductors; a reactive *equilibrium supercurrent non-linearity* and a dissipative *non-equilibrium heating non-linearity*, which emerges in the presence of a strong RF current and is associated with sub-gap Cooper pair breaking. It could be that the pump powers required to produce the desired gain for this KITWPA design mean that the KITWPA will be operating in the dissipative non-linear regime, meaning that it is unlikely work as a KITWPA, even if the device yield is substantially improved. This dissipative behaviour may simply be due to the design of the device, however, and the film itself may still be used to create a successful KITWPA if care is taken to ensure it is operating in the lossless, non-BCS regime.

If we look at the measured transmission data for the different film resistivities in Fig. 5.8, we see that the films with higher resistivities are those whose transmission spectra deviate furthest from that predicted by BCS theory, suggesting that these would be better candidates for KITWPA applications as these can simultaneously achieve a higher L_k with the same R_s, in contrary to what we concluded in Chap. 3. If this is true, then there may be other ways in which we could also increase L_k whilst maintaining a small R_s, such as making the superconducting film thinner or making the dimensions of the transmission line smaller. If we look at the successful KITWPA devices reported in the literature, we in fact notice that all of them use superconducting films thinner than the 100 nm we have used here, and most of them use finer transmission line dimensions, some down to several hundred nanometres [82], which is an order of magnitude smaller than the dimensions of our KITWPA design. Whilst the minimum transmission line dimensions of our KITWPA design are limited by our current fabrication capabilities, we have more flexibility in the choice of film thickness, with the 100 nm thickness being based on the analysis in Chap. 3. In subsequent design variations, therefore, I would suggest to reduce the thickness of the TiN film and experimentally characterise the effect this has on performance of the KITWPA. If this extends the lossless, non-linear regime, i.e. higher P_{lossless}, it would confirm the above hypothesis that our previous KITWPA design was simply operating in the wrong regime, meaning that TiN may still be suitable for KITWPA operation. If this is confirmed, then it would be important to upgrade our fabrication capabilities to include E-beam lithography for finer transmission line patterning, allowing us to potentially further enhance the lossless, non-linear regime, as well as allowing for more compact devices.

Of course, a more fundamental obstacle to successful KITWPA operation could be the choice of superconducting material. Virtually all of the successful KITWPAs reported in the literature are fabricated from NbTiN, however, our use of TiN over NbTiN was again motivated by our current fabrication capabilities. Furthermore, from the EM analysis presented in Chap. 3 using standard BCS theory, we did not find any significant difference between NbTiN and TiN, provided the film thickness was appropriately engineered. Whilst there is a regime where TiN displays lossless non-linearity, it may be the case that this regime occurs at a pump power level that is too low for practical KITWPA operation. To investigate this possibility, I suggest recreating the KITWPA design presented here but replace the TiN with NbTiN to explore what effect material choice has on the KITWPA performance and whether we draw the same conclusions as those in Chap. 3.

Another issue that requires addressing is that of the gain ripples. Focusing on the raw (not smoothed) transmission curves in Fig. 5.8 and the raw gain curves in Figs. 5.12, 5.19, and 5.20, we see that all of them have a great deal of structure, with huge variations in the gain profile as a function of frequency; in some cases $> \pm 10\,\mathrm{dB}$. These large ripples are observed in most KITWPAs reported in the literature and are perhaps the biggest issue facing KITWPA performance, as the shear size of the ripples renders the KITWPA devices essentially useless. Whilst the true source of these ripples is still currently under investigation, there a several possible reasons for their presence. The first of these is reflections of the signal tone due to an impedance mismatch at the ends of the KITWPA transmission lines. As shown in Tab. 5.2, the variation in the TiN film resitivity between batches leads to a substantial increase in the characteristic impedance of the CPW line from the desired $50\,\Omega$, leading to a substantial impedance mismatch at the ends of the lines. This hypothesis as the possible source of the gain ripples is supported by the transmission profiles in Fig. 5.8, where the amplitude of the ripples appears to be much larger for the devices with the largest ρ_N, hence the largest impedance mismatch. The extremely long electrical length of the KITWPA transmission lines means that any ripples in the gain profile will be packed very closely together. This is in contrast to equivalent narrow-band parametric amplifiers, as discussed previously in § 2.1, which, due to their much smaller size, will exhibit gain variation on a much larger frequency scale beyond their operational bandwidths, hence they do not show this rippling effect in their narrow gain profiles. If an impedance mismatch at the ends of the line is the source of the ripples, then the solution to this would be to carefully engineer the impedance of the line such that it exactly matches to $50\,\Omega$ during operation.

Another mechanism by which an impedance mismatch could create ripples in the gain profile is due to backward amplification from a reflected signal and pump tone [119]. Fig. 5.22(a) shows that we do indeed observe a backward gain under certain conditions, which we surmise to arise from reflections of the pump tone at the ends of the KITWPA. From the discussion in [119], we see that for a loop gain larger than 0 dB, the KITWPA amplification becomes unstable, leading to oscillations. When the loop gain is less than 0 dB but non-negligible, then the backward amplification due to reflections can lead to unwanted interference in the form of ripples in the gain profile. The onset of these ripples is determined by the amplitude of the incoming pump tone, hence if the ripples are caused by this backward gain mechanism, there exists a limit on the maximum pump power that be applied to the KITWPA. Careful KITWPA design is, therefore, required to ensure that the pump level required to give the desired gain also produces a negligible loop gain.

An alternative source of the gain ripples could be the periodic loading structure of the KITWPA transmission line. From Fig. 3.16(a), we see that in addition to the band gaps, the period loadings create a 'ringing' effect next to the band gaps, i.e., ripples. Whilst these ripples appear to be rather small in the simulated spectra compared to the measured spectra, this could be simply due to the fact that we have underestimated the strength of the ripples in our simulations. Again, this would explain why we do not see gain ripples in the narrow band parametric amplifiers, as these devices do not have periodic loading structures. If this 'ringing' effect is the source of the ripples, then it would suggest that the standard periodic loading technique is fundamentally flawed, necessitating a completely different phase matching technique that does not cause this 'ringing' effect in the transmission profiles.

To summarise, the effects of film thickness and material choice are the only aspects that I have not yet had the chance to experimentally explore due to time limitations. Of course, this does not rule out the fact that there may be other aspects that we have not presently considered, however, we suspect the above aspects could have a high chance of success in producing a well-functioning TiN KITWPA with high gain.

Chapter 6

Advanced TWPAs

6.1 Introduction

In this chapter we present some advanced TWPA concepts, which are designs and configurations that exist separately from the main body of research presented in this thesis, which we did not have time to fully characterise experimentally. The chapter is divided into two parts. The first part presents the concept of a dual-pump KITWPA, which we argue to be a viable technique to produce a broadband amplifier at mm/sub-mm frequencies. The second part presents the concept of a balanced TWPA; a novel parallel TWPA architecture, which we show to be able to solve some of the major obstacles to widespread TWPA implementation. For each part, we present the concept, justification, and simulation results. Note that both concepts presented in this chapter are not restricted to KITWPAs, and can be applied to both JTWPAs and SQUID-TWPAs.

6.2 Dual-Pump TWPA

As previously stated, the operation of a KITWPA in the D-4WM regime leads to the creation of a large zero-gain gap in the centre of the gain profile where the peak gain is normally located, hence reducing the operational bandwidth of the device. This has been mitigated in designs operating in the DC-3WM regime as this allows the gap to be tuned away from the amplification band, however, the required DC bias leads to a more complicated experimental setup and potentially to unwanted

heat leak in the cryogenic environment. Additionally, operation with a DC bias becomes challenging at higher frequencies.

In this section, we present the concept of a KITWPA operating in the ND-4WM regime using the generalised CME formulation presented in (2.28a)-(2.28d), whereby the injection of two pump tones along with a detected signal results in a broad, flat gain profile that removes the zero-gain gap and eliminates the need for a DC bias and the complexities associated with it. This wave mixing regime has previously been experimentally verified using JTWPAs [130, 131] and in the optical regime [132, 133] but not in KITWPAs, which have several different aspects that must be considered when operating in the ND-4WM mode. We demonstrate how a ND-4WM regime is feasible to achieve broadband amplification at a range of frequencies, first at microwave frequency ranges where most KITWPAs reported to-date have been successfully experimentally characterised, before extending to mm bands to illustrate how we can use this technique to design a front-end pre-amplifier that covers the Atacama Large Millimetre/sub-millimetre Array (ALMA) Bands 2–5 range.

6.2.1 Design Considerations

In § 2.5, we have shown that our generalised ND-4WM CMEs can be reduced to special cases, which involve the use of only a single pump tone with or without DC current, where most of the reported KITWPAs operate [21, 68, 74]. In this section, we present the realistic design of a ND-4WM KITWPA that has yet to be considered before. We make use of a design centred at 9 GHz as an example here.

To illustrate the advantages of utilising a ND-4WM KITWPA, we compare the behaviour of the ND-4WM design to a standard D-4WM KITWPA, including some additional design considerations. As stated in § 2.7, the non-linearity of the transmission line forming the KITWPA naturally leads to a phase-mismatch between the various propagating tones that needs correcting in order to maximise the gain. Furthermore, harmonics of the pump tone are also generated in the non-linear medium, which require suppression in order to prevent shock-wave formation. Both of these effects exist in a TWPA regardless of the operational mode i.e., D-4WM or DC-3WM, however, from § 2.7, we demonstrate that they can be mitigated via dispersion engineering.

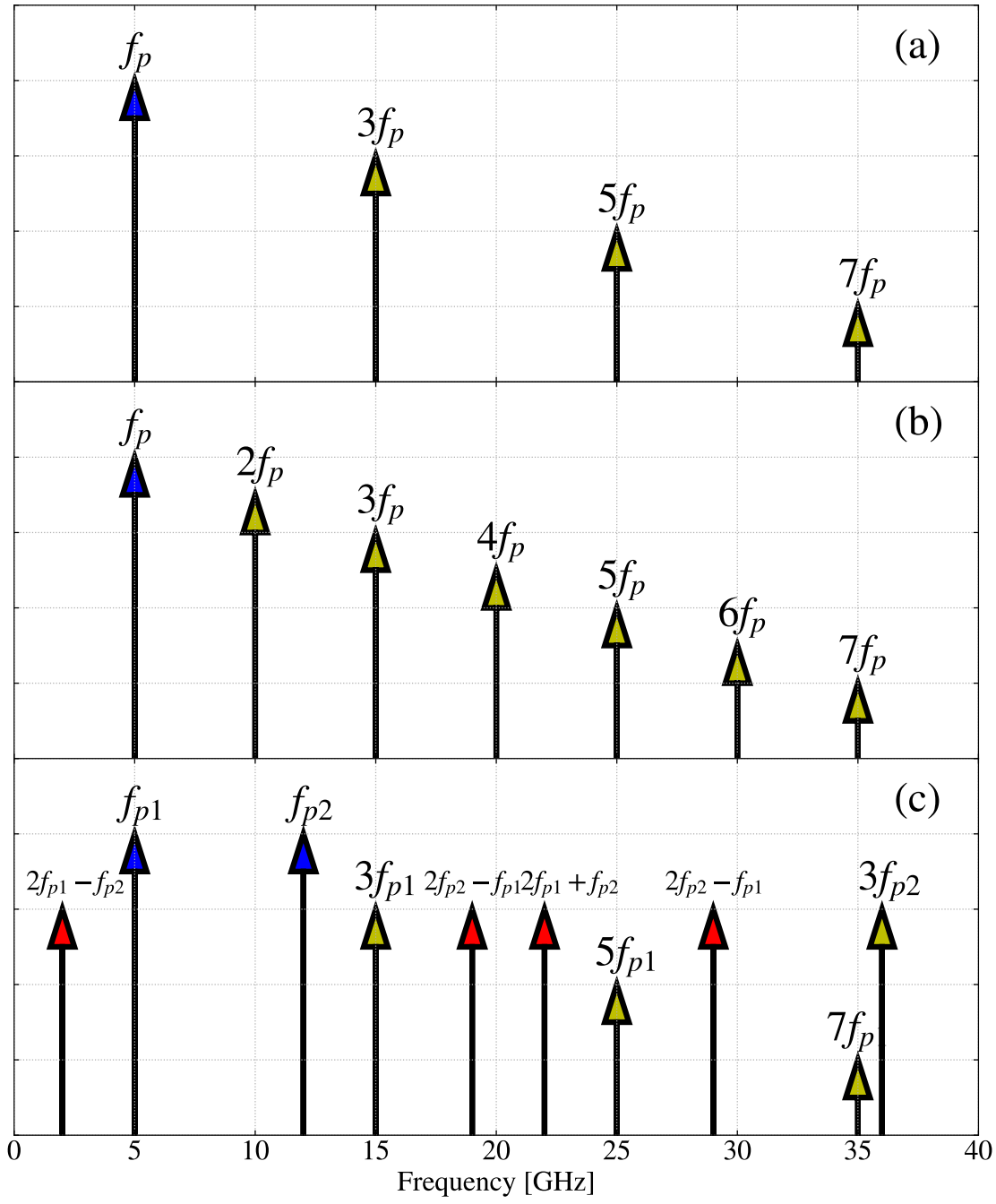

Figure 6.1: Pump harmonic comparison between (a) D-4WM, (b) DC-3WM, and (c) ND-4WM. The blue arrows indicate the pump tones, the yellow arrows indicate the harmonics of the pump tones and the red arrows indicate the cross-harmonics between the pump tones in ND-4WM.

The same would be required for a ND-4WM KITWPA, however, there are a few more subtleties, which need to be taken into account to ensure proper operation with two pump tones. Figs. 6.1(a)-(b) compare the primary pump harmonics gen-

erated for D-4WM, DC-3WM, and ND-4WM devices in the absence of dispersion engineering. For D-4WM in Fig. 6.1(a), a strong third harmonic of the pump tone is generated due to the Kerr-3 non-linearity of the superconducting transmission line, which is followed by further, subsequent odd harmonics of the pump tone. This is similar in the case of DC-3WM in Fig. 6.1(b), except now odd and even harmonics are both generated in this operational mode. For the ND-4WM case illustrated in Fig. 6.1(c), we see that the two pump tones both create odd harmonics of themselves, with the added complexity coming from the numerous cross-terms generated by the two pumps interacting with each other. In D-4WM, suppressing the third harmonic is sufficient to suppress all further harmonics and to prevent shock-wave formation, which can easily be achieved by introducing a band gap at $3f_p$. For the ND-4WM case, however, this becomes extremely difficult as there are now many harmonics and cross-terms that are not placed periodically.

6.2.1.1 Harmonics Suppression

Although Fig. 6.1(c) shows that the pump harmonics are positioned irregularly in the ND-4WM mode, there are indeed cases where they can be lined up periodically, with the harmonic suppression mechanism being made easier by utilising the standard periodic loading technique. Consider the case where we inject the two pump tones into the KITWPA with the second pump having (nearly) exactly double the frequency of the first pump tone i.e., $2f_{p_1} \approx f_{p_2}$ as example. Tab. 6.1 summarises the first few generated harmonics when the two pump tones are injected into a KITWPA with $f_{p_1} = 6\,\text{GHz}$ and $f_{p_2} = 12\,\text{GHz}$. We notice that in this case, the harmonics are in fact all generated at integer multiples of 6 GHz, which provides us with a convenient solution i.e., we can engineer our periodic loading structures to create band gaps in the transmission profile at integer multiples of 6 GHz. Placing the two pump tones on the edge of the first and second band gaps, respectively, will result in them acquiring the additional phase shift required for phase matching, while the harmonics of the pump tones will be attenuated by the larger subsequent band gaps at 18, 24, 30, 36 GHz etc.

To demonstrate the feasibility of this configuration, here we present a 6–12 GHz design of the ND-4WM KITWPA simulated using the procedure described in Chap. 3. Fig. 6.2 shows a drawing of the KITWPA design, which comprises an IMS line comprising 550 unit cells to give a total transmission line length of 42 mm. The 250 nm wide IMS is formed with a wiring layer of 35 nm NbTiN (normal-state resistivity,

Term	Frequency [GHz]
f_{p1}	6
f_{p2}	12
$2f_{p1} - f_{p2}$	0
$2f_{p2} - f_{p1}$	18
$3f_{p1}$	18
$2f_{p1} + f_{p2}$	24
$2f_{p2} + f_{p1}$	30
$3f_{p2}$	36

Table 6.1: Frequencies of the pump tones and their harmonics for ND-4WM in the case where $f_{p_1} = 6\,\text{GHz}$ and $f_{p_2} = 12\,\text{GHz}$.

$\rho_\text{N} = 200\,\mu\Omega\,\text{cm}$ and critical temperature, $T_c = 15\,\text{K}$), which is deposited onto a 675 µm thick high-resistivity silicon substrate. The wiring layer is then covered by a 100 nm-thick amorphous silicon (a-Si) dielectric, topped by another 200 nm Nb sky-plane[1].

To achieve a 50 Ω transmission line, the conducting strip of the IMS is shunted with additional stubs, which increase the capacitance per unit length to balance the high kinetic inductance of the NbTiN film. To create the desired band gaps, periodic loadings sections are created by altering the characteristic impedance of the transmission line by changing the length of the shunted stubs as shown in the inset of Fig. 6.2. The physical dimensions of the transmission line making up the KITWPA are summarised in Tab. 6.2.

Fig. 6.3 shows the simulated $|S_{21}|$ transmission spectrum for the 6–12 GHz ND-4WM device showing the band gaps at integer multiples of ∼6 GHz, as generated by the periodic loadings. With the placement of $f_{p_1} = 6.148\,\text{GHz}$ and $f_{p_2} = 12.291\,\text{GHz}$ on the leading edges of the first and second band gaps, respectively, we show that the pump harmonics and their cross-terms would fall into the subsequent band gaps at higher frequencies. Note that the $|S_{21}|$ spectrum presented here was simulated using the realistic modelling technique described in Chap. 3, and has shown to be able to accurately predict the measured performance of KITWPAs when the surface resistance is calibrated to be less than 5% of the BCS prediction [134]. Fig. 6.4(a) shows the gain-bandwidth profile for the KITWPA that was calculated

[1]In contrast with the previous chapter, we now assume the use of NbTiN with a much narrower line width for reasons described in Chap. 5, which we believe should have a higher chance of success.

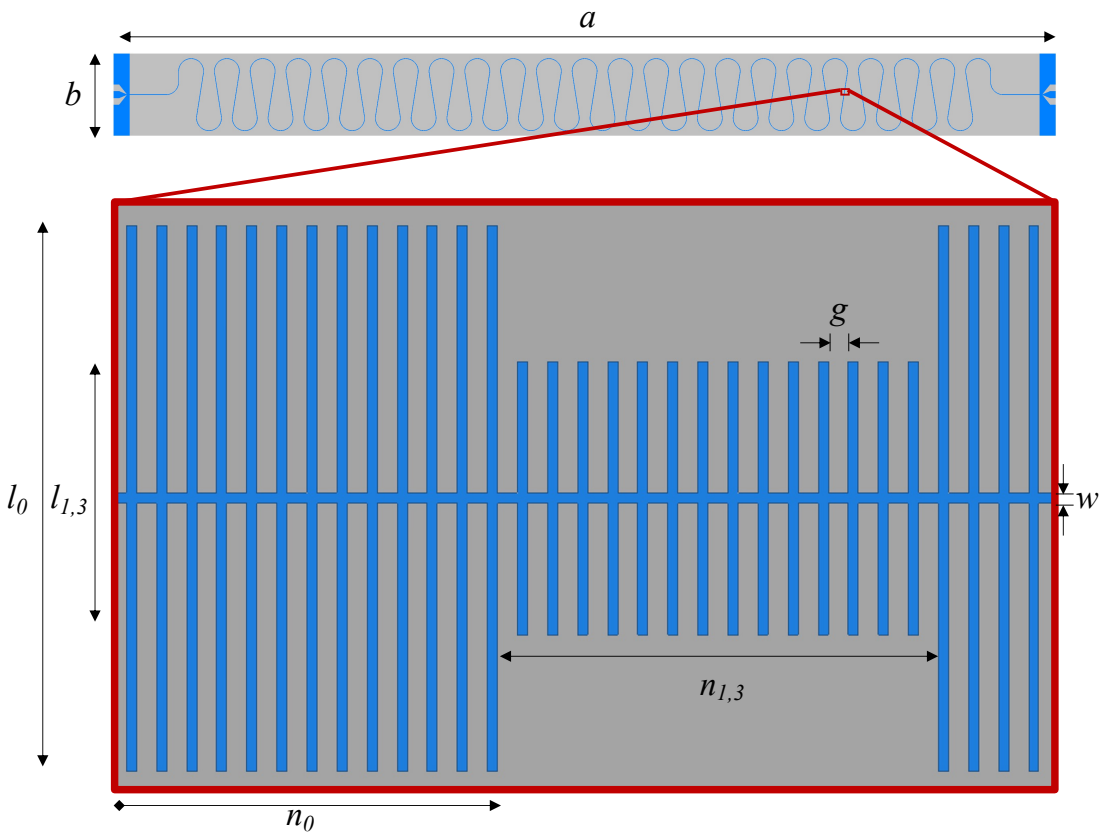

Figure 6.2: Layout of the 6–12 GHz KITWPA design drawn using the techniques described in § 4.2, showing the wiring layer (blue) of the inverted microstrip, which is wound into a 'hairpin' pattern to fit the design onto a compact configuration. The substrate is shown in grey and the dielectric and sky planes are not shown for clarity. The inset highlights the periodic loading structure of the transmission line.

by numerically solving the CMEs in (2.28a)-(2.28d), and demonstrates a gain greater than 20 dB over the frequency band from 6–12 GHz with the pump currents set at $I_{p_1} = I_{p_2} = 0.078 I_*$.

Comparing this gain curve to an equivalent D-4WM KITWPA operating in the same frequency range, we can see a number of improvements in the ND-4WM curve. First, the gain of the ND-4WM KITWPA remains roughly constant over the targeted band, which is in stark contrast to the D-4WM gain curve where the gain rolls off severely towards the edges of the band i.e., the target gain of 20 dB is only achieved for a very small region towards the centre of the gain profile. Second, operating in the ND-4WM regime also eliminates the central zero-gain region in the D-4WM gain curve. Additionally, the ND-4WM device can also be operated in the D-4WM mode, as shown in Fig. 6.4(b), allowing the bandwidth to be extended below 6 GHz

Description	Parameter	Value
Chip length	a	34.65 mm
Chip width	b	3.0 mm
Microstrip width	w	250 nm
Stub gap	g	500 nm
Stub length (50 Ω)	l_0	13.0 µm
Stub length (1st loading)	l_1	8.8 µm
Stub length (3rd loading)	l_3	6.4 µm
No. of stubs (50 Ω section)	n_0	82
No. of stubs (1st loading)	n_1	10
No. of stubs (3rd loading)	n_3	10
Total no. of cells	n_{tot}	550

Table 6.2: Summary of physical design parameters for the 6–12 GHz ND-4WM KITWPA.

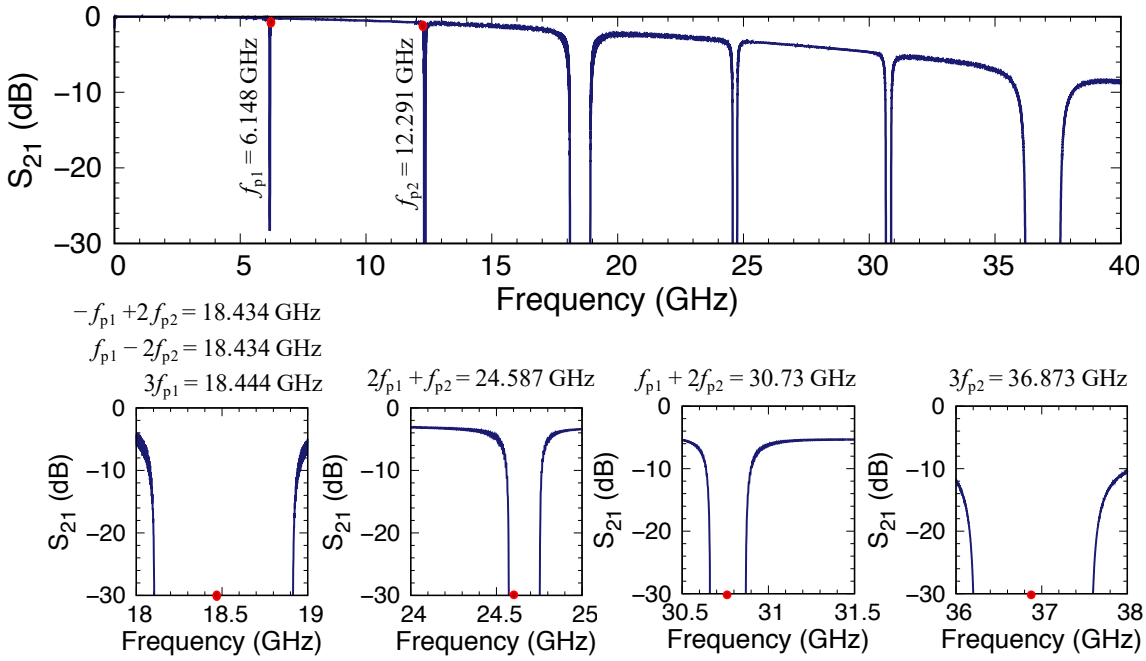

Figure 6.3: Transmission spectrum of the 6–12 GHz ND-4WM KITWPA, highlighting the positions of the pump tones and the generated harmonics, which can be suppressed by the engineered higher frequency stopbands.

and above 12 GHz.

A further advantage of this dual-pump configuration is the possibility to substantially widen the bandwidth by re-configuring the frequencies of the pump tones.

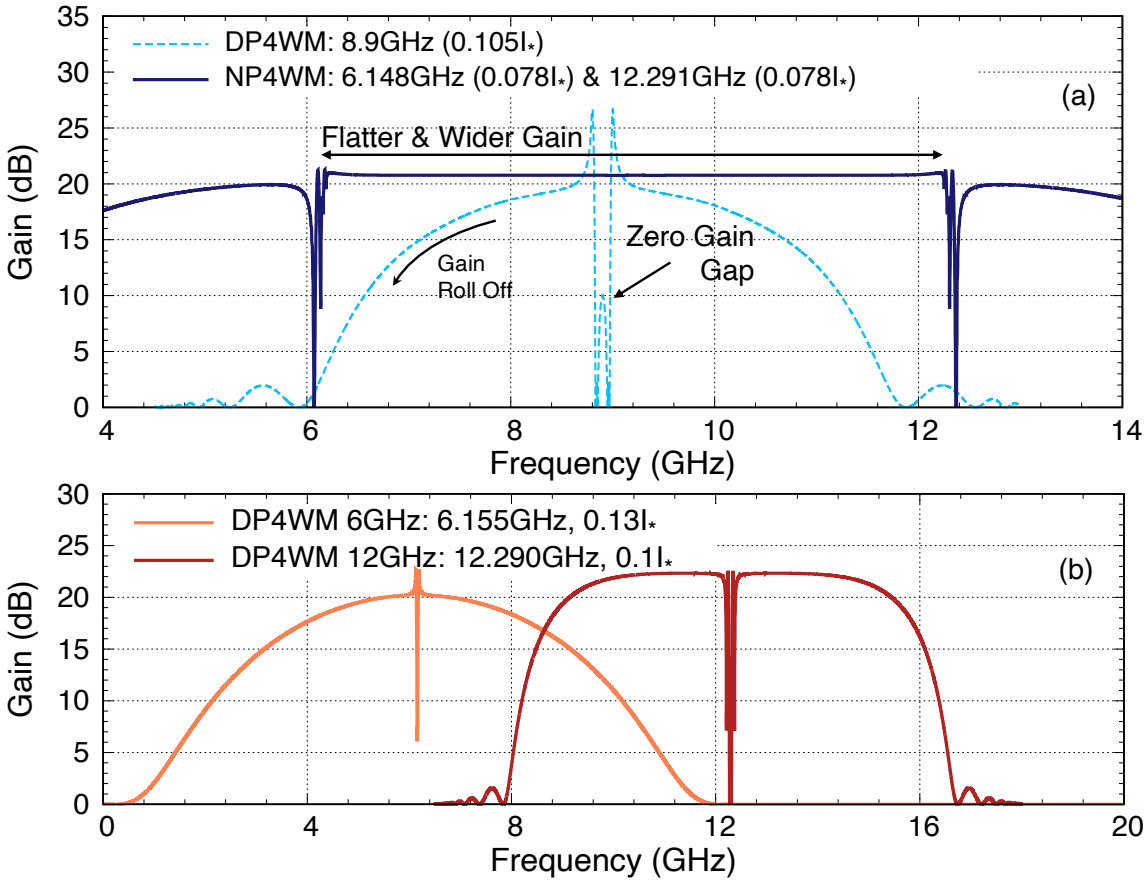

Figure 6.4: (a) Gain-bandwidth profile for a KITWPA operating in the ND-4WM regime (dark blue) highlighting the broad, flat gain profile compared to a D-4WM KITWPA (light blue) operating in the same frequency range. (b) D-4WM gain-bandwidth profiles for the 6–12 GHz KITWPA design, highlighting how this design is not restricted to operation in the ND-4WM mode.

As the periodic loading creates band gaps at integer multiples of ∼6 GHz, we can place the pump tones on the edges of different band gaps to operate our KITWPA over different frequency bands. This is demonstrated in Fig. 6.5 where we show how the pump frequencies can be adjusted to produce an enormous 6–34 GHz tunable bandwidth KITWPA using exactly the same design as presented Fig. 6.2, emphasising the flexibility of the ND-4WM KITWPA design. This is similar to the D-4WM mode, except the ND-4WM has a larger bandwidth coverage due to the different tunable bands being much closer together.

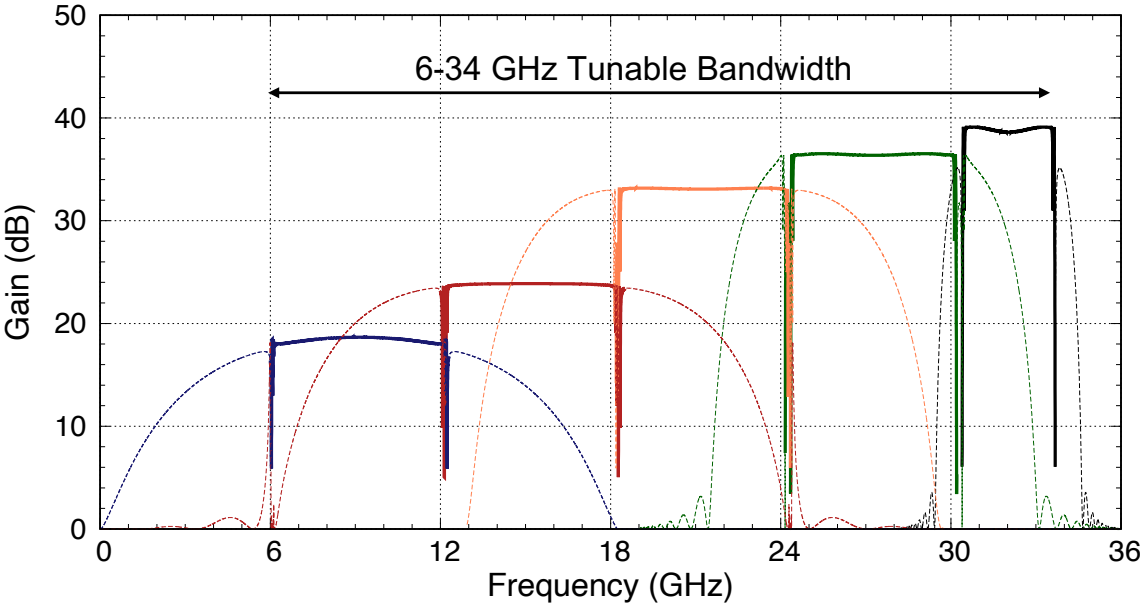

Figure 6.5: Tunable bandwidth of dual-pump KITWPA.

6.2.2 Millimetre KITWPA Designs

In § 6.2.1 we presented the design concept for a microwave ND-4WM KITWPA operating over the frequency range 6–12 GHz. Despite the many advantages this design presents over a KITWPA operating in the D-4WM regime, it remains that a DC-3WM KITWPA could offer similar broadband performance apart from the roll-off of the gain profile near the edges of the band, and the need for a DC-biasing current. At higher operational frequencies, however, such as in the regime of mm/sub-mm wavelength, the use of a DC-3WM KITWPA may become challenging, as the need for a DC-biasing current may also incur additional heating effects through the DC wires to the cryogenic stages. In this sense, we argue that the main avenue where ND-4WM KITWPA operation is most advantageous compared to other variants is when the TWPA is operating at high frequency beyond the microwave range, where most of the EM transmission is via waveguides instead of coaxial cabling. In this section, we present a series of ND-4WM designs operating at mm-wave frequencies covering ALMA Bands 1–5 to demonstrate this advantage, along with several other design considerations required when operating a KITWPA in a waveguide environment.

6.2.2.1 ALMA Band 1

ALMA Band-1 covers a frequency range of 35–50 GHz [23], and is currently the lowest frequency band in operation at the ALMA observatory. The current technology used in the Band-1 signal detection scheme utilises high electron mobility transistor (HEMT) amplifiers as first-stage detectors with receiver noise temperatures approaching 32 K [23], which unfortunately is still not near the ultimate quantum-noise limit.

Within the Band-1 range, it is in principle possible to drive the first-stage amplifier via coaxial cables with 'v'-connectors rated for operation up to 70 GHz, which implies that it is possible to replace the HEMT amplifiers with DC-3WM KITWPAs, provided that similarly broadband bias-tees are available. Operating a DC-3WM KITWPA, however, requires the pump frequency to be set to at least twice the centre frequency of the gain profile i.e., close to 90 GHz, which is beyond the operational range of 'v'-connectors. This means that the successful operation of a Band-1 KITWPA may require the entire ALMA Band-1 RF-signal cabling network to be replaced with 1.35 mm or 1.0 mm ('w') connectors to support such a high-frequency pump, which complicates the design and increases the cost. Even if one replaces the coaxial connections with waveguides, it is still very challenging to construct an ultra broadband waveguide probe antenna that can cover such wide (close to 3:1) bandwidth. Given that the pump frequencies for a ND-4WM KITWPA are much closer to the operational frequency band, it means that both the signal and the pumps can be transmitted using either a common coaxial cable or a waveguide probe with reasonable bandwidth performance.

We present here a ND-4WM KITWPA designed for covering the ALMA Band-1 range using the 'v'-type coaxial connection, and is similar to the design shown earlier in Fig. 6.2. The physical parameters of the Band-1 KITWPA are summarised in Tab. 6.3 echoing that of Tab. 6.2. As with the 6–12 GHz design, we use an IMS structure fabricated from the same 35 nm NbTiN film patterned onto the 675 µm silicon substrate, with a 100 nm a-Si dielectric, and 200 nm Nb sky plane.

Fig. 6.6(a) shows the gain-bandwidth profile of the KITWPA with a flat gain over 20 dB that comfortably covers the entire Band-1 bandwidth. The pump currents used to simulate the gain profile are $I_{p_1} = I_{p_2} = 0.075 I_*$ with the pump frequencies $f_{p_1} = 29.1\,\text{GHz}$ and $f_{p_2} = 57.7\,\text{GHz}$, which in contrast to the DC-3WM case, lie comfortably with the frequency specification of 'v'-connectors. Fig. 6.6(b) shows

Description	Parameter	Value
Chip length	a	6.5 mm
Chip width	b	2.0 mm
Microstrip width	w	250 nm
Stub gap	g	500 nm
Stub length (50 Ω)	l_0	12.8 µm
Stub length (1st loading)	l_1	9.0 µm
Stub length (3rd loading)	l_3	4.8 µm
No. of stubs (50 Ω section)	n_0	18
No. of stubs (1st loading)	n_1	2
No. of stubs (3rd loading)	n_3	2
Total no. of cells	n_{tot}	500

Table 6.3: Summary of physical design parameters for ALMA Band 1 KITWPA. Here, we assume $n_{\text{loss}} = 5\%$ for the reasons argued in Chaps. 3 and 5.

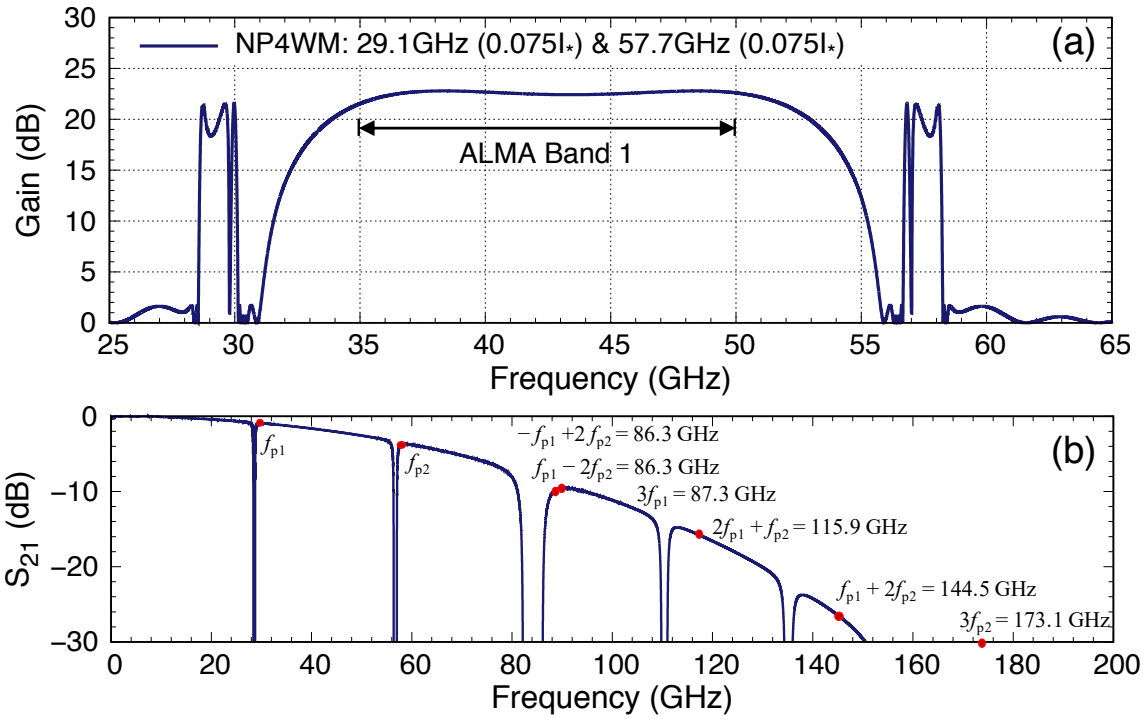

Figure 6.6: (a) Gain and (b) S_{21} transmission of ALMA Band 1 ND-4WM KITWPA.

the $|S_{21}|$ transmission profile, highlighting the positions for the pump tones and the generated harmonics. One will notice that unlike the 6–12 GHz KITWPA, the pump harmonics do not line up exactly with the band gaps. This example was shown here on purpose to demonstrate that there is indeed another design scheme where one could utilise to produce an operable ND-4WM KITWPA.

One may have noticed that in this example, we do not alter the stub length to be significantly different from that of the 6–12 GHz design. In § 6.2.1, we explained that the use of stubs shunted to the main conductor line allowed for 50 Ω impedance matching, however, they have an additional effect i.e., creating a resonant frequency at the very high frequency end, which in this example is near to 450 GHz for a stub length of 9 µm. Due to the closeness of the operational frequencies here to the resonant frequency, the wavevector of the transmission line would inevitably diverge away from the otherwise linear relation much faster than the case without any stubs. This in turn causes the $|S_{21}|$ profile to start to experience frequency-dependent attenuation, which is less noticeable for the 6–12 GHz case where the frequency band is very far away from the resonant frequency. Both of these behaviours have the property of attenuating and phase-mismatching any of the pumps' harmonics, hence we do not need to engineer them directly into the band gaps to suppress their generation. This further demonstrates that ND-4WM mode is in fact better suited to higher frequency operation at mm/sub-mm frequencies than at microwave frequencies.

6.2.2.2 ALMA Bands 2-5

ALMA Bands 2–5 cover the electromagnetic spectrum over the range of 67–211 GHz [23], and at these frequencies, we can no longer use coaxial lines for signal transmission and are instead reliant on waveguide transmission. DC-biasing a DC-3WM KITWPA mounted within a waveguide may be complicated as a pair of additional DC lines would need to be electrically connected to the chip, which is now much smaller in size at such high frequency. For operation in this range, therefore, ND-4WM is preferable. In this section, we present two designs, which cover the ALMA Bands 2–3 and 4–5, respectively.

As stated earlier, signal coupling using a waveguide structure necessitates the design of a waveguide-to-planar circuit transition (or an on-chip antenna). It is, therefore, crucial that the design of the antenna is carried out first, as this sets the limitations and restrictions on the transmission line dimensions and materials, as well as the characteristic impedance of the line, which no longer needs to be matched to a 50 Ω.

Fig. 6.7(a) shows the layout of our antenna designed to couple the pumps and signal to our KITWPA chips, with the physical parameters specified in Tab. 6.4 for

Band	60-120 GHz	120-240 GHz
a_{wg} (mm)	2.60	1.50
b_{wg} (mm)	1.30	0.65
l_{bs} (mm)	0.80	0.42
t_{sub} (µm)	80	40
w_{sub} (µm)	216.2	115.6
r_{pr} (µm)	690	380
w_{pr} (µm)	196.2	95.6
θ_{pr} (°)	41.7	45.4
Z_{ant} (Ω)	70.6	67.7

Table 6.4: Summary of physical design parameters for ALMA Band 2-5 KITWPA antennae.

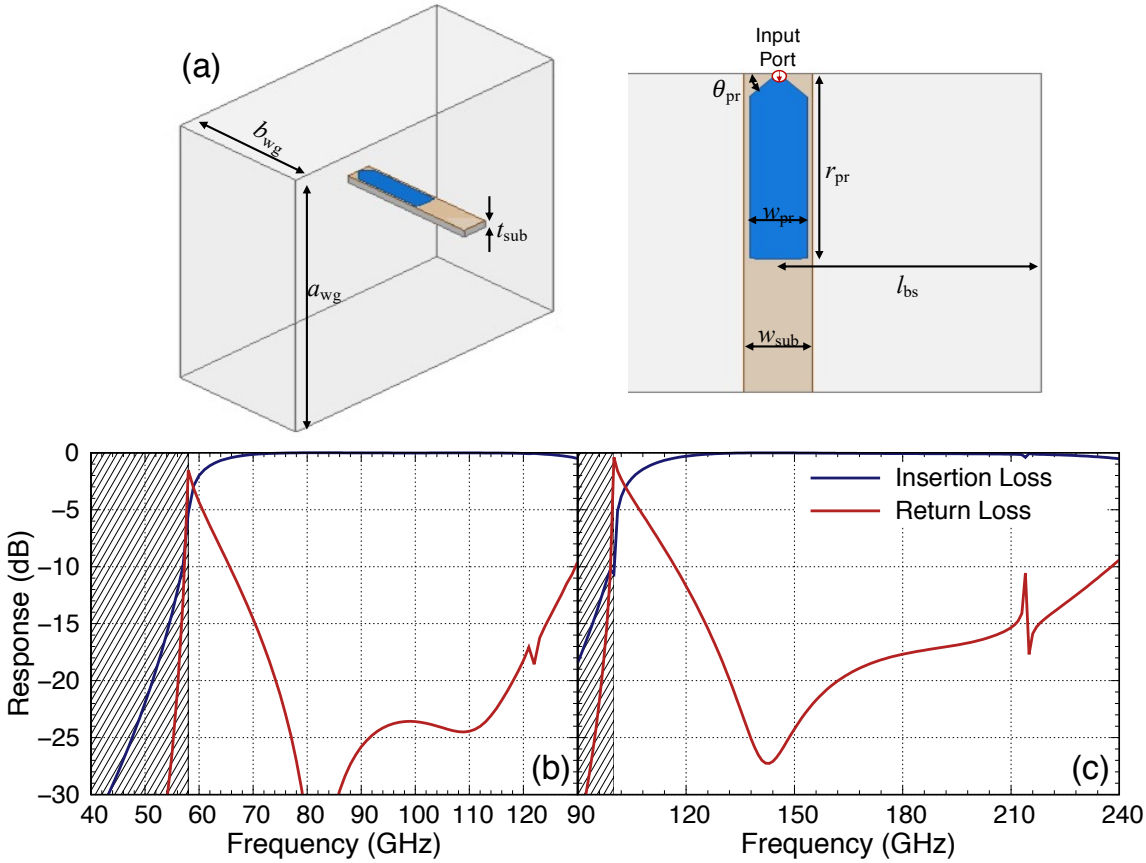

Figure 6.7: (a)Model of antenna used in mm-wave ND-4WM KITWPA, with parameters specified in Tab. 6.4. Antenna bandwidth for (b) Band 2-3 and (c) Band 4-5 designs.

both the Band 2–3 and Band 4–5 KITWPAs. The probe antenna is expected to be formed using the same 35 nm NbTiN film used in previous designs, except it is now

deposited onto a 80 µm thick quartz substrate for the Band 2–3 and 40 µm for the Band 4–5 design, as the lower dielectric constant provides a better coupling to the antenna compared to a higher dielectric constant silicon substrate.

Figs. 6.7(b)-(c) show the antenna bandwidth for the Band 2–3 and Band 4–5 designs, respectively, simulated using HFSS. One immediately notices the finite bandwidth of the antenna, which makes it difficult to couple a pump tone to the KITWPA at twice the central frequency of the amplification band, hence making operation in the DC-3WM mode very challenging. This again highlights why ND-4WM mode is more realistic for high frequency operation.

Parameter	60-120 GHz	120-240 GHz
a	17.5 mm	9.5 mm
b	2.0 mm	2.0 mm
w_0 (µm)	1.02	1.06
w_1 (µm)	1.18	1.15
w_3 (µm)	1.25	1.19
l_0 (µm)	32.3	16.4
l_1 (µm)	3.6	1.8
l_3 (µm)	3.6	1.8
n_{tot}	500	500

Table 6.5: Summary of physical design parameters for ALMA Band 2-5 KITWPAs.

Having designed the KITWPA antennae, we can now proceed to the design of the KITWPA itself. From Tab. 6.4, we notice that the output impedance for both antennae is approximately 70 Ω, meaning that we would need to match the characteristic impedance of the main sections of the TWPA line to this value, instead of the usual 50 Ω.

Fig. 6.8 shows a drawing of the KITWPA design used for both frequency bands, which are identical in form except the physical dimensions vary between each design, as summarised in Tab. 6.5. Contrary to the lower frequency KITWPA devices, these devices comprise a regular (non-inverted) MS design, which is formed by depositing a 200 nm Nb ground plane onto an 80 µm quartz substrate for the Band 2–3 or 40 µm quartz substrate for the Band 4–5 design, followed by a 100 nm a-Si dielectric, which is topped by the 35 nm NbTiN wiring layer. The reason for swapping the IMS structure with a regular MS is because the use of such a thin substrate with lower dielectric constant means that when the device is mounted onto a metallic

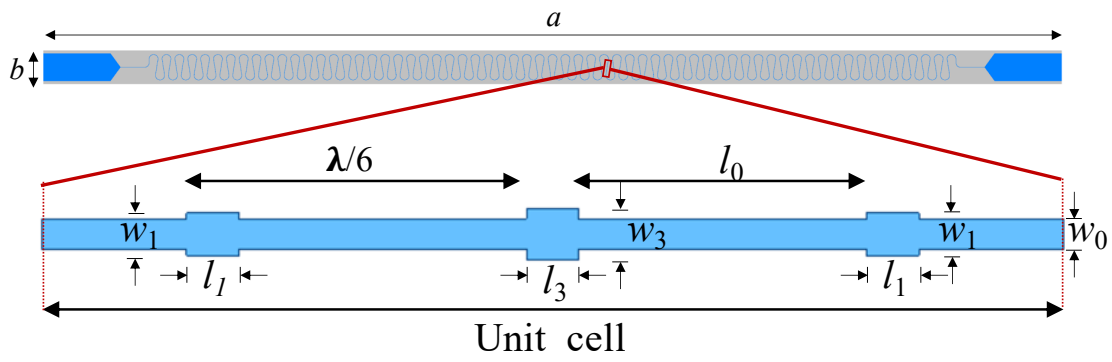

Figure 6.8: The common layout used for Bands 2–3 & 4–5 KITWPA designs, showing the wiring layer (blue) of the microstrip, which is wound into a 'hairpin' pattern to fit the design onto a single chip. The substrate is shown in grey and the dielectric and ground planes are not shown for clarity. The inset highlights the periodic loading structure of a unit cell.

block, the IMS would support a stripline propagation mode as the electric field in the transmission line now 'sees' the metallic surface of the block as another 'ground' plane. This mode has a completely different characteristic impedance to the microstrip propagation mode, hence virtually no power would be coupled into the transmission line from the antenna.

Additionally, one will notice from Fig. 6.8 that the Band 2–5 microstrip lines do not use the shunted stubs to achieve the desired impedance and instead rely solely on the width of the main strip. As previously discussed, this is due to the fact that the resonant frequency of the shunted stubs attenuates the transmission profile significantly towards higher frequencies, meaning that the use of the stubs would make the KITWPA far too lossy at high frequencies and narrows down the operational bandwidth substantially.

Fig. 6.9(a) shows the gain-bandwidth profile for the Band 2–3 KITWPA device, clearly showing a relatively flat gain curve above 25 dB over a bandwidth of 60–120 GHz, which comfortably covers the entirety of ALMA Bands 2 and 3. This gain profile is achieved with pump currents of $I_{p_1} = I_{p_2} = 0.065 I_*$ and pump frequencies set at $f_{p_1} = 60.34$ GHz and $f_{p_2} = 119.74$ GHz, with the generated harmonic frequencies falling neatly into higher subsequent band gaps as shown in Fig. 6.9(b).

Similarly, Fig. 6.10(a) shows the gain-bandwidth profile for the Band 4–5 KITWPA device, again showing a flat gain curve above 25 dB over a bandwidth of 120–

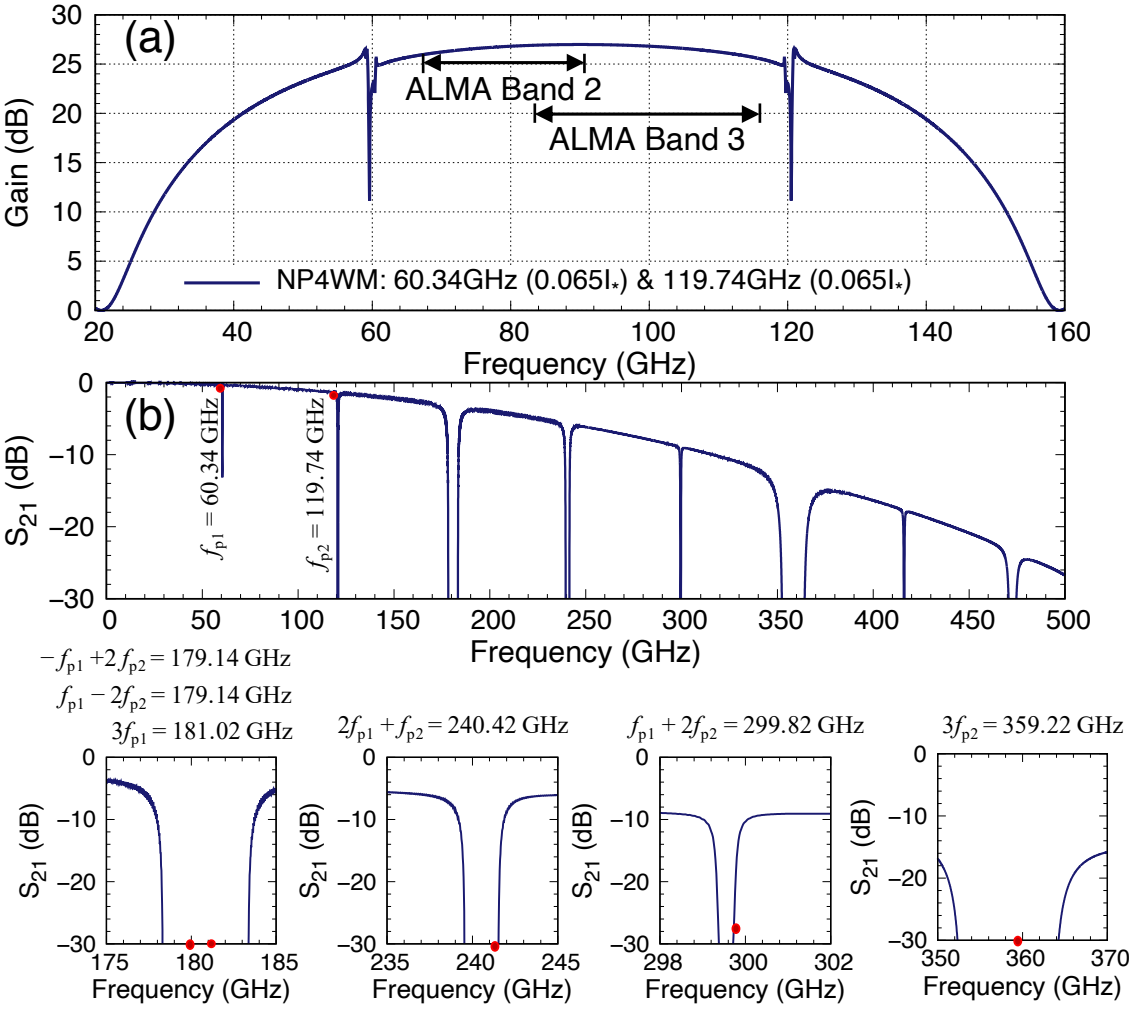

Figure 6.9: (a) Gain and (b) $|S_{21}|$ transmission of ALMA Band 2-3 KITWPA.

240 GHz, which comfortably covers the entirety of ALMA Bands 4 and 5, as well as the lower half of Band 6. This gain profile is achieved for pump currents of $I_{p_1} = I_{p_2} = 0.065 I_*$ and pump frequencies of $f_{p_1} = 60.34$ GHz and $f_{p_2} = 119.74$ GHz, with the majority of the generated harmonic frequencies falling neatly into higher subsequent band gaps, with the exceptions of the two highest harmonics, which are attenuated below –20 dB by the transmission profile, as shown in Fig. 6.10(b).

6.3 Balanced-TWPA

KITWPAs have been extensively discussed in this thesis, demonstrating their enormous potential to dramatically improve ultra-sensitive measurements of weak signals in cryogenic environments. Despite their enormous potential, they have yet to be

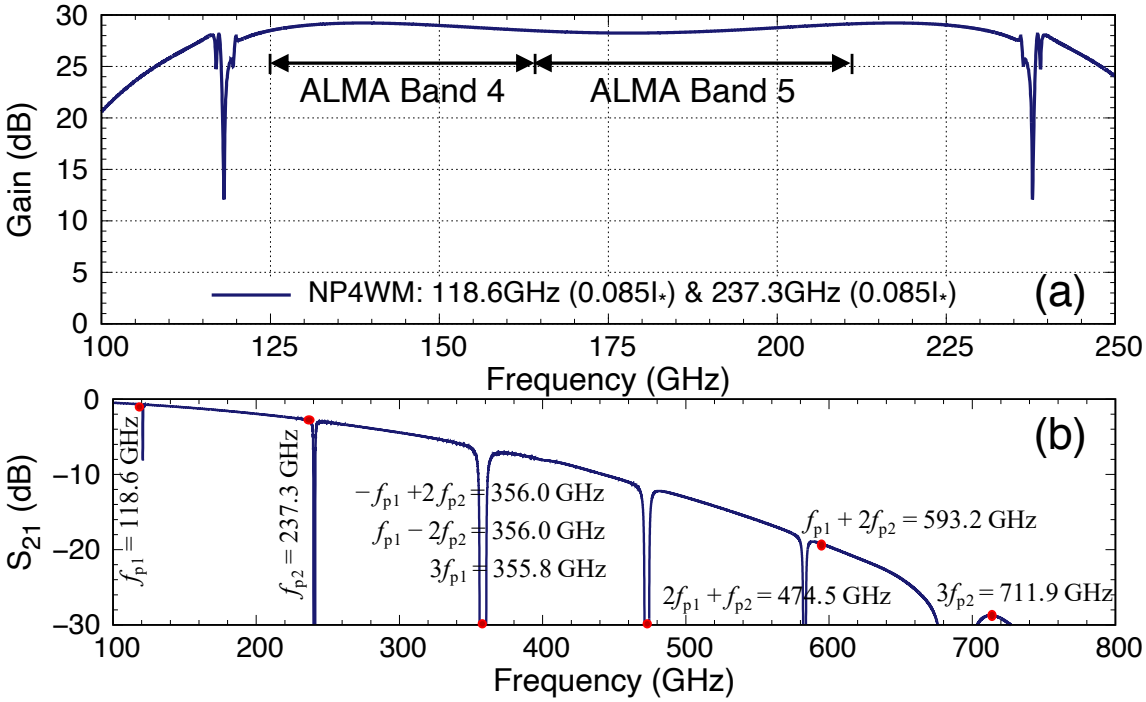

Figure 6.10: (a) Gain and (b) $|S_{21}|$ transmission of ALMA Band 4-5 KITWPA.

widely used in real experiments due to a number of practical limitations. In this section, we present the concept of a balanced-TWPA, which aims to address these limitations and pave the way toward widespread TWPA use.

6.3.1 Current Obstacles to TWPA Operation

Fig. 6.11 shows an example D-4WM gain profile compared to the gain curve of an ideal amplifier. It is clear from this plot that there are a number of undesirable properties of the D-4WM curve compared to the ideal case, however, the solution to some of these has already been discussed, for example the zero-gain gap and gain roll-off towards the edge of the band can be mitigated by operating in the dual-pump ND-4WM regime or the DC-3WM regime. Additionally, the gain ripple can be reduced by carefully controlling the impedance of the line [135]. The remaining issues are discussed in more detail in following.

Whilst the elimination of the resonant architecture associated with narrow-band JPAs allows for amplification over a broad bandwidth, it means that the idler tone, which is generated for momentum conservation, will be at a different frequency to the signal tone, as shown in Fig. 6.12(a). A fact that is not often discussed in the literature is that the generated idler will heavily distort an amplified spectrum.

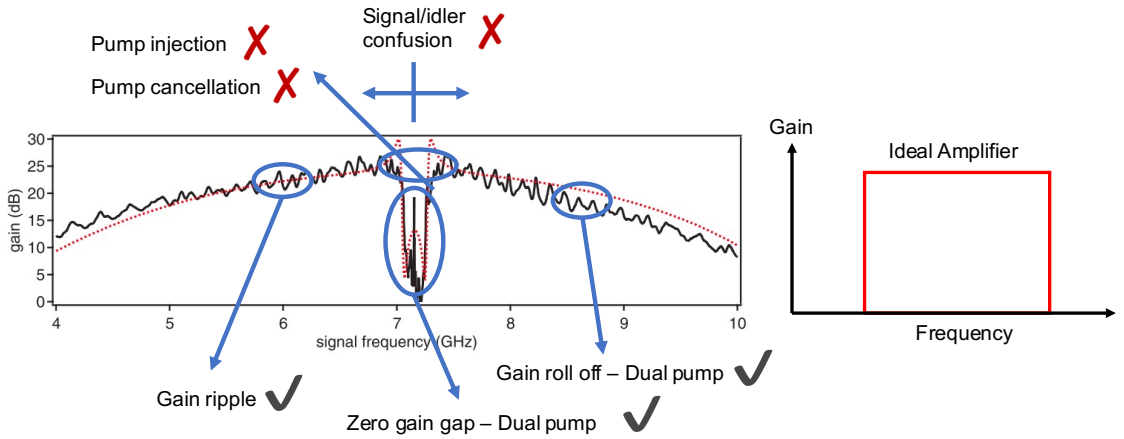

Figure 6.11: Example TWPA gain spectrum operating in the D-4WM regime, showing numerous operational obstacles, when compared to an ideal amplifier on the right.

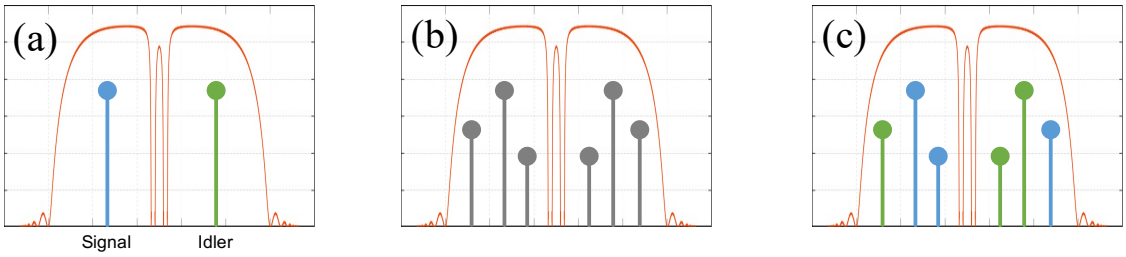

Figure 6.12: Examples highlighting the contamination of the amplified signal by the idler tone. (a) Output spectrum from TWPA, highlighting the amplified signal and generated idler. (b) Output spectrum from TWPA with more input tones, highlighting how without prior knowledge, it is impossible to distinguish between the amplified signal and generated idler tones. (c) Same spectrum as (b), now with the signal and idler tones colour coded to highlighting particular input tones.

Consider the spectrum in Fig. 6.12(b), which shows the output spectrum after the amplification of three detected input frequencies by a TWPA. Clearly, the output spectrum in fact contains six peaks, with three being the amplified signal frequencies and the other three being the generated idler frequencies. Assuming no prior knowledge of the input frequencies, which is usual, it is impossible to distinguish between the signal and idler tones, as shown in Fig. 6.12(b), meaning the input spectrum cannot be recovered from the output spectrum; a fact that renders the TWPA essentially useless.

Fig. 6.13 shows a potential solution to this signal-idler contamination issue, whereby

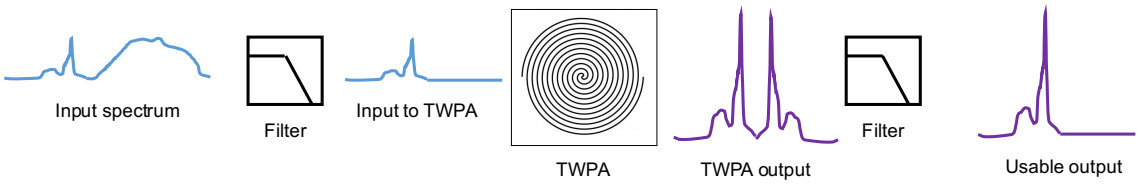

Figure 6.13: Possible idler removal technique, whereby half the spectrum is filtered before and after amplification.

an incoming signal spectrum is filtered prior to amplification such that only signal frequencies lower than the centre frequency of the amplification band are amplified by the TWPA[2]. The removal of the higher frequency signal means that it will not generate a lower frequency idler that would distort the lower frequency side of the signal spectrum. Further filtering post-amplification removes the higher frequency idler generated by the lower frequency signal, which results in an undistorted and amplified spectrum of the lower half of the original spectrum. Whilst this technique solves the signal-idler contamination problem, it is an inelegant solution, as it instantly halves the operational bandwidth of the TWPA, which is the particular parameter we are trying to extend compared to JPAs. The signal-idler contamination, therefore, remains an important problem that needs addressing.

Another obstacle to practical TWPA operation is the complicated setup required to use them. Fig. 6.14 shows a typical experimental setup used to operate a ND-4WM TWPA device, which clearly highlights the number of additional components, such as directional couplers, power dividers, variable attenuators, and phase shifters that are required to combine the pump and signal tones and to subsequently cancel the pump tones post-amplification. These additional components are often much larger than the TWPA itself, taking up valuable space within the cryostat. The pump cancellation also requires additional coaxial lines to run down to the cold stages of the cryostat, placing a greater thermal load upon it. This becomes a big limitation when scaling experimental setups to arrays, as the number of additional required components places unreasonable thermal and power loads on the cryostat, in an already highly constrained environment. It is, therefore, highly necessary to simplify the integration of TWPAs into cryogenic experimental setups.

Another, perhaps more minor, issue with TWPA operation is their reciprocal nature, which allows radiation to pass through them in the reverse direction. If

[2]This analysis can also be done if the signal frequency is higher than the centre frequency, as long as it is only on one side of the centre frequency.

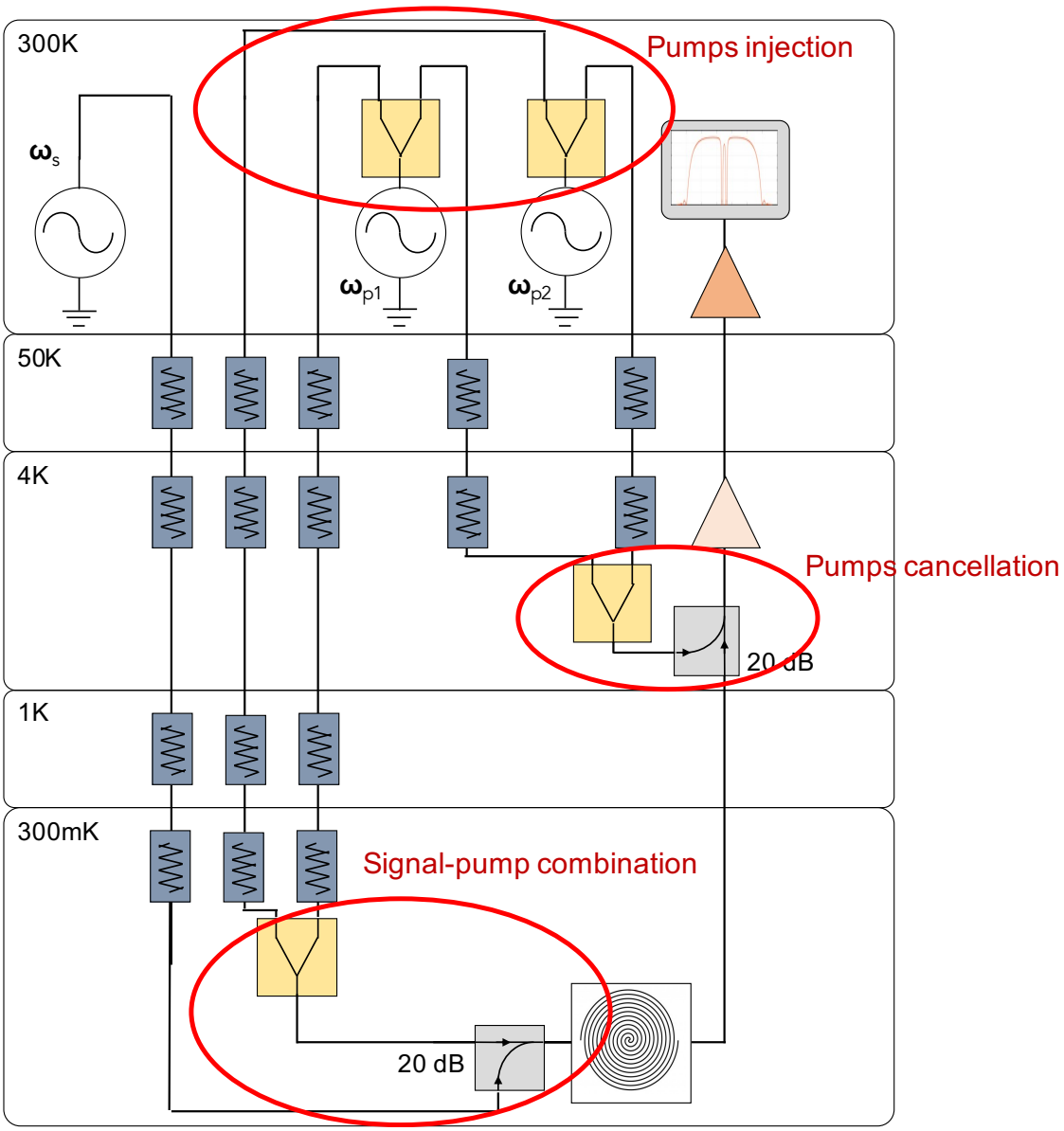

Figure 6.14: Complicated experimental setup required to operate TWPAs. This example is for ND-4WM.

we consider a conventional transistor amplifier, the magnitude of its reverse transmission, $|S_{12}|$, is typically extremely small, meaning that any back radiation from components after the amplifier is prevented from radiating through the amplifier and disturbing the potentially sensitive device under test (DUT), such as a qubit. With a TWPA, however, the $|S_{12}|$ is nominally the same as the un-pumped $|S_{21}|$, meaning that any back-radiation may be transmitted through the TWPA and disturb the DUT. The prevention of this requires the use of an additional circulator, from which arises additional thermal, spacial, and financial costs, as well as imposing bandwidth restrictions and introducing losses. It is, therefore, desired to introduce some sort

of non-reciprocity into the TWPA to eliminate this requirement.

A further issue facing TWPA operation is stability, where the gain of the amplifier can oscillate somewhat chaotically if the amplifier is unstable. Due to the reciprocity of a TWPA transmission line and the potential for impedance mismatches, it is possible for backward amplification to occur due to reflected signal and pump tones, as discussed in Chap. 5. For low backwards gains, the backward amplification can lead to ripples in the gain profile [119], such as those seen in Chap. 5, as well as other devices reported in the literature [21, 70–74]. For large backwards gains, the backward amplification can lead to amplifier instability [119]. The mitigation of this issue, therefore, requires the elimination of any pump reflection, since the reflection of a signal alone will not lead to any parametric backward amplification.

6.3.2 Parallel TWPA Architecture

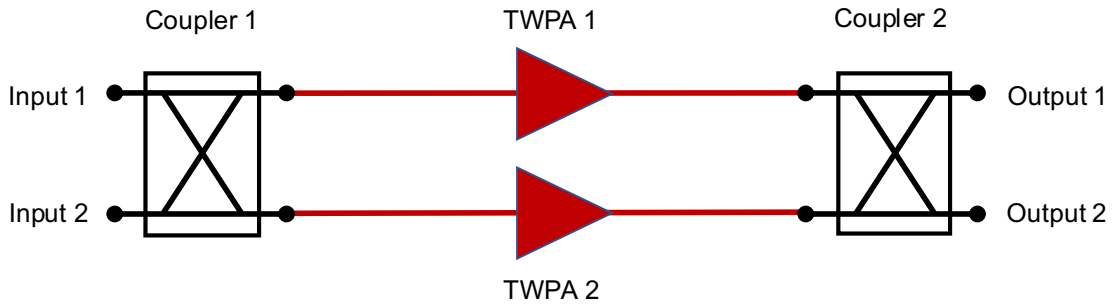

Figure 6.15: Schematic of parallel TWPA architecture, showing a pair of parallel TWPA devices between a pair of generic RF couplers.

Our proposed solution to the obstacles discussed in the previous section is the use of a parallel TWPA architecture, a schematic of which is shown Fig. 6.15. This configuration comprises a pair of TWPA devices in parallel between a pair of generic RF couplers, which typically have multiple input and output ports. The use of certain RF couplers, such as quadrature hybrids, introduces a phase shift to the propagating tones before and after entering the TWPAs. By carefully controlling the phases of the various tones propagating through the TWPAs, it is possible to engineer constructive and destructive interference at the output ports, meaning it is possible to cleanly separate out the pump, signal, and idler tones.

This structure bears significant resemblance to balanced amplifiers [136, 137], which comprise a pair of near-identical amplifiers between a pair of directional cou-

plers or hybrids. Balanced amplifier designs are used extensively as microwave amplifiers [138–140], primarily due to their convenient impedance matching, gain flatness, phase linearity, gain compression, and intermodulation characteristics, which can be achieved without the need for tuning adjustments to the amplifier. Our parallel TWPA architecture is able to offer the same advantages of a traditional balanced amplifier, whilst additionally being able to solve the previously-discussed issues that are specifically related to TWPA operation.

Central to the successful operation of this parallel TWPA architecture is the phase control of the propagating tones. Let us consider the total current passing along a TWPA, as described by the ansatz in (2.23), which can be generalised slightly to,

$$I\left(z,t\right)=\sum_{j}A_{j}\left(z\right)e^{i\left(k_{j}z-\omega_{j}t+\delta_{j}\right)}+c.c., \tag{6.1}$$

where δ_j is the arbitrary initial phase of the j^{th} current component. In most formulations of the CMEs, including those presented in Chap. 2, δ_j is not explicitly included and it is assumed that $\delta_j = 0$. To preserve generality, however, we can include δ_j in the CME formulations and assume that, in general, it is non-zero. Conveniently, as shown in the following, δ_j can be absorbed into the complex amplitude of the current,

$$\begin{aligned} I\left(z,t\right) &= \sum_{j}A_{j}\left(z\right)e^{i\left(k_{j}z-\omega_{j}t+\delta_{j}\right)}+c.c. \\ &= \sum_{j}A_{j}\left(z\right)e^{i\delta_{j}}e^{i\left(k_{j}z-\omega_{j}t\right)}+c.c. \\ &= \sum_{j}A'_{j}\left(z\right)e^{i\left(k_{j}z-\omega_{j}t\right)}+c.c., \end{aligned} \tag{6.2}$$

where,

$$A'_{j}\left(z\right)=A_{j}\left(z\right)e^{i\delta_{j}}, \tag{6.3}$$

and the CMEs will remain the same. When solving the CMEs, an initial condition for the propagating tones must be provided, which is conventionally given as a real number. Since the CMEs deal with complex current values, however, the initial conditions need not be restricted to real values, but in general can be complex, i.e. we can make the transformation,

$$I_{j}(0)\rightarrow I_{j}(0)e^{i\delta_{j}}. \tag{6.4}$$

The question now is what effect does this arbitrary phase shift have on the wave mixing processes taking place along the TWPA. Here, we shall explore the phase

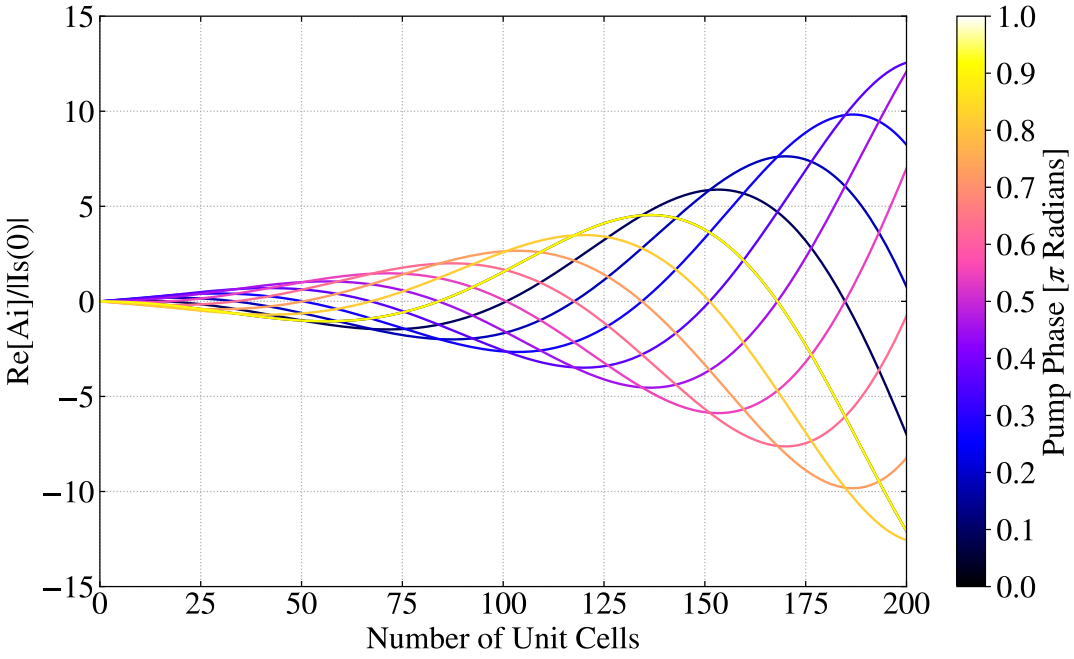

Figure 6.16: The real component of the idler amplitude, A_i, normalised by the amplitude of the initial signal current, $I_s(0)$, as the phase of the pump tone is swept. This is calculated by numerically solving the CMEs.

relations of the tones propagating along a TWPA operating in the D-4WM regime, however, the following analysis can also be extend to other wave mixing regimes.

Fig. 6.16 shows the real component of the idler amplitude, $\Re(A_i)$, normalised to the initial signal current amplitude, $|I_s(0)|$, as a function of position along the length of an example TWPA for various arbitrary initial phases of the pump tone. Whilst the magnitude of the idler component remains unchanged as the initial pump phase is varied, as given by the positive envelope function of each of the curves, the phase of the idler tone does shift with the initial pump phase. The lack of change in the magnitude of the idler is expected to be independent of an arbitrary phase shift, as this means that any (conversion) gain is unchanged by the initial phase shift. The shift in the phase of the idler tone is interesting, however, as it suggests that we are able to control it externally by controlling the phase of the pump.

This behaviour is further explored in Fig. 6.17, which shows the initial idler phase varying as a function of the initial pump phase for different initial signal phases. From this plot, we clearly see that shifting the pump phase by $\Delta\delta_p$ will shift the idler phase by $2\Delta\delta_p$, and that shifting the signal phase by $\Delta\delta_s$ will shift the idler phase by $-\Delta\delta_s$. The phase shift of the idler tone, $\Delta\delta_i$ as a function of $\Delta\delta_p$ and $\Delta\delta_s$

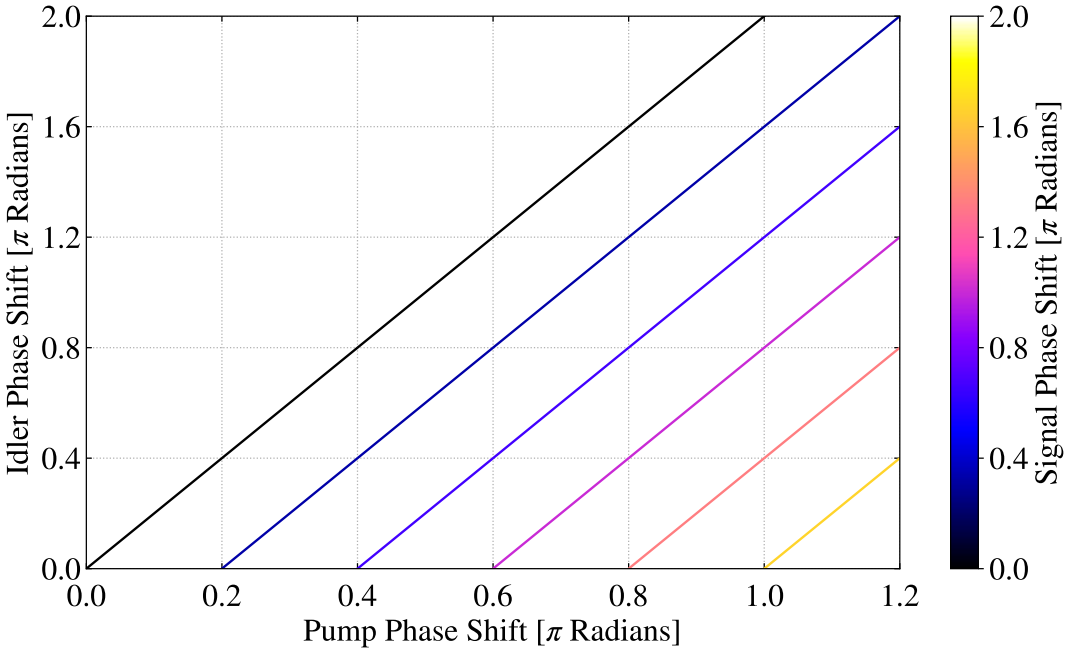

Figure 6.17: The idler phase shift as a function of the pump phase shift and signal phase shift.

can, therefore, be summarised by,

$$\Delta\delta_i = 2\Delta\delta_p - \Delta\delta_s, \tag{6.5}$$

which is of the same form as the equation of energy conservation,

$$\omega_i = 2\omega_p - \omega_s. \tag{6.6}$$

This relation between the phase shifts is important, as it means that it is possible to control the idler tone independently from the signal tone by tuning the phase of the pump tone. I will now demonstrate how we can utilise this to provide some elegant solutions to the various issues I have previously described with regards to practical TWPA operation by considering the case of a pair of parallel TWPAs.

Suppose we have two identical TWPA devices which are fed by identical, in-phase signal tones and are pumped at the same magnitude and frequency, and we combine their outputs. This is demonstrated in Fig. 6.18(a), which shows a pair of TWPAs operating in the D-4WM mode between a pair of in-phase Wilkinson power dividers/couplers. A pump tone of equal magnitude and frequency is injected into each TWPA, with the pump tone in the bottom arm having a $\frac{\pi}{2}$ radian phase shift relative to the pump tone in the top arm. As we can see from Fig. 6.18(a) and (6.5), a $\frac{\pi}{2}$ radian phase shift in the pump tone results in a π radian phase shift to

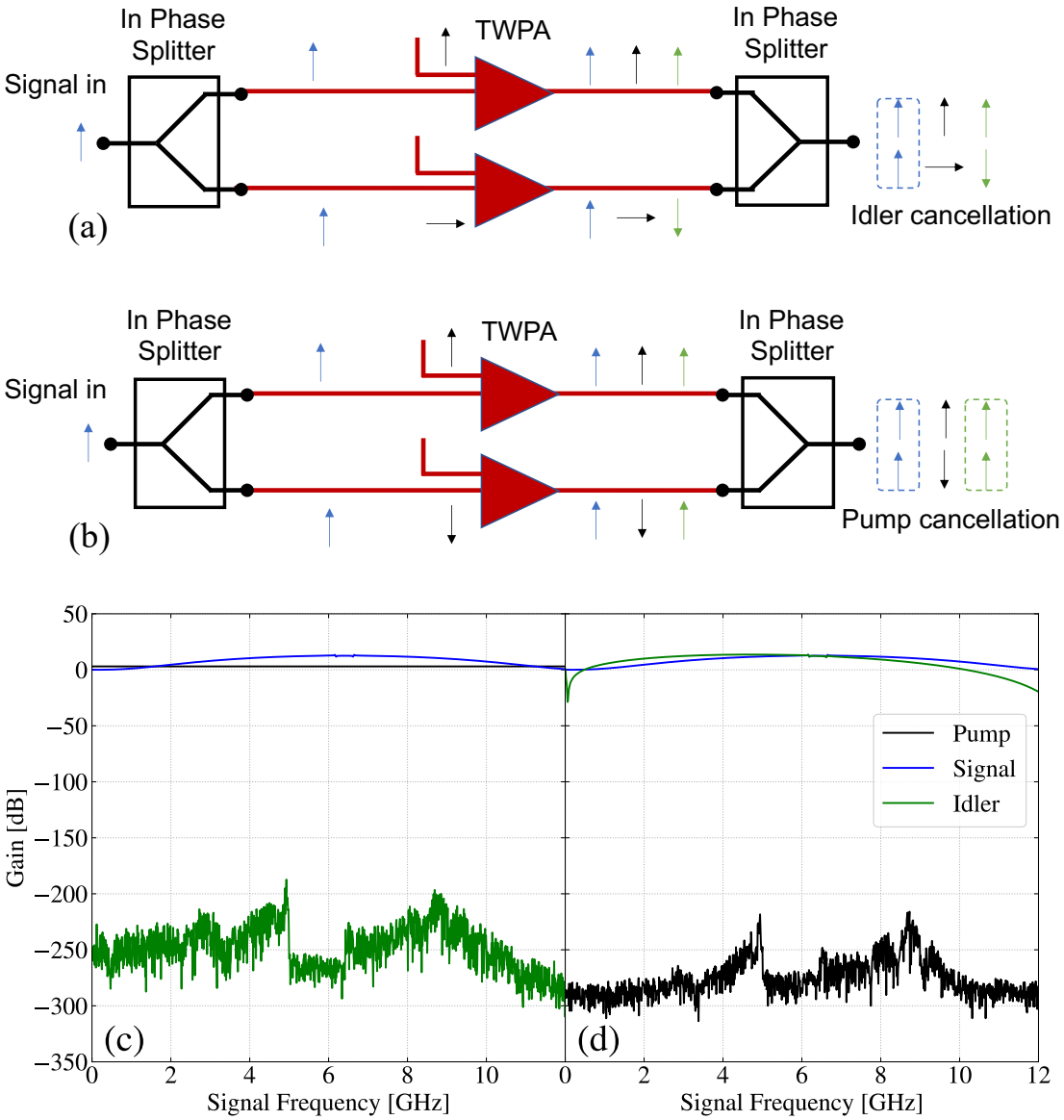

Figure 6.18: Circuit diagrams of a D-4WM parallel TWPA with in-phase Wilkinson power dividers/combiners. The blue, black, and green arrows represent the signal, pump, and idler, respectively, and the direction of each arrow indicates the relative phase of each tone. In (a) the pump tone of the bottom arm is shifted by $\frac{\pi}{2}$ radians relative to the top arm, leading the idler tones being π radians out-of-phase at the output, and thus cancelling. (b) Shows the identical setup but with the pump tone feeding the bottom arm now being π radians out-of-phase relative to the top arm, leading to pump cancellation. (c) Simulated gain profiles of the output tones for parallel TWPA configuration shown in (a). (d) Simulated gain profiles of the output tones for parallel TWPA configuration shown in (b).

the idler tone in the lower TWPA relative to the upper TWPA, which means that upon recombination by the second power combiner, the idler tones, which are now in antiphase, cancel. This idler cancellation means that only the signal and the pump (which can be subsequently cancelled using other techniques) are present at the output, solving the signal-idler contamination problem described in Figs. 6.12(a)-(c). This demonstrates how our parallel TWPA architecture can enable full-bandwidth TWPA operation without catastrophic contamination from the idler tone.

The signal-idler contamination is not the only obstacle that can be reconciled using the parallel TWPA architecture. If we use the identical setup to the previous analysis but now shift the pump tone in the lower TWPA by a further $\frac{\pi}{2}$ radians such that the pump tones in each TWPA are now π radians out-of-phase, the setup can be operated in a regime such that the pump tones are now cancelled at the output, which is illustrated in Fig. 6.18(b). The advantage of this configuration is that we can now easily remove the pump from the subsequent amplified signal spectrum without the need for additional coaxial lines and RF components, as all of the TWPAs and couplers used in the parallel TWPA can be fabricated onto a single chip.

To verify the behaviour of the parallel TWPA architecture in Figs. 6.18(a)-(b), we have simulated the gain profiles for each component at the output port of the parallel TWPA. This is shown in Fig. 6.18(c) for the configuration in Fig. 6.18(a), and Fig. 6.18(d) for the configuration in Fig. 6.18(b). The simulation procedure for the parallel TWPA architecture involves appropriately modifying the initial phases of the input tones, before separately solving the CMEs for each TWPA in the parallel TWPA setup using the methodology in Chap. 3. The output tones from each TWPA are then summed together and used to calculate the gain of each tone, relative to their initial value. Note that for the idler tone, we calculate the gain relative to the input signal tone, hence it is technically a conversion gain, but is referred to here simply as gain. The pair of TWPAs used in Figs. 6.18(c)-(d) are identical to the TiN CPW design described in Chap. 5.

The above examples highlight the versatility of the parallel TWPA architecture, which we call a balanced-TWPA as it shares similarities with the conventional balanced amplifier, as well as the balanced mixer. The ease of use comes from the fact that it can be switched between different operational modes in-situ simply by externally controlling the phase difference between the pump tones propagating along

the TWPA devices, which allows various combinations of the obstacles to TWPA operation described above to be overcome.

6.3.3 Balanced TWPAs

In the previous section, I chose the simplest balanced TWPA configuration to demonstrate the functionality of the scheme. Whilst it may seem that such a balanced-TWPA can only solve one issue at a time, this is in fact not true and is simply due to the particular example I used previously. Here, I will describe a few examples, which are closer to the configurations that would be used in reality, to demonstrate the versatility of the technique and to show that there are indeed schemes that can solve all of the above issues using one setup. These configurations are derived using the same phase-controlling technique as that presented in the previous section, so only a brief description is given for each.

In practice, using a 3-port power splitter is not ideal, as they are typically lossy due to a resistive element required to provide isolation between the two split ports. A better option would be to use 4-port quadrature hybrids, as these do not suffer from the same losses as 3-port splitters.

Fig. 6.19(a) shows a similar setup to those shown in Figs. 6.18(a)-(b), except this time the signal is fed into one input port of a quadrature hybrid, with the other input port being terminated, before the signal is injected into the TWPAs. Two in-phase pump tones are each injected into the TWPAs and the subsequent tones are recombined by a second quadrature hybrid. Fig. 6.19(b) shows the simulation results for this configuration, where the quadrature hybrids are modelled as ideal couplers, where the power at the output ports of the hybrid, P_{out}, are given by,

$$P_{\text{out}}^{(\text{Port 1})} = \frac{1}{\sqrt{2}}\left(P_{\text{in}}^{(\text{Port 1})}e^{-i\frac{\pi}{2}} + P_{\text{in}}^{(\text{Port 2})}e^{-i\pi}\right) \tag{6.7a}$$

$$P_{\text{out}}^{(\text{Port 2})} = \frac{1}{\sqrt{2}}\left(P_{\text{in}}^{(\text{Port 1})}e^{-i\pi} + P_{\text{in}}^{(\text{Port 2})}e^{-i\frac{\pi}{2}}\right), \tag{6.7b}$$

where P_{in} denotes the power at the input port of the hybrid. Eqs. (6.7a)-(6.7b) is used to calculated the initial phases of the input tones to each TWPA, and subsequently used to combine the output tones from each TWPA.

In the setup in Fig. 6.19(a), not only is the idler tone removed from the signal output, but it is present at its own output port, i.e., we have idler separation, rather

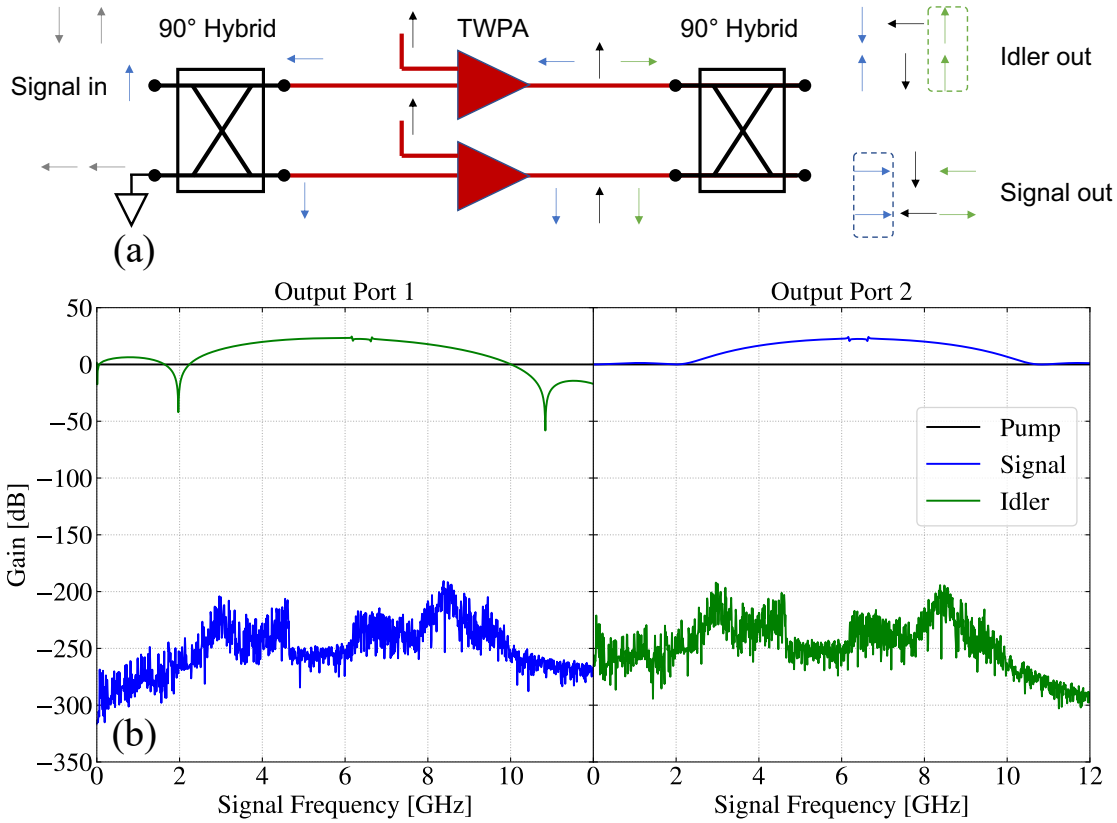

Figure 6.19: (a) Circuit diagram of a D-4WM balanced-TWPA with quadrature hybrids. The blue, black, green, and grey arrows represent the signal, pump, idler, and reflected idler, respectively, and the direction of each arrow indicates the relative phase of each tone. This setup uses a quadrature hybrid to split the incoming signal with a phase difference of $\frac{\pi}{2}$ radians between the two arms. Injecting in-phase pump tones into the TWPAs results in the signal and idler tones exiting different ports of the parallel TWPA, thus being separated. Additionally, any reflected power at the input of the TWPA will be terminated at the unused input port. (b) Simulated gain profiles of the output tones at each output port for configuration shown in (a).

than cancellation, which is advantageous for several reasons. First, separating the idler results in it's noise contribution being removed, improving the noise performance of the TWPA. Second, as the frequency relation between the signal and idler is known, the idler can in fact be used post-amplification, for example by converting back to the signal frequency to further increase the gain or to create a 'circulator' mode in the balanced TWPA.

As discussed previously, the reciprocal nature of a TWPA transmission line means that any back-radiation from subsequent components, such as an LNA with a poor $|S_{11}|$ performance, is radiated through the TWPA and can disturb the po-

tentially sensitive DUT in front of the TWPA. This is the same for the balanced-TWPA in Fig. 6.19(a) if the output signal is measured, as any back-radiation will be transmitted to the signal input port. If we instead read out the output idler tone and terminate the output signal port, we are able to create a non-reciprocity in the TWPA device, as any back-radiation emitted into the output idler port will be transmitted back to the terminated input port, rather than the DUT. This is powerful, as it means we can potentially measure an extremely sensitive DUT without the need for additional circulators, just by reading out the idler instead of the signal. As stated, due to the fact that the idler frequency is a known function of the signal frequency, the input signal spectrum can be trivially recovered from the output idler spectrum during post-processing.

It should be noted here that the particular configuration in Fig. 6.19(a) is similar to the conventional balanced amplifier, in that the signal enters at one of the input ports and the other input port is terminated. This allows for any impedance mismatch between the amplifiers and external circuitry to be mitigated, as any reflections from the input ports of the amplifiers will be reflected to the terminated input port of the balanced amplifier instead of to the DUT. Whilst the impedance mismatch correction is the only advantage to using the balanced amplifier, however, our balanced-TWPA scheme is able to correct for the impedance mismatch while simultaneously solving the other obstacles to practical TWPA operation as discussed previously.

Whilst the example in Fig. 6.19(a) again resolves the signal-idler contamination issue, the pump injection scheme remains complicated, as the pump needs to be injected into both TWPAs independently in the traditional way. Instead of terminating one of the hybrid input ports, as shown in Fig. 6.19(a), the signal and pump can instead be injected into separate input ports of the hybrid, which is shown in Fig. 6.20(a), with the corresponding simulation shown in Fig. 6.20(b). This drastically simplifies the pump injection mechanism, removing the need for additional couplers and freeing space within the cryostat. Additionally, the phase relations in this simple setup provide an easy and convenient way to remove the pump tone from the middle of the gain profile without having to send in a separate pump-cancellation tone, again removing the need for additional couplers, phase shifters, and variable attenuators, as well as additional RF lines running into the cryostat. The added advantage of separating out the pump tone from the signal is that the output pump from one balanced-TWPA can be subsequently used to pump another, providing a

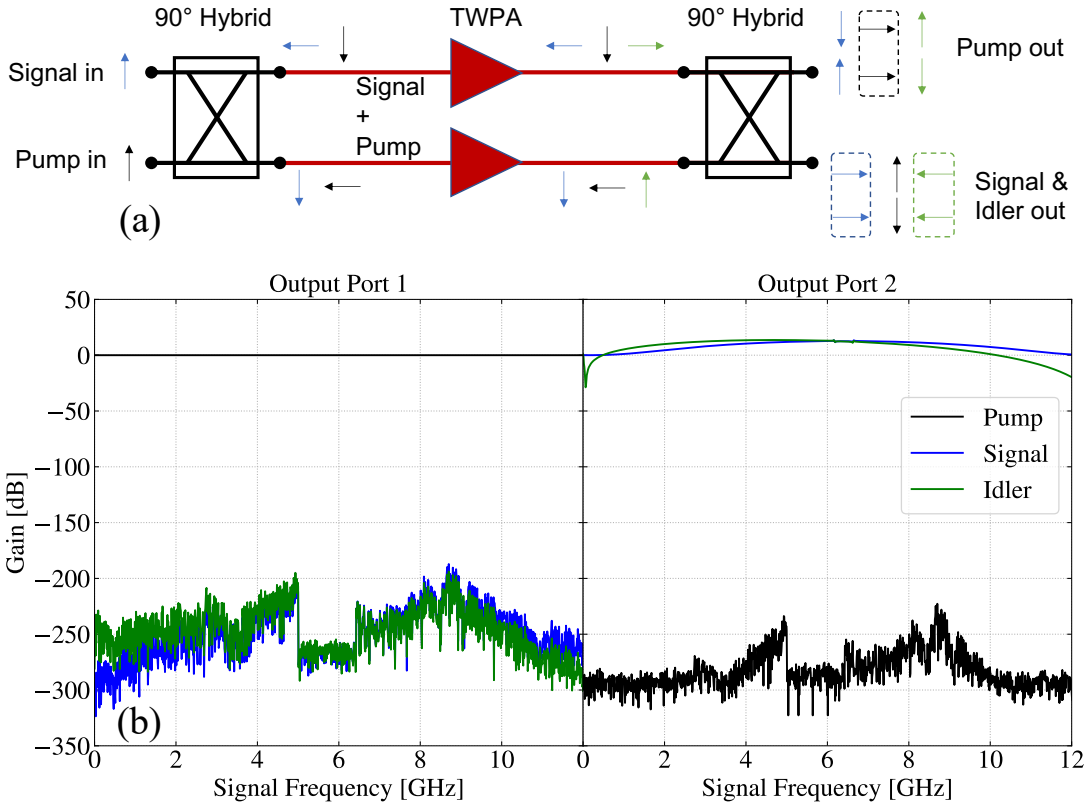

Figure 6.20: (a) Circuit diagram of a D-4WM balanced-TWPA with quadrature hybrids. The blue, black, and green arrows represent the signal, pump, and idler, respectively, and the direction of each arrow indicates the relative phase of each tone. This setup involves injecting the signal and pump tones into separate input ports of the first hybrid, which creates different relative phases at each TWPA. Combining the resultant signals at the second hybrid results in the pump exiting at one port and the signal and idler exiting at the other. (b) Simulated gain profiles of the output tones at each output port for configuration shown in (a).

possible way of creating an array of TWPAs with just one pump line, as illustrated in Fig. 6.21.

All of the previous examples have focused on the D-4WM wave mixing regime, although the same principle can be applied to other wave mixing modes, such as ND-4WM. The phase relation for ND-4WM can be summarised by,

$$\Delta\delta_i = \Delta\delta_{p1} + \Delta\delta_{p2} - \Delta\delta_s, \tag{6.8}$$

and we can clearly see from this that we now have three separate phase shifts that we can control to affect the idler tone.

Fig. 6.22(a) shows the balanced TWPA configuration for ND-4WM with signal

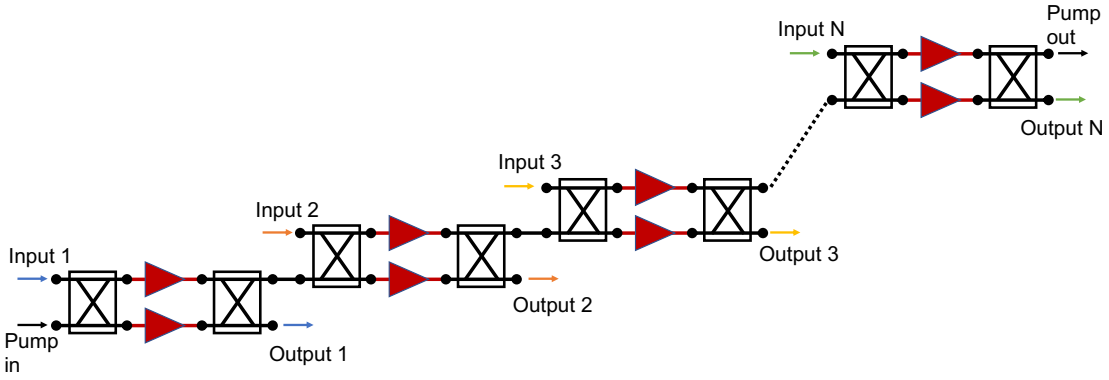

Figure 6.21: Circuit diagram of same balanced-TWPA configuration as in Fig. 6.20(a), highlighting how the convenient separation of the pump and signal tones means the configuration can be transformed relatively simply into an array by connecting the output pump from the first balanced-TWPA into the pump input of the second, and so on, thereby pumping many balanced-TWPAs with just a single pump line.

and idler separation, with the corresponding simulation shown in Fig. 6.22(b). The physical configuration is identical to that shown in Fig. 6.20(a), except an additional pump tone is injected at the same input port as the signal. This results in the signal and one of the pump tones being present at one of the output ports, and the idler and other pump tone being present at the other. As with Fig. 6.19(a), this configuration solves the signal-idler contamination, however, the added advantage of operating a balanced TWPA in the ND-4WM regime, as discussed in § 6.2, is that there is now no zero-gain gap in the centre of the gain profile, resulting in an extremely wide and flat gain profile, all of which can be used. Whilst it may seem inconvenient to have a pump tone at each output port, the fact that they are located at the very edge of the gain profile means they can be easily filtered out.

The phase-control technique can be further applied to a 3WM regime, with the phase shift for this regime being summarised by,

$$\Delta\delta_i = \Delta\delta_p - \Delta\delta_s. \tag{6.9}$$

Fig. 6.23(a) shows a balanced-TWPA configuration operating in a 3WM regime and unlike the previous configurations, 180-degree hybrids are used due to the different phase relation in this regime. The 180-degree hybrids are modelled as ideal with the output powers, P_{out}, being given by,

$$P_{\text{out}}^{(\text{Port 1})} = \frac{1}{\sqrt{2}}\left(P_{\text{in}}^{(\text{Port 1})}e^{-i\frac{\pi}{2}} + P_{\text{in}}^{(\text{Port 2})}e^{-i\frac{\pi}{2}}\right) \tag{6.10a}$$

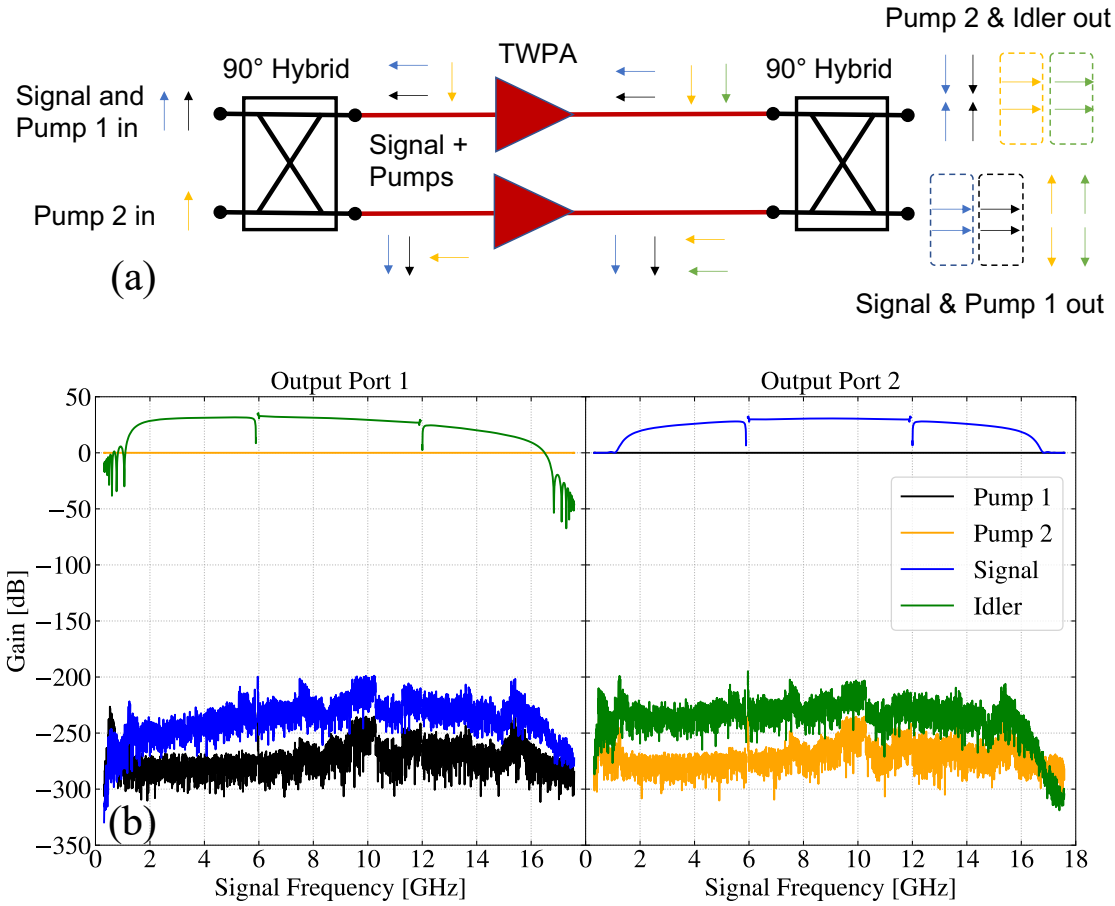

Figure 6.22: (a) Circuit diagram of a ND-4WM balanced-TWPA with quadrature hybrids. The blue, black, orange, and green arrows represent the signal, first pump, second pump, and idler, respectively, and the direction of each arrow indicates the relative phase of each tone. This setup involves injecting the signal and first pump tones into one port of the first hybrid and the second pump tone into the other. Combining the resultant tones at the second hybrid results in the signal and first pump exiting at one port and the second pump and idler exiting at the other. (b) Simulated gain profiles of the output tones at each output port for configuration shown in (a).

$$P_{\text{out}}^{(\text{Port 2})} = \frac{1}{\sqrt{2}}\left(P_{\text{in}}^{(\text{Port 1})}e^{-i\frac{\pi}{2}} + P_{\text{in}}^{(\text{Port 2})}e^{-i\frac{3\pi}{2}}\right) \tag{6.10b}$$

where P_{in} denotes the input power. Fig. 6.23(b) shows the simulated gain profiles for this setup. In this configuration, the signal and pump are injected into separate input ports, which simplifies the pump injection, and the signal is also conveniently separated from the pump and idler tones. This not only addresses the signal-idler contamination, but also provides a convenient pump injection and removal for a straightforward experimental setup, and can be operated in a circulator mode if the

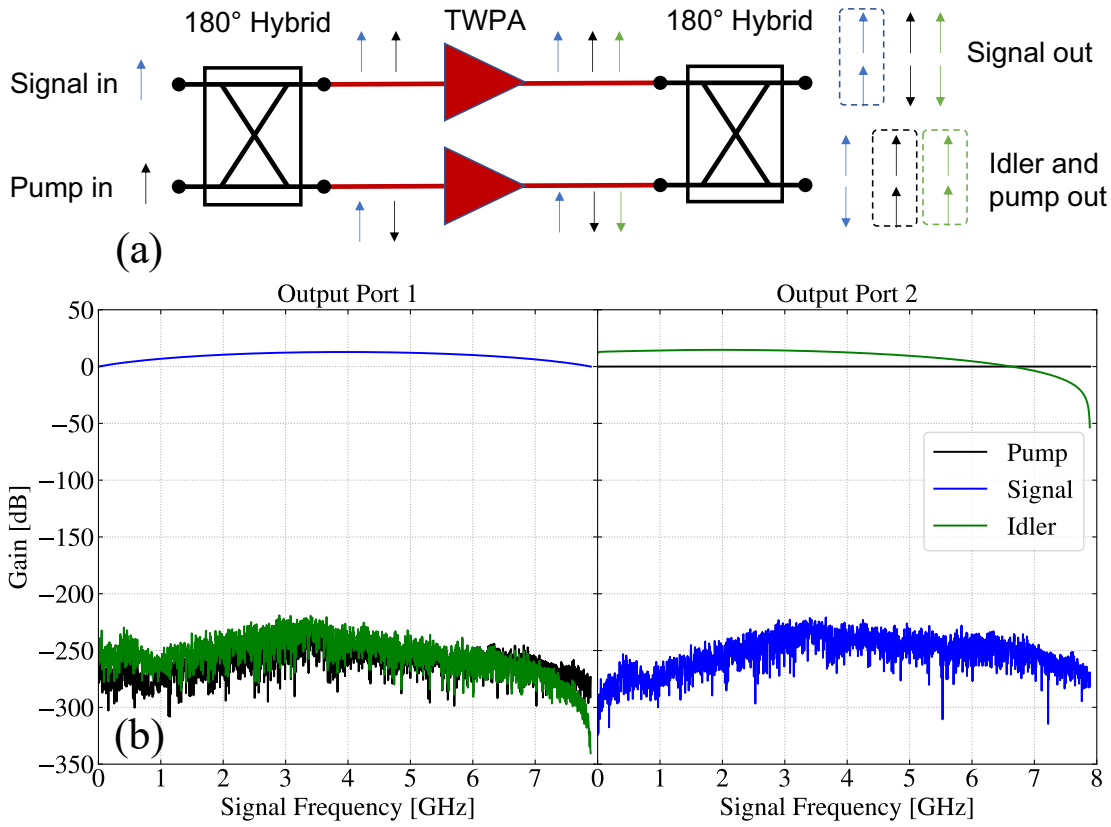

Figure 6.23: (a) Circuit diagram of a 3WM balanced-TWPA with 180-degree hybrids. The blue, black, and green arrows represent the signal, pump, and idler, respectively, and the direction of each arrow indicates the relative phase of each tone. This setup involves injecting the signal and pump tones into separate ports of the first hybrid, which results in the signals being in-phase relative to each arm and the pumps being in anti-phase. Combining the resultant tones at the second hybrid results in the signal exiting at one port and the pump and idler exiting at the other. (b) Simulated gain profiles of the output tones at each output port for configuration shown in (a).

idler is read out.

Note that the examples presented above are just a small subset of the many configurations made possible by the balanced-TWPA scheme, be it using ND-4WM, D-4WM, or DC-3WM. These configurations can be applied to KITWPAs, JTWPAs, SQUID-TWPAs, and importantly JPAs, which are already widely used in ultra-sensitive cryogenic experiments.

6.4 Summary

In this chapter, I have presented some advanced TWPA concepts, which could help to solve some of the practical obstacles to TWPA operation in the future.

In the first part of the chapter, I presented a series of KITWPA designs operating in the ND-4WM regime, whereby the injection of two pump tones along with a detected signal results in a broad, flat gain profile which removes the zero-gain gap that plagues other KITWPA devices and eliminates the need for a DC bias and the complexities associated with it. We first presented a design concept at microwave frequencies, before extending to mm frequencies, where this solution presents itself as a preferred solution for ultra-low-noise amplification at high (mm-wave) frequencies compared to the D-4WM and DC-3WM modes.

In the second part of the chapter, I described some of the key obstacles facing widespread TWPA operation and how these can be addressed by using a balanced-TWPA; a parallel TWPA architecture that manipulates the phases of the propagating tones to separate them using constructive and destructive interference, with the different configurations summarised in Tab. 6.6. Our configurations have been further verified by performing harmonic balance simulations using the technique described by [141], with the results being in agreement with the predicted balanced-TWPA behaviour. The beauty of this configuration is that once we have a pair of identical TWPA devices, which have been verified to work properly, we can quickly test the concept in a 'plug-and-play' setup by connecting the TWPAs to a pair of commercial RF hybrid couplers. Should this prove successful, the setup can be miniaturised by fabricating the TWPAs and couplers onto a single chip, thus producing an elegant TWPA package.

Configuration	Wave Mixing	Signal/Idler Separation	Simple Pump Injection	Simple Pump Removal	Circulator Mode
Fig. 6.18	D-4WM	✓†		✓†	
Fig. 6.19	D-4WM	✓			✓
Fig. 6.20	D-4WM		✓	✓	
Fig. 6.22	ND-4WM	✓			✓
Fig. 6.23	DC-3WM	✓	✓	✓†	✓†

† Properties cannot be simultaneously achieved within single configuration.

Table 6.6: Summary of balanced-TWPA configurations.

Chapter 7

Conclusions and Future Work

This thesis reports my work on the development of KITWPAs at microwave frequencies during the course of my four-year DPhil programme, including the disruptive period of pandemic restrictions and lockdown, and it encompasses the very first stage of TWPA development by the group. It began with basic theoretical framework foundations, before progressing to novel TWPA simulation techniques, the construction of cryostats and experimental setups from scratch, and the learning of all of the subtleties of device characterisation, before finally resulting in the measurement of several gain curves in our KITWPA devices.

In Chap. 2, we presented a general set of coupled-mode equations, derived from first principles, which demonstrated how the different wave mixing regimes reported in the literature are special cases of the general ND-4WM mixing regime. We also presented a novel multi-sinusoidal periodic loading scheme, allowing for alternative dispersion engineering approaches and potentially a novel band-stop filter able to generate an arbitrary number of stop bands at arbitrary frequencies.

Chap. 3 presented a rigorous KITWPA modelling technique, which uses the commercial EM software, HFSS, to perform EM simulations on an arbitrary transmission line, before feeding the output into SuperTWPA; a python package that I developed, which calculates the gain performance of a TWPA by solving the CMEs. The main advantage of this technique is the inclusion of subtle EM effects that are not taken into account in analytical transmission line models, and its enormous flexibility, as it allows any transmission line to be modelled without the need to completely re-derive the behaviour of the line from transmission line theory.

The chapter then proceeded to an analysis of how to optimise a KITWPA design, including the film and geometry choices. We conclude from an analysis of several superconducting films using standard BCS theory that the choice of material is seemingly unimportant, provided the correct thickness can be appropriately engineered. This, as well as the limitations of our current fabrication capabilities, justified our choice of 100 nm TiN as the film for our KITWPA designs. Whilst subsequent analysis revealed that the key behaviour for KITWPA operation appears to deviate from that predicted by standard BCS theory, the main analysis part of this chapter still remains valid as a 'worst case scenario'.

Chap. 5 presented the full experimental characterisation of the TiN KITWPA devices. Whilst the characterisation of the early test devices revealed the TiN film to exhibit a lossless non-linear regime at low powers, measurements of the full KITWPA devices revealed much higher RF losses than expected, meaning we were not able to measure high gain in the designed D-4WM regime. This implies that the pump powers required to achieve the desired high-gain performance of the KITWPA result in the film operating in a dissipative non-linear regime, which is not suitable for KITWPA operation. We found the losses to be highly frequency dependent, with the highest losses observed around 4 GHz. By placing the pump at higher frequencies, where the losses appeared to be smaller, and operating in a DC-3WM mode, we were able to measure gain, with the best spectrum giving a peak averaged gain of 5 dB with a bandwidth over 3-13 GHz at a pump frequency of 17.7 GHz.

Chap. 6 presented a series of designs for a dual-pump, ND-4WM KITWPA. We initially introduced the concept for low frequencies, but subsequently extended it to mm frequencies, where we demonstrated how ND-4WM is the most feasible way to realise a high frequency KITWPA. In the second part of the chapter, we presented a balanced-TWPA concept and discussed how it can address many of the obstacles to practical TWPA operation. We explained the underlying physics in terms of the phase control of the TWPAs and presented simulation results of several different balanced-TWPA configurations.

Moving forward, it is important to conclude whether there is some fundamental obstacle to using TiN for KITWPAs, or whether there is some issue with our design. Comparing to the literature, we see that our KITWPA design presented in Chap. 5 has much larger transmission line dimensions and uses a thicker film than devices that are typically reported, which may have an effect on the range of the lossless non-linear regime. Whilst the minimum transmission line dimensions are determined by

our photolithography capabilities, the thickness of the film can be altered. To test if the film thickness affects the above hypothesis, we are currently in the process of fabricating two further batches of TiN KITWPA devices with thickness 30 nm and 50 nm, respectively. If reducing the thickness of the film extends the non-linear regime closer to I_c, this would imply that the dimensions of the transmission line have more of an effect on the behaviour of the film than initially thought, hence require careful design consideration. It would also potentially justify the upgrade of our fabrication capabilities to include E-Beam lithography for finer transmission line patterning. We are also in the process of fabricating a NbTiN KITWPA device[1] with similar dimensions to our TiN device, to ascertain how the choice of material effects KITWPA performance in practice. If the NbTiN device is successful, it would suggest that material choice is important, although it would not necessarily rule out TiN for future KITWPA applications, just that NbTiN displays a much larger lossless non-linear regime.

Another key area to further investigate is the source of the ripples, which are seen in the measured transmission and gain profiles, since the presence of these ripples is currently a major obstacle to widespread TWPA use. We suspect the likely cause of these ripples to be impedance mismatches at the end of the KITWPA transmission lines, leading either to reflections of the signal, which interfere with the froward propagating signal to create ripples, or backward amplification due to the reflected signal and pump tones, which in the extreme case can lead to instability. To investigate the possible sources of the ripples, it would be of merit to experimentally measure the full set of 2-port S-parameters for the KITWPA devices, as this would allow the reflection coefficient at the ends of the KITWPA to be calculated. Inserting this reflection coefficient into a model for the loop gain of a KITWPA [119] to calculate the ripples in the gain profile then comparing this to the measured spectrum would allow us to infer whether the impedance mismatch is the likely source of the gain ripples.

In other future work, we plan on fabricating a microwave dual-pump KITWPA[2] based on the design in Chap. 6 to experimentally verify the concept. Additionally, we plan to experimentally verify the balanced-TWPA concept, initially in a 'plug-and-play' setup using two nominally identical TWPA devices and a pair of commercial RF couplers, but future work could progress to integrating all components 'on-chip' for an elegant TWPA package.

[1] To be fabricated at SRON, Leiden, The Netherlands.

[2] To be fabricated at Jet Propulsion Laboratory, Pasadena, California, USA.

The original aims for this thesis were to design, fabricate, and experimentally characterise a TiN-based KITWPA, including measurements of both the gain and the noise performance of the KITWPA devices. It was then envisaged that a prototype KITWPA would be used in combination with an SIS mixer or a qubit to ascertain whether the use of a KITWPA would significantly improve the noise performance of the receiver chain. In practice, many of these aims had to be significantly scaled back due to time constraints. Nevertheless, as detailed in this thesis, I have been able to experimentally characterise several TiN KITWPA devices, reporting one of, if not, the first gain measurements of a TiN KITWPA device reported in the literature. Whilst the measured gain is in disagreement with the predicted gain, this discrepancy allowed us to investigate some of the underlying physics of the KITWPA devices, pointing towards some curious behaviour of certain superconducting films. Aside from experimental characterisation, another unique contribution made in this thesis was the concept of a balanced-TWPA, which could provide a way to solve many of the problems commonly associated with KITWPA operation. The material presented in this thesis provides a solid base from which to build upon with further research and design iterations towards the end goal of a general-purpose, easy-to-use, high-gain, ultra-low-noise KITWPA device.

Appendix A

Coupled-Mode Equations Derivation and Solution

A.1 Full Derivation of the Coupled-Mode Equations

A.1.1 Obtaining Wave Equation

Begin with the Telegrapher Equations in (2.18a)-(2.18b), which describe the current (I) and voltage (V) in a transmission line (TL) with a series inductance per unit length, L, shunt capacitance per unit length, C, series resistance, R, and a shunt conductance, G.

Assuming that R, G, and C are constant but that L varies with current, differentiating (2.18a) with respect to t and (2.18b) with respect to z produce (A.1a) -(A.1b).

$$\frac{\partial^2 V}{\partial t \partial z} = -R\frac{\partial I}{\partial t} - \frac{\partial}{\partial t}\left[L\frac{\partial I}{\partial t}\right] \tag{A.1a}$$

$$\frac{\partial^2 I}{\partial z^2} = -G\frac{\partial V}{\partial z} - C\frac{\partial V^2}{\partial z \partial t} \tag{A.1b}$$

Assuming that $\frac{\partial^2 V}{\partial t \partial z} = \frac{\partial^2 V}{\partial z \partial t}$, substituting (2.18a) and (A.1a) into (A.1b) produces a lossy wave equation that describes the current along the TL, shown in Equation (A.2).

$$\frac{\partial^2 I}{\partial z^2} = RGI + (LG + RC)\frac{\partial I}{\partial t} + C\frac{\partial}{\partial t}\left[L\frac{\partial I}{\partial t}\right] \tag{A.2}$$

The non-linearity then comes from the fact that the kinetic inductance varies quadratically with the current, as shown in (A.3), where I_* is a term that sets the non-linearity of the kinetic inductance.

$$L = L_{k,0}\left(1 + \frac{I^2}{I_*^2}\right) + L_{\text{geo}} \tag{A.3}$$

Subbing (A.3) into (A.2) produces a non-linear wave equation.

$$\frac{\partial^2 I}{\partial z^2} = RGI + \left(\left(L_{k,0}\left(1 + \frac{I^2}{I_*^2}\right) + L_{\text{geo}}\right)G + RC\right)\frac{\partial I}{\partial t} + C\frac{\partial}{\partial t}\left[\left(L_{k,0}\left(1 + \frac{I^2}{I_*^2}\right) + L_{\text{geo}}\right)\frac{\partial I}{\partial t}\right] \tag{A.4}$$

This can be simplified to give (A.5), where $L_0 = L_{k,0} + L_{\text{geo}}$.

$$\frac{\partial^2 I}{\partial z^2} = RGI + (L_0 G + RC)\frac{\partial I}{\partial t} + L_{k,0}G\frac{I^2}{I_*^2}\frac{\partial I}{\partial t} + L_0 C\frac{\partial^2 I}{\partial t^2} + L_{k,0}C\frac{\partial}{\partial t}\left[\frac{I^2}{I_*^2}\frac{\partial I}{\partial t}\right] \tag{A.5}$$

A.1.2 Obtaining Coupled Mode Equations

To obtain the CME's an ansatz for the various current contributions is substituted into (A.5). This ansatz is shown in (A.6), where A_j is the slowly varying complex amplitude of the component, ω_j is the frequency of the component, $\gamma_j = \alpha_j + i\beta_j$ is the complex propagation constant, $j = p, s, i$ are the pump, signal, and idler components, respectively, and *c.c.* denotes the complex conjugate.

$$I = \frac{1}{2}\sum_{j=p,s,i} A_j(z)e^{i\omega_j t - \gamma_j z} + c.c. \tag{A.6}$$

Substituting (A.6) into (A.5) will generate a large number of terms, so consider each term in (A.5) separately to begin with.

First, take the spatial derivative of the current, starting with $\frac{\partial I}{\partial z}$, as shown in,

$$\begin{aligned}\frac{\partial I}{\partial z} = \frac{1}{2}\sum_{j=p,s,i} &\frac{dA_j}{dz}e^{i\omega_j t - \gamma_j z} - \gamma_j A_j e^{i\omega_j t - \gamma_j z} \\ &+ \frac{dA_j^*}{dz}e^{-i\omega_j t - \gamma_j^* z} - \gamma_j^* A_j^* e^{-i\omega_j t - \gamma_j^* z}.\end{aligned} \tag{A.7}$$

Next take $\frac{\partial^2 I}{\partial z^2}$, as shown in,

$$\begin{aligned}\frac{\partial^2 I}{\partial z^2} = \frac{1}{2}\sum_{j=p,s,i} &\frac{d^2 A_j}{dz^2}e^{i\omega_j t - \gamma_j z} - 2\gamma_j\frac{dA_j}{dz}e^{i\omega_j t - \gamma_j z} \\ &+ \gamma_j^2 A_j e^{i\omega_j t - \gamma_j z} + \frac{d^2 A_j^*}{dz^2}e^{-i\omega_j t - \gamma_j^* z} \\ &- 2\gamma_j^*\frac{dA_j^*}{dz}e^{-i\omega_j t - \gamma_j^* z} + \gamma_j^{*2} A_j^* e^{-i\omega_j t - \gamma_j^* z}.\end{aligned} \tag{A.8}$$

Eq. (A.8) can be simplified be using the slowly varying envelope approximation, $\left|\frac{d^2A_j}{dz^2}\right| \ll \left|\gamma_j \frac{dA_j}{dz}\right|$, to give,

$$\begin{aligned}\frac{\partial^2 I}{\partial z^2} = \frac{1}{2}\sum_{j=p,s,i} &- 2\gamma_j \frac{dA_j}{dz} e^{i\omega_j t - \gamma_j z} + \gamma_j^2 A_j e^{i\omega_j t - \gamma_j z} \\ &- 2\gamma_j^* \frac{dA_j^*}{dz} e^{-i\omega_j t - \gamma_j^* z} + \gamma_j^{*2} A_j^* e^{-i\omega_j t - \gamma_j^* z}.\end{aligned} \tag{A.9}$$

Next, move on to the time derivatives, starting with $\frac{\partial I}{\partial t}$, as shown in,

$$\frac{\partial I}{\partial t} = \frac{1}{2}\sum_{j=p,s,i} i\omega_j A_j e^{i\omega_j t - \gamma_j z} - i\omega_j A_j^* e^{-i\omega_j t - \gamma_j^* z}. \tag{A.10}$$

Then take $\frac{\partial^2 I}{\partial t^2}$, as shown in,

$$\frac{\partial^2 I}{\partial t^2} = \frac{1}{2}\sum_{j=p,s,i} -\omega_j^2 A_j e^{i\omega_j t - \gamma_j z} - \omega_j^2 A_j e^{-i\omega_j t - \gamma_j^* z}. \tag{A.11}$$

Using these and the definition, $\gamma = \sqrt{(R + i\omega L)(G + i\omega C)}$, the 1st, 2nd, and 4th terms in (A.5) simplify to,

$$\frac{1}{2}\sum_{j=p,s,i} \gamma_j^2 A_j e^{i\omega_j t - \gamma_j z} + \gamma_j^{*2} A_j^* e^{-i\omega_j t - \gamma_j^* z}. \tag{A.12}$$

These terms then cancel with terms 2 and 4 in (A.9). Eq. (A.5) then simplifies to,

$$-\sum_{j=p,s,i} \gamma_j \frac{dA_j}{dz} e^{i\omega_j t - \gamma_j z} + \gamma_j^* \frac{dA_j^*}{dz} e^{-i\omega_j t - \gamma_j^* z} = L_{k,0} G \frac{I^2}{I_*^2}\frac{\partial I}{\partial t} + L_{k,0} C \frac{\partial}{\partial t}\left[\frac{I^2}{I_*^2}\frac{\partial I}{\partial t}\right]. \tag{A.13}$$

The terms involving the non-linearity generate a large number of cross terms, which are computed with Mathematica.

$$\begin{aligned}I^2 \frac{\partial I}{\partial t} = \frac{1}{8}\Bigg(& e^{-3z(\gamma_i)^* - 3it\omega_i}(-i)\omega_i \left((A_i)^*\right)^3 \\ & - 2ie^{-2z(\gamma_i)^* - z(\gamma_p)^* - 2it\omega_i - it\omega_p}\left(A_p\right)^*\omega_i \left((A_i)^*\right)^2 \\ & - 2ie^{-2z(\gamma_i)^* - z(\gamma_s)^* - 2it\omega_i - it\omega_s}\left(A_s\right)^*\omega_i \left((A_i)^*\right)^2 \\ & - ie^{-2z(\gamma_i)^* - z\gamma_i - it\omega_i} A_i\omega_i \left((A_i)^*\right)^2 \\ & - 2ie^{-2z(\gamma_i)^* - z\gamma_p - 2it\omega_i + it\omega_p} A_p\omega_i \left((A_i)^*\right)^2 \\ & - 2ie^{-2z(\gamma_i)^* - z\gamma_s - 2it\omega_i + it\omega_s} A_s\omega_i \left((A_i)^*\right)^2 \\ & - ie^{-2z(\gamma_i)^* - z(\gamma_p)^* - 2it\omega_i - it\omega_p}\left(A_p\right)^*\omega_p \left((A_i)^*\right)^2 \\ & + e^{-2z(\gamma_i)^* - z\gamma_p - 2it\omega_i + it\omega_p} iA_p\omega_p \left((A_i)^*\right)^2 \\ & - ie^{-2z(\gamma_i)^* - z(\gamma_s)^* - 2it\omega_i - it\omega_s}\left(A_s\right)^*\omega_s \left((A_i)^*\right)^2\end{aligned}$$

$$+ e^{-2z(\gamma_i)^* - z\gamma_s - 2it\omega_i + it\omega_s} iA_s\omega_s \left((A_i)^*\right)^2$$
$$- ie^{-z(\gamma_i)^* - 2z(\gamma_p)^* - it\omega_i - 2it\omega_p} \left((A_p)^*\right)^2 \omega_i (A_i)^*$$
$$- ie^{-z(\gamma_i)^* - 2z(\gamma_s)^* - it\omega_i - 2it\omega_s} \left((A_s)^*\right)^2 \omega_i (A_i)^*$$
$$+ e^{-z(\gamma_i)^* - 2z\gamma_i + it\omega_i} iA_i^2\omega_i (A_i)^* - ie^{-z(\gamma_i)^* - 2z\gamma_p - it\omega_i + 2it\omega_p} A_p^2\omega_i (A_i)^*$$
$$- ie^{-z(\gamma_i)^* - 2z\gamma_s - it\omega_i + 2it\omega_s} A_s^2\omega_i (A_i)^*$$
$$- 2ie^{-z(\gamma_i)^* - z(\gamma_p)^* - z(\gamma_s)^* - it\omega_i - it\omega_p - it\omega_s} (A_p)^* (A_s)^* \omega_i (A_i)^*$$
$$- 2ie^{-z(\gamma_i)^* - z(\gamma_p)^* - z\gamma_p - it\omega_i} (A_p)^* A_p\omega_i (A_i)^*$$
$$- 2ie^{-z(\gamma_i)^* - z(\gamma_s)^* - z\gamma_p - it\omega_i + it\omega_p - it\omega_s} (A_s)^* A_p\omega_i (A_i)^*$$
$$- 2ie^{-z(\gamma_i)^* - z(\gamma_p)^* - z\gamma_s - it\omega_i - it\omega_p + it\omega_s} (A_p)^* A_s\omega_i (A_i)^*$$
$$- 2ie^{-z(\gamma_i)^* - z(\gamma_s)^* - z\gamma_s - it\omega_i} (A_s)^* A_s\omega_i (A_i)^*$$
$$- 2ie^{-z(\gamma_i)^* - z\gamma_p - z\gamma_s - it\omega_i + it\omega_p + it\omega_s} A_pA_s\omega_i (A_i)^*$$
$$- 2ie^{-z(\gamma_i)^* - 2z(\gamma_p)^* - it\omega_i - 2it\omega_p} \left((A_p)^*\right)^2 \omega_p (A_i)^*$$
$$+ 2e^{-z(\gamma_i)^* - 2z\gamma_p - it\omega_i + 2it\omega_p} iA_p^2\omega_p (A_i)^*$$
$$- 2ie^{-z(\gamma_i)^* - z(\gamma_p)^* - z(\gamma_s)^* - it\omega_i - it\omega_p - it\omega_s} (A_p)^* (A_s)^* \omega_p (A_i)^*$$
$$- 2ie^{-z(\gamma_i)^* - z(\gamma_p)^* - z\gamma_i - it\omega_p} (A_p)^* A_i\omega_p (A_i)^*$$
$$+2e^{-z(\gamma_i)^* - z(\gamma_s)^* - z\gamma_p - it\omega_i + it\omega_p - it\omega_s} i (A_s)^* A_p\omega_p (A_i)^* + 2e^{-z(\gamma_i)^* - z\gamma_i - z\gamma_p + it\omega_p} iA_iA_p\omega_p (A_i)^*$$
$$- 2ie^{-z(\gamma_i)^* - z(\gamma_p)^* - z\gamma_s - it\omega_i - it\omega_p + it\omega_s} (A_p)^* A_s\omega_p (A_i)^*$$
$$+ 2e^{-z(\gamma_i)^* - z\gamma_p - z\gamma_s - it\omega_i + it\omega_p + it\omega_s} iA_pA_s\omega_p (A_i)^*$$
$$- 2ie^{-z(\gamma_i)^* - 2z(\gamma_s)^* - it\omega_i - 2it\omega_s} \left((A_s)^*\right)^2 \omega_s (A_i)^*$$
$$+ 2e^{-z(\gamma_i)^* - 2z\gamma_s - it\omega_i + 2it\omega_s} iA_s^2\omega_s (A_i)^*$$
$$- 2ie^{-z(\gamma_i)^* - z(\gamma_p)^* - z(\gamma_s)^* - it\omega_i - it\omega_p - it\omega_s} (A_p)^* (A_s)^* \omega_s (A_i)^*$$
$$- 2ie^{-z(\gamma_i)^* - z(\gamma_s)^* - z\gamma_i - it\omega_s} (A_s)^* A_i\omega_s (A_i)^*$$
$$- 2ie^{-z(\gamma_i)^* - z(\gamma_s)^* - z\gamma_p - it\omega_i + it\omega_p - it\omega_s} (A_s)^* A_p\omega_s (A_i)^*$$
$$+ 2e^{-z(\gamma_i)^* - z(\gamma_p)^* - z\gamma_s - it\omega_i - it\omega_p + it\omega_s} i (A_p)^* A_s\omega_s (A_i)^*$$
$$+ 2e^{-z(\gamma_i)^* - z\gamma_i - z\gamma_s + it\omega_s} iA_iA_s\omega_s (A_i)^* + 2e^{-z(\gamma_i)^* - z\gamma_p - z\gamma_s - it\omega_i + it\omega_p + it\omega_s} iA_pA_s\omega_s (A_i)^*$$
$$+ e^{3it\omega_i - 3z\gamma_i} iA_i^3\omega_i$$
$$+ 2e^{-z(\gamma_p)^* - 2z\gamma_i + 2it\omega_i - it\omega_p} i (A_p)^* A_i^2\omega_i$$
$$+ 2e^{-z(\gamma_s)^* - 2z\gamma_i + 2it\omega_i - it\omega_s} i (A_s)^* A_i^2\omega_i$$
$$+ e^{-z\gamma_i - 2z\gamma_p + it\omega_i + 2it\omega_p} iA_iA_p^2\omega_i$$
$$+ e^{-z\gamma_i - 2z\gamma_s + it\omega_i + 2it\omega_s} iA_iA_s^2\omega_i$$
$$+ e^{-2z(\gamma_p)^* - z\gamma_i + it\omega_i - 2it\omega_p} i \left((A_p)^*\right)^2 A_i\omega_i$$
$$+ e^{-2z(\gamma_s)^* - z\gamma_i + it\omega_i - 2it\omega_s} i \left((A_s)^*\right)^2 A_i\omega_i$$

$$+ 2e^{-z(\gamma_p)^*-z(\gamma_s)^*-z\gamma_i+it\omega_i-it\omega_p-it\omega_s} i \left(A_p\right)^* \left(A_s\right)^* A_i\omega_i$$
$$+ 2e^{-2z\gamma_i-z\gamma_p+2it\omega_i+it\omega_p} iA_i^2A_p\omega_i$$
$$+ 2e^{-z(\gamma_p)^*-z\gamma_i-z\gamma_p+it\omega_i} i \left(A_p\right)^* A_iA_p\omega_i$$
$$+ 2e^{-z(\gamma_s)^*-z\gamma_i-z\gamma_p+it\omega_i+it\omega_p-it\omega_s} i \left(A_s\right)^* A_iA_p\omega_i$$
$$+ 2e^{-2z\gamma_i-z\gamma_s+2it\omega_i+it\omega_s} iA_i^2A_s\omega_i$$
$$+ 2e^{-z(\gamma_p)^*-z\gamma_i-z\gamma_s+it\omega_i-it\omega_p+it\omega_s} i \left(A_p\right)^* A_iA_s\omega_i$$
$$+ 2e^{-z(\gamma_s)^*-z\gamma_i-z\gamma_s+it\omega_i} i \left(A_s\right)^* A_iA_s\omega_i$$
$$+ 2e^{-z\gamma_i-z\gamma_p-z\gamma_s+it\omega_i+it\omega_p+it\omega_s} iA_iA_pA_s\omega_i$$
$$- ie^{-3z(\gamma_p)^*-3it\omega_p} \left(\left(A_p\right)^*\right)^3\omega_p + e^{3it\omega_p-3z\gamma_p} iA_p^3\omega_p$$
$$- ie^{-z(\gamma_p)^*-2z(\gamma_s)^*-it\omega_p-2it\omega_s} \left(A_p\right)^* \left(\left(A_s\right)^*\right)^2\omega_p$$
$$- ie^{-z(\gamma_p)^*-2z\gamma_i+2it\omega_i-it\omega_p} \left(A_p\right)^* A_i^2\omega_p + e^{-z(\gamma_p)^*-2z\gamma_p+it\omega_p} i \left(A_p\right)^* A_p^2\omega_p$$
$$+ 2e^{-z(\gamma_s)^*-2z\gamma_p+2it\omega_p-it\omega_s} i \left(A_s\right)^* A_p^2\omega_p$$
$$+ 2e^{-z\gamma_i-2z\gamma_p+it\omega_i+2it\omega_p} iA_iA_p^2\omega_p$$
$$- ie^{-z(\gamma_p)^*-2z\gamma_s-it\omega_p+2it\omega_s} \left(A_p\right)^* A_s^2\omega_p$$
$$+ e^{-z\gamma_p-2z\gamma_s+it\omega_p+2it\omega_s} iA_pA_s^2\omega_p$$
$$- 2ie^{-2z(\gamma_p)^*-z(\gamma_s)^*-2it\omega_p-it\omega_s} \left(\left(A_p\right)^*\right)^2 \left(A_s\right)^*\omega_p$$
$$- 2ie^{-2z(\gamma_p)^*-z\gamma_i+it\omega_i-2it\omega_p} \left(\left(A_p\right)^*\right)^2 A_i\omega_p$$
$$- 2ie^{-z(\gamma_p)^*-z(\gamma_s)^*-z\gamma_i+it\omega_i-it\omega_p-it\omega_s} \left(A_p\right)^* \left(A_s\right)^* A_i\omega_p$$
$$- ie^{-2z(\gamma_p)^*-z\gamma_p-it\omega_p} \left(\left(A_p\right)^*\right)^2 A_p\omega_p$$
$$+ e^{-2z(\gamma_s)^*-z\gamma_p+it\omega_p-2it\omega_s} i \left(\left(A_s\right)^*\right)^2 A_p\omega_p$$
$$+ e^{-2z\gamma_i-z\gamma_p+2it\omega_i+it\omega_p} iA_i^2A_p\omega_p$$
$$+ 2e^{-z(\gamma_s)^*-z\gamma_i-z\gamma_p+it\omega_i+it\omega_p-it\omega_s} i \left(A_s\right)^* A_iA_p\omega_p$$
$$- 2ie^{-2z(\gamma_p)^*-z\gamma_s-2it\omega_p+it\omega_s} \left(\left(A_p\right)^*\right)^2 A_s\omega_p$$
$$+ 2e^{-2z\gamma_p-z\gamma_s+2it\omega_p+it\omega_s} iA_p^2A_s\omega_p$$
$$- 2ie^{-z(\gamma_p)^*-z(\gamma_s)^*-z\gamma_s-it\omega_p} \left(A_p\right)^* \left(A_s\right)^* A_s\omega_p$$
$$- 2ie^{-z(\gamma_p)^*-z\gamma_i-z\gamma_s+it\omega_i-it\omega_p+it\omega_s} \left(A_p\right)^* A_iA_s\omega_p$$
$$+ 2e^{-z(\gamma_s)^*-z\gamma_p-z\gamma_s+it\omega_p} i \left(A_s\right)^* A_pA_s\omega_p$$
$$+ 2e^{-z\gamma_i-z\gamma_p-z\gamma_s+it\omega_i+it\omega_p+it\omega_s} iA_iA_pA_s\omega_p$$
$$- ie^{-3z(\gamma_s)^*-3it\omega_s} \left(\left(A_s\right)^*\right)^3\omega_s$$
$$+ e^{3it\omega_s-3z\gamma_s} iA_s^3\omega_s$$
$$- 2ie^{-z(\gamma_p)^*-2z(\gamma_s)^*-it\omega_p-2it\omega_s} \left(A_p\right)^* \left(\left(A_s\right)^*\right)^2\omega_s$$
$$- ie^{-z(\gamma_s)^*-2z\gamma_i+2it\omega_i-it\omega_s} \left(A_s\right)^* A_i^2\omega_s$$

$$
\begin{aligned}
&- ie^{-z(\gamma_s)^*-2z\gamma_p+2it\omega_p-it\omega_s}\left(A_s\right)^* A_p^2\omega_s \\
&+ 2e^{-z(\gamma_p)^*-2z\gamma_s-it\omega_p+2it\omega_s} i\left(A_p\right)^* A_s^2\omega_s \\
&+ e^{-z(\gamma_s)^*-2z\gamma_s+it\omega_s} i\left(A_s\right)^* A_s^2\omega_s \\
&+ 2e^{-z\gamma_i-2z\gamma_s+it\omega_i+2it\omega_s} iA_iA_s^2\omega_s \\
&+ 2e^{-z\gamma_p-2z\gamma_s+it\omega_p+2it\omega_s} iA_pA_s^2\omega_s \\
&- ie^{-2z(\gamma_p)^*-z(\gamma_s)^*-2it\omega_p-it\omega_s}\left(\left(A_p\right)^*\right)^2\left(A_s\right)^*\omega_s \\
&- 2ie^{-2z(\gamma_s)^*-z\gamma_i+it\omega_i-2it\omega_s}\left(\left(A_s\right)^*\right)^2 A_i\omega_s \\
&- 2ie^{-z(\gamma_p)^*-z(\gamma_s)^*-z\gamma_i+it\omega_i-it\omega_p-it\omega_s}\left(A_p\right)^*\left(A_s\right)^* A_i\omega_s \\
&- 2ie^{-2z(\gamma_s)^*-z\gamma_p+it\omega_p-2it\omega_s}\left(\left(A_s\right)^*\right)^2 A_p\omega_s \\
&- 2ie^{-z(\gamma_p)^*-z(\gamma_s)^*-z\gamma_p-it\omega_s}\left(A_p\right)^*\left(A_s\right)^* A_p\omega_s \\
&- 2ie^{-z(\gamma_s)^*-z\gamma_i-z\gamma_p+it\omega_i+it\omega_p-it\omega_s}\left(A_s\right)^* A_iA_p\omega_s \\
&+ e^{-2z(\gamma_p)^*-z\gamma_s-2it\omega_p+it\omega_s} i\left(\left(A_p\right)^*\right)^2 A_s\omega_s \\
&- ie^{-2z(\gamma_s)^*-z\gamma_s-it\omega_s}\left(\left(A_s\right)^*\right)^2 A_s\omega_s \\
&+ e^{-2z\gamma_i-z\gamma_s+2it\omega_i+it\omega_s} iA_i^2A_s\omega_s \\
&+ e^{-2z\gamma_p-z\gamma_s+2it\omega_p+it\omega_s} iA_p^2A_s\omega_s \\
&+ 2e^{-z(\gamma_p)^*-z\gamma_i-z\gamma_s+it\omega_i-it\omega_p+it\omega_s} i\left(A_p\right)^* A_iA_s\omega_s \\
&+ 2e^{-z(\gamma_p)^*-z\gamma_p-z\gamma_s+it\omega_s} i\left(A_p\right)^* A_pA_s\omega_s \\
&+ 2e^{-z\gamma_i-z\gamma_p-z\gamma_s+it\omega_i+it\omega_p+it\omega_s} iA_iA_pA_s\omega_s\Bigg) \qquad \text{(A.14)}
\end{aligned}
$$

And time derivative.

$$
\begin{aligned}
\frac{\partial}{\partial t}\left[I^2\frac{\partial I}{\partial t}\right] = \frac{1}{8}\Bigg(&- 3e^{-3z(\gamma_i)^*-3it\omega_i}\omega_i^2\left(\left(A_i\right)^*\right)^3 \\
&- e^{-2z(\gamma_i)^*-z\gamma_i-it\omega_i} A_i\omega_i^2\left(\left(A_i\right)^*\right)^2 \\
&- ie^{-2z(\gamma_i)^*-z(\gamma_p)^*-2it\omega_i-it\omega_p}\left(A_p\right)^*\left(-2i\omega_i - i\omega_p\right)\omega_p\left(\left(A_i\right)^*\right)^2 \\
&- 2ie^{-2z(\gamma_i)^*-z\gamma_p-2it\omega_i+it\omega_p} A_p\omega_i\left(i\omega_p - 2i\omega_i\right)\left(\left(A_i\right)^*\right)^2 \\
&+ e^{-2z(\gamma_i)^*-z\gamma_p-2it\omega_i+it\omega_p} iA_p\omega_p\left(i\omega_p - 2i\omega_i\right)\left(\left(A_i\right)^*\right)^2 \\
&- 2ie^{-2z(\gamma_i)^*-z(\gamma_p)^*-2it\omega_i-it\omega_p}\left(A_p\right)^*\omega_i\left(-2i\omega_i - i\omega_p\right)\left(\left(A_i\right)^*\right)^2 \\
&- ie^{-2z(\gamma_i)^*-z(\gamma_s)^*-2it\omega_i-it\omega_s}\left(A_s\right)^*\left(-2i\omega_i - i\omega_s\right)\omega_s\left(\left(A_i\right)^*\right)^2 \\
&- 2ie^{-2z(\gamma_i)^*-z\gamma_s-2it\omega_i+it\omega_s} A_s\omega_i\left(i\omega_s - 2i\omega_i\right)\left(\left(A_i\right)^*\right)^2 \\
&+ e^{-2z(\gamma_i)^*-z\gamma_s-2it\omega_i+it\omega_s} iA_s\omega_s\left(i\omega_s - 2i\omega_i\right)\left(\left(A_i\right)^*\right)^2 \\
&- 2ie^{-2z(\gamma_i)^*-z(\gamma_s)^*-2it\omega_i-it\omega_s}\left(A_s\right)^*\omega_i\left(-2i\omega_i - i\omega_s\right)\left(\left(A_i\right)^*\right)^2 \\
&- e^{-z(\gamma_i)^*-2z\gamma_i+it\omega_i} A_i^2\omega_i^2\left(A_i\right)^*
\end{aligned}
$$

$$
\begin{aligned}
&- 2e^{-z(\gamma_i)^*-z(\gamma_p)^*-z\gamma_p-it\omega_i}\left(A_p\right)^* A_p\omega_i^2\left(A_i\right)^* \\
&- 2e^{-z(\gamma_i)^*-z(\gamma_s)^*-z\gamma_s-it\omega_i}\left(A_s\right)^* A_s\omega_i^2\left(A_i\right)^* \\
&- 2e^{-z(\gamma_i)^*-z(\gamma_p)^*-z\gamma_i-it\omega_p}\left(A_p\right)^* A_i\omega_p^2\left(A_i\right)^* \\
&- 2e^{-z(\gamma_i)^*-z\gamma_i-z\gamma_p+it\omega_p}A_iA_p\omega_p^2\left(A_i\right)^* \\
&- 2e^{-z(\gamma_i)^*-z(\gamma_s)^*-z\gamma_i-it\omega_s}\left(A_s\right)^* A_i\omega_s^2\left(A_i\right)^* \\
&- 2e^{-z(\gamma_i)^*-z\gamma_i-z\gamma_s+it\omega_s}A_iA_s\omega_s^2\left(A_i\right)^* \\
&- 2ie^{-z(\gamma_i)^*-2z(\gamma_p)^*-it\omega_i-2it\omega_p}\left(\left(A_p\right)^*\right)^2\left(-i\omega_i-2i\omega_p\right)\omega_p\left(A_i\right)^* \\
&- ie^{-z(\gamma_i)^*-2z\gamma_p-it\omega_i+2it\omega_p}A_p^2\omega_i\left(2i\omega_p-i\omega_i\right)\left(A_i\right)^* \\
&+ 2e^{-z(\gamma_i)^*-2z\gamma_p-it\omega_i+2it\omega_p}iA_p^2\omega_p\left(2i\omega_p-i\omega_i\right)\left(A_i\right)^* \\
&- ie^{-z(\gamma_i)^*-2z(\gamma_p)^*-it\omega_i-2it\omega_p}\left(\left(A_p\right)^*\right)^2\omega_i\left(-i\omega_i-2i\omega_p\right)\left(A_i\right)^* \\
&- 2ie^{-z(\gamma_i)^*-z(\gamma_s)^*-z\gamma_p-it\omega_i+it\omega_p-it\omega_s}\left(A_s\right)^* A_p\left(-i\omega_i+i\omega_p-i\omega_s\right)\omega_s\left(A_i\right)^* \\
&- 2ie^{-z(\gamma_i)^*-z(\gamma_p)^*-z(\gamma_s)^*-it\omega_i-it\omega_p-it\omega_s}\left(A_p\right)^*\left(A_s\right)^*\left(-i\omega_i-i\omega_p-i\omega_s\right)\omega_s\left(A_i\right)^* \\
&- 2ie^{-z(\gamma_i)^*-2z(\gamma_s)^*-it\omega_i-2it\omega_s}\left(\left(A_s\right)^*\right)^2\left(-i\omega_i-2i\omega_s\right)\omega_s\left(A_i\right)^* \\
&- 2ie^{-z(\gamma_i)^*-z\gamma_p-z\gamma_s-it\omega_i+it\omega_p+it\omega_s}A_pA_s\omega_i\left(-i\omega_i+i\omega_p+i\omega_s\right)\left(A_i\right)^* \\
&+ 2e^{-z(\gamma_i)^*-z\gamma_p-z\gamma_s-it\omega_i+it\omega_p+it\omega_s}iA_pA_s\omega_p\left(-i\omega_i+i\omega_p+i\omega_s\right)\left(A_i\right)^* \\
&+ 2e^{-z(\gamma_i)^*-z\gamma_p-z\gamma_s-it\omega_i+it\omega_p+it\omega_s}iA_pA_s\omega_s\left(-i\omega_i+i\omega_p+i\omega_s\right)\left(A_i\right)^* \\
&- 2ie^{-z(\gamma_i)^*-z(\gamma_p)^*-z\gamma_s-it\omega_i-it\omega_p+it\omega_s}\left(A_p\right)^* A_s\omega_i\left(-i\omega_i-i\omega_p+i\omega_s\right)\left(A_i\right)^* \\
&- 2ie^{-z(\gamma_i)^*-z(\gamma_p)^*-z\gamma_s-it\omega_i-it\omega_p+it\omega_s}\left(A_p\right)^* A_s\omega_p\left(-i\omega_i-i\omega_p+i\omega_s\right)\left(A_i\right)^* \\
&+ 2e^{-z(\gamma_i)^*-z(\gamma_p)^*-z\gamma_s-it\omega_i-it\omega_p+it\omega_s}i\left(A_p\right)^* A_s\omega_s\left(-i\omega_i-i\omega_p+i\omega_s\right)\left(A_i\right)^* \\
&- ie^{-z(\gamma_i)^*-2z\gamma_s-it\omega_i+2it\omega_s}A_s^2\omega_i\left(2i\omega_s-i\omega_i\right)\left(A_i\right)^* \\
&+ 2e^{-z(\gamma_i)^*-2z\gamma_s-it\omega_i+2it\omega_s}iA_s^2\omega_s\left(2i\omega_s-i\omega_i\right)\left(A_i\right)^* \\
&- 2ie^{-z(\gamma_i)^*-z(\gamma_s)^*-z\gamma_p-it\omega_i+it\omega_p-it\omega_s}\left(A_s\right)^* A_p\omega_i\left(-i\omega_i+i\omega_p-i\omega_s\right)\left(A_i\right)^* \\
&+ 2e^{-z(\gamma_i)^*-z(\gamma_s)^*-z\gamma_p-it\omega_i+it\omega_p-it\omega_s}i\left(A_s\right)^* A_p\omega_p\left(-i\omega_i+i\omega_p-i\omega_s\right)\left(A_i\right)^* \\
&- 2ie^{-z(\gamma_i)^*-z(\gamma_p)^*-z(\gamma_s)^*-it\omega_i-it\omega_p-it\omega_s}\left(A_p\right)^*\left(A_s\right)^*\omega_i\left(-i\omega_i-i\omega_p-i\omega_s\right)\left(A_i\right)^* \\
&- 2ie^{-z(\gamma_i)^*-z(\gamma_p)^*-z(\gamma_s)^*-it\omega_i-it\omega_p-it\omega_s}\left(A_p\right)^*\left(A_s\right)^*\omega_p\left(-i\omega_i-i\omega_p-i\omega_s\right)\left(A_i\right)^* \\
&- ie^{-z(\gamma_i)^*-2z(\gamma_s)^*-it\omega_i-2it\omega_s}\left(\left(A_s\right)^*\right)^2\omega_i\left(-i\omega_i-2i\omega_s\right)\left(A_i\right)^* \\
&- 3e^{3it\omega_i-3z\gamma_i}A_i^3\omega_i^2 \\
&- 2e^{-z(\gamma_p)^*-z\gamma_i-z\gamma_p+it\omega_i}\left(A_p\right)^* A_iA_p\omega_i^2 \\
&- 2e^{-z(\gamma_s)^*-z\gamma_i-z\gamma_s+it\omega_i}\left(A_s\right)^* A_iA_s\omega_i^2 \\
&- 3e^{-3z(\gamma_p)^*-3it\omega_p}\left(\left(A_p\right)^*\right)^3\omega_p^2 \\
&- 3e^{3it\omega_p-3z\gamma_p}A_p^3\omega_p^2 \\
&- e^{-z(\gamma_p)^*-2z\gamma_p+it\omega_p}\left(A_p\right)^* A_p^2\omega_p^2
\end{aligned}
$$

$$
\begin{aligned}
&- e^{-2z(\gamma_p)^* - z\gamma_p - it\omega_p} \left((A_p)^*\right)^2 A_p \omega_p^2 \\
&- 2e^{-z(\gamma_p)^* - z(\gamma_s)^* - z\gamma_s - it\omega_p} (A_p)^* (A_s)^* A_s \omega_p^2 \\
&- 2e^{-z(\gamma_s)^* - z\gamma_p - z\gamma_s + it\omega_p} (A_s)^* A_p A_s \omega_p^2 \\
&- 3e^{-3z(\gamma_s)^* - 3it\omega_s} \left((A_s)^*\right)^3 \omega_s^2 \\
&- 3e^{3it\omega_s - 3z\gamma_s} A_s^3 \omega_s^2 \\
&- e^{-z(\gamma_s)^* - 2z\gamma_s + it\omega_s} (A_s)^* A_s^2 \omega_s^2 \\
&- 2e^{-z(\gamma_p)^* - z(\gamma_s)^* - z\gamma_p - it\omega_s} (A_p)^* (A_s)^* A_p \omega_s^2 \\
&- e^{-2z(\gamma_s)^* - z\gamma_s - it\omega_s} \left((A_s)^*\right)^2 A_s \omega_s^2 \\
&- 2e^{-z(\gamma_p)^* - z\gamma_p - z\gamma_s + it\omega_s} (A_p)^* A_p A_s \omega_s^2 \\
&- ie^{-z(\gamma_p)^* - 2z\gamma_i + 2it\omega_i - it\omega_p} (A_p)^* A_i^2 (2i\omega_i - i\omega_p) \omega_p \\
&- 2ie^{-2z(\gamma_p)^* - z\gamma_i + it\omega_i - 2it\omega_p} \left((A_p)^*\right)^2 A_i (i\omega_i - 2i\omega_p) \omega_p \\
&+ 2e^{-2z\gamma_i - z\gamma_p + 2it\omega_i + it\omega_p} i A_i^2 A_p \omega_i (2i\omega_i + i\omega_p) \\
&+ e^{-2z\gamma_i - z\gamma_p + 2it\omega_i + it\omega_p} i A_i^2 A_p \omega_p (2i\omega_i + i\omega_p) \\
&+ e^{-z\gamma_i - 2z\gamma_p + it\omega_i + 2it\omega_p} i A_i A_p^2 \omega_i (i\omega_i + 2i\omega_p) \\
&+ 2e^{-z\gamma_i - 2z\gamma_p + it\omega_i + 2it\omega_p} i A_i A_p^2 \omega_p (i\omega_i + 2i\omega_p) \\
&+ 2e^{-z(\gamma_p)^* - 2z\gamma_i + 2it\omega_i - it\omega_p} i (A_p)^* A_i^2 \omega_i (2i\omega_i - i\omega_p) \\
&+ e^{-2z(\gamma_p)^* - z\gamma_i + it\omega_i - 2it\omega_p} i \left((A_p)^*\right)^2 A_i \omega_i (i\omega_i - 2i\omega_p) \\
&- ie^{-z(\gamma_s)^* - 2z\gamma_i + 2it\omega_i - it\omega_s} (A_s)^* A_i^2 (2i\omega_i - i\omega_s) \omega_s \\
&- ie^{-2z(\gamma_p)^* - z(\gamma_s)^* - 2it\omega_p - it\omega_s} \left((A_p)^*\right)^2 (A_s)^* (-2i\omega_p - i\omega_s) \omega_s \\
&- 2ie^{-z(\gamma_s)^* - z\gamma_i - z\gamma_p + it\omega_i + it\omega_p - it\omega_s} (A_s)^* A_i A_p (i\omega_i + i\omega_p - i\omega_s) \omega_s \\
&- ie^{-z(\gamma_s)^* - 2z\gamma_p + 2it\omega_p - it\omega_s} (A_s)^* A_p^2 (2i\omega_p - i\omega_s) \omega_s \\
&- 2ie^{-z(\gamma_p)^* - z(\gamma_s)^* - z\gamma_i + it\omega_i - it\omega_p - it\omega_s} (A_p)^* (A_s)^* A_i (i\omega_i - i\omega_p - i\omega_s) \omega_s \\
&- 2ie^{-2z(\gamma_s)^* - z\gamma_i + it\omega_i - 2it\omega_s} \left((A_s)^*\right)^2 A_i (i\omega_i - 2i\omega_s) \omega_s \\
&- 2ie^{-z(\gamma_p)^* - 2z(\gamma_s)^* - it\omega_p - 2it\omega_s} (A_p)^* \left((A_s)^*\right)^2 (-i\omega_p - 2i\omega_s) \omega_s \\
&- 2ie^{-2z(\gamma_s)^* - z\gamma_p + it\omega_p - 2it\omega_s} \left((A_s)^*\right)^2 A_p (i\omega_p - 2i\omega_s) \omega_s \\
&+ 2e^{-2z\gamma_i - z\gamma_s + 2it\omega_i + it\omega_s} i A_i^2 A_s \omega_i (2i\omega_i + i\omega_s) \\
&+ e^{-2z\gamma_i - z\gamma_s + 2it\omega_i + it\omega_s} i A_i^2 A_s \omega_s (2i\omega_i + i\omega_s) \\
&- 2ie^{-2z(\gamma_p)^* - z\gamma_s - 2it\omega_p + it\omega_s} \left((A_p)^*\right)^2 A_s \omega_p (i\omega_s - 2i\omega_p) \\
&+ e^{-2z(\gamma_p)^* - z\gamma_s - 2it\omega_p + it\omega_s} i \left((A_p)^*\right)^2 A_s \omega_s (i\omega_s - 2i\omega_p) \\
&+ 2e^{-z\gamma_i - z\gamma_p - z\gamma_s + it\omega_i + it\omega_p + it\omega_s} i A_i A_p A_s \omega_i (i\omega_i + i\omega_p + i\omega_s) \\
&+ 2e^{-z\gamma_i - z\gamma_p - z\gamma_s + it\omega_i + it\omega_p + it\omega_s} i A_i A_p A_s \omega_p (i\omega_i + i\omega_p + i\omega_s) \\
&+ 2e^{-z\gamma_i - z\gamma_p - z\gamma_s + it\omega_i + it\omega_p + it\omega_s} i A_i A_p A_s \omega_s (i\omega_i + i\omega_p + i\omega_s)
\end{aligned}
$$

$$
\begin{aligned}
&+2e^{-2z\gamma_p-z\gamma_s+2it\omega_p+it\omega_s}iA_p^2A_s\omega_p\left(2i\omega_p+i\omega_s\right)+e^{-2z\gamma_p-z\gamma_s+2it\omega_p+it\omega_s}iA_p^2A_s\omega_s\left(2i\omega_p+i\omega_s\right)\\
&+2e^{-z(\gamma_p)^*-z\gamma_i-z\gamma_s+it\omega_i-it\omega_p+it\omega_s}i\left(A_p\right)^*A_iA_s\omega_i\left(i\omega_i-i\omega_p+i\omega_s\right)\\
&-2ie^{-z(\gamma_p)^*-z\gamma_i-z\gamma_s+it\omega_i-it\omega_p+it\omega_s}\left(A_p\right)^*A_iA_s\omega_p\left(i\omega_i-i\omega_p+i\omega_s\right)\\
&+2e^{-z(\gamma_p)^*-z\gamma_i-z\gamma_s+it\omega_i-it\omega_p+it\omega_s}i\left(A_p\right)^*A_iA_s\omega_s\left(i\omega_i-i\omega_p+i\omega_s\right)\\
&+e^{-z\gamma_i-2z\gamma_s+it\omega_i+2it\omega_s}iA_iA_s^2\omega_i\left(i\omega_i+2i\omega_s\right)\\
&+2e^{-z\gamma_i-2z\gamma_s+it\omega_i+2it\omega_s}iA_iA_s^2\omega_s\left(i\omega_i+2i\omega_s\right)\\
&-ie^{-z(\gamma_p)^*-2z\gamma_s-it\omega_p+2it\omega_s}\left(A_p\right)^*A_s^2\omega_p\left(2i\omega_s-i\omega_p\right)\\
&+2e^{-z(\gamma_p)^*-2z\gamma_s-it\omega_p+2it\omega_s}i\left(A_p\right)^*A_s^2\omega_s\left(2i\omega_s-i\omega_p\right)\\
&+e^{-z\gamma_p-2z\gamma_s+it\omega_p+2it\omega_s}iA_pA_s^2\omega_p\left(i\omega_p+2i\omega_s\right)\\
&+2e^{-z\gamma_p-2z\gamma_s+it\omega_p+2it\omega_s}iA_pA_s^2\omega_s\left(i\omega_p+2i\omega_s\right)\\
&+2e^{-z(\gamma_s)^*-2z\gamma_i+2it\omega_i-it\omega_s}i\left(A_s\right)^*A_i^2\omega_i\left(2i\omega_i-i\omega_s\right)\\
&-2ie^{-2z(\gamma_p)^*-z(\gamma_s)^*-2it\omega_p-it\omega_s}\left(\left(A_p\right)^*\right)^2\left(A_s\right)^*\omega_p\left(-2i\omega_p-i\omega_s\right)\\
&+2e^{-z(\gamma_s)^*-z\gamma_i-z\gamma_p+it\omega_i+it\omega_p-it\omega_s}i\left(A_s\right)^*A_iA_p\omega_i\left(i\omega_i+i\omega_p-i\omega_s\right)\\
&+2e^{-z(\gamma_s)^*-z\gamma_i-z\gamma_p+it\omega_i+it\omega_p-it\omega_s}i\left(A_s\right)^*A_iA_p\omega_p\left(i\omega_i+i\omega_p-i\omega_s\right)\\
&+2e^{-z(\gamma_s)^*-2z\gamma_p+2it\omega_p-it\omega_s}i\left(A_s\right)^*A_p^2\omega_p\left(2i\omega_p-i\omega_s\right)\\
&+2e^{-z(\gamma_p)^*-z(\gamma_s)^*-z\gamma_i+it\omega_i-it\omega_p-it\omega_s}i\left(A_p\right)^*\left(A_s\right)^*A_i\omega_i\left(i\omega_i-i\omega_p-i\omega_s\right)\\
&-2ie^{-z(\gamma_p)^*-z(\gamma_s)^*-z\gamma_i+it\omega_i-it\omega_p-it\omega_s}\left(A_p\right)^*\left(A_s\right)^*A_i\omega_p\left(i\omega_i-i\omega_p-i\omega_s\right)\\
&+e^{-2z(\gamma_s)^*-z\gamma_i+it\omega_i-2it\omega_s}i\left(\left(A_s\right)^*\right)^2A_i\omega_i\left(i\omega_i-2i\omega_s\right)\\
&-ie^{-z(\gamma_p)^*-2z(\gamma_s)^*-it\omega_p-2it\omega_s}\left(A_p\right)^*\left(\left(A_s\right)^*\right)^2\omega_p\left(-i\omega_p-2i\omega_s\right)\\
&+e^{-2z(\gamma_s)^*-z\gamma_p+it\omega_p-2it\omega_s}i\left(\left(A_s\right)^*\right)^2A_p\omega_p\left(i\omega_p-2i\omega_s\right)\Bigg)
\end{aligned}
\tag{A.15}
$$

To caluclate the pump CME, sub both (A.14) and (A.15) into (A.13) and collect terms with the frequency component equal to ω_p.

$$
\begin{aligned}
-\gamma_p\frac{dA_p}{dz}e^{i\omega_pt-\gamma_pz}=\frac{L_{k,0}G}{8I_*^2}\Bigg(&2e^{-z(\gamma_i)^*-z\gamma_i-z\gamma_p+it\omega_p}iA_iA_p\omega_p\left(A_i\right)^*\\
&+2e^{-z(\gamma_p)^*-z\gamma_i-z\gamma_s+it\omega_i-it\omega_p+it\omega_s}i\left(A_p\right)^*A_iA_s\omega_i\\
&+e^{-z(\gamma_p)^*-2z\gamma_p+it\omega_p}i\left(A_p\right)^*A_p^2\omega_p\\
&-2ie^{-z(\gamma_p)^*-z\gamma_i-z\gamma_s+it\omega_i-it\omega_p+it\omega_s}\left(A_p\right)^*A_iA_s\omega_p\\
&+2e^{-z(\gamma_s)^*-z\gamma_p-z\gamma_s+it\omega_p}i\left(A_s\right)^*A_pA_s\omega_p\\
&+2e^{-z(\gamma_p)^*-z\gamma_i-z\gamma_s+it\omega_i-it\omega_p+it\omega_s}i\left(A_p\right)^*A_iA_s\omega_s\Bigg)\\
&+\frac{i\omega_pL_{k,0}C}{8I_*^2}\Bigg(2e^{-z(\gamma_i)^*-z\gamma_i-z\gamma_p+it\omega_p}iA_iA_p\omega_p\left(A_i\right)^*
\end{aligned}
$$

$$+ 2e^{-z(\gamma_p)^* - z\gamma_i - z\gamma_s + it\omega_i - it\omega_p + it\omega_s} i \left(A_p\right)^* A_i A_s \omega_i$$
$$+ e^{-z(\gamma_p)^* - 2z\gamma_p + it\omega_p} i \left(A_p\right)^* A_p^2 \omega_p$$
$$- 2ie^{-z(\gamma_p)^* - z\gamma_i - z\gamma_s + it\omega_i - it\omega_p + it\omega_s} \left(A_p\right)^* A_i A_s \omega_p$$
$$+ 2e^{-z(\gamma_s)^* - z\gamma_p - z\gamma_s + it\omega_p} i \left(A_s\right)^* A_p A_s \omega_p$$
$$+ 2e^{-z(\gamma_p)^* - z\gamma_i - z\gamma_s + it\omega_i - it\omega_p + it\omega_s} i \left(A_p\right)^* A_i A_s \omega_s \Bigg) \quad \text{(A.16)}$$

Bring coefficients to front of LHS.

$$-\gamma_p \frac{dA_p}{dz} = \frac{L_{k,0}\left(G + i\omega_p C\right)}{8I_*^2} \Bigg(e^{-z(\gamma_p)^* - z\gamma_p} i \left(A_p\right)^* A_p^2 \omega_p$$
$$+ 2e^{-z(\gamma_s)^* - z\gamma_s} i \left(A_s\right)^* A_p A_s \omega_p + 2e^{-z(\gamma_i)^* - z\gamma_i} i A_i A_p \omega_p \left(A_i\right)^*$$
$$+ 2e^{-z(\gamma_p)^* - z\gamma_i - z\gamma_s + z\gamma_p} i \left(A_p\right)^* A_i A_s \omega_i$$
$$- 2ie^{-z(\gamma_p)^* - z\gamma_i - z\gamma_s + z\gamma_p} \left(A_p\right)^* A_i A_s \omega_p$$
$$+ 2e^{-z(\gamma_p)^* - z\gamma_i - z\gamma_s + z\gamma_p} i \left(A_p\right)^* A_i A_s \omega_s \Bigg) \quad \text{(A.17)}$$

Simplify.

$$\frac{dA_p}{dz} = -\frac{i\omega_p L_{k,0}\left(G + i\omega_p C\right)}{8\gamma_p I_*^2} \Bigg(e^{-z(\gamma_p)^* - z\gamma_p} \left(A_p\right)^* A_p^2$$
$$+ 2e^{-z(\gamma_s)^* - z\gamma_s} \left(A_s\right)^* A_p A_s + 2e^{-z(\gamma_i)^* - z\gamma_i} A_i A_p \left(A_i\right)^*$$
$$+ 2e^{-z(\gamma_p)^* - z\gamma_i - z\gamma_s + z\gamma_p} \left(A_p\right)^* A_i A_s \Bigg) \quad \text{(A.18)}$$

Tidy up.

$$\frac{dA_p}{dz} = -\frac{i\omega_p L_{k,0}\left(G + i\omega_p C\right)}{8\gamma_p I_*^2} \Bigg(\Big(e^{-\left(\gamma_p + \gamma_p^*\right)z} \left|A_p\right|^2 + 2e^{-\left(\gamma_s + \gamma_s^*\right)z} \left|A_s\right|^2$$
$$+ 2e^{-\left(\gamma_i + \gamma_i^*\right)z} \left|A_i\right|^2 \Big) A_p + 2e^{\left(\gamma_p - \gamma_p^* - \gamma_s - \gamma_i\right)z} A_i A_s A_p^* \Bigg) \quad \text{(A.19)}$$

Recall $L_{k,0} = L_0 - L_{\text{geo}}$.

$$\frac{dA_p}{dz} = -\frac{i\omega_p \left(L_0 - L_{\text{geo}}\right)\left(G + i\omega_p C\right)}{8\gamma_p I_*^2} \Bigg(\Big(e^{-\left(\gamma_p + \gamma_p^*\right)z} \left|A_p\right|^2 + 2e^{-\left(\gamma_s + \gamma_s^*\right)z} \left|A_s\right|^2$$
$$+ 2e^{-\left(\gamma_i + \gamma_i^*\right)z} \left|A_i\right|^2 \Big) A_p + 2e^{\left(\gamma_p - \gamma_p^* - \gamma_s - \gamma_i\right)z} A_i A_s A_p^* \Bigg) \quad \text{(A.20)}$$

From Pozar, we know that $\frac{\gamma}{Z} = G + i\omega C$.

$$\frac{dA_p}{dz} = -\frac{i\omega_p \left(L_0 - L_{\text{geo}}\right)}{8 Z_p I_*^2}\Bigg(\Big(e^{-\left(\gamma_p+\gamma_p^*\right)z}\left|A_p\right|^2 + 2e^{-(\gamma_s+\gamma_s^*)z}\left|A_s\right|^2 + 2e^{-\left(\gamma_i+\gamma_i^*\right)z}\left|A_i\right|^2\Big)A_p + 2e^{\left(\gamma_p-\gamma_p^*-\gamma_s-\gamma_i\right)z}A_iA_sA_p^*\Bigg) \quad \text{(A.21)}$$

From Pozar, we know that $L = \frac{\Im(\gamma Z)}{\omega}$. This gives the pump CME, where the superscript 'super' denotes parameter from HFSS model with surface impedance boundary condition and 'pec' denotes parameter from HFSS model without surface impedance boundary.

$$\frac{dA_p}{dz} = -\frac{i\left(\Im(\gamma_p^{\text{super}} Z_p^{\text{super}}) - \Im(\gamma_p^{\text{pec}} Z_p^{\text{pec}})\right)}{8 Z_p^{\text{super}} I_*^2}\Bigg(\Big(e^{-\left(\gamma_p+\gamma_p^*\right)z}\left|A_p\right|^2 + 2e^{-(\gamma_s+\gamma_s^*)z}\left|A_s\right|^2 + 2e^{-\left(\gamma_i+\gamma_i^*\right)z}\left|A_i\right|^2\Big)A_p + 2e^{\left(\gamma_p-\gamma_p^*-\gamma_s-\gamma_i\right)z}A_iA_sA_p^*\Bigg) \quad \text{(A.22)}$$

Now the signal equation.

$$\begin{aligned}
-\gamma_s\frac{dA_s}{dz}e^{i\omega_s t-\gamma_s z} = \frac{L_{k,0}G}{I_*^2}\Bigg(& - ie^{-z(\gamma_i)^*-2z\gamma_p-it\omega_i+2it\omega_p}A_p^2\omega_i\left(A_i\right)^* \\
& + 2e^{-z(\gamma_i)^*-2z\gamma_p-it\omega_i+2it\omega_p}iA_p^2\omega_p\left(A_i\right)^* \\
& + 2e^{-z(\gamma_i)^*-z\gamma_i-z\gamma_s+it\omega_s}iA_iA_s\omega_s\left(A_i\right)^* \\
& + e^{-z(\gamma_s)^*-2z\gamma_s+it\omega_s}i\left(A_s\right)^*A_s^2\omega_s \\
& + 2e^{-z(\gamma_p)^*-z\gamma_p-z\gamma_s+it\omega_s}i\left(A_p\right)^*A_pA_s\omega_s\Bigg) \\
+ \frac{i\omega_s L_{k,0}C}{I_*^2}\Bigg(& - ie^{-z(\gamma_i)^*-2z\gamma_p-it\omega_i+2it\omega_p}A_p^2\omega_i\left(A_i\right)^* \\
& + 2e^{-z(\gamma_i)^*-2z\gamma_p-it\omega_i+2it\omega_p}iA_p^2\omega_p\left(A_i\right)^* \\
& + 2e^{-z(\gamma_i)^*-z\gamma_i-z\gamma_s+it\omega_s}iA_iA_s\omega_s\left(A_i\right)^* \\
& + e^{-z(\gamma_s)^*-2z\gamma_s+it\omega_s}i\left(A_s\right)^*A_s^2\omega_s \\
& + 2e^{-z(\gamma_p)^*-z\gamma_p-z\gamma_s+it\omega_s}i\left(A_p\right)^*A_pA_s\omega_s\Bigg)
\end{aligned} \quad \text{(A.23)}$$

Bring coefficients to front of LHS.

$$-\gamma_s\frac{dA_s}{dz} = \frac{L_{k,0}\left(G + i\omega_s C\right)}{I_*^2}\Bigg(- ie^{-z(\gamma_i)^*-2z\gamma_p+\gamma_s z}A_p^2\omega_i\left(A_i\right)^*$$

$$+ 2e^{-z(\gamma_i)^*-2z\gamma_p+\gamma_s z} i A_p^2 \omega_p \left(A_i\right)^* + 2e^{-z(\gamma_i)^*-z\gamma_i} i A_i A_s \omega_s \left(A_i\right)^* + e^{-z(\gamma_s)^*-z\gamma_s} i \left(A_s\right)^* A_s^2 \omega_s + 2e^{-z(\gamma_p)^*-z\gamma_p} i \left(A_p\right)^* A_p A_s \omega_s \Bigg) \quad \text{(A.24)}$$

Simplify.

$$\frac{dA_s}{dz} = -\frac{i\omega_s L_{k,0}\left(G + i\omega_s C\right)}{\gamma_s I_*^2}\Bigg(e^{-z(\gamma_s)^*-z\gamma_s}\left(A_s\right)^* A_s^2 + 2e^{-z(\gamma_i)^*-z\gamma_i} A_i A_s \left(A_i\right)^* + 2e^{-z(\gamma_p)^*-z\gamma_p}\left(A_p\right)^* A_p A_s + e^{-z(\gamma_i)^*-2z\gamma_p+\gamma_s z} A_p^2 \left(A_i\right)^* \Bigg) \quad \text{(A.25)}$$

Tidy up.

$$\frac{dA_s}{dz} = -\frac{i\omega_s L_{k,0}\left(G + i\omega_s C\right)}{\gamma_s I_*^2}\Bigg(\Big(e^{-(\gamma_s+\gamma_s^*)z}|A_s|^2 + 2e^{-\left(\gamma_i+\gamma_i^*\right)z}|A_i|^2 + 2e^{-\left(\gamma_p+\gamma_p^*\right)z}|A_p|^2\Big) A_s + e^{(\gamma_s-\gamma_i{}^*-2\gamma_p)z} A_i^* A_p^2 \Bigg) \quad \text{(A.26)}$$

Recall $L_{k,0} = L_0 - L_{\text{geo}}$.

$$\frac{dA_s}{dz} = -\frac{i\omega_s \left(L_0 - L_{\text{geo}}\right)\left(G + i\omega_s C\right)}{\gamma_s I_*^2}\Bigg(\Big(e^{-(\gamma_s+\gamma_s^*)z}|A_s|^2 + 2e^{-\left(\gamma_i+\gamma_i^*\right)z}|A_i|^2 + 2e^{-\left(\gamma_p+\gamma_p^*\right)z}|A_p|^2\Big) A_s + e^{(\gamma_s-\gamma_i{}^*-2\gamma_p)z} A_i^* A_p^2 \Bigg) \quad \text{(A.27)}$$

From Pozar, we know that $\frac{\gamma}{Z} = G + i\omega C$.

$$\frac{dA_s}{dz} = -\frac{i\omega_s \left(L_0 - L_{\text{geo}}\right)}{Z_s^{\text{s}} I_*^2}\Bigg(\Big(e^{-(\gamma_s+\gamma_s^*)z}|A_s|^2 + 2e^{-\left(\gamma_i+\gamma_i^*\right)z}|A_i|^2 + 2e^{-\left(\gamma_p+\gamma_p^*\right)z}|A_p|^2\Big) A_s + e^{(\gamma_s-\gamma_i{}^*-2\gamma_p)z} A_i^* A_p^2 \Bigg) \quad \text{(A.28)}$$

From Pozar, we know that $L = \frac{\Im(\gamma Z)}{\omega}$. This gives the signal CME.

$$\frac{dA_s}{dz} = -\frac{i\left(\Im(\gamma_s^{\text{super}} Z_s^{\text{super}}) - \Im(\gamma_s^{\text{pec}} Z_s^{\text{pec}})\right)}{8 Z_s^{\text{super}} I_*^2}\Bigg(\Big(e^{-(\gamma_s+\gamma_s^*)z}|A_s|^2 + 2e^{-\left(\gamma_i+\gamma_i^*\right)z}|A_i|^2 + 2e^{-\left(\gamma_p+\gamma_p^*\right)z}|A_p|^2\Big) A_s + e^{(\gamma_s-\gamma_i{}^*-2\gamma_p)z} A_i^* A_p^2 \Bigg) \quad \text{(A.29)}$$

By analogy, the idler CME can be written down.

$$\frac{dA_i}{dz} = -\frac{i\left(\Im(\gamma_i^{\text{super}} Z_i^{\text{super}}) - \Im(\gamma_i^{\text{pec}} Z_i^{\text{pec}})\right)}{8 Z_i^{\text{super}} I_*^2}\Bigg(\Big(e^{-\left(\gamma_i+\gamma_i^*\right)z}|A_i|^2 + 2e^{-\left(\gamma_p+\gamma_p^*\right)z}|A_p|^2 + 2e^{-(\gamma_s+\gamma_s^*)z}|A_s|^2\Big)A_i + e^{(\gamma_i-{\gamma_s}^*-2\gamma_p)z}A_s^* A_p^2\Bigg) \quad \text{(A.30)}$$

So the full set of CMEs is:

$$\frac{dA_p}{dz} = -\frac{i\left(\Im(\gamma_p^{\text{super}} Z_p^{\text{super}}) - \Im(\gamma_p^{\text{pec}} Z_p^{\text{pec}})\right)}{8 Z_p^{\text{super}} I_*^2}\Bigg(\Big(e^{-\left(\gamma_p+\gamma_p^*\right)z}|A_p|^2 + 2e^{-(\gamma_s+\gamma_s^*)z}|A_s|^2 + 2e^{-\left(\gamma_i+\gamma_i^*\right)z}|A_i|^2\Big)A_p + 2e^{\left(\gamma_p-\gamma_p^*-\gamma_s-\gamma_i\right)z}A_i A_s A_p^*\Bigg) \quad \text{(A.31a)}$$

$$\frac{dA_s}{dz} = -\frac{i\left(\Im(\gamma_s^{\text{super}} Z_s^{\text{super}}) - \Im(\gamma_s^{\text{pec}} Z_s^{\text{pec}})\right)}{8 Z_s^{\text{super}} I_*^2}\Bigg(\Big(e^{-(\gamma_s+\gamma_s^*)z}|A_s|^2 + 2e^{-\left(\gamma_i+\gamma_i^*\right)z}|A_i|^2 + 2e^{-\left(\gamma_p+\gamma_p^*\right)z}|A_p|^2\Big)A_s + e^{(\gamma_s-{\gamma_i}^*-2\gamma_p)z}A_i^* A_p^2\Bigg) \quad \text{(A.31b)}$$

$$\frac{dA_i}{dz} = -\frac{i\left(\Im(\gamma_i^{\text{super}} Z_i^{\text{super}}) - \Im(\gamma_i^{\text{pec}} Z_i^{\text{pec}})\right)}{8 Z_i^{\text{super}} I_*^2}\Bigg(\Big(e^{-\left(\gamma_i+\gamma_i^*\right)z}|A_i|^2 + 2e^{-\left(\gamma_p+\gamma_p^*\right)z}|A_p|^2 + 2e^{-(\gamma_s+\gamma_s^*)z}|A_s|^2\Big)A_i + e^{(\gamma_i-{\gamma_s}^*-2\gamma_p)z}A_s^* A_p^2\Bigg) \quad \text{(A.31c)}$$

A.1.3 Alternative Solution in Low-Loss Limit

From Pozar, we can take the low-loss limit, where $\Re(\gamma)$ is small but non-zero. We can start with our derived CMEs in (A.32a)-(A.32c).

$$\frac{dA_p}{dz} = -\frac{i\omega_p L_{k,0}\left(G + i\omega_p C\right)}{8\gamma_p I_*^2}\Bigg(\Big(e^{-\left(\gamma_p+\gamma_p^*\right)z}|A_p|^2 + 2e^{-(\gamma_s+\gamma_s^*)z}|A_s|^2 + 2e^{-\left(\gamma_i+\gamma_i^*\right)z}|A_i|^2\Big)A_p + 2e^{\left(\gamma_p-\gamma_p^*-\gamma_s-\gamma_i\right)z}A_i A_s A_p^*\Bigg) \quad \text{(A.32a)}$$

$$\frac{dA_s}{dz} = -\frac{i\omega_s L_{k,0}\left(G + i\omega_s C\right)}{\gamma_s I_*^2}\Bigg(\Big(e^{-(\gamma_s+\gamma_s^*)z}|A_s|^2 + 2e^{-\left(\gamma_i+\gamma_i^*\right)z}|A_i|^2 + 2e^{-\left(\gamma_p+\gamma_p^*\right)z}|A_p|^2\Big)A_s + e^{(\gamma_s-{\gamma_i}^*-2\gamma_p)z}A_i^* A_p^2\Bigg) \quad \text{(A.32b)}$$

$$\frac{dA_i}{dz} = -\frac{i\omega_i L_{k,0}\left(G + i\omega_i C\right)}{\gamma_i I_*^2}\Bigg(\Big(e^{-\left(\gamma_i+\gamma_i^*\right)z}|A_i|^2 + 2e^{-\left(\gamma_p+\gamma_p^*\right)z}|A_p|^2 + 2e^{-(\gamma_s+\gamma_s^*)z}|A_s|^2\Big)A_i + e^{(\gamma_i-{\gamma_s}^*-2\gamma_p)z}A_s^* A_p^2\Bigg) \quad \text{(A.32c)}$$

In the low-loss limit, we can assume that $G \ll \omega C$. We can also substitute $L_{k,0} = \alpha L_0$, where α is the fractional kinetic inductance, i.e. $\alpha = \frac{L_k}{L_{\text{tot}}}$. The CMEs then simplify to (A.33a)-(A.33c).

$$\frac{dA_p}{dz} = \frac{\omega_p^2 \alpha L_0 C}{8\gamma_p I_*^2}\Bigg(\Big(e^{-\left(\gamma_p+\gamma_p^*\right)z}\left|A_p\right|^2 + 2e^{-(\gamma_s+\gamma_s^*)z}\left|A_s\right|^2 + 2e^{-\left(\gamma_i+\gamma_i^*\right)z}\left|A_i\right|^2\Big)A_p + 2e^{\left(\gamma_p-\gamma_p^*-\gamma_s-\gamma_i\right)z}A_i A_s A_p^*\Bigg) \quad \text{(A.33a)}$$

$$\frac{dA_s}{dz} = \frac{\omega_s^2 \alpha L_0 C}{\gamma_s I_*^2}\Bigg(\Big(e^{-(\gamma_s+\gamma_s^*)z}|A_s|^2 + 2e^{-\left(\gamma_i+\gamma_i^*\right)z}|A_i|^2 + 2e^{-\left(\gamma_p+\gamma_p^*\right)z}|A_p|^2\Big)A_s + e^{(\gamma_s-{\gamma_i}^*-2\gamma_p)z}A_i^* A_p^2\Bigg) \quad \text{(A.33b)}$$

$$\frac{dA_i}{dz} = \frac{\omega_i^2 \alpha L_0 C}{\gamma_i I_*^2}\Bigg(\Big(e^{-\left(\gamma_i+\gamma_i^*\right)z}|A_i|^2 + 2e^{-\left(\gamma_p+\gamma_p^*\right)z}|A_p|^2 + 2e^{-(\gamma_s+\gamma_s^*)z}|A_s|^2\Big)A_i + e^{(\gamma_i-{\gamma_s}^*-2\gamma_p)z}A_s^* A_p^2\Bigg) \quad \text{(A.33c)}$$

In the low-loss limit, the real and imaginary components of γ can be approximated to $\Re(\gamma) \approx \frac{1}{2}\left(R\sqrt{\frac{C}{L}} + G\sqrt{\frac{L}{C}}\right)$ and $\Im(\gamma) \approx \omega\sqrt{LC}$, respectively. The CMEs then become (A.33a)-(A.33c), which are essentially the lossy CMEs that we normally use.

$$\frac{dA_p}{dz} = \frac{\alpha\Im(\gamma_p)^2}{8\gamma_p I_*^2}\Bigg(\Big(e^{-\left(\gamma_p+\gamma_p^*\right)z}\left|A_p\right|^2 + 2e^{-(\gamma_s+\gamma_s^*)z}\left|A_s\right|^2$$

$$+ 2e^{-\left(\gamma_i+\gamma_i^*\right)z}\left|A_i\right|^2\Big)A_p + 2e^{\left(\gamma_p-\gamma_p^*-\gamma_s-\gamma_i\right)z}A_iA_sA_p^*\Bigg) \quad \text{(A.34a)}$$

$$\frac{dA_s}{dz} = \frac{\alpha\Im(\gamma_s)^2}{\gamma_s I_*^2}\Bigg(\Big(e^{-(\gamma_s+\gamma_s^*)z}|A_s|^2 + 2e^{-\left(\gamma_i+\gamma_i^*\right)z}|A_i|^2 + 2e^{-\left(\gamma_p+\gamma_p^*\right)z}|A_p|^2\Big)A_s + e^{(\gamma_s-{\gamma_i}^*-2\gamma_p)z}A_i^*A_p^2\Bigg) \quad \text{(A.34b)}$$

$$\frac{dA_i}{dz} = \frac{\alpha\Im(\gamma_i)^2}{\gamma_i I_*^2}\Bigg(\Big(e^{-\left(\gamma_i+\gamma_i^*\right)z}|A_i|^2 + 2e^{-\left(\gamma_p+\gamma_p^*\right)z}|A_p|^2 + 2e^{-(\gamma_s+\gamma_s^*)z}|A_s|^2\Big)A_i + e^{(\gamma_i-{\gamma_s}^*-2\gamma_p)z}A_s^*A_p^2\Bigg) \quad \text{(A.34c)}$$

A.2 Analytical Solution to the Coupled-Mode Equations

Following the method in the previous section, a set of three coupled differential equations has been obtained. (Technically six equations have been obtained but the second three are simply the complex conjugates of the first three, so are strictly equivalent.) The three coupled equations are:

$$\begin{aligned}
\frac{dA_p}{dz} + \frac{ik_p}{8I_*^2}\Bigg(\Big(|A_p|^2 + 2|A_s|^2 + 2|A_i|^2\Big)A_p + 2A_iA_sA_p^*e^{-i\Delta kz}\Bigg) &= 0 \\
\frac{dA_s}{dz} + \frac{ik_s}{8I_*^2}\Bigg(\Big(|A_s|^2 + 2|A_i|^2 + 2|A_p|^2\Big)A_s + A_i^*A_p^2e^{i\Delta kz}\Bigg) &= 0 \\
\frac{dA_i}{dz} + \frac{ik_i}{8I_*^2}\Bigg(\Big(|A_i|^2 + 2|A_s|^2 + 2|A_p|^2\Big)A_i + A_s^*A_p^2e^{i\Delta kz}\Bigg) &= 0
\end{aligned} \quad \text{(A.35)}$$

In general, the three above equations cannot be solved analytically, however, they can be under certain assumptions. Assume that the pump is much stronger than the signal and the idler (strong pump approximation) i.e. $A_p \gg A_s, A_i$. Under this assumption, all terms of order A_s^2, A_i^2, and A_sA_i can be ignored. The pump differential equation therefore simplifies to:

$$\frac{dA_p}{dz} + \frac{ik_p}{8I_*^2}|A_p|^2A_p = 0 \quad \text{(A.36)}$$

At this point, make a second approximation that the pump is undepleted as it travels through the line, i.e., implying $|A_p|$ is constant. The equation can therefore be written as:

$$\frac{dA_p}{dz} - i\alpha_p A_p = 0 \tag{A.37}$$

where $\alpha_p \equiv \frac{-k_p}{8I_*^2}|A_p|^2$ is a constant. This can be easily solved to give:

$$A_p(z) = A_p(0)e^{i\alpha_p z} \tag{A.38}$$

The solution for A_p can now be inserted into the other differential equations in (A.35), starting with the signal in the strong pump approximation:

$$\frac{dA_s}{dz} + \frac{ik_s}{8I_*^2}\left(2|A_p|^2 A_s + A_i^* A_p^2 e^{i\Delta k z}\right) = 0 \tag{A.39}$$

Subbing A_p gives:

$$\frac{dA_s}{dz} + \frac{ik_s}{8I_*^2}\left(2|A_p(0)|^2 A_s + A_i^* A_p^2(0) e^{i(\Delta k + 2\alpha_p)z}\right) = 0 \tag{A.40}$$

or

$$\frac{dA_s}{dz} - i\alpha_s A_s - i\kappa_s A_i^* e^{i(\Delta k + 2\alpha_p)z} = 0 \tag{A.41}$$

where $\alpha_s \equiv \frac{-k_s}{4I_*^2}|A_p(0)|^2$ and $\kappa_s \equiv \frac{-k_s}{8I_*^2}A_p^2(0)$. Performing the analogous technique for the idler gives:

$$\frac{dA_i}{dz} - i\alpha_i A_i - i\kappa_i A_s^* e^{i(\Delta k + 2\alpha_p)z} = 0 \tag{A.42}$$

where $\alpha_i \equiv \frac{-k_i}{4I_*^2}|A_p(0)|^2$ and $\kappa_i \equiv \frac{-k_i}{8I_*^2}A_p^2(0)$.

This now gives just two coupled equations to be solved:

$$\frac{dA_s}{dz} - i\alpha_s A_s - i\kappa_s A_i^* e^{i(\Delta k + 2\alpha_p)z} = 0 \tag{A.43a}$$

$$\frac{dA_i}{dz} - i\alpha_i A_i - i\kappa_i A_s^* e^{i(\Delta k + 2\alpha_p)z} = 0 \tag{A.43b}$$

Substitute the following probe equations into the above:

$$A_s(z) = a_s(z)e^{i\alpha_s z} \tag{A.44a}$$

$$A_i(z) = a_i(z)e^{i\alpha_i z} \tag{A.44b}$$

to give:

$$\frac{da_s}{dz} - i\kappa_s a_i^* e^{i\Delta\beta z} = 0 \tag{A.45a}$$

$$\frac{da_i}{dz} - i\kappa_i a_s^* e^{i\Delta\beta z} = 0 \tag{A.45b}$$

where $\Delta\beta \equiv \Delta k + 2\alpha_p - \alpha_s - \alpha_i$.

These two equations can now be solved using the ansatz:

$$a_s(z) = \Big(Fe^{gz} + Ge^{-gz}\Big)e^{\frac{i\Delta\beta z}{2}} \tag{A.46a}$$

$$a_i(z) = \Big(Ce^{gz} + De^{-gz}\Big)e^{\frac{i\Delta\beta z}{2}} \tag{A.46b}$$

where F, G, C, and D are real but g is complex. Subbing these into (A.45a) yields:

$$g\big(Fe^{gz} - Ge^{-gz}\big)e^{\frac{i\Delta\beta z}{2}} + \frac{i\Delta\beta}{2}\big(Fe^{gz} + Ge^{-gz}\big)e^{\frac{i\Delta\beta z}{2}} - i\kappa_s\big(Ce^{-gz} + De^{gz}\big)e^{-\frac{i\Delta\beta z}{2}}e^{i\Delta\beta z} = 0 \tag{A.47}$$

Cancelling the $e^{\frac{i\Delta\beta z}{2}}$ terms and collecting together the terms of order $e^{\pm gz}$ gives:

$$\left[\Big(g + \frac{i\Delta\beta}{2}\Big)F - i\kappa_s D\right]e^{gz} + \left[\Big(-g + \frac{i\Delta\beta}{2}\Big)G - i\kappa_s C\right]e^{-gz} = 0 \tag{A.48}$$

This therefore implies that:

$$\Big(g + \frac{i\Delta\beta}{2}\Big)F = i\kappa_s D \tag{A.49a}$$

$$\Big(-g + \frac{i\Delta\beta}{2}\Big)G = i\kappa_s C \tag{A.49b}$$

Repeating this technique but substituting into (A.45b) results in:

$$\Big(-g + \frac{i\Delta\beta}{2}\Big)D = i\kappa_i F \tag{A.50a}$$

$$\Big(g + \frac{i\Delta\beta}{2}\Big)C = i\kappa_i G \tag{A.50b}$$

Take the two equations involving D and F (or alternatively C and G) and write them together as a matrix equation:

$$\begin{bmatrix} -i\kappa_s & g + \frac{i\Delta\beta}{2} \\ -g + \frac{i\Delta\beta}{2} & -i\kappa_i \end{bmatrix}\begin{bmatrix} D \\ F \end{bmatrix} = 0 \tag{A.51}$$

The determinant of this matrix must be equal to zero, therefore by multiplying out, it can be shown that:

$$g = \sqrt{\kappa_s\kappa_i - \frac{\Delta\beta^2}{4}} \tag{A.52}$$

Going back to the ansatz in (A.46a)-(A.46b) and assuming that a_s and a_i are known at $z = 0$:

$$\begin{aligned} a_s(0) &= F + G \\ a_i(0) &= C + D \end{aligned} \tag{A.53}$$

These two equations can combined with those in (A.49a)-(A.49b) and (A.50a)-(A.50b) to find expressions for the unknown coefficients. Start with (A.49a)-(A.49b) and rearrange them accordingly:

$$\Big(g + \frac{i\Delta\beta}{2}\Big)F = i\kappa_s D \rightarrow \Big(\frac{-2ig + \Delta\beta}{2\kappa_s}\Big)F = D \tag{A.54a}$$

$$\Big(-g + \frac{i\Delta\beta}{2}\Big)G = i\kappa_s C \rightarrow \Big(\frac{2ig + \Delta\beta}{2\kappa_s}\Big)G = C \tag{A.54b}$$

Substitute these into $a_i(0) = C + D$ to give:

$$a_i(0) = \Big(\frac{2ig + \Delta\beta}{2\kappa_s}\Big)G + \Big(\frac{-2ig + \Delta\beta}{2\kappa_s}\Big)F \tag{A.55}$$

Now sub in $F = a_s(0) - G$ to give:

$$a_i(0) = \Big(\frac{2ig + \Delta\beta}{2\kappa_s}\Big)G + \Big(\frac{-2ig + \Delta\beta}{2\kappa_s}\Big)\big(a_s(0) - G\big) \tag{A.56}$$

Expanding RHS and rearranging:

$$\Big(\frac{2ig + \Delta\beta}{2\kappa_s}\Big)G - \Big(\frac{-2ig + \Delta\beta}{2\kappa_s}\Big)G = a_i(0) - \Big(\frac{-2ig + \Delta\beta}{2\kappa_s}\Big)a_s(0) \tag{A.57}$$

Simplifying LHS:

$$\Big(\frac{2ig}{\kappa_s}\Big)G = a_i(0) - \Big(\frac{-2ig + \Delta\beta}{2\kappa_s}\Big)a_s(0) \tag{A.58}$$

Therefore G is equal to:

$$G = \frac{\big(2g + i\Delta\beta\big)a_s(0) - 2i\kappa_s a_i(0)}{4g} \tag{A.59}$$

An expression for F can be obtained using $F = a_s(0) - G$:

$$F = a_s(0) - \frac{\big(2g + i\Delta\beta\big)a_s(0) - 2i\kappa_s a_i(0)}{4g} \tag{A.60}$$

This simplifies to:

$$F = \frac{\big(2g - i\Delta\beta\big)a_s(0) + 2i\kappa_s a_i(0)}{4g} \tag{A.61}$$

An expression for C can be obtained using the relation $C = \Big(\frac{2ig+\Delta\beta}{2\kappa_s}\Big)G$:

$$C = \left(\frac{2ig + \Delta\beta}{2\kappa_s}\right)\left(\frac{\big(2g + i\Delta\beta\big)a_s(0) - 2i\kappa_s a_i(0)}{4g}\right) \tag{A.62}$$

Combining into one fraction

$$C = \frac{\big(2ig + \Delta\beta\big)\big(2g + i\Delta\beta\big)a_s(0) - \big(2ig + \Delta\beta\big)2i\kappa_s a_i(0)}{8\kappa_s g} \tag{A.63}$$

This gives:

$$C = \frac{i\big(4g^2 + \Delta\beta^2\big)a_s(0) + \big(4g - 2i\Delta\beta\big)\kappa_s a_i(0)}{8\kappa_s g} \tag{A.64}$$

Finally, an expression for D can be obtained using $D = a_i(0) - C$:

$$D = a_i(0) - \frac{i\big(4g^2 + \Delta\beta^2\big)a_s(0) + \big(4g - 2i\Delta\beta\big)\kappa_s a_i(0)}{8\kappa_s g} \tag{A.65}$$

Combining into one fraction:

$$D = \frac{-i\big(4g^2 + \Delta\beta^2\big)a_s(0) + 8\kappa_s g a_i(0) - \big(4g - 2i\Delta\beta\big)\kappa_s a_i(0)}{8\kappa_s g} \tag{A.66}$$

This simplifies to:

$$D = \frac{-i\big(4g^2 + \Delta\beta^2\big)a_s(0) + \big(4g + 2i\Delta\beta\big)\kappa_s a_i(0)}{8\kappa_s g} \tag{A.67}$$

Now that all of these coefficients have been calculated, they can be reinserted into the ansatz in (A.46a)-(A.46b). Starting with the signal, i.e. (A.46a):

$$a_s(z) = \Bigg(\underbrace{\frac{\big(2g - i\Delta\beta\big)a_s(0) + 2i\kappa_s a_i(0)}{4g}}_{F} e^{gz} + \underbrace{\frac{\big(2g + i\Delta\beta\big)a_s(0) - 2i\kappa_s a_i(0)}{4g}}_{G} e^{-gz} \Bigg) e^{\frac{i\Delta\beta z}{2}} \tag{A.68}$$

Expanding and rearranging:

$$a_s(z) = \Bigg(\underbrace{\frac{a_s(0)}{2}e^{gz} + \frac{a_s(0)}{2}e^{-gz}}_{a_s(0)\cosh(gz)} \underbrace{- \frac{i\Delta\beta a_s(0)}{4g}e^{gz} + \frac{i\Delta\beta a_s(0)}{4g}e^{-gz}}_{-\frac{i\Delta\beta a_s(0)}{2g}\sinh(gz)} \underbrace{+ \frac{i\kappa_s a_i(0)}{2g}e^{gz} - \frac{i\kappa_s a_i(0)}{2g}e^{-gz}}_{\frac{i\kappa_s a_i(0)}{g}\sinh(gz)} \Bigg) e^{\frac{i\Delta\beta z}{2}} \tag{A.69}$$

Therefore $a_s(z)$ is given by:

$$a_s(z) = \left[a_s(0)\left(\cosh(gz) - \frac{i\Delta\beta}{2g}\sinh(gz) \right) + \frac{i\kappa_s a_i(0)}{g}\sinh(gz) \right] e^{\frac{i\Delta\beta z}{2}} \tag{A.70}$$

This process can now be repeated for the idler, i.e. (A.46b):

$$a_i(z) = \Bigg(\underbrace{\frac{i\big(4g^2 + \Delta\beta^2\big)a_s(0) + \big(4g - 2i\Delta\beta\big)\kappa_s a_i(0)}{8\kappa_s g}}_{C} e^{gz}$$

$$+\underbrace{\frac{-i\big(4g^2+\Delta\beta^2\big)a_s(0)+\big(4g+2i\Delta\beta\big)\kappa_s a_i(0)}{8\kappa_s g}}_{D}e^{-gz}\Big)e^{\frac{i\Delta\beta z}{2}} \tag{A.71}$$

Expanding and rearranging:

$$a_i(z)=\Bigg(\underbrace{\frac{i\big(4g^2+\Delta\beta^2\big)a_s(0)}{8\kappa_s g}e^{gz}-\frac{i\big(4g^2+\Delta\beta^2\big)a_s(0)}{8\kappa_s g}e^{-gz}}_{\frac{i\left(4g^2+\Delta\beta^2\right)a_s(0)}{4\kappa_s g}\sinh(gz)}$$
$$\underbrace{+\frac{a_i(0)}{2}e^{gz}+\frac{a_i(0)}{2}e^{-gz}}_{a_i(0)\cosh(gz)}\underbrace{-\frac{i\Delta\beta a_i(0)}{4g}e^{gz}+\frac{i\Delta\beta a_i(0)}{4g}e^{-gz}}_{-\frac{i\Delta\beta a_i(0)}{2g}\sinh(gz)}\Bigg)e^{\frac{i\Delta\beta z}{2}} \tag{A.72}$$

So:

$$a_i(z)=\left[\frac{i\big(4g^2+\Delta\beta^2\big)a_s(0)}{4\kappa_s g}\sinh(gz)+a_i(0)\left(\cosh(gz)-\frac{i\Delta\beta}{2g}\sinh(gz)\right)\right]e^{\frac{i\Delta\beta z}{2}} \tag{A.73}$$

The coefficient of the $a_s(0)$ term can be simplified using the relation $g=\sqrt{\kappa_s\kappa_i-\frac{\Delta\beta^2}{4}}$ from earlier:

$$\frac{i\big(4g^2+\Delta\beta^2\big)a_s(0)}{4\kappa_s g}=\frac{i\big(4\kappa_s\kappa_i\big)a_s(0)}{4\kappa_s g}=\frac{i\kappa_i a_s(0)}{g} \tag{A.74}$$

So the equation for the idler becomes:

$$a_i(z)=\left[a_s(0)\frac{i\kappa_i}{g}\sinh(gz)+a_i(0)\left(\cosh(gz)-\frac{i\Delta\beta}{2g}\sinh(gz)\right)\right]e^{\frac{i\Delta\beta z}{2}} \tag{A.75}$$

This now gives the two solutions for the signal and idler waves in the CPW. These can be simplified further under the assumption that the amplitude of the idler is zero initially, i.e. $a_i(0)=0$. This then gives:

$$a_s(z)=a_s(0)\left(\cosh(gz)-\frac{i\Delta\beta}{2g}\sinh(gz)\right)e^{\frac{i\Delta\beta z}{2}} \tag{A.76a}$$

$$a_i(z)=a_s(0)\frac{i\kappa_i}{g}\sinh(gz)e^{\frac{i\Delta\beta z}{2}} \tag{A.76b}$$

The signal gain of the parametric amplifier, G_s, as a function of distance along the CPW is defined as:

$$G_s(z)=\frac{|A_s(z)|^2}{|A_s(0)|^2}=\frac{|a_s(z)|^2}{|a_s(0)|^2} \tag{A.77}$$

since the complex exponents cancel due to the modulus signs. So inserting the expression from (A.76a) gives:

$$G_s(z) = \left|\cosh(gz) - \frac{i\Delta\beta}{2g}\sinh(gz)\right|^2 \tag{A.78}$$

This, in turn, can be written in decibels:

$$G_s(dB) = 10\log\left(\left|\cosh(gz) - \frac{i\Delta\beta}{2g}\sinh(gz)\right|^2\right) \tag{A.79}$$

or

$$G_s(dB) = 20\log\left(\left|\cosh(gz) - \frac{i\Delta\beta}{2g}\sinh(gz)\right|\right) \tag{A.80}$$

Bibliography

[1] Boon-Kok Tan, Faouzi Boussaha, Christine Chaumont, Joseph C. Longden, and Javier Navarro Montilla. Engineering the thin film characteristics for optimal performance of superconducting kinetic inductance amplifiers using a rigorous modelling technique. *Open Research Europe*, 2:88, 2022.

[2] Joseph C. Longden, Christine Chaumont, Faouzi M. Boussaha, and Boon-Kok Tan. A compact kinetic inductance travelling wave parametric amplifier with continuous periodic loading structure. *Proc. SPIE 12190, Millimeter, Submillimeter, and Far-Infrared Detectors and Instrumentation for Astronomy XI*, 12190(121902X):38, 2022.

[3] Joseph C. Longden, Faouzi Boussaha, Christine Chaumont, Nikita Klimovich, and Boon-kok Tan. Measuring the nonlinearity of titanium nitride film for applications as kinetic inductance travelling wave parametric amplifiers. In *Proceedings of the 32nd International Symposium on Space Terahertz Technology*, 2022.

[4] Harald Trap Friis. Noise Figures of Radio Receivers. *Proceedings of the IRE*, 32(7):419–422, 1944.

[5] L Hogan, D Rigopoulou, S García-Burillo, A Alonso-Herrero, L Barrufet, F Combes, I García-Bernete, G E Magdis, M Pereira-Santaella, N Thatte, and A Weiß. Unveiling the main sequence to starburst transition region with a sample of intermediate redshift luminous infrared galaxies. *Monthly Notices of the Royal Astronomical Society*, 512(2):2371–2388, Feb 2022.

[6] Lauren Rhodes, Rob Fender, David R A Williams, and Kunal Mooley. An early peak in the radio light curve of short-duration gamma-ray burst 200826A. *Monthly Notices of the Royal Astronomical Society*, 503(2):2966–2972, Mar 2021.

[7] P. A.R. Ade et al. Planck intermediate results. XIV. Dust emission at millimetre wavelengths in the Galactic plane. *Astronomy and Astrophysics*, 564:1–13, 2014.

[8] David Ball, Chi-kwan Chan, Pierre Christian, Buell T. Jannuzi, Junhan Kim, Daniel P. Marrone, Lia Medeiros, Feryal Ozel, Dimitrios Psaltis, Mel Rose, Arash Roshanineshat, Tyler Trent, Thomas W. Folkers, David C. Forbes, Robert Freund, Christopher H. Greer, Kyle D. Massingill, Martin P. McColl, Chi H. Nguyen, George Reiland, and Lucy Ziurys. First M87 Event Horizon Telescope results. I. The shadow of the supermassive black hole. *Astrophysical Journal Letters*, 2019.

[9] Ran Wang, Jeff Wagg, Chris L Carilli, Fabian Walter, Lindley Lentati, Xiaohui Fan, Dominik A Riechers, Frank Bertoldi, Desika Narayanan, Michael A Strauss, Pierre Cox, Alain Omont, Karl M Menten, Kirsten K Knudsen, Roberto Neri, and Linhua Jiang. Star Formation and Gas Kinematics of Quasar Host Galaxies at z $\sim$ 6: New Insights from ALMA. *The Astrophysical Journal*, 773(10pp):44, 2013.

[10] Mark Birkinshaw. The Sunyaev-Zel'dovich effect. *Physics Reports*, 310(2):97–195, 1999.

[11] S Joardar, S Bhattacharyya, A B Bhattacharya, and C R Datta. Radio Astronomy and Super-Synthesis: A Survey. Technical report, 2010.

[12] Alwyn Wootten. The Atacama Large Millimeter Array (ALMA). In Jacobus M. Oschmann and Larry M. Stepp, editors, *Large Ground-based Telescopes*, volume 4837, pages 110 – 118. International Society for Optics and Photonics, SPIE, 2003.

[13] M. Carter, B. Lazareff, D. Maier, J. Y. Chenu, A. L. Fontana, Y. Bortolotti, C. Boucher, A. Navarrini, S. Blanchet, A. Greve, D. John, C. Kramer, F. Morel, S. Navarro, J. Peñalver, K. F. Schuster, and C. Thum. The EMIR multi-band mm-wave receiver for the IRAM 30-m telescope. *Astronomy and Astrophysics*, 538:1–13, 2012.

[14] Justin L Jonas and The MeerKAT Team in South Africa. The MeerKAT Radio Telescope PoS(MeerKAT2016)001. *Proceedings of Science*, pages 1–23, 2016.

[15] F. Villa, M. Bersanelli, C. Burigana, R. C. Butler, N. Mandolesi, A. Mennella, G. Morgante, M. Sandri, L. Terenzi, L. Valenziano, and Planck Collaboration. The Planck Telescope. *AIP Conference Proceedings*, 616(1):224–228, May 2002.

[16] Sheperd Doeleman, Eric Agol, Don Backer, Fred Baganoff, Geoffrey C. Bower, Avery Broderick, Andrew Fabian, Vincent Fish, Charles Gammie, Paul Ho, Mareki Honma, Thomas Krichbaum, Avi Loeb, Dan Marrone, Mark Reid, Alan E. E. Rogers, Irwin Shapiro, Peter Strittmatter, Remo Tilanus, Jonathan Weintroub, Alan Whitney, Melvyn Wright, and Lucy Ziurys. Imaging an Event Horizon: submm-VLBI of a Super Massive Black Hole, 2009.

[17] Carlton M. Caves. Quantum limits on noise in linear amplifiers. *Phys. Rev. D*, 26:1817–1839, Oct 1982.

[18] Isaac Lopez-Fernandez, Carmen Diez, Juan Daniel Gallego, and Alberto Barcia. Wide band cryogenic IF amplifiers for ALMA and Herschel receivers. In *Proceedings of the 14th International Symposium on Space Terahertz Technology*, 2003.

[19] V. Belitsky, M. Bylund, V. Desmaris, A. Ermakov, S. E. Ferm, M. Fredrixon, S. Krause, I. Lapkin, D. Meledin, A. Pavolotsky, H. Rashid, S. Shafiee, M. Strandberg, E. Sundin, P. Yadranjee Aghdam, R. Hesper, J. Barkhof, M. E. Bekema, J. Adema, R. De Haan, A. Koops, W. Boland, P. Yagoubov, G. Marconi, G. Siringo, E. Humphreys, G. H. Tan, R. Laing, L. Testi, T. Mroczkowski, W. Wild, K. S. Saini, and E. Bryerton. ALMA Band 5 receiver cartridge: Design, performance, and commissioning. *Astronomy and Astrophysics*, 611:1–10, 2018.

[20] A M Baryshev, R Hesper, F P Mena, T M Klapwijk, T A Van Kempen, M R Hogerheijde, B D Jackson, J Adema, G J Gerlofsma, M E Bekema, J Barkhof, A Koops, K Keizer, C Pieters, T Zijlstra, M Kroug, C F J Lodewijk, K Wielinga, W Boland, M W M De Graauw, E F Van Dishoeck, H Jager, and W Wild. Astrophysics The ALMA Band 9 receiver. *Astronomy and Astrophysics*, 577:A129, 2015.

[21] Byeong Ho Eom, Peter K. Day, Henry G. Leduc, and Jonas Zmuidzinas. A wideband, low-noise superconducting amplifier with high dynamic range. *Nature Physics*, 8(8):623–627, 2012.

[22] Omid Noroozian. Cycle 5 NRAO ALMA Development Study Report Technology Development of Quantum-Limited , Ultra-Wideband RF Amplifiers for ALMA : A 65-150 GHz Test Case. (April), 2020.

[23] ALMA Receiver Bands — ESO.

[24] A. Karpov, B. Plathner, J. Blondel, M. Schicke, K.H. Gundlach, M. Aoyagi, and S. Takada. Noise and gain in frequency mixers with NbN SIS junctions. *IEEE Transactions on Applied Superconductivity*, 7(2):1077–1080, 1997.

[25] John D. Garrett, Boon-Kok Tan, Christine Chaumont, Faouzi Boussaha, and Ghassan Yassin. A 230-GHz endfire SIS mixer with near quantum-limited performance. *IEEE Microwave and Wireless Components Letters*, 32(12):1435–1438, 2022.

[26] Jakob Wenninger, Faouzi Boussaha, Christine Chaumont, Boon Kok Tan, and Ghassan Yassin. Design of a 240 GHz on-chip dual-polarization receiver for SIS mixer arrays. *Superconductor Science and Technology*, 36(5), 2023.

[27] A. Karpov, D. Miller, F. Rice, J. A. Stern, B. Bumble, H. G. LeDuc, and J. Zmuidzinas. Low noise 1 THz–1.4 THz mixers using Nb/Al-AlN/NbTiN SIS junctions. *IEEE Transactions on Applied Superconductivity*, 17(2):343–346, 2007.

[28] B. K. Tan, K. Rudakov, V. P. Koshelets, A. Khudchenko, A. M. Baryshev, and G. Yassin. Comparing the performance of 850 GHz integrated bias-tee superconductor-insulator-superconductor (SIS) mixers with single- and parallel-junction tuner. *Superconductor Science and Technology*, 35(12), 2022.

[29] Ling Jiang, Shoichi Shiba, Ken Shimbo, Nami Sakai, Tetsuya Yamakura, Mika Sugimura, P. G. Ananthasubramanian, Hiroyuki Maezawa, Yoshihisa Irimajiri, and Satoshi Yamamoto. Development of THz waveguide NbTiN HEB mixers. *IEEE Transactions on Applied Superconductivity*, 19(3):301–304, 2009.

[30] Y. Gan, B. Mirzaei, J. R. G. D. Silva, J. Chang, S. Cherednichenko, F. van der Tak, and J. R. Gao. Low noise MgB2 hot electron bolometer mixer operated at 5.3 THz and at 20 K. *Applied Physics Letters*, 119(20):202601, Nov 2021.

[31] Peter K. Day, Henry G. LeDuc, Benjamin A. Mazin, Anastasios Vayonakis, and Jonas Zmuidzinas. A broadband superconducting detector suitable for use in large arrays. *Nature*, 425:817–821, 2003.

[32] S. K. Choi, J. Austermann, K. Basu, N. Battaglia, F. Bertoldi, D. T. Chung, N. F. Cothard, S. Duff, C. J. Duell, P. A. Gallardo, J. Gao, T. Herter, J. Hubmayr, M. D. Niemack, T. Nikola, D. Riechers, K. Rossi, G. J. Stacey, J. R. Stevens, E. M. Vavagiakis, M. Vissers, and S. Walker. Sensitivity of the Prime-Cam Instrument on the CCAT-Prime Telescope. *Journal of Low Temperature Physics*, 199(3-4):1089–1097, 2020.

[33] Peter S. Barry, Clarence. C. Chang, Sunil Golwala, and Erik Shirokoff. Large-Format, Transmission-Line-Coupled Kinetic Inductance Detector Arrays for HEP at Millimeter Wavelengths. 2022.

[34] H. Smith, J. Buckle, R. Hills, G. Bell, J. Richer, E. Curtis, S. Withington, J. Leech, R. Williamson, W. Dent, P. Hastings, R. Redman, B. Wooff, K. Yeung, P. Friberg, C. Walther, R. Kackley, T. Jenness, R. Tilanus, J. Dempsey, M. Kroug, T. Zijlstra, and T. M. Klapwijk. HARP: a submillimetre heterodyne array receiver operating on the James Clerk Maxwell Telescope. *Millimeter and Submillimeter Detectors and Instrumentation for Astronomy IV*, 7020(July 2008):70200Z, 2008.

[35] I. Barrueto, U. U. Graf, C. E. Honingh, K. Jacobs, M. Justen, H. Kruger, M. Schultz, K. Vynokurova, L. Weikert, S. Wulff, and J. Stutzki. CCAT-prime Heterodyne Instrument (CHAI) advances. *International Conference on Infrared, Millimeter, and Terahertz Waves, IRMMW-THz*, 2022-August(Fig 3):2022–2023, 2022.

[36] Taku Nakajima, Takeshi Sakai, Shin'ichiro Asayama, Kimihiro Kimura, Masayuki Kawamura, Yoshinori Yonekura, Hideo Ogawa, Nario Kuno, Takashi Noguchi, Masato Tsuboi, and Ryohei Kawabe. A New 100-GHz Band Front-End System with a Waveguide-Type Dual-Polarization Sideband-Separating SIS Receiver for the NRO 45-m Radio Telescope. *Publications of the Astronomical Society of Japan*, 60(3):435–443, Jun 2008.

[37] Frank Arute et al. Quantum supremacy using a programmable superconducting processor. *Nature*, 574(7779):505–510, 2019.

[38] Guoji Zheng, Nodar Samkharadze, Marc L. Noordam, Nima Kalhor, Delphine Brousse, Amir Sammak, Giordano Scappucci, and Lieven M.K. Vandersypen. Rapid gate-based spin read-out in silicon using an on-chip resonator. *Nature Nanotechnology*, 14(8):742–746, 2019.

[39] Johannes Heinsoo, Christian Kraglund Andersen, Ants Remm, Sebastian Krinner, Theodore Walter, Yves Salathé, Simone Gasparinetti, Jean Claude Besse, Anton Potočnik, Andreas Wallraff, and Christopher Eichler. Rapid High-fidelity Multiplexed Readout of Superconducting Qubits. *Physical Review Applied*, 10(3):1–14, 2018.

[40] J. Stehlik, Y.-Y. Liu, C. M. Quintana, C. Eichler, T. R. Hartke, and J. R. Petta. Fast charge sensing of a cavity-coupled double quantum dot using a josephson parametric amplifier. *Phys. Rev. Appl.*, 4:014018, Jul 2015.

[41] R. D. Peccei and Helen R. Quinn. CP conservation in the presence of pseudoparticles. *Phys. Rev. Lett.*, 38:1440–1443, Jun 1977.

[42] T. Braine, R. Cervantes, N. Crisosto, N. Du, S. Kimes, L. J. Rosenberg, G. Rybka, J. Yang, D. Bowring, A. S. Chou, R. Khatiwada, A. Sonnenschein, W. Wester, G. Carosi, N. Woollett, L. D. Duffy, R. Bradley, C. Boutan, M. Jones, B. H. Laroque, N. S. Oblath, M. S. Taubman, J. Clarke, A. Dove, A. Eddins, S. R. O'kelley, S. Nawaz, I. Siddiqi, N. Stevenson, A. Agrawal, A. V. Dixit, J. R. Gleason, S. Jois, P. Sikivie, J. A. Solomon, N. S. Sullivan, D. B. Tanner, E. Lentz, E. J. Daw, J. H. Buckley, P. M. Harrington, E. A. Henriksen, and K. W. Murch. Extended Search for the Invisible Axion with the Axion Dark Matter Experiment. *Physical Review Letters*, 124(10):101303, 2020.

[43] Ian Bailey, Bhaswati Chakraborty, Gemma Chapman, Edward J. Daw, John Gallop, Gianluca Gregori, Edward Hardy, Ling Hao, Edward Laird, Peter Leek, John March-Russell, Phil Meeson, Seaárbhan Ó' Peatáin, Yuri Pashkin, Mitchell G. Perry, Michele Piscitelli, Edward Romans, Subir Sarkar, Paul J. Smith, Ningqiang Song, Mahesh Soni, Boon K. Tan, Stephen West, and Stafford Withington. Searching for wave-like dark matter with QSHS. *SciPost Phys. Proc.*, page 040, 2023.

[44] K. Ramanathan, N. Klimovich, R. Basu Thakur, B. H. Eom, H. G. Leduc, S. Shu, A. D. Beyer, and P. K. Day. Wideband direct detection constraints on hidden photon dark matter with the qualiphide experiment. *Phys. Rev. Lett.*, 130:231001, Jun 2023.

[45] Y. Fukuda et al. Evidence for oscillation of atmospheric neutrinos. *Phys. Rev. Lett.*, 81:1562–1567, Aug 1998.

[46] Ali Ashtari Esfahani, David M Asner, Sebastian Böser, Raphael Cervantes, Christine Claessens, Luiz de Viveiros, Peter J Doe, Shepard Doeleman, Justin L Fernandes, Martin Fertl, Erin C Finn, Joseph A Formaggio, Daniel Furse, Mathieu Guigue, Karsten M Heeger, A Mark Jones, Kareem Kazkaz, Jared A Kofron, Callum Lamb, Benjamin H LaRoque, Eric Machado, Elizabeth L McBride, Michael L Miller, Benjamin Monreal, Prajwal Mohanmurthy, James A Nikkel, Noah S Oblath, Walter C Pettus, R G Hamish Robertson, Leslie J Rosenberg, Gray Rybka, Devyn Rysewyk, Luis Saldaña, Penny L Slocum, Matthew G Sternberg, Jonathan R Tedeschi, Thomas Thümmler, Brent A VanDevender, Laura E Vertatschitsch, Megan Wachtendonk, Jonathan Weintroub, Natasha L Woods, André Young, and Evan M Zayas. Determining the neutrino mass with cyclotron radiation emission spectroscopy – Project 8. *Journal of Physics G: Nuclear and Particle Physics*, 44(5):054004, Mar 2017.

[47] Anonymous. Minutes of the philadelphia meeting december 28, 29, 30, 1926. *Phys. Rev.*, 29:350–373, Feb 1927.

[48] J. B. Johnson. Thermal agitation of electricity in conductors. *Phys. Rev.*, 32:97–109, Jul 1928.

[49] H. Nyquist. Thermal agitation of electric charge in conductors. *Phys. Rev.*, 32:110–113, Jul 1928.

[50] Analog Devices. *High Gain Bandwidth Product, Precision FastFET Op Amp*, 2012. Rev. B.

[51] H. W. Bode. Relations between attenuation and phase in feedback amplifier design. *The Bell System Technical Journal*, 19(3):421–454, 1940.

[52] R.M. Fano. Theoretical limitations on the broadband matching of arbitrary impedances. *Journal of the Franklin Institute*, 249(1):57–83, 1950.

[53] M. Wohlers. On gain-bandwidth limitations for physically realizable systems. *IEEE Transactions on Circuit Theory*, 12(3):329–333, 1965.

[54] Govind P. Agrawal. *Nonlinear Fiber Optics*. Academic Press, fourth edition, 2006.

[55] William B. Case. The pumping of a swing from the standing position. *American Journal of Physics*, 64(3):215–220, 1996.

[56] Hugo Gernsback. Radio-Electronics, 1958.

[57] H Zimmer. Parametric Amplification of Microwaves in Superconducting Josephson Tunnel Junctions. *Appl. Phys. Lett*, 10:193, 1967.

[58] M A Castellanos-Beltran and K W Lehnert. Widely tunable parametric amplifier based on a superconducting quantum interference device array resonator. *Appl. Phys. Lett*, 91:83509, 2007.

[59] R. Vijay, D. H. Slichter, and I. Siddiqi. Observation of quantum jumps in a superconducting artificial atom. *Physical Review Letters*, 106(11):110502, Mar 2011.

[60] K. W. Murch, S. J. Weber, C. Macklin, and I. Siddiqi. Observing single quantum trajectories of a superconducting quantum bit. *Nature*, 502(7470):211–214, Oct 2013.

[61] D. Ristè, M. Dukalski, C. A. Watson, G. De Lange, M. J. Tiggelman, Ya M. Blanter, K. W. Lehnert, R. N. Schouten, and L. Dicarlo. Deterministic entanglement of superconducting qubits by parity measurement and feedback. *Nature*, 502(7471):350–354, Oct 2013.

[62] Jinsu Kim, Ohjoon Kwon, Çağlar Kutlu, Woohyun Chung, Andrei Matlashov, Sergey Uchaikin, Arjan Ferdinand Van Loo, Yasunobu Nakamura, Seonjeong Oh, Hee Su Byun, Danho Ahn, and Yannis K. Semertzidis. Near-Quantum-Noise Axion Dark Matter Search at CAPP around 9.5 μeV. *Physical Review Letters*, 130(9):1–6, 2023.

[63] T. Yamamoto, K. Inomata, M. Watanabe, K. Matsuba, T. Miyazaki, W. D. Oliver, Y. Nakamura, and J. S. Tsai. Flux-driven Josephson parametric amplifier. *Applied Physics Letters*, 93(4), 2008.

[64] B Yurke, M L Roukes, R Movshovich, and A N Pargellis. A low-noise series-array Josephson junction parametric amplifier. *Appl. Phys. Lett*, 69:3078, 1996.

[65] Leonardo Ranzani, Guilhem Ribeill, Brian Hassick, and Kin Chung Fong. Wideband josephson parametric amplifier with integrated transmission line transformer. In *2022 IEEE International Conference on Quantum Computing and Engineering (QCE)*, pages 314–319, 2022.

[66] O. Yaakobi, L. Friedland, C. Macklin, and I. Siddiqi. Parametric amplification in Josephson junction embedded transmission lines. *Physical Review B - Condensed Matter and Materials Physics*, 87(14), Apr 2013.

[67] Kevin O'Brien, Chris Macklin, Irfan Siddiqi, and Xiang Zhang. Resonant phase matching of Josephson junction traveling wave parametric amplifiers. *Physical Review Letters*, 113(15), Oct 2014.

[68] T. C. White, J. Y. Mutus, I. C. Hoi, R. Barends, B. Campbell, Yu Chen, Z. Chen, B. Chiaro, A. Dunsworth, E. Jeffrey, J. Kelly, A. Megrant, C. Neill, P. J.J. O'Malley, P. Roushan, D. Sank, A. Vainsencher, J. Wenner, S. Chaudhuri, J. Gao, and John M. Martinis. Traveling wave parametric amplifier with Josephson junctions using minimal resonator phase matching. *Applied Physics Letters*, 106(24), Jun 2015.

[69] C. Macklin, K. O'Brien, D. Hover, M. E. Schwartz, V. Bolkhovsky, X. Zhang, W. D. Oliver, and I. Siddiqi. A near-quantum-limited Josephson traveling-wave parametric amplifier. *Science*, 350(6258):307–310, Oct 2015.

[70] C. Bockstiegel, J. Gao, M. R. Vissers, M. Sandberg, S. Chaudhuri, A. Sanders, L. R. Vale, K. D. Irwin, and D. P. Pappas. Development of a broadband NbTiN traveling wave parametric amplifier for MKID readout. In *Journal of Low Temperature Physics*, volume 176, pages 476–482. Springer New York LLC, 2014.

[71] Wenlei Shan, Yutaro Sekimoto, and Takashi Noguchi. Parametric Amplification in a Superconducting Microstrip Transmission Line. *IEEE Transactions on Applied Superconductivity*, 26(6), Sep 2016.

[72] M. R. Vissers, R. P. Erickson, H. S. Ku, Leila Vale, Xian Wu, G. C. Hilton, and D. P. Pappas. Low-noise kinetic inductance traveling-wave amplifier using three-wave mixing. *Applied Physics Letters*, 108(1), Jan 2016.

[73] S. Chaudhuri, D. Li, K. D. Irwin, C. Bockstiegel, J. Hubmayr, J. N. Ullom, M. R. Vissers, and J. Gao. Broadband parametric amplifiers based on nonlinear kinetic inductance artificial transmission lines. *Applied Physics Letters*, 110(15):152601, Apr 2017.

[74] M. Malnou, M. R. Vissers, J. D. Wheeler, J. Aumentado, J. Hubmayr, J. N. Ullom, and J. Gao. A three-wave mixing kinetic inductance traveling-wave amplifier with near-quantum-limited noise performance. *arXiv*, Jul 2020.

[75] Patrick Winkel, Ivan Takmakov, Dennis Rieger, Luca Planat, Wiebke Hasch-Guichard, Lukas Grünhaupt, Nataliya Maleeva, Farshad Foroughi, Fabio Henriques, Kiril Borisov, Julian Ferrero, Alexey V. Ustinov, Wolfgang Wernsdorfer, Nicolas Roch, and Ioan M. Pop. Non-degenerate parametric amplifiers based on dispersion engineered Josephson junction arrays. Sep 2019.

[76] Luca Planat, Arpit Ranadive, Remy Dassonneville, Javier Puertas Martinez, Sebastien Leger, Cecile Naud, Olivier Buisson, Wiebke Hasch-Guichard, Denis M. Basko, and Nicolas Roch. A photonic crystal Josephson traveling wave parametric amplifier. *Physical Review X*, 10, Jul 2020.

[77] Tom Dixon, Jacob W. Dunstan, George B. Long, Jonathan M. Williams, Phil J. Meeson, and Connor D. Shelly. Capturing Complex Behaviour in Josephson Travelling Wave Parametric Amplifiers. Dec 2019.

[78] Nicholas Zobrist, Byeong Ho Eom, Peter Day, Benjamin A. Mazin, Seth R. Meeker, Bruce Bumble, Henry G. LeDuc, Grégoire Coiffard, Paul Szypryt, Neelay Fruitwala, Isabel Lipartito, and Clint Bockstiegel. Wide-band parametric amplifier readout and resolution of optical microwave kinetic inductance detectors. *Applied Physics Letters*, 115(4):042601, Jul 2019.

[79] A. A. Adamyan, S. E. De Graaf, S. E. Kubatkin, and A. V. Danilov. Superconducting microwave parametric amplifier based on a quasi-fractal slow propagation line. *Journal of Applied Physics*, 119(8):1–9, 2016.

[80] L. Ranzani, M. Bal, Kin Chung Fong, G. Ribeill, X. Wu, J. Long, H. S. Ku, R. P. Erickson, D. Pappas, and T. A. Ohki. Kinetic inductance traveling-wave amplifiers for multiplexed qubit readout. *Applied Physics Letters*, 113(24), 2018.

[81] Samuel Goldstein, Naftali Kirsh, Elisha Svetitsky, Yuval Zamir, Ori Hachmo, Clovis Eduardo Mazzotti De Oliveira, and Nadav Katz. Four wave-mixing in a microstrip kinetic inductance travelling wave parametric amplifier. *Applied Physics Letters*, 116(15), 2020.

[82] S. Shu, N. Klimovich, B. H. Eom, A. D. Beyer, R. Basu Thakur, H. G. Leduc, and P. K. Day. Nonlinearity and wide-band parametric amplification in a (Nb,Ti)N microstrip transmission line. *Physical Review Research*, 3(2):1–9, 2021.

[83] M. Malnou, J. Aumentado, M.R. Vissers, J.D. Wheeler, J. Hubmayr, J.N. Ullom, and J. Gao. Performance of a kinetic inductance traveling-wave parametric amplifier at 4 Kelvin: Toward an alternative to semiconductor amplifiers. *Phys. Rev. Appl.*, 17:044009, Apr 2022.

[84] S Golwala, A Beyer, D Datta, F Defrance, J Sayers, B H Eom, and P Day. Rf loss tangent and two-level-system noise of amorphous silicon and crystalline silicon dielectrics for mm/submm/FIR astronomy applications, poster. In *18th International Workshop on Low Temperature Detectors*, 2019.

[85] B.T. Buijtendorp, S. Vollebregt, K. Karatsu, D.J. Thoen, V. Murugesan, K. Kouwenhoven, S. Hähnle, J.J.A. Baselmans, and A. Endo. Hydrogenated amorphous silicon carbide: A low-loss deposited dielectric for microwave to submillimeter-wave superconducting circuits. *Phys. Rev. Appl.*, 18:064003, Dec 2022.

[86] Nikita Sergeevich Klimovich. *Traveling Wave Parametric Amplifiers and Other Nonlinear Kinetic Inductance Devices*. PhD thesis, California Institute of Technology, 2022.

[87] C. N. Thomas, S. Withington, Z. Sun, T. Skyrme, and D. J. Goldie. Nonlinear effects in superconducting thin film microwave resonators. *New Journal of Physics*, 22(7), 2020.

[88] Songyuan Zhao, S Withington, D J Goldie, and C N Thomas. Suppressed-gap millimetre wave kinetic inductance detectors using DC-bias current. *Journal of Physics D: Applied Physics*, 53(34), 2020.

[89] Christopher N. Thomas, Stafford Withington, and Songyuan Zhao. Effects of reactive, dissipative and rate-limited nonlinearity on the behaviour of superconducting resonator parametric amplifiers. 2022.

[90] Songyuan Zhao, S. Withington, and C. N. Thomas. Nonlinear characteristics of Ti, Nb, and NbN superconducting resonators for parametric amplifiers. *Superconductor Science and Technology*, 36(10):1–13, 2023.

[91] A. Anthore, H. Pothier, and D. Esteve. Density of states in a superconductor carrying a supercurrent. *Phys. Rev. Lett.*, 90:127001, Mar 2003.

[92] H. Kamerlingh Onnes. Further experiments with liquid helium. *Leiden Comm.*, 120b, 122b, 124c, 1911.

[93] W Meissner and R Ochsenfeld. Ein neuer Effekt bei Eintritt der Supraleitfähigkeit. *Naturwissenschaften*, 21:787–788, 1933.

[94] F. London and H. London. The electromagnetic equations of the supraconductor. *Proceedings of the Royal Society of London. Series A - Mathematical and Physical Sciences*, 149(866):71–88, 1935.

[95] V. L. Ginzburg and L. D. Landau. On the theory of superconductivity. *Zh. Eksperim. Teor. Fiz.*, 20:1064, 1950.

[96] V. L. Ginzburg and L. D. Landau. *On the Theory of Superconductivity*, pages 113–137. Springer Berlin Heidelberg, Berlin, Heidelberg, 2009.

[97] J. Bardeen, L. N. Cooper, and J. R. Schrieffer. Microscopic theory of superconductivity. *Phys. Rev.*, 106:162–164, Apr 1957.

[98] J. Bardeen, L. N. Cooper, and J. R. Schrieffer. Theory of superconductivity. *Phys. Rev.*, 108:1175–1204, Dec 1957.

[99] Leon N. Cooper. Bound electron pairs in a degenerate Fermi gas. *Phys. Rev.*, 104:1189–1190, Nov 1956.

[100] D.C. Mattis and J. Bardeen. Theory of the anomalous skin effect in normal and superconducting metals. *Physical Review*, 111(2):412–417, 1958.

[101] Jonas Zmuidzinas. Superconducting Microresonators: Physics and Applications. *The Annual Review of Condensed Matter Physics is Annu. Rev. Condens. Matter Phys*, 3:169–214, 2012.

[102] R Meservey and P M Tedrow. Measurements of the Kinetic Inductance of Superconducting Linear Structures. *Journal of Applied Physics*, 40:2028–2034, 1969.

[103] A R Kerr. Surface Impedance of Superconductors and Normal Conductors in EM Simulators 1, 1999.

[104] Benjamin A. Mazin. Superconducting Materials for Microwave Kinetic Inductance Detectors. 2020.

[105] Byeong Ho Eom, Peter K. Day, Henry G. Leduc, and Jonas Zmuidzinas. A wideband, low-noise superconducting amplifier with high dynamic range. *Nature Physics*, 8 (Suppl.)(8):623–627, 2012.

[106] E. F.C. Driessen, P. C.J.J. Coumou, R. R. Tromp, P. J. De Visser, and T. M. Klapwijk. Strongly disordered tin and NbTiN S-wave superconductors probed by microwave electrodynamics. *Physical Review Letters*, 109(10):1–5, 2012.

[107] B. Sacépé, C. Chapelier, T. I. Baturina, V. M. Vinokur, M. R. Baklanov, and M. Sanquer. Disorder-induced inhomogeneities of the superconducting state close to the superconductor-insulator transition. *Phys. Rev. Lett.*, 101:157006, Oct 2008.

[108] J. Gao, M. R. Vissers, M. O. Sandberg, F. C. S. da Silva, S. W. Nam, D. P. Pappas, D. S. Wisbey, E. C. Langman, S. R. Meeker, B. A. Mazin, H. G. Leduc, J. Zmuidzinas, and K. D. Irwin. A titanium-nitride near-infrared kinetic inductance photon-counting detector and its anomalous electrodynamics. *Applied Physics Letters*, 101(14):142602, 10 2012.

[109] David M Pozar. *Pozar. Microwave Engineering.* John Wiley & Sons, Inc., fourth edition, 2012.

[110] Songyuan Zhao, S. Withington, D. J. Goldie, and C. N. Thomas. Loss and saturation in superconducting travelling-wave parametric amplifiers. *Journal of Physics D: Applied Physics*, 52(41), Jul 2019.

[111] Robert W. Boyd. *Nonlinear Optics.* Academic Press, third edition, 2008.

[112] Saptarshi Chaudhuri. *Measurement , Simulation , and Design of the Dispersion-Engineered Traveling-Wave Kinetic Inductance Amplifier.* PhD thesis, California Institute of Technology, 2013.

[113] Rolf Landauer. Parametric amplification along nonlinear transmission lines. *Journal of Applied Physics*, 31(3):479–484, 1960.

[114] Aaron D. O'Connell, M. Ansmann, R. C. Bialczak, M. Hofheinz, N. Katz, Erik Lucero, C. McKenney, M. Neeley, H. Wang, E. M. Weig, A. N. Cleland, and J. M. Martinis. Microwave dielectric loss at single photon energies and millikelvin temperatures. *Applied Physics Letters*, 92(11):1–4, 2008.

[115] Saptarshi Chaudhuri, Jiansong Gao, and Kent Irwin. Simulation and analysis of superconducting traveling-wave parametric amplifiers. *IEEE Transactions on Applied Superconductivity*, 25(3), Jun 2015.

[116] D. M. Glowacka, D. J. Goldie, S. Withington, H. Muhammad, G. Yassin, and B. K. Tan. Development of a NbN Deposition Process for Superconducting Quantum Sensors. pages 3–7, 2014.

[117] Songyuan Zhao, D. J. Goldie, C. N. Thomas, and S. Withington. Calculation and measurement of critical temperature in thin superconducting multilayers. *Superconductor Science and Technology*, 31(10), 2018.

[118] Faouzi Boussaha, Samir Beldi, Alessandro Monfardini, Jie Hu, Martino Calvo, Christine Chaumont, Florence Levy-Bertrand, Thibaut Vacelet, Alessandro Traini, Josiane Firminy, Michel Piat, and Florent Reix. Development of TiN Vacuum-Gap Capacitor Lumped-Element Kinetic Inductance Detectors. *Journal of Low Temperature Physics*, 199(3-4):994–1003, 2020.

[119] Songyuan Zhao and Stafford Withington. Quantum analysis of second-order effects in superconducting travelling-wave parametric amplifiers. *Journal of Physics D: Applied Physics*, 54(36):365303, jun 2021.

[120] Joseph C. Longden, Faouzi M. Boussaha, Christine Chaumont, Kitti Ratter, and Boon-Kok Tan. Preliminary characterisation of titanium nitride thin film at 300 mK for the development of kinetic inductance travelling wave parametric amplifiers. *Quantum Technology: Driving Commercialisation of an Enabling Science II*, 1188113(October 2021):38, 2021.

[121] A. Kher, P. K. Day, B. H. Eom, J. Zmuidzinas, and H. G. Leduc. Kinetic Inductance Parametric Up-Converter. *Journal of Low Temperature Physics*, 184(1-2):480–485, 2016.

[122] Henry G. Leduc, Bruce Bumble, Peter K. Day, Byeong Ho Eom, Jiansong Gao, Sunil Golwala, Benjamin A. Mazin, Sean McHugh, Andrew Merrill, David C. Moore, Omid Noroozian, Anthony D. Turner, and Jonas Zmuidzinas. Titanium nitride films for ultrasensitive microresonator detectors. *Applied Physics Letters*, 97(10):1–4, 2010.

[123] Paul Nicaise. *Development of Microwave Kinetic Inductance Detectors for Applications in Optical to Near-IR Astronomy.* PhD thesis, Observatoire de Paris, PSL Université, 2022.

[124] Anritsu Company. *IMD Measurements Using Dual Source and Multiple Source Control*, 2015.

[125] Michael R. Vissers, Jiansong Gao, Jeffrey S. Kline, Martin Sandberg, Martin P. Weides, David S. Wisbey, and David P. Pappas. Characterization and in-situ monitoring of sub-stoichiometric adjustable superconducting critical temperature titanium nitride growth. *Thin Solid Films*, 548:485–488, 2013.

[126] M. V. Feigel'man and M. A. Skvortsov. Universal broadening of the bardeen-cooper-schrieffer coherence peak of disordered superconducting films. *Phys. Rev. Lett.*, 109:147002, Oct 2012.

[127] David Johannes Thoen, Boy Gustaaf Cornelis Bos, E. A.F. Haalebos, T. M. Klapwijk, J. J.A. Baselmans, and Akira Endo. Superconducting NbTin Thin Films with Highly Uniform Properties over a 100 mm Wafer. *IEEE Transactions on Applied Superconductivity*, 27(4):1–5, 2017.

[128] Songyuan Zhao. *Physics of Superconducting Travelling-Wave Parametric Amplifiers*. PhD thesis, University of Cambridge, 2022.

[129] Songyuan Zhao, S Withington, and C N Thomas. Nonlinear mechanisms in Al and Ti superconducting travelling-wave parametric amplifiers. *Journal of Physics D: Applied Physics*, 55(36):365301, Jun 2022.

[130] C. Kow, V. Podolskiy, and A. Kamal. Self phase-matched broadband amplification with a left-handed Josephson transmission line. 2022.

[131] Jack Y. Qiu, Arne Grimsmo, Kaidong Peng, Bharath Kannan, Benjamin Lienhard, Youngkyu Sung, Philip Krantz, Vladimir Bolkhovsky, Greg Calusine, David Kim, Alex Melville, Bethany M. Niedzielski, Jonilyn Yoder, Mollie E. Schwartz, Terry P. Orlando, Irfan Siddiqi, Simon Gustavsson, Kevin P. O'Brien, and William D. Oliver. Broadband squeezed microwaves and amplification with a Josephson travelling-wave parametric amplifier. *Nature Physics*, 19(5):706–713, 2023.

[132] K. Inoue. Four-wave mixing in an optical fiber in the zero-dispersion wavelength region. *Journal of Lightwave Technology*, 10(11):1553–1561, 1992.

[133] Osamu Aso, Masateru Tadakuma, and Shu Namiki. Four-wave mixing in optical fibers and its applications. *Furukawa Review*, (19):63–68, 2000.

[134] Publication In Preparation.

[135] Kitti Ratter and Boon Kok Tan. A dispersion-engineered josephson travelling wave parametric amplifier with periodic impedance perturbation. *Proceedings of the 31st Symposium on Space Terahertz Technology, ISSTT 2020*, pages 94–97, 2020.

[136] R.S. Engelbrecht and K. Kurokawa. A wide-band low noise l-band balanced transistor amplifier. *Proceedings of the IEEE*, 53(3):237–247, 1965.

[137] K. Kurokawa. Design theory of balanced transistor amplifiers. *Bell System Technical Journal*, 44(8):1675–1698, 1965.

[138] Roberto Quaglia and Steve Cripps. A load modulated balanced amplifier for telecom applications. *IEEE Transactions on Microwave Theory and Techniques*, 66(3):1328–1338, 2018.

[139] Weijuan Chen, Yongle Wu, Shaobo Li, and Weimin Wang. Fully-integrated broadband gaas mmic load modulated balanced amplifier for sub-6 ghz applications. *IEEE Transactions on Circuits and Systems II: Express Briefs*, 70(8):2834–2838, 2023.

[140] Saeedeh Makhsuci, Seyedeh Masoumeh Navidi, Mihai Sanduleanu, and Mohammed Ismail. A review of doherty power amplifier and load modulated balanced amplifier for 5g technology. *International Journal of Circuit Theory and Applications*, 51(5):2422–2445, 2023.

[141] T Sweetnam, D Banys, V Gilles, M A McCulloch, and L Piccirillo. Simulating the behaviour of travelling wave superconducting parametric amplifiers using a commercial circuit simulator. *Superconductor Science and Technology*, 35(9):095011, Aug 2022.